Crystal Engineering of Anisotropic Gold Nanoparticles through Modulation of Seed Size and Crystal Structure

Zeliha Cansu Canbek

UNIVERSITÉ DE VERSAILLES ST-QUENTIN-EN-YVELINES

UFR DES SCIENCES

THESE DE DOCTORAT DE L'UNIVERSITE DE VERSAILLES SAINT-QUENTIN-EN-YVELINES

Présentée par

Zeliha Cansu Canbek

Crystal Engineering of Anisotropic Gold Nanoparticles through Modulation of Seed Size and Crystal Structure

« Influence de taille et de la structure des germes dans la formation de nanoparticules d'or Anisotropes »

Soutenue le 16 Décembre 2014 devant le jury composé de :

Chantal Larpent	Professeur-UVSQ, Versaille	Présidente
Laurence Motte	Professeur-Université Paris-Nord	Rapporteuse
Francois Ribot	Chargé de Recherche-LCMCP, Paris	Rapporteur
Suzanne Giorgio	Professeur-AMU, Marseille	Examinateur
Hynd Remita	Directrice de Recherche-Université Paris-Sud	Examinatrice
Mona Treguer-Delapierre	Maitre de Conférence, Université de Bordeaux	Examinatrice
Fabienne Testard	Chercheuse, CEA,Saclay	Directrice de thèse
Nicolas Menguy	Professeur-UPMC, Paris	Co-Directeur de thèse

THESE DE DOCTORAT DE

L'UNIVERSITE DE VERSAILLES SAINT-QUENTIN-EN-YVELINES

Présentée par

Zeliha Cansu Canbek

pour obtenir le grade de

DOCTEUR de l'UNIVERSITE de VERSAILLES SAINT-QUENTIN-En-YVELINES

Domaine: Physico-Chimie

Crystal Engineering of Anisotropic Gold Nanoparticles through Modulation of Seed Size and Structure

Influence de taille et de la structure des germes dans la formation de nanoparticules d'or Anisotropes

Soutenue le 16 Décembre 2014 devant le jury composé de :

Chantal Larpent	Professeur-UVSQ, Versaille	Présidente
Laurence Motte	Professeur-Université Paris-Nord	Rapporteuse
Francois Ribot	Chargé de Recherche-LCMCP, Paris	Rapporteur
Suzanne Giorgio	Professeur-AMU, Marseille	Examinateur
Hynd Remita	Directrice de Recherche-Université Paris-Sud	Examinatrice
Mona Treguer-Delapierre	Maitre de Conférence, Université de Bordeaux	Examinatrice
Fabienne Testard	Chercheuse, CEA,Saclay	Directrice de thèse
Nicolas Menguy	Professeur-UPMC, Paris	Co-Directeur de thèse

Acknowledgements

People who know me would agree that my journey in Paris during my PhD thesis have been quite colorful. So now I would like to use this opportunity to express my gratitude to everyone who supported me throughout this time and participated to this colorful journey with me.

To begin with, I would like to express my special appreciation and thanks to the thesis committee members, Laurence Motte and Francois Ribot for accepting to be reporters on this dissertation. I also want to thank to Suzanne Giorgio, Hynd Remita and Mona Treguer-Delapierre for their participation to my thesis as jury members and Chantal Larpent for directing as president.

During my PhD thesis I was lucky because instead of having one I had three incredible scientists supporting me all this time as my supervisors. Fabienne Testard, you have been a tremendous mentor for me during this time. Thank you for allowing me to grow as a research scientist with your strong guidance, priceless advices and end full patience. Nicolas Menguy, this project would not be possible without your valuable contributions. You enthusiasm and immense knowledge helped me all this time to improve myself and become better every day. And lastly Olivier Spalla, your inspiring ideas were most valuable during this research and making it possible me to accomplish this PhD.

In this ANR project I had the honor to work with great scientist whom I am truly grateful. Luc Belloni, Florent Malloggi, Claudine Noguera, Jacek Goniakowski, Ali Abou Hassan and Veronique Peyre thank you for your insightful comments and precious discussions. I am so glad to meet both Robinson Cortes-Huerto and Blaise Fleury great young scientists and sincere friends.

If you have read my thesis you would understand that this work has been achieved mostly with the help of our valuable collaborators: Damien Alloyeau, Guillaume Yangshu Wang and Christian Ricolleau thank you for your great help and patience during *in-situ* STEM experiments. Ovidiu Ersen, Simona Moldovan and Andreas Wisnet thank you for your contributions to this thesis with the tomography experiments. Hynd Remita, thank you for letting us this opportunity to use gamma source for radiolysis experiments and obtaining the most beautiful nanorods sample that we have ever produced. Lastly Pierre-Eugene Coluon, thank you for your helps in microscopy experiments.

I was cherished with great colloquies during this journey who motivate me every day and helped me to pass such a memorable time in LIONS, CEA. So thank you so much Elodie, Valerie, Olivier Tache, Michelle, Stephanie, Debasish, Sergio and all the other members of LIONS team.

And lastly, I am incredibly grateful to my two families: to my mother, aunt and brothers for supporting me all my life and to my surrogate family Brigitte Barraud and Dominique Coudignac for making my life easier here 3000 km away from my home town. I will always be there for you when you need me as you were for me.

Sebastien Monteagudo, thank you for telling me that everything will be perfect. In fact you were right, it did. I hope we meet again one day.

Abstract

Between the ongoing research on various type of nanomaterials to tune the particle size and crystal design in nanoscale for their potential applications, anisotropic gold nanoparticles has attracted the most intention not only because of their divine color but also their enhanced catalytic activities, optical properties and electrical conductivities. Event though, many efforts have been already made in the field of synthesis of anisotropic gold nanoparticles, with defined sizes and structures, growth mechanism of many unique anisotropic shapes is still a controversial subject.

Overall objective of this thesis is to understand the origin of anisotropy during the formation of anisotropic gold nanoparticles, especially gold nanorods, in liquid phase. For our envisaged aim, between numerous synthetic methods developed for production of nanoparticles, seed mediated approach is chosen for the fabrication of final anisotropic gold nanoparticles from small seeds which is grown into final nanoparticle later on. During the synthesis of nanoparticles, those seeds play critical role as precursors to control the yield of and the crystal structure of final anisotropic nanoparticle. Here we offer a systematical study on the origin of anisotropy with respect to “seed size” and “crystal morphology”. Since these small particles are the genesis of anisotropic metal nanoparticle synthesis, in this thesis we answer following questions to explain the origin of anisotropy;

i. How to control the crystal structure and the size of the seeds?

ii. What are the influences of controlled seed size and structure on the kinetics of nanoparticle growth?

Résume

De par leurs nombreuses applications potentielles, de nombreux efforts de recherche ont été poursuivis dans le domaine de la synthèse de nanoparticules. Cependant le mécanisme à l'origine des formes anisotropes de nanoparticules d'or, pour une taille et une structure bien définies, reste encore un sujet controverse.

L'objectif général de cette thèse est de comprendre l'origine de cette anisotropie, lors de la formation de nanoparticules d'or, en particulier sous la forme de nano-bâtonnets d'or, en phase liquide. Parmi les nombreux procédés de synthèse existants, la "synthèse de particules anisotropes par croissance à partir de germes" a été retenu, car il permet un contrôle précis de la taille et de la structure des nanoparticules. Lors de la synthèse de nanoparticules, les germes jouent un rôle de précurseur et permettent ainsi de maitriser la structure cristalline des nanoparticules finales. Si le rôle crucial des germes a déjà pu être étudié par différents groupes de recherche, une étude systématique sur la genèse de l'anisotropie par rapport à la taille et la structure initale des germes restait à réaliser. Ce travail a ainsi pour objectif de répondrre aux deux questions :

i. Comment contrôler la structure cristalline et de la taille des germes?

ii. Quelles sont les influences de la taille des germes et de leur structure sur la cinétique de la croissance?

Table of Contents

Abbreviations

AuNPS	Gold nanoparticles
GNR	Gold Nanorods
BIPY	Bipyramid
UV	Ultra-Violet Visible Spectroscopy
SAXS	Small Angle X-Ray Scattering
DLS	Dynamic Light Scattering
PdI	Polydispersity Index
TEM	Transmission Electron Microscopy
HRTEM	High Resolution Transmission Electron Microscopy
FFT	Fast Fourier Transformation
AR	Aspect Ratio
CTAB	Cetyl-trimethyl ammonium bromide
CTAC	Cetyl-trimethyl ammonium chloride
DTAB	Dodecyl- ammonium bromide
WAXS	Wide Angle X-Ray Scattering
UPD	Under Potential Deposition
STEM	Scanning Transmission Electron Microcopy
HAADF-STEM	High angle annular dark field STEM
SC	Single Crystal
PTC	Penta-twinned Crystal
MTC	Multi-twinned Crystal
AA	L-Ascorbic Acid
SPR	Surface Plasmon Resonance
L-SPR	Longitudinal Surface Plasmon Resonance
T-SPR	Transversal Surface Plasmon Resonance

Introduction

Creating stronger, lighter, more reactive or more conductive materials to be used in technological innovations, biomedicine or energy sectors, is one of the strong reason that pushes scientists to produce nanoparticles. Indeed, the bottom-up approach of nanotechnology will make use of nanoparticles as first building units and aims to assemble them into the materials of future. So the first challenge before any application is to produce nanoparticles with desired properties, to benefit from the strong size and morphology dependence of the properties of materials with one nano scale dimension. By controlling these two parameters, the properties of a chosen nano system can be tuned for the desired application. Further success of the targeted application is generally defined by the homogeneity of the size and the shape of the nanoparticles employed and the means (*physical, chemical*) to tune their properties.

Among various types of nanomaterials, gold has attracted the most of the intention because of its optical properties, enhanced catalytic activities at very small scale and electrical conductivity. Listed improved properties can be ameliorated even more (*especially the optical ones*) when the shape of the gold nanoparticle is controlled to produce anisotropic morphologies. Such unusual shapes are the source of the optical response in near infrared region (> 800 nm), which makes them important candidates for biological applications. Even though many efforts have already been made in the field of anisotropic gold nanoparticle synthesis in water, with defined sizes and structures, the knowledge about the mechanism at the origin of the growth of many different anisotropic shapes (*rods, stars, bipyramids, beans*) is still incomplete.

Anisotropic gold nanoparticles in water are generally obtained through the seeded growth method in the presence of a mild reducing agent and an excess of surfactant, typically the bromide cetyl-trimethyl ammonium cationic ones. The specific role of this surfactant has been described both as a stabilizer for nanoparticles through 1) the formation of a double layer around the nanoparticles, which favors alimentation at the extremity of the nanorods 2) a stabilization of some facets (*due to its adsorption*) leading to their preferential formation and a micellar carrier of the reactants during the reaction. The promotion of anisotropy is strongly related to the nature and the concentration of different reactants and particularly the presence

of some added salt in the growth media. These salts can strongly modulate the adsorption properties of the surfactant, through a complex formation, leading to the stabilization of different facets of the particle. The kinetic of monomer alimentation is also an important parameter to preserve the anisotropy during the growth since faster kinetic unfavors the development of anisotropy. The temperature has also been shown to be a crucial parameter, hence, the temperature closer to Kraft point works in favor of the anisotropy. Finally the nature, size and the internal structure of seeds can modify the nature of the final anisotropic shapes obtained during the growth stage. As a consequence, the development of the anisotropy results from a complex interplay between the nature of the seeds and the conditions of the growth. That's why, obtaining a final states with homogeneous size and shape distribution, is quite difficult to achieve. Experimentally, the syntheses of anisotropic shapes are always polluted by other isotropic shapes and the post-synthetic purification steps are always needed. If some tendencies for the internal mechanism have been obtained from kinetic studies, the particular role of the seeds is not fully described until now [1,2].

To date there is no systematic study on the genesis of anisotropy with respect to "seed size" and "crystal morphology", analyzing the complete structural characterization of the initial and the final objects. With the general aim of understanding the origin of anisotropy, the driving's questions along the present thesis were:

i. How to control the crystal structure and the size of seeds?

ii. What are the influences of controlled seed size and structure on the kinetics of growth?

We have related the initial seeds to final nanoparticles by employing traditional techniques used for nanoparticle research (*UV-Vis Spectroscopy, Transmission Electron Microcopy, Dynamic Light Scattering and Small Angle X-Ray Scattering*) and a recent innovative technique *in-situ* Transmission Electron Microcopy designed to visualize the crystal growth in liquid state. Additionally, we have introduced an original competitive approach to emphasize the critical role played by the precursors, via simultaneous growth of different as-prepared seeds (*with non-identical size and crystal structure*) in the same reaction container.

The results of these studies unravel a general picture of the source of the anisotropy in gold nanoparticle systems and are reported here in five chapters with their key conclusions.

The opening chapter describes the brief history of the synthesis of anisotropic gold nanoparticles with the evaluation of seeds throughout the time.

In the second chapter, we discuss the growth kinetics of a set of well-characterized seeds (*with controlled crystal structure and size*) in a chosen growth media, using UV-Vis spectroscopy and transmission electron microscopy to quantify the growth kinetics.

For further understanding on the importance of the crystalline structure of seeds over the growth kinetics, an original competitive approach (*simultaneous growth of as prepared seeds in the same reaction container*) is used in chapter 3. Again, quantification of growth kinetics is achieved by spectroscopic and microscopic techniques.

Chapter 4 is dedicated to reveal the role of the growth solution during the formation of anisotropic nanoparticles, obtained in chapter 3 for a given seed (*nanorods and bipyramids*). The crystalline structures of both types of nanoparticles were analyzed by microscopy techniques as well as 3D re-constructed volume analysis obtained by electron tomography. Additionally, we examine the growth mechanism of bipyramids from initial seeds. The question regarding their symmetry is the main focus of the HRTEM and the 3D reconstruction experiments.

Finally in Chapter 5, results on the following the nucleation and growth of NPs in a confined cell, by using recent development in microscopy, *in-situ* STEM are presented, showing that other different shapes such as stars can also be produced in a reproducible manner. The general conclusion offers a perspective on the implications of the crucial importance of the seeds structure and the challenges still opened after this work regarding their control and use.

References

[1] A. Gole and C. J. Murphy, Chem Mater 16 (2004) 3633.

[2] Susanne Köppl, Seed-Mediated Synthesis of High Aspect Ratio Nanorods and Nanowires of Gold and Silver, Univ., Technische Universität München, 2011.

CHAPTER I

General Introduction

CHAPTER I

Chapter 1

General Introduction

1.1 Brief Overview on Metallic Nanoparticles

Production of unique metallic nanoparticles has been initiated by medieval artisans, through the discovery of alchemical experimentation. For instance, by adding gold chloride and silver nitrate to molten glass one can obtain red tint and yellow tint, respectively [1]. Although the reason of such optical property was not really known, the technique has been continuously used for coloring various artistic objects (*e.g. Lycurgus cup*) and windows of medieval churches (*e.g. Notre Dame Cathedral in Paris, Figure I.1*) through the history [1,2].

Figure I. 1 *South rose window of Notre Dame Cathedral from 13th century [1]*

Later on, growing technologies on imaging techniques helped scientist to understand that the reason of such coloration is due to the presence of different shaped colloidal metallic nanoparticles trapped in glass. Along the way, it has been discovered that when the matter is organized in nano scale, it gains various properties that are not available for bulk size, such as; higher strength, increased control of light spectrum, large surface area to volume ratio (*helping to improve the surface reactivity of the material*) [2], etc. Dependence of given properties to size, shape and composition of the metallic nanoparticles let them to find place in many different application fields ranging from catalysis, sensing, electronics, magnetics, photonics and biomedicine [3–7]. Since, all kind of applications of any nanomaterial require

particles with well-defined sizes and shapes, the control over given parameters became fundamental goal of material scientists. Nowadays, shape controlled synthesis of unique metallic nano structures possessing characteristic sizes can be realized by two different methods: top-down to bottom-up synthesis. In case of top down method, which is also known as break down, an external force is applied on solid metal to divide it into multiple smaller pieces. The bottom-up approach includes use of chemical or physical forces, operating at nanoscale, to assemble basic units into larger structures.

Among all metallic nanoparticles, gold has specific place and has been widely studied by material scientists.

1.2 Gold Nanoparticles: Why they are more valuable than bulk gold?

The case of gold has drawn strong interest in nanoscale materials; hence the physical and the chemical properties in nanoscale may considerably be different than the respected bulk metal itself. Change of the physical state of bulk gold bar into liquid ruby colored (*spherical*) gold nanoparticle solution is a good illustration of such variation (Figure I.2).

Figure I. 2 *Variation of properties between bulk gold and isotropic gold nanoparticles*

Optical response of such nanoparticle solution shown in Figure I.2, results from the collective oscillation of free conduction electrons in the metal surface under light irradiation at a resonance frequency, giving rise to significant surface plasmons resonance (SPR) [7]. This specific interaction with light has been first described by Mie theory, with a solution to Maxwell equations, explaining the scattering of electromagnetic radiation by sphere [8]. In his expression Mie defined the wavelength-dependent extinction cross section ($C_{ext}(\lambda)$) of a single particle as;

$$C_{ext}(\lambda) = \frac{24\pi^2 R^3 \varepsilon_m^{3/2}}{\lambda} \frac{\varepsilon''(\lambda)}{(\varepsilon'(\lambda)+2\varepsilon_m)+\varepsilon''(\lambda)^2} \quad (1.1)$$

in which, R is the radius of the particle and ε is the dielectric constant of the medium. Basically, this equation defines the energy loss in the direction of propagation of the incident light due to scattering and absorption of particle. As the size of the nanoparticle varies, the surface geometry changes resulting in a shift in the electric field density on the surface of the material. The frequency of this oscillation for spherical gold nanoparticles is found generally in the visible region of UV-Vis spectra (~520 nm). By changing the size of spherical nanoparticles, one can manipulate slightly the length of the plasmon peak to alter the optical properties of material [9] (Figure I. 3).

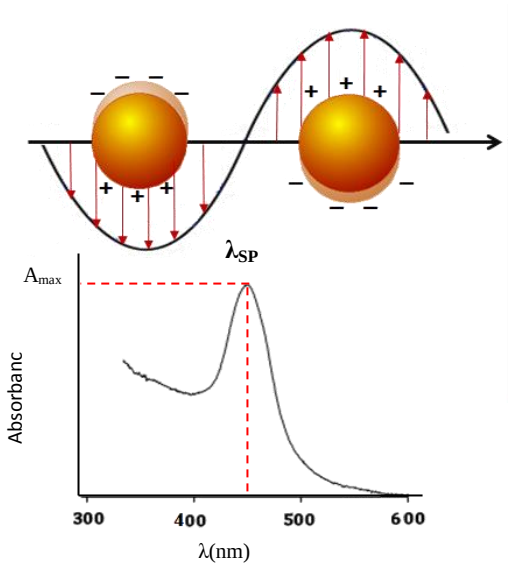

Figure I. 3 *Schematic representation of surface plasmon absorbance in gold spheres*

Such an optical advantage makes gold nanoparticles more valuable than bulk gold itself for various applications, like plasmonics where gold nanoparticles are used as biomedical labels and sensors [7,10]. Also gold plasmon resonance is the basis for enhanced spectroscopy techniques such as Surface Enhanced Raman Spectroscopy (SERS) [11] and Surface Enhanced Fluorescence Spectroscopy [12] which can be used to detect analytes with ultrahigh sensitivity. Given reasons are the origins of high interest on gold nanoparticles.

1.2.1 Anisotropic Gold Nanoparticles: Properties and Synthesis

When spherical gold nanoparticles are replaced with anisotropic analogues, like gold nanorods, the optical properties become much size dependent since single SPR in this case splits into two different modes; a transverse surface plasmon resonance (T-SPR), corresponding to the light absorption and scattering along the short axis of the particle, and a longitudinal surface plasmon resonance (L-SPR), corresponding to light absorption and scattering along the long axis of the particles as represented in Figure I.4 [9,13–15].

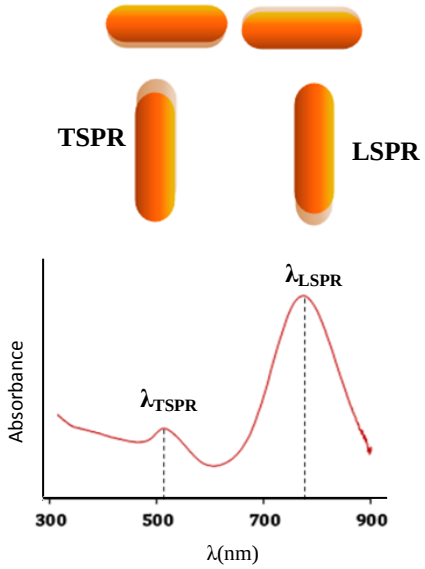

Figure I. 4 *Surface plasmon response of Gold nanorods showing distinct TSPR and LSPR*

The optical absorption spectrum of randomly oriented elongated plasmonic nanoparticles with defined aspect ratios (AR) has been first modelled by Gans in 1912 using the extension of the Mie theory [8,16]. In his expression it has been demonstrated that the position of the LSPR varies widely according to the aspect ratio of the particle (*length to diameter ratio, L/D*) [5] rather than absolute dimensions.

Apart from the optical features, electronical and magnetic properties of the anisotropic nanoparticles may also be superior to those obtained for spherical nanoparticles [17]. This kind of amelioration make them more desirable than the isotropic morphologies for variable applications like biomedicine, sensing, photo thermal therapy and photonic [5,6,15,18–20]. Since each type of application demands specific properties (*e.g. biomedical applications demanding a longitudinal absorption band located in the near infrared region*), shape control is strongly needed for anisotropic nanoparticles.

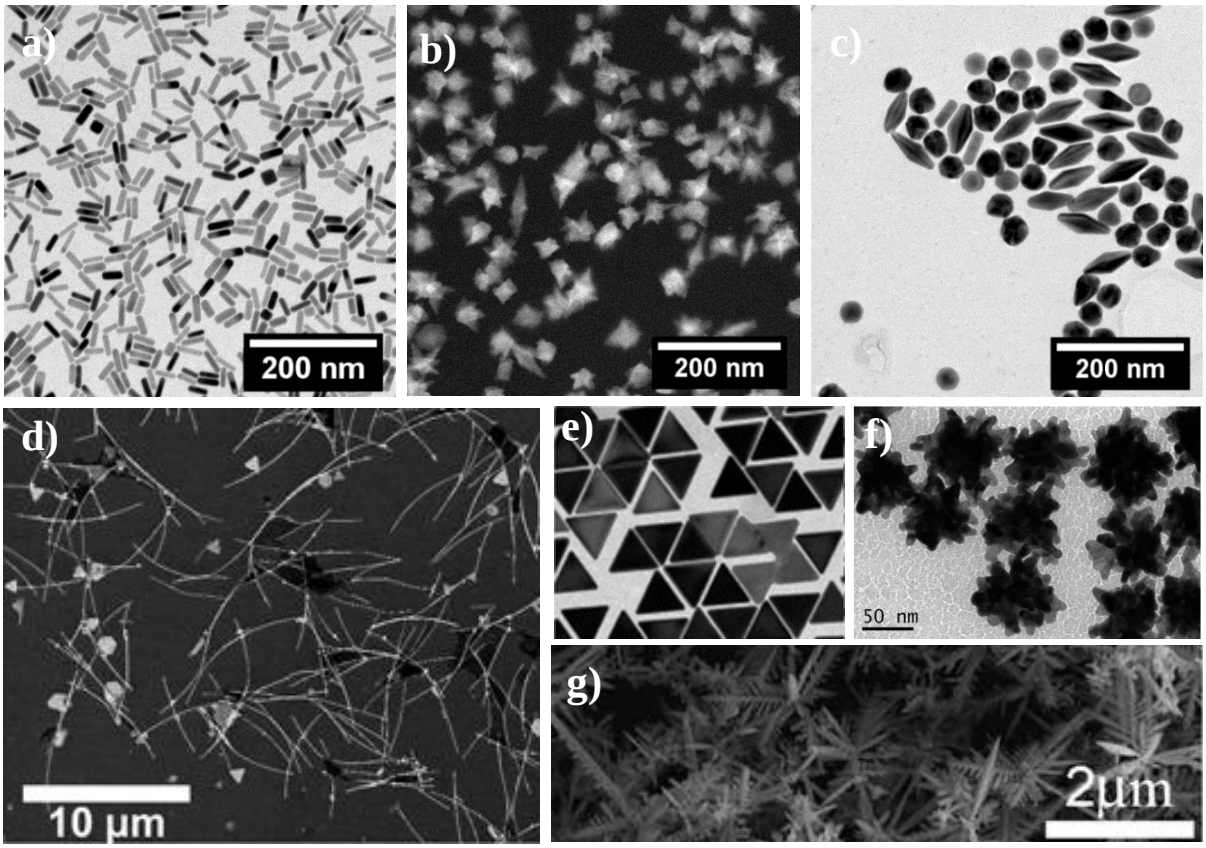

Figure I. 5 *Variety of Anisotropic AuNPs can be synthesized via seed mediated synthesis a) Nanorod b) Branched NPs with elongated pyramid like structures c) Bipyramids d) Nanowires [21] e) Nanotriangles [22]- f) Nanoflowers [20] g) Au Nanodentrites [23]*

The figure I.5 shows some exotic examples of different shaped nanoparticles that can be obtained for gold in solution, such as; nanorods, branched nanoparticles, triangle shapes, gold nanodentrites, etc. Between different shapes, first dedicated researches on anisotropy basically focus on nanorods (Figure I.5a). Today, the interest for bipyramids (Figure I.5c) is increasing due to higher plasmon enhancement properties related to their sharp tips [24]. Because of their potential applications in bio-sensing, imaging and potential vivo implementation due to their high tissue penetration, another remarkable and highly desired morphology is branched gold nanoparticles (Figure I.5b) [10,17,25].

Multiple methods can be used for the synthesis of given structures, in liquid phase, like; chemical reduction (*via strong reducing agent*)–, γ irradiation (*reduction by radicals and aqueous electrons*) [26,27], photochemical reduction etc. [28]. Whatever the way chosen to produce the nano material, there are crucial requirements that the final particles should exhibit: well defined sizes, shapes, crystal structures and compositions, minimum amount of

pollution from other shapes, high stability of the final dispersion, high reproducibility of synthesis and finally, low cost with high mass production [29].

Among different synthetic processes known to produce high yield of anisotropic gold nanoparticles, wet chemical synthesis via seed mediated approach is a well-known cost effective method for small scale production and easy handle of protocol. In the next section, we will focus on background, brief history and the mechanism of seed mediated synthesis of gold nanorods in liquid state. Mechanism of particle formation will be extended to other anisotropic analogues (*bipyramids and branched nanoparticles*) in the following chapters.

1.2.1.1. Milestones in Seed Mediated Synthesis of Gold Nanorods (GNRs)

Seed mediated synthesis, also known as "*two pot*" synthesis of nanorods in water solution, involves the preparation of small sized nanoparticles called seeds in one reaction pot and their growth into anisotropic structures in a second reaction pot. The chemical composition of the growth solution as well as the structure and the size of the seeds have great importance in the production of gold nanorods.

Nature of the seeds used for nanorod production has been modified over time, with respect to the type of reducing agent and the ligand used during preparation, to synthesize monocrystalline or multi-twinned nanorods with different aspect ratios and other additional shapes.

Today's version of seed mediated synthesis, known to obtain high yield nanorods, is developed in the early 2000's [28, 29]. Initially, the technique involved the use of sub-5 nm citrate capped seeds (*produced by the reduction of a gold salt, i.e. $HAuCl_4$, via a strong reducing agent, i.e. $NaBH_4$*) in a growth media containing high concentration of Cetyl-trimethyl ammonium bromide (CTAB) surfactant, gold precursor ($HAuCl_4$) and L-Ascorbic Acid (Vitamin C) as mild reducing agent. After being isolated, obtained gold nanorods can be grown further by following the same protocol, *i.e.* by replacing the initial seeds with obtained nanorod solution to attain higher aspect ratio gold nanorods (~20) with a typical penta-twinned crystal structures. The major drawback of this synthesis was the production of very low yield of nanorods during the first step of the growth (less than 5%).

The yield of nanorods later has been ameliorated by using small size CTAB seeds (1.5 nm) and introducing small amount of $AgNO_3$ into the growth solution [7, 29, 32]. However,

in this case the obtained nanorods exhibit single crystalline structures with smaller aspect ratios [9, 32]. It was established that by varying $AgNO_3$ concentration, one can control the aspect ratio of final nanorods and increase the yield up to 95%. Up to now the precise role played by each chemical compounds in the mechanism of production of gold nanorods is still not fully understood [15].

Later on, Liu and Guyot-Sionnest [33] have proven that pentagonal gold bipyramids, with multiple twining faults, can be prepared similarly in the presence of $AgNO_3$ via citrate capped seeds.

Lately, Murray et al. [34] have shown that the polydispersity in nanorod aspect ratio (AR) can be reduced by the use of organic additives in a growth solution (*e.g. 5-Bromosalicylic acid*) prepared with lower amount of surfactant, CTAB, (0.05 M) than known seed mediated methods (0.1 M). Systematical study, to understand the effect of salicylic acid on the synthesis of gold nanorods, revealed that this compound acts as both stabilizing factor by penetrating into the hydrophobic tail of CTAB molecules anchored on nanorod surface [34] and as a pre-reducing agent during the reduction of Au(I) from gold precursor, Au(III) [35].

Then, in opposition to seed mediated synthesis, Jana et al. [36] has developed a seedless synthesis based on the direct injection of a few amount of strong reducing agent into the growth solution with a similar composition as the seeded growth procedure. Here, the formation of small nuclei and their growth into nanorods arise in the same reaction container. The separation between the nucleation and the growth process is ensured by the difference in the kinetic of formation of seeds (*fast process*) and the growth of the formed seeds into final nanoparticles (*slow process*).

In conclusion, in case of seed mediated synthesis even though the technique has great deal of benefits to control the size and the structure of seeds to be grown in final nanoparticles, it lacks of reproducibility of seeds with similar sizes and crystal structures. Small fluctuations in the size of mentioned precursors can drastically change the yield of final nanoparticles. Therefore, it is important to emphasize the critical role of the seeds during the formation of anisotropy. Additionally, monodisperse GNRs are generally obtained after a long purification procedure involving high speed centrifugation. Such procedure may result with the modification of nanoparticle surface, sometimes ending up with an irreversible

aggregation. Yet, there is still needs for improving the synthetic scheme allowing the production of high yield of monodisperse nanorods without any purification procedure. The complexity of used solutions, the role of pH and the ionic strength render difficulties for full understanding of the mechanism and finally the optimization of the procedure. Understanding the accurate role of the seed and the growth solution would help researchers to produce high yield of anisotropic nanoparticles without the need for further purification.

1.2.1.2. Shape Control in Seed Mediated Synthesis of GNRs

For classical seed mediated growth of gold nananorods in liquid phase, there is a need to control the shape and the structure of the initial seeds as well as the composition of the growth solution used to propagate anisotropy on as-synthesized precursors since both factors play crucial role for development of anisotropy.

The effect of different parameters over the growth of gold nanorods can be followed by *in-situ* techniques (*UV-Vis Spectroscopy [37], Small Angle X-Ray Scattering (SAXS) [38]* and *X-ray Absorption Near Edge Structure (XANES)[39]*) as well as *ex-situ* techniques (*TEM, HRTEM, UV, SAXS* [15,20,38,39] *etc.).*

- **Role of Growth Solution in the Formation of Anisotropy**

  - In seed mediated synthesis, developed to obtain GNRs, the cationic surfactant CTAB, consisting of a hydrophilic cationic head group and a hydrophobic tail (Figure I.6a), has been employed traditionally as stabilizing agent to control the growth of anisotropic shape [40].

a)

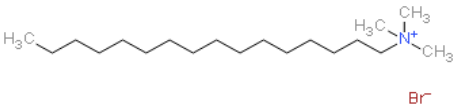

CTAB - Cetyl-trimethylammonium bromide

b)

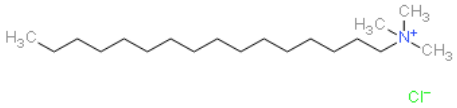

CTAC - Cetyl-trimethylammonium chloride

c)

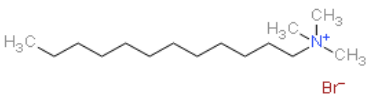

DTAB - Dodecyl-trimethyl-ammonium bromide

Figure I. 6 *Various surfactants used for the preparation of gold nanoparticles with different shapes a) CTAB b) CTAC and c) DTAB*

The first important role of CTAB is to form strong complexes with Au(III), Au(I) and Au(0) with a direct effect on the oxydo-reduction potential of the gold species. After the formation of initial CTA-Au(III) complex, a first reduction is achieved by the mild reducing agent, ascorbic acid (AA), via following chemical reaction (Eq. 1.2) [41];

$$\text{First reduction: } Au^{3+} + 2\,e^- \longrightarrow Au^{1+} \qquad (1.2)$$

$$[AuBr_4]^-\text{-}CTA^+ + C_6H_8O_6 \rightleftharpoons [AuBr_2]^-\text{-}CTA^+ + 2Br^- + 2H^+ + C_6H_6O_6$$

The further reduction cannot be obtained directly by the ascorbic acid without the presence of seeds. This is because the $[AuBr_2]^-$-CTA^+ complex has a standard potential lower than the gold ion itself, making it quite stable and harder to reduce by AA with pH less than 4 [28,41,42]. As soon as seeds are added in the growth solution, the second step of the reduction is catalyzed by their surface [15,43]:

$$\text{Second reduction: } Au^{1+} + e^- \rightleftharpoons Au^0 \qquad (1.3)$$

$$2[AuBr_4]^-\text{-}CTA^+ + 3\,C_6H_8O \rightleftharpoons 2Au + 2CTA^+ + 8Br^- + 6H^+ + 3C_6H_6O_6$$

The second important role of CTAB is to solubilize the metal precursor (*the precursor is not soluble in water without the presence of micelles*), and to stabilize the obtained nanorods by forming a bilayer around the particle [15,44] (Figure I.7).

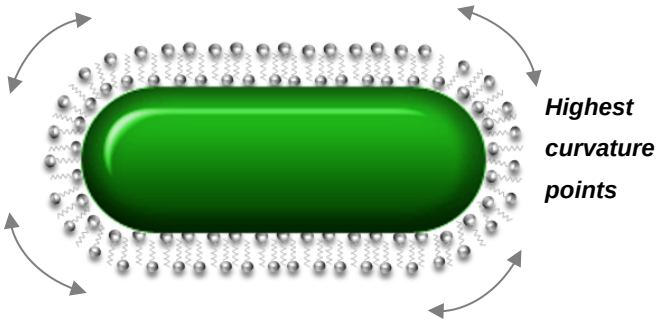

Figure I. 7 *CTAB Bilayer on the surface of gold nanorods*

It is remarkable that in similar chemical conditions, the replacement of CTAB by CTAC (*cetyl-trimethyl ammonium chloride),* given in Figure I.6b, or DTAB (*dodecyltrimethylammonium bromide*), given in Figure I.6c, prevents the formation of nanorods. This experimental behavior can be related to the phase diagram of these surfactants shown in Figure I.8. For each of them the spherical micelles (L_1), formed above the critical micelle concentration, are transformed into elongated micelles which is then organized into hexagonal phase (H_1) at higher concentrations. While DTAB and CTAC form spherical micelles on a large concentration range, CTAB spherical micelles transit towards elongated micelles well below the transition between L_1 and H_1. This is due to the strong reduction of the surface per polar head of the surfactant when bromide is replaced with the chloride counter ions of cetyl-trimethyl ammonium cations. For DTAB, this reduction is not strong enough to allow this transition.

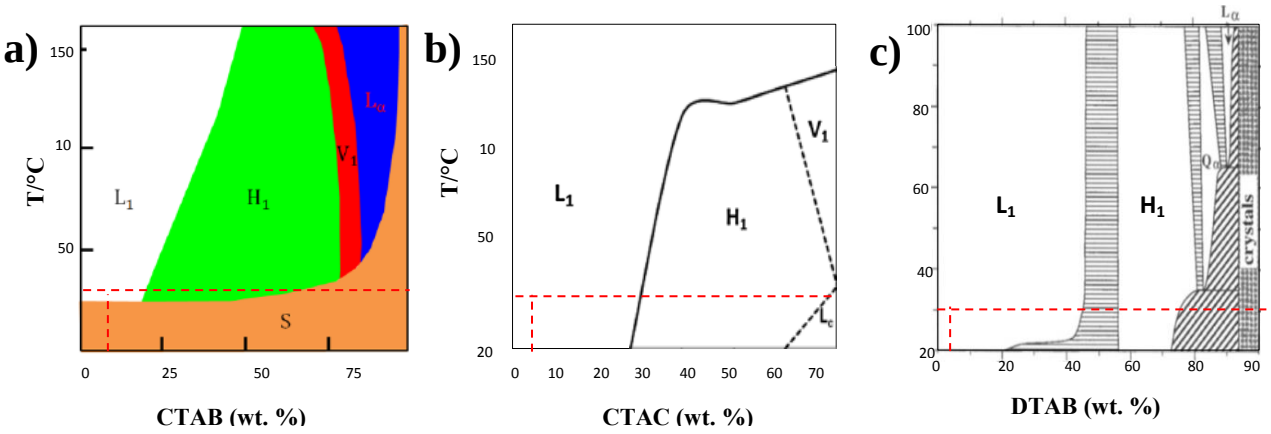

Figure I. 8 *Phase diagrams of (a) CTAB-water and (b) CTAC-water (d) DTAB-water highlighting in red the temperature used during the synthesis of anisotropic nanoparticles (~30 °C)*

The surface per polar head can be also modified by some external additives, such as 5-Bromo Salicylic acid, to promote the formation of elongated threadlike micelles in CTAC and DTAB [45–47]. Recently, Yoo et al. [48] have demonstrated that the anisotropic bipyramids can be obtained by using CTAC and salicylic acid mixture in classical seed mediated growth. Additionally, Murray et al. [34] have shown that addition of derivative of salicylic acid into CTAB solution improve the formation of nanorods.

It is thus remarkable that the efficiency of any surfactant used to produce anisotropic nanoparticles may be related to its ability to form elongated micelles at low concentrations

and temperatures in water solution. This is an indication of the importance of the curvature points induced by the elongated micelles of the surfactant, used to produce the nanoparticles (Figure I.7). These curvature points can be quantified by the packing of the surfactant (*packing parameter = surfactant tail volume/ area of the surfactant head group X the length of the tail*) [49]. The main importance of this curvature property is the induction of strong effect on the feeding of monomers during the growth. Namely, the feeding proceeds by the tip of the particle due to the electrostatic interactions between the micelles and the bilayer [50] and also because of the less dense packing layer at the tip of the nanorods because of high curvature. These correlation underlines one important question still unsolved today in the development of anisotropy in gold nanoparticles: Is it the stabilization of the bilayer which promotes the anisotropy or an epitaxy of the surfactant head on chosen plane of the nanoparticles?

- Effectively, the complex role of CTAB also includes specific adsorption on certain facets of gold nanorods. In particular, when $AgNO_3$ is used as shape directing agent, in the form of complex CTA-$AgBr_2^-$ (named CTASB) which blocks the growth along transversal axis [43]. The role of silver nitrate during formation of gold nanorods is to promote the anisotropy and to increase the yield of NRs. However the mechanism to achieve such complex task is still under debate [15]. The other proposed mechanism is the under potential deposition (UPD) mechanism which states the deposition of metallic silver sub-monolayer on the longitudinal axis of nanorods to favor the growth in the opposite direction of the deposition [13,20].
- Apart from CTAB and $AgNO_3$, another important feature of the producing nanorods is the use of a smooth reducing agent for the growth step. Even though many reducing agent is commercially possible such as hydroquinone, salicylic acid, *etc.* [5,35], general tendency is the use of Ascorbic Acid [15,30,42].

Even though all these mechanisms, explained in relation to each chemical reagent, may have been responsible to have a control on aspect ratio and the yield of gold NRs, yet they fail to explain the symmetry breaking between the initial seed which assumed to be isotropic and the final anisotropic particle.

- **Role of Seeds in the Formation of Anisotropy**

In all represented techniques to prepare anisotropic gold nanoparticles, a strategy of symmetry breaking must be developed to alter the crystallographic isotropy inherited to the face centered cubic (fcc) structure of gold [28]. Namely, if the formation of nanoparticles is divided into three stages; (*i*) nucleation, (*ii*) the evolution of nuclei into seeds and (*iii*) the growth of anisotropic structures from isotropic seeds [51], the most important step during the formation of anisotropy would be the breaking of the symmetry of isotropic seeds. In 2009, Xia and coworkers have defined the pathways for fcc metal crystals leading to anisotropic nanoparticles [51] and summarized the results in the following Figure I. 9.

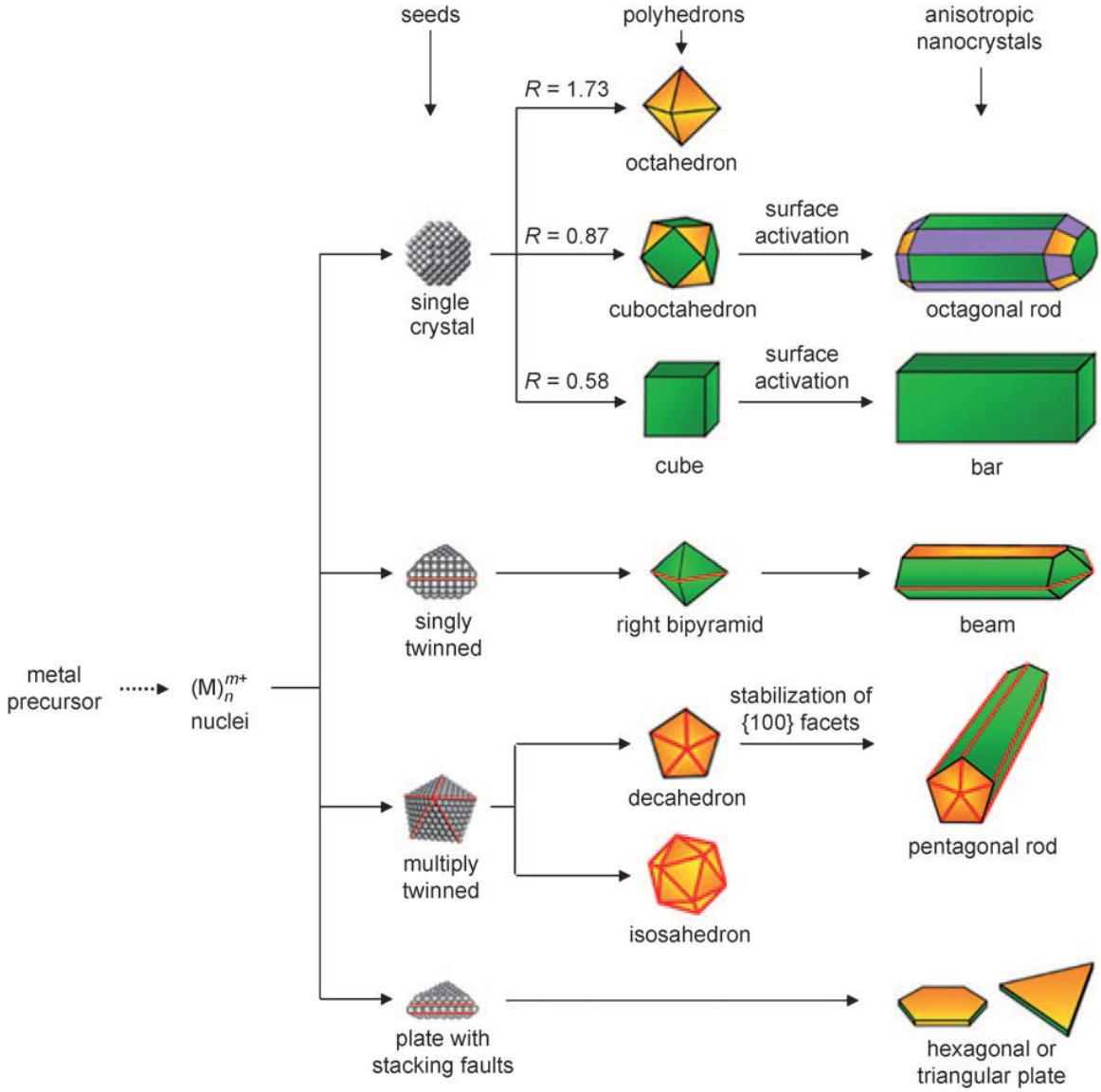

Figure I. 9 *Reaction pathways to obtain nanocrystals with different shapes via seed mediated technique [51]*

In this representation, the very first stage of the crystallization process (*nucleation*) starts with the reduction of a metal precursor to generate zero-valent atoms to form building blocks of crystal called nuclei. However, the mechanism of formation of such nuclei from the metal precursor is still an unclear subject, since all detection methods stay insufficient to capture the crystal at these small sizes [51]. The nucleation theory developed by Lamer et al in the 1950's [52] and largely improved later by Kashchiev et al. [49] and Sugimoto et al. [53] can explain the distribution in size but do not allow any insight in the internal structure of the nanoparticles and particularly the numbers of defects.

As soon as the nuclei are formed, they continue their growth which causes structural fluctuations forcing crystal to form well-defined structures (*seeds*) to minimize the energy cost [51]. Depending on various factors, the crystal structure of seeds may vary from single crystalline to singly twinned or multiply twinned structures. Some of the predicted Wulff conditions for small size particles are given in Figure I.10. Even though the equilibrium shape for a small size NP is estimated as single crystalline truncated octahedron (TOh) by the Wulff constructions (*due to its spherical profile yielding the minimum number of surface atoms per volume and the minimum surface energy*) [54,55], deviations from such structure may result in reconfiguration in the crystal to induce various defects and twining faults to generate more complex structures (Dh & IOh).

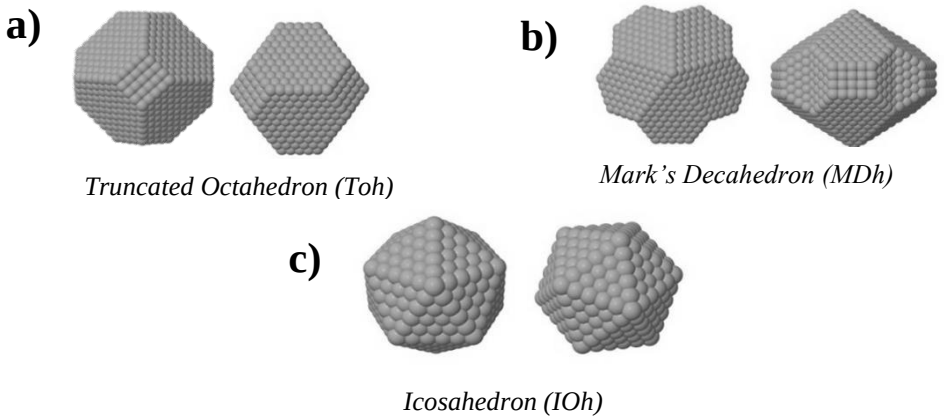

Figure I. 10 *Structure of a) TOh nanoparticle enclosed by low Miller index facets {100} and {111} b) MDh composed of five tetrahedron bounded by common {111} twin planes and oriented along single common twining axis [011] with additional small truncation on the side edges to form small {100} facets -c) IOh structured formed by 20 tetrahedral subunits joining each other via 30 twin boundaries resulting in a surface enclosed by 20 {111} facets (reproduced from [56])*

In solution, to access the internal structure of small sized nanoparticles and to relate the morphology to the estimated Wulff shapes is a challenging task. Due to such difficulties, Guyot-Sionnest [33] have performed HRTEM analysis (*with limited resolution*) on dried samples and deduced a monocrystalline structure for seeds prepared in presence of CTAB and multi-twinned structures for seeds prepared with citrate.

As described previously, GNRs can only be obtained via the growth from CTAB capped seeds, assumed to be monocrystalline and initially isotropic, even though the precise structure is not yet supported by any further experimental observations. And the transition from isotropic monocrystalline seeds to final anisotropic nanorods still remains unclear. All the proposed mechanisms involve the explanation of the elongation of nanoparticle after symmetry is already broken [15].

In 2010 Hubert et al. [57] observed a bifurcation point (BP) in the *L*, *W* representation of gold nanorods (Figure I.11), hence the genesis of anisotropy below this size is still under debate. This bifurcation point around 5 nm has been retrieved in the seeded growth method in the work of Gomez at al. [44].

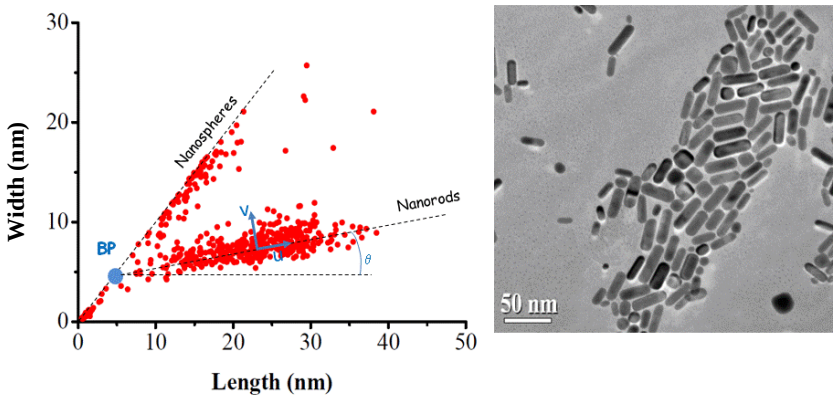

Figure I. 11 *Size analysis of TEM images represented as length vs diameter diagram revealing BP mechanism in NR formation [57]*

- **Crystal Structure of Anisotropic Gold Nanoparticles Obtained by Seed Mediated Synthesis**

Single Crystalline Nanorods

Numerous descriptions on GNRs structure can be found in literature [58–61]. A classical description about the crystal structure of final nanorods prepared by electrochemical methods has been published by Wang et al. [58] in 1999, stating that the particle is enclosed by low index {100} and {110} facets with a [001] growth axis. Later on, Guyot-Sionnest et al. [33] have supported this seminal results by analyzing nanorods prepared via seed mediated synthesis with CTAB capped seeds in presence of $AgNO_3$.

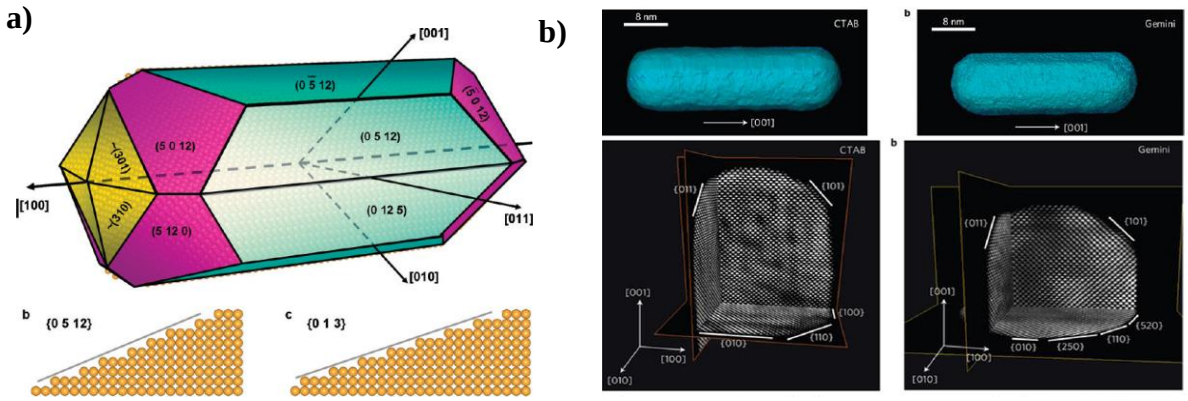

Figure I. 12 *Reconstructed tomogram of single gold NR from 2D tilt series images a) at low resolution revealing {0 5 12} high index external facets for the surface of NR- b) at atomic resolution exhibiting low Miller index faces for CTAB nanorods, high index {2 5 0} for Gemini nanorod*

With the latest development on electron tomography, two different groups similarly stated that the surface of NRs, prepared by seed mediated growth, are bound by higher index facets [60,61] on contrary to previous observations of Wang et al. [58] on gold nanorods, obtained by electrochemical methods. The first description, from Katz-Boon et al. [60], reports that NRs having octagonal sections are mainly packed by {0 5 12} side facets terminating with pyramidal facets on the tips enclosed {0 1 3} surfaces (Figure 12a). The

second description, from Goris et al. [61], for gold NRs prepared with Gemini surfactant (*bis(hexa-decyl-dimethyl-ammonium)diethyl ether bromide*), states that the particles bear also octagonal cross sections and they are formed by 8 high index {2 5 0} facets (Figure 12b-*right*). Same group, additionally performed similar type of analysis on NRs prepared with CTAB and show that when CTAB is used during preparation, low index facets {100} and {110} (Figure I. 12b-*left*) continuous its existence supporting the analysis of Wang [58] on single crystalline nanorods.

Gold Bipyramids

It is known that gold bipyramids can only be obtained by growth from citrate capped seeds in a growth media containing $AgNO_3$ [33,62]. The mechanism of formation of bipyramids, is generally explained by the silver under potential deposition (UPD) along the lateral facets of the decahedral seeds, leading to faster growth along the twinning axis of the nanoparticle [33], even though there is limited experimental information supporting the role of silver during growth.

Crystal structures of final bipyramids have also become a question of debate between researchers due to the complex internal structure of the particles. Initial explanation came from Guyot-Sionnest et al. [33], who was inspired by the work of Lisiecki et al. [63] on copper nanorods, to use Selected Area Diffraction Pattern (SAED) of single particle to reveal the crystal structure. They have shown that particle exhibits various twinning faults as in the case of classical decahedra with an elongation on common twining axis. These results later on have been supported by various groups and the pentagonal structure is accepted as the morphology of bipyramid [62,64,65].

However, recently an irregular six fold cross section (Figure I.13a-c), with highly stepped {151} side facets (Figure I.13b), has been proposed by Burgin et al. [66] to explain the crystal structure of single bipyramid by the use of HRTEM and electron tomography analysis.

Further structural analysis on such type of nanoparticles is needed to explain the complex internal structure of the bipyramid in correlation to the initial precursor.

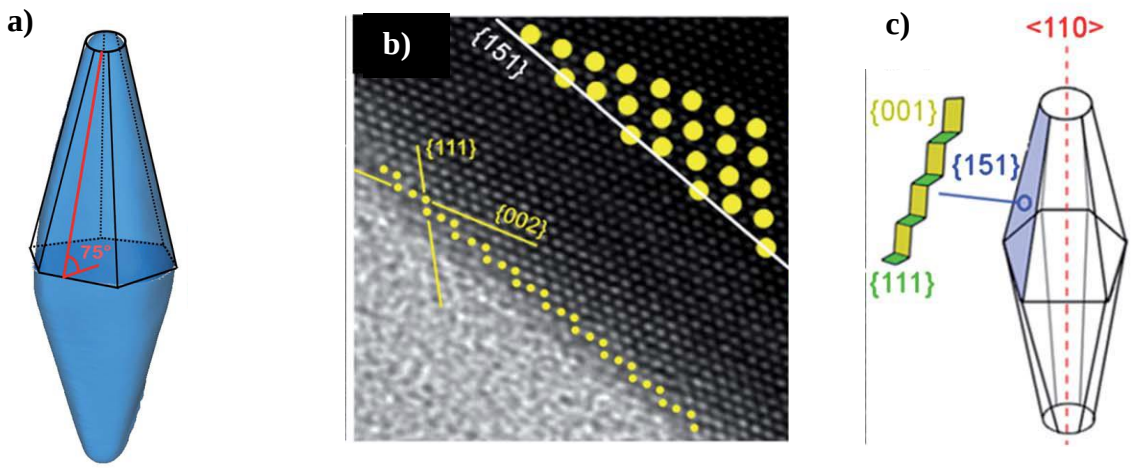

Figure I. 13 *a) 3D reconstructed model of single bipyramid showing irregular 6 fold twinning b)Atomic resolution image of the edge of the bipyramid with high index {151} facets c) Schematic model of the particle oriented along 110 direction exhibiting {151} stepped surface [66]*

1.3 Characterization Methods

1.3.1 UV-Vis Spectroscopy

Extinction spectra's of final nanoparticles were measured by using Shimadzu UV-2550 UV-Vis Spectrophotometer with UV Probe Software. Spectra's were collected over the wavelength range from 200-900 nm. For static experiments, UV spectra's were taken the day after the injection of seeds to make sure that the growth is completed.

Kinetic spectra's are collected directly after the addition of seed into the growth media. Basically, 300 µL of this resulting mixture, after injection of seed, was added directly in a 1 mm UV cell and 20 spectra's were recorded with time interval of 90 s at controlled temperature of 30°C.

1.3.2 Transmission Electron Microscopy (TEM)

The morphology and the mean size of the nanoparticles were examined by transmission electron microscopy (TEM). Low resolution TEM images were taken by Philips CM 30 operating at 300 kV (*Ecole Polytechnique/LSI*). An 8 µL drop of concentrated gold

nanoparticles solution was dried on a carbon coated cupper grid the night before TEM analysis. For high resolution images, diluted solution is used for observation. HRTEM observations were achieved by using two different microscopes: JEOL 2100F microscope equipped with Gatan US4000 CCD Camera operating at 200 kV (*installed at IMPMC, Université Pierre et Marie Curie, Paris, France*) and JEOL ARM 200 F Cold FEG equipped with a CEOS Cs-image corrector operating at 80 kV or 200 kV (*installed at MPQ-Université Paris Diderot, Paris France*).

1.3.3 *In-Situ* Scanning Transmission Electron Microscopy (*in-situ* STEM)

In-situ growth experiments were performed by using JEOL ARM 200 F Cold FEG equipped with Posedion TEM holder operating at 200 kV (*installed at MPQ*). Sample preparation as well as operating conditions for *in-situ* STEM experiments will be explained in detail in Chapter V.

1.3.4 Electron Tomography

The experimental data for tomography were acquired in a JEOL 2100F transmission electron microscope with a field emission gun, equipped with a spherical aberration (Cs) probe corrector and operating at 200 kV. The acquisition of BF and DF tilt series was carried out simultaneously in the scanning mode (STEM), by using a circular detector for the BF and a high angle annular detector for the HAADF. A camera length of 10 cm was chosen for this experiment. It corresponds to inner and outer semi-angles of 60 and 160 mrad, respectively for the HAADF detector. A 100 µm condenser aperture was employed, allowing one to reach a probe diameter of about 0.12 nm with a current density of 0.5 pA.$Å^{-2}$. Under these conditions, the tomography series have been acquired by using the Digital Micrograph software (tomography plugin).

It gives access to an automatic increment of the tilt angles and a sharp control of the specimen drift and defocusing. A high tilt specimen holder from Gatan has been employed for a tilting range from -65° to 65°, with an equal angular step of 2.5°. By using analytical relations from Midgley et al [67] the tomogram resolution has been estimated at about 0.16 nm in the direction perpendicular to the electron beam. For the direction of the electron beam, the resolution diminishes with a factor of 1.22, due to the missing wedge from data acquisition.

Once the series acquisition completed and given the high contrast achieved in the HAADF mode, a cross-correlation algorithm was sufficient to properly align the images from the series. The volume reconstruction has been carried out by discrete algebraic reconstruction techniques (DART) using the Tomo J plugin under the Fiji (ImageJ) software. The very same software has been used for the volume visualization and analysis.

1.3.5 Dynamic Light Scattering (DLS)

The size distribution of isotropic gold NPs was monitored using dynamic light scattering (DLS). Analysis was carried out using a Zetasizer (MALVERN Instruments) at 25^{o}C. The size analysis of seeds was carried out immediately after the preparation. The volume size distribution, the Z-average diameter (Z-ave) and the polydispersity index (PdI) were obtained from the autocorrelation function using general purpose mode for all samples.

1.3.6 Small Angle X-Ray Scattering (SAXS)

SAXS experiments have been performed on a home-made apparatus with a wave vector range 0.02 $Å^{-1}$ < q < 0.35$Å^{-1}$. The X-ray source (rotating copper anode, λ=1.542 Å) is collimated via an Osmic mirror. The scattered beam is collected on a Pilatus3R 200K detector of 83.8 mm^2 x 70.0 mm^2 dimension. Calibration (i.e. normalized intensity) is ensured with 3 mm Lupolen (I_{max} = 6 cm^{-1}) and 1.5 mm water (I=0.016 cm^{-1}) after a classical radial averaging procedure. The average flux is 2.6 10^6 ph/s. Samples are measured in 1.5 mm glass capillaries.

Wide angle X-ray scattering (WAXS) have been performed on a homemade apparatus in the wave vector 0.02 A^{-1}< q < 3 A^{-1}. The X-ray source (rotating molybdenum anode, λ=0.712 Å) is collimated via an Osmic mirror through two hybrid slits (1x1 mm^2). The scattered beam is collected on a Mar 345 image plate. 3 mm Lupolen and 3 mm water are used for calibration after classical averaging procedure. The incoming flux is found to be 9 10^7 photons per second. Samples are measured in a 3 mm glass capillary.

1.4 References

[1] C. Chi, Chem. Herit. Mag. (2008).

[2] Nano.gov (2014).

[3] J. Xiao, L. Qi, Nanoscale 3 (2011) 1383.

[4] D.T. Thompson, Nano Today 2 (2007) 40.

[5] L. Vigderman , B. P. Khanal , and E.R. Zubarev, Adv. Mater. (2012).

[6] G. Maltzahn, J. Park, A. Agrawal, N. K. Bandaru, S. K. Das, M. J. Sailor and S. N. Bhatia, Cancer Res. 69 (2009) 3982.

[7] M. Hu, J. Chen, Z.-Y. Li, L. Au, G.V. Hartland, X. Li, M. Marquez, Y. Xia, Chem. Soc. Rev. 35 (2006) 1084.

[8] G. Mie, Ann Phy 25 (1908) 377.

[9] K.L. Kelly, E. Coronado, L.L. Zhao, G.C. Schatz, J. Phys. Chem. B 107 (2002) 668.

[10] S.K. Dondapati, T.K. Sau, C. Hrelescu, T.A. Klar, F.D. Stefani, J. Feldmann, ACS Nano 4 (2010) 6318.

[11] P. Sajanlal, T. Pradeep, Nano Res. 2 (2009) 306.

[12] Y. Li, J. Sun, L. Wu, J. Ji, X. Sun, Y. Qian, Biosens. Bioelectron. 62 (2014) 255.

[13] C.J. Murphy, T.K. Sau, A.M. Gole, C.J. Orendorff, J. Gao, L. Gou, S.E. Hunyadi, T. Li, J. Phys. Chem. B 109 (2005) 13857.

[14] I.O. Sosa, C. Noguez, R.G. Barrera, J. Phys. Chem. B 107 (2003) 6269.

[15] S.E. Lohse, C.J. Murphy, Chem. Mater. 25 (2013) 1250.

[16] R. Gans, Ann. Phys. 342 (1912) 881.

[17] N. Li, P. Zhao, D. Astruc, Angew. Chem. Int. Ed. (2014) 1756.

[18] X. Huang, S. Neretina, and M. A. El-Sayed, Adv. Mater. 21 (2009) 1.

[19] A. V. Alekseeva, V. A. Bogatyrev, B. N. Khlebtsov, A. G. Mel'nikov, L. A. Dykman and N. G. Khlebtsov, Colloid Journal. 68 (2006) 661.

[20] M. Grzelczak, J. Perez-Juste, P. Mulvaney, L.M. Liz-Marzan, Chem Soc Rev 37 (2008) 1783.

[21] F. Kim, K. Sohn, J. Wu, J. Huang, J. Am. Chem. Soc. 130 (2008) 14442.

[22] L. Scarabelli, M. Coronado-Puchau, J.J. Giner-Casares, J. Langer, L.M. Liz-Marzán, ACS Nano 8 (2014) 5833.

[23] T. Huang, F. Meng, L. Qi, Langmuir 26 (2009) 7582.

[24] J. Burgin, M. Liu, P. Guyot-Sionnest, J. Phys. Chem. C 112 (2008) 19279.

[25] H. Yuan, K.G. Khoury, H. Hwang, C.M. Wilson, G.A. Grant, T. Vo-Dinh, Nanotechnology 23 (2012) 075102.

[26] E. Gachard, H. Remita, J. Khatouri, B. Keita, L. Nadjo, and Jacqueline Belloni, New J Chem 22 (1998) 1257.

[27] W. Abidi, P.R. Selvakannan, Y. Guillet, I. Lampre, P. Beaunier, B. Pansu, B. Palpant, H. Remita, J. Phys. Chem. C 114 (2010) 14794.

[28] C. Louis, O. Pluchery, Gold Nanoparticles for Physics, Chemistry and Biology, Imperial College Press, London, 2012.

[29] S. Horikoshi, N. Serpone, in:, Microw. Nanoparticle Synth., Wiley-VCH Verlag GmbH & Co. KGaA, 2013, pp. 1–24.

[30] N.R. Jana, L. Gearheart, C.J. Murphy, Adv. Mater. 13 (2001) 1389.

[31] J. Rodríguez-Fernández, J. Pérez-Juste, P. Mulvaney, L.M. Liz-Marzán, J. Phys. Chem. B 109 (2005) 14257.

[32] N. Babak, M.A. El-Sayed, Chem. Mater. 15 (2003) 1957.

[33] M. Liu, P. Guyot-Sionnest, J. Phys. Chem. B 109 (2005) 22192.

[34] X. Ye, L. Jin, H. Caglayan, J. Chen, G. Xing, C. Zheng, V. Doan-Nguyen, Y. Kang, N. Engheta, C. R. Kagan and C. B. Murray, ACS Nano 6 (2012) 2804.

[35] L. Scarabelli, M. Grzelczak, L.M. Liz-Marzán, Chem. Mater. 25 (2013) 4232.

[36] N.R. Jana, L. Gearheart, C.J. Murphy, J. Phys. Chem. B 105 (2001) 4065.

[37] C. Bullen, P. Zijlstra, E. Bakker, M. Gu, C. Raston, Cryst. Growth Des. 11 (2011) 3375.

[38] H. Koerner, R.I. MacCuspie, K. Park, R.A. Vaia, Chem. Mater. 24 (2012) 981.

[39] F. Hubert, F. Testard, A. Thill, Q. Kong, O. Tache, and O. Spalla, Cryst. Growth Des. 12 (2012) 1548.

[40] J. Xiao, L. Qi, Nanoscale 3 (2011) 1383.

[41] K. Park, Synthesis, Characterization, and Self –Assembly of Size Tunable Gold Nanorods, Georgia Institute of Technology, 2006.

[42] C. J. Johnson, E. Dujardin, S. A. Davis, C. J. Murphy and S. Mann, J Mater Chem 12 (2002) 1765.

[43] F. Hubert, F. Testard, O. Spalla, Langmuir 24 (2008) 9219.

[44] S. Gómez-Graña, F. Hubert, F. Testard, A. Guerrero-Martínez, I. Grillo, L.M. Liz-Marzán, O. Spalla, Langmuir 28 (2011) 1453.

[45] T.M. Clausen, P.K. Vinson, J.R. Minter, H.T. Davis, Y. Talmon, W.G. Miller, J. Phys. Chem. 96 (1992) 474.

[46] Z. Wang, R.G. Larson, J. Phys. Chem. B 113 (2009) 13697.

[47] T. Imae, S. Ikeda, Colloid Polym. Sci. 265 (1987) 1090.

[48] H. Yoo and M. H. Jang, Nanoscale 5 (2013) 6708.

[49] D. Kashchiev, J. Chem. Phys. 125 (2006).

[50] N. Almora-Barrios, G. Novell-Leruth, P. Whiting, L.M. Liz-Marzán, N. López, Nano Lett. 14 (2014) 871.

[51] Y. Xia, Y. Xiong, B. Lim, S.E. Skrabalak, Angew. Chem. Int. Ed. 48 (2009) 60.

[52] V.K. LaMer, R.H. Dinegar, J. Am. Chem. Soc. 72 (1950) 4847.

[53] T. Sugimoto, Adv. Colloid Interface Sci. 28 (1987) 65.

[54] G. Wulff, Z.Kristallogr. 34 (1901) 449.

[55] E. Ringe, R.P. Van Duyne, L.D. Marks, J. Phys. Chem. C 117 (2013) 15859.

[56] R. Cortes-Huerto, J. Goniakowski, C. Noguera, J. Chem. Phys. 138 (2013) 244706.

[57] F. Hubert, F. Testard, G. Rizza, O. Spalla, Langmuir 26 (2010) 6887.

[58] Z.L. Wang, M.B. Mohamed, S. Link, M.A. El-Sayed, Surf. Sci. 440 (1999) 809.

[59] E. Carbó-Argibay, B. Rodríguez-González, S. Gómez-Graña, A. Guerrero-Martínez, I. Pastoriza-Santos, J. Pérez-Juste, L.M. Liz-Marzán, Angew. Chem. Int. Ed. 49 (2010) 9397.

[60] H. Katz-Boon, C.J. Rossouw, M. Weyland, A.M. Funston, P. Mulvaney, J. Etheridge, Nano Lett. 11 (2010) 273.

[61] B. Goris, S. Bals, W. Van den Broek, E. Carbó-Argibay, S. Gómez-Graña, L. M. Liz-Marzán and G. Van Tendeloo, Nat. Mater. 11 (2012) 930.

[62] X. Kou, S. Zhang, C.-K. Tsung, M.H. Yeung, Q. Shi, G.D. Stucky, L. Sun, J. Wang, C. Yan, J. Phys. Chem. B 110 (2006) 16377.

[63] I. Lisiecki, A. Filankembo, H. Sack-Kongehl, K. Weiss, M.-P. Pileni, J. Urban, Phys. Rev. B 61 (2000) 4968.

[64] X. Kou, W. Ni, C.-K. Tsung, K. Chan, H.-Q. Lin, G.D. Stucky, J. Wang, Small 3 (2007) 2103.

[65] G. Zhou, Y. Yang, S. Han, W. Chen, Y. Fu, C. Zou, L. Zhang, and S. Huang, ACS Appl Mater Interfaces 5 (2013) 13340.

[66] J. Burgin, I. Florea, J. Majimel, A. Dobri, O. Ersen, M. Treguer-Delapierre, Nanoscale 4 (2012) 1299.

[67] P.A. Midgley, M. Weyland, Proc. Int. Workshop Strateg. Adv. At. Level Spectrosc. Anal. 96 (2003) 413.

CHAPTER II

Role of Seed on the Development of Anisotropy

CHAPTER II

Chapter 2

Role of Seed on the Development of Anisotropy

Our motivation in this work is to understand the mechanism behind the morphological formation of anisotropic nanoparticles, by relating them to initial isotropic seeds. We have used the seed mediated approach for the fabrication of nanoparticles [1,2] to have a good control over the shape, the size and the structure of the precursor to be grown. Different seeds were obtained (*with different surface charges*) at variable size ranges and different crystal structures (*single crystal-SC or multiple twinned crystal-MTC*) by simple variation of the surface ligand and the reducing conditions used for the synthesis.

Controlled addition of as-prepared seeds into a specific growth solution leads to production of final nanoparticles. This chapter will give quantitative relation on the growth kinetics of initial seeds into final nanoparticles by using *in-situ* UV-Vis Spectroscopy (UV-Vis) and transmission electron microscopy (TEM) techniques.

2.1 Materials and Methods

Cetyltrimethylammonium bromide (CTAB 99%) was purchased from G-Biosciences. Chloroauric acid (extra pure), silver nitrate (extra pure), sodium borohydride (98%), trisodium citrate and L-ascorbic acid were obtained from Sigma without further purification. All the glassware was cleaned with aqua regia and washed with distilled water before the experiments.

2.1.1 Synthesis of Different Seeds

2.1.1.1 Preparation of CTAB Capped Seeds (Type 1)

CTAB capped seeds were prepared through the modification of seed mediated method published by Nikoobakht and El-Sayed [2]. Briefly, the nanoparticles were synthesized by the addition of freshly prepared ice cold $NaBH_4$ solution (0.1 mL, 0.0264 M) into a solution composed of $HAuCl_4$ (0.025 mL, 0.05 M) and CTAB (4.7 mL, 0.1 M). The mixture was strongly stirred for 2 minutes and kept at 28 °C. The obtained solution with a light brown color is used after 1 hour of its preparation.

2.1.1.2 Preparation of Citrate Capped Seeds

- **Type 2**

Preparation of these seeds was inspired from the work of Murphy et al. [3]. The synthesis involves the addition of 0.3 mL of ice cold 0.01 M $NaBH_4$ into a mixture of 10 mL of 0.25 mM $HAuCl_4$ and 0.25 mM sodium citrate under vigorous stirring at 28 °C. The color of the mixture immediately turned into orange red. Citrate stabilized seeds were aged for 2 hours prior to their use to ensure the fully decomposition of excess borohydride in the solution.

- **Type 3**

Synthesis of Type 3 seeds is originated from Siveraman et al. [4] Briefly, nanoparticles were prepared by reversing the reactants addition order in standard Turkevich method [5] to obtain smaller sized nanoparticles and have better control on the size distribution. This experiment involves the addition of 0.25 mL of 25.4 mM $HAuCl_4$ into 24.75 mL of 5.2 mM boiling citrate solution (T~90°C). Boiling is stopped after 250 seconds with the termination of the reaction. Size of the prepared seed is analyzed directly after its preparation by DLS and repeated the day after right before grown into the final NPs to make sure that the average diameter stays constant. Particles are used 24 hours later.

2.1.1.3 Preparation of Ascorbic Acid Capped Gold Seeds

- **Type 4**

Preparation of Type 4 seeds issued form our group and has been detailed in the publication of Han et al. [6]. The synthesis is based on a kinetic control over the gold NP's size by modulating the reducing power of ascorbic acid via pH variation. In a typical experiment, 10 mL of an aqueous solution of $HAuCl_4$ (0.5 mM) was mixed with 10 mL of 8.6 mM ascorbic acid (AA) solution whose pH was adjusted to a value of 11 by the addition of a strong base (0.1 M NaOH) just before the mixing with gold. A rapid mixing of the reactants was established by using a continuous turbulent millifluidic flow through a homemade millifluidic mixer. The injection was operated with two syringes pumps (PHD 2000, Harvard Instruments) with an injection rate of 15 mL/min per syringe. Obtained seeds were used 24 hours later.

Chemical conditions used during the preparation of all given seeds belonging different families is summarized in Table II.1.

Table II. 1 *Summary of the different synthetic conditions used to prepare four classes of seeds with same final gold concentration ($[Au^{3+}]_{final}$=0.25 mM)*

Seed	Ligand/surfactant				$[Au^{3+}]$		Reducing agent				Total volume**** (mL)
	Type	$C_{initial}$ (mM)	$V_{initial}$ (mL)	C_{final} (mM)	$V_{initial}$ (mL)	$C_{initial}$ (mM)	Type	$C_{initial}$ (mM)	$V_{initial}$ (mL)	C_{final} (mM)	
Type 1	CTAB	100	4.70	0.10	0.025	50.0	$NaBH_4$	26.4	0.1	0.55	4.80
Type 2	Citrate	4.76	0.52	0.25	0.050	50.0	$NaBH_4$	10.0	0.3	0.29	10.3
Type 3	Citrate*	5.20	24.7	5.14	0.250	25.4	Citrate**	-	-	-	25.0
Type 4	AA***	8.60	10.0	4.30	10.00	0.50	AA	-	-	-	20.0

*T=90°C
**Gold added into boiling citrate solution
***$pH_{initial}$=11
****completed by addition of H_20

2.1.2 Growth of Seeds

The same growth solution was used for all type of seeds, to see the influence of the initial seed structure on the final nanoparticle size and morphology. Chemical composition of the reference growth solution is given in Table II.2. Several growth experiments, presented in the part 2.2.4, were also carried out by using higher volume of $AgNO_3$ (140 µL) in order to observe the direct effect of silver salt concentration on the final nanoparticles.

Table II. 2 *Synthetic conditions for the reference growth solution*

Reagents	**Quantity (mL)**	**[C_{final}] (mM)**
0.05M $HAuCl_4 \cdot 3H_2O$	0.1	0.5
0.1 M CTAB (cetyltrimethylammonium bromide)	10	10
0.01 M $AgNO_3$	0.045	0.045
0.1 M Ascorbic Acid	0.075	0.75

Variable volumes of as-prepared seed solutions were injected into the given growth solution (120 µL, 60 µL, 400 µL, 400 µL respectively for Type 1, 2, 3 and 4 seeds). Resulting mixtures were gently mixed for 15 seconds and kept at 28 °C without disturbance overnight to ensure that the growth is terminated.

Entire kinetic experiments presented throughout this thesis, illustrates the final growth solution before any kind of purification. After termination of growth final nanoparticle solutions (10 mL) were cleaned from excess reactants by two cycles of centrifugation (8440 g, 40 min) using 15 mL *VWR High Performance Centrifugation Tubes (Ref:* 525-0400). After the first step of centrifugation, supernatant was discarded and remaining sediment was re-dispersed in pure water to attain the same final volume of solution (10 mL). Following the second step of centrifugation nanoparticle solution is concentrated to 1 mL for microscopy observations.

2.2 Results

2.2.1 Full Characterization of Seeds

To study the importance of seeds in the formation of anisotropy, we have fabricated different set of seeds at variable sizes and crystalline structures. In this section we will present the characterization of different as-prepared seeds by combining UV-Vis Spectroscopy, DLS, SAXS and HRTEM data's.

2.2.1.1 Size Analysis by UV-Vis Spectroscopy, DLS and SAXS

- **Analysis of Different Seeds by Ultraviolet-Visible Spectroscopy (UV-Vis)**

Figure II. 1 presents the corresponding UV-Vis absorption spectrum of Type 1 seed, prepared in presence of CTAB. Basically, in the spectrum no distinct SPR is visible in the UV-Vis region. For nanoparticles below than 2.5 nm, it has been shown that the plasmon resonance around 500 nm vanishes [7].

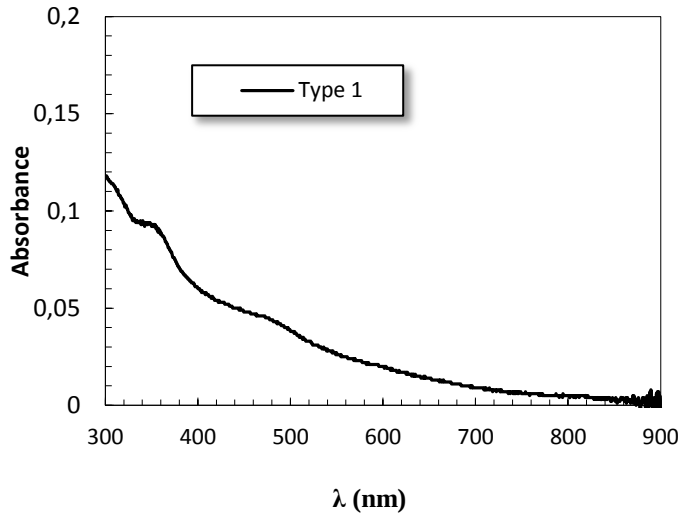

Figure II. 1 *UV-Vis Spectrum of positively charged CTAB seeds*

Appearance of large absorption band around 500 nm, in Figure II.2, for Type 2, 3 and 4 seeds is an indication that particle size is larger than 2.5 nm [7–9]. Low absorbance values at surface plasmon resonances (SPR) of all seeds can be explained by the fact that all

experiments are realized at low gold ion concentration (*all seeds have been prepared with 0.25mM of $HAuCl_4$ prior to the addition of the reducing agent*).

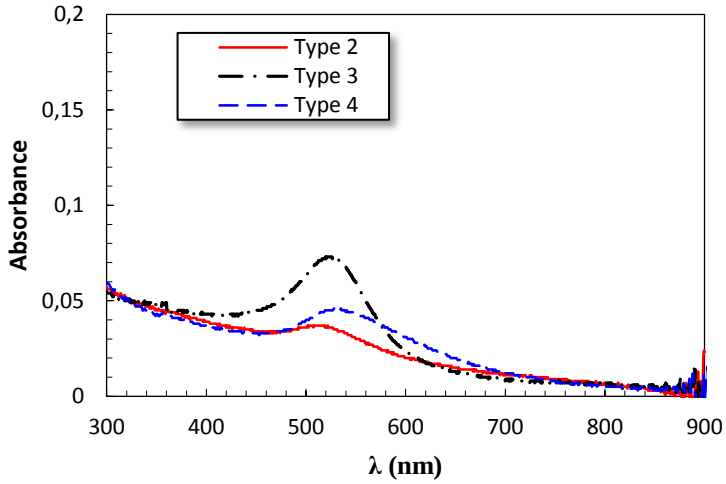

Figure II. 2 *UV-Vis Spectrum of negatively charged seeds*

Table II.3 summarizes the position of SPR (λ_{SPR}) for all seeds with corresponding absolute absorbance (A_{SPR}) values, as well as the nature of the ligand used during the preparation, the reaction temperature and the color of the final seed solution.

Table II. 3 *Summarized table describing the effect of stabilizer on the λ_{SPR}, A_{SPR} and color of the solution of nanoparticles*

Seed Type	**Nature of ligand**	**Reaction temperature (°C)**	**λ_{SPR} (nm)**	**A_{SPR}**	**Color**
[1]	CTAB	30	-	-	Light brown
[2]	Citrate	30	514	0.037	Orange red
[3]	Citrate	90	525	0.073	Dark red
[4]	Ascorbic A.	23	528	0.046	Light pink

The comparison of the absolute absorbance's reveals that, Type 3 seeds, exhibiting a transversal band around 525 nm, bear the highest absorbance value (0.073). The absorbance is damped for Type 2 seeds (0.037) with additional blue shift in SPR (A_{SPR_2} =514 nm). For both

Type 2 and Type 3 seeds, even though the same ligand is used to synthesize NPs, such deviation in the position of surface plasmon band and the corresponding absorbance may be explained by the fact that, nanoparticle size is getting larger for Type 3 seeds. In last, when ascorbic acid (*at pH 11*) is used as reducing agent during the preparation of seeds, large plasmon peak around 528 appears (Type 4).

At 400 nm, the signal is characteristic of Au(0) present in the solution [10]. Reminding the fact that same initial Au(III) concentration has been used for all seeds, i.e. 0.25 mM, it is probable that the yield of the reaction is quite close for type 2, 3 and 4 seeds since the absorbance at 400 nm is very similar for the three solutions. For Type 1 seeds, due to the presence of CTAB, the signal in this region varies vastly and could not be compared directly.

- **Size Distribution Analysis by Dynamic Light Scattering (DLS)**

Dynamic Light Scattering (DLS) has been employed as principal tool to measure the average diameter of the nanoparticles prior to their growth. For Type 1 seeds, large excess of CTAB prevents any DLS characterization (*due to the coexistence of high concentration of charged micelles with low concentration of gold nanoparticles*). The volume size distribution, the Z-average diameter (Z-ave) and the polydispersity index (PdI), obtained from the autocorrelation function using the general purpose mode for all samples, have been summarized in Figure II.2.

Type 2 seeds, synthesized in presence of trisodium citrate as ligand, exhibit relatively small size with mean diameter of 4.9 nm ± 1.5 nm (with PdI = 0.179). However, these seeds are highly instable and generally evolve through aggregation process (*See Appendix 2*). To prevent any differences in final NPs, may induced by the difference of the seed size distribution, DLS have been performed systematically before the growth of those seeds. Only the seeds with distribution similar to the one shown in Figure II.3 were used for further growth. In addition, the seeds were used every time after 2 hours of their preparation for growth experiments, to ensure the reproducibility.

Size analysis of Type 3 seeds disclose that the particles manifest average size of 8.7 nm ± 3 nm (with PdI = 0.128).

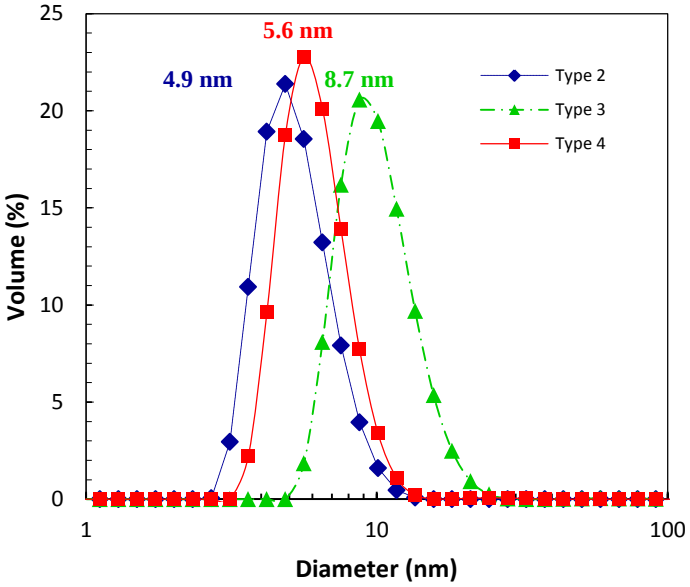

Figure II. 3 *DLS Histograms of Type 2, 3 and 4 seeds*

As indicated previously, even though both Type 2 and 3 seeds are prepared by using sodium citrate in the reaction medium, difference in the size of both seeds can be explained by the fact that, both particles are prepared with different synthetic processes. Type 2 seeds are obtained by the addition of a strong reducing agent ($NaBH_4$) in the presence of a small amount of sodium citrate (0.25 mM), while Type 3 seeds are obtained by reverse Turkevitch method (*meaning gold is added into solution containing citrate)* using large concentration of trisodium citrate (5.2 mM) to ensure the formation of small size nanoparticles by pH control [4]. In both cases citrate stabilizes the nanoparticles by surface adsorption.

Lastly, Type 4 particles (*prepared by the reaction of gold precursor with AA (pH 11) in a microfluidic set-up*) shows average particle size of 5.6 nm ± 1.6 nm (PdI=0.326).

- **Size Distribution Analysis via Small Angle X-Ray Scattering (SAXS)**

SAXS spectra's of freshly prepared seed solutions (*containing 0.25 mM of gold atoms*) is given in Figure II.4. While scattered signal represented can be obtained for Type 2, 3 and 4 [6], the Type 1 could not be analyzed on the SAXS laboratory set-up based on copper source (λ=1.542 Å) due to the high CTAB concentration (0.1M). A small signal can be obtained on the WAXS set-up based on molybdenum source (λ= 0.709 A) allowing to have an estimation of the average size of the nanoparticles in solution.

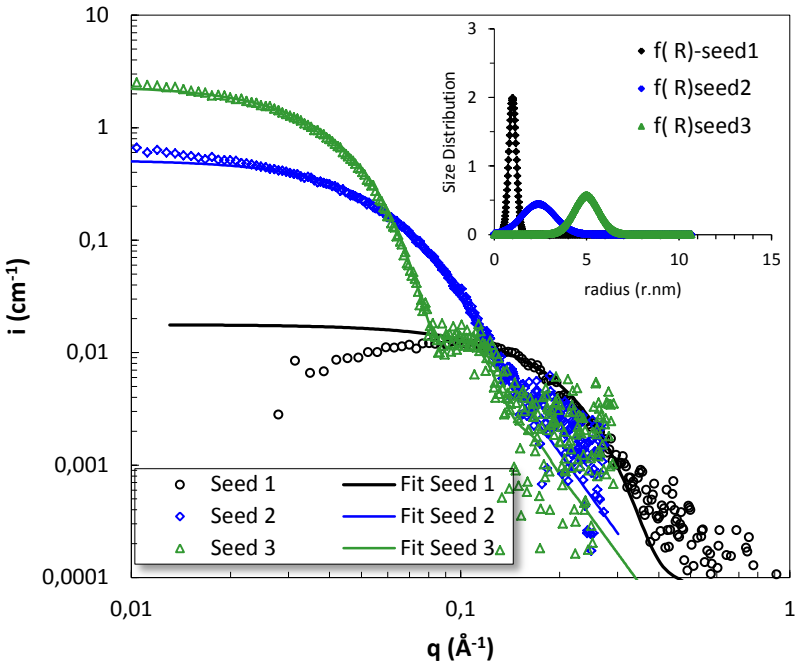

Figure II. 4 *SAXS patterns of: Type 1 seeds, synthesized in presence of CTAB, Type 2 seeds, synthesized in presence of citrate and Type 3 seeds, synthesized via reverse Turkevich method. Lines correspond to the theoretical curves. Distribution curves obtained for four different seeds are given in the inset of the figure*

Associated fits using a Gaussian distribution of spheres are shown in the resulting spectrum with the size distribution curves obtained for the three different seeds (*Figure II.4, inset*). The number density of the particles deduced from the Gaussian fit is given in the Table II.4 as well as the relative polydispersity and the average radius. For Type 4 seeds, the distribution was reproduced from the work of Han et al. [6] for seeds prepared in similar conditions.

Size distributions obtained by SAXS are in good agreement with the ones obtained by DLS with small deviation in case of Type 3 seeds. For Type 3 seeds the difference may be explained by the fact that, the size distribution obtained by SAXS is more sensitive and reliable for those very low sizes. Even though freshly prepared seeds were analyzed in both measurements, time of acquisition varies between two techniques. Namely, for freshly prepared seeds size distribution can be obtained by DLS in 3 minutes, whereas for SAXS time of the acquisition is set for 30 minutes. During this time, particles may increase their sizes.

Table II.4 *Total number of particles obtained by SAXS with obtained radius*

Type of seed	**Seed 1**	**Seed 2**	**Seed 3**	******Seed 4**
***N_d (part/cm^3)**	4.6 10^{14}	2.0 10^{13}	5.0 10^{12}	8.0 10^{13}
****<r> (nm)**	1.00	2.40	5.00	3.15
*****σ/<r>**	0.20	0.37	0.14	0.38

* N_d=number density

** r= radius obtained by SAXS

***σ=Relative polydispersity

****Reproduced from reference [6]

To summarize, two size families are obtained, one with smaller size (2 nm) coated by a cationic surfactant, and the others with larger sizes (4-10 nm) coated by negative charges (citrate or ascorbate).

2.2.1.2 Structure Analysis by High Resolution Transmission Electron Microscopy (HRTEM)

High resolution transmission electron microscopy (HRTEM) was used to extract the size and relative internal structure of as-prepared seeds. Apart from Type 1 seeds, all microscopy observations were realized at 200 kV. For Type 1 seeds, clear morphological transformation of small sized nanoparticles (~2 nm) has been observed at high voltage (200 kV). So, to prevent any kind of transformation of particles due to beam damage, high resolution imaging has been performed at 80 kV on single seeds. Figure II.5 shows resulting HRTEM images of four different gold seeds with corresponding Fast Fourier Transformations (FFT).

For Type 1 seeds, HRTEM images and FFT analysis reveal that 2.1 nm particle adopt single crystalline (SC) structure with well-defined facets (*See Figure II.5a,b and Appendix II*). For highly symmetrical crystalline material like gold, thermodynamic equilibrium shape of such small sized SC seed is generally predicted as truncated octahedron by using Wulff condition [11,12].

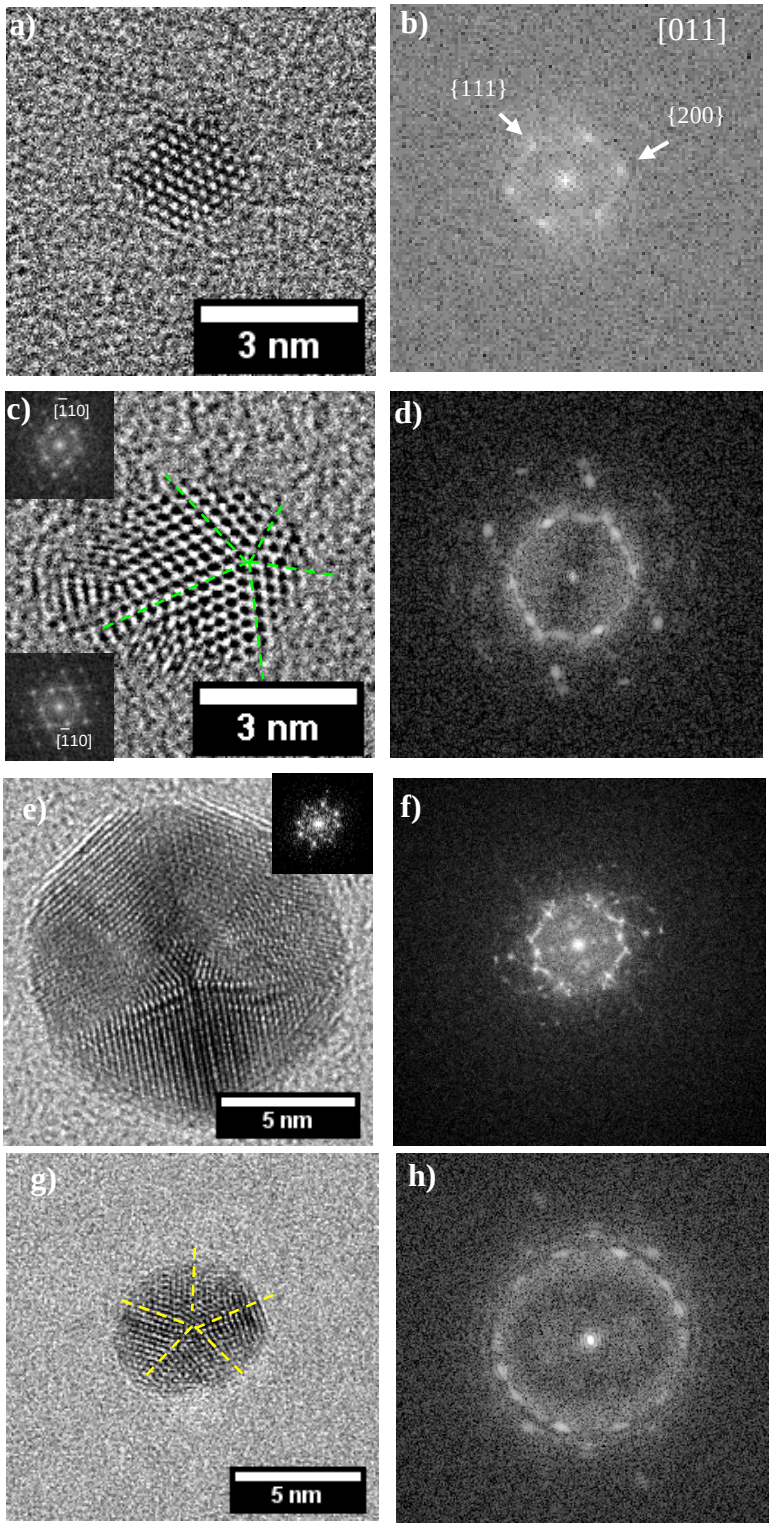

Figure II. 5 *HRTEM images and corresponding FFT spectrums of (a, b) Type 1-CTAB capped Seeds (c, d) Type 2-Citrate capped Seeds kinetic conditions (e, f) Type 3-Citrate capped seeds thermodynamic conditions (g, h) Type 4 seeds-Ascorbic Acid kinetic conditions ([13])*

To characterize morphology of Type 2 seeds, we have studied small sized NPs found in the final solution after the growth stage since unstable structure of NP restricts TEM observations (*See Appendix 2*). We already know that after growth some seeds remain unaffected by the reduction of metal salt in the solution as indicated also by Lofton et al [14]. Therefore, those small sized particles have been taken as representative of the seeds after their addition into growth solution prepared with CTAB. HRTEM image of such kind of particle with an apparent fivefold axis is presented in Figure II.5c. The FFT corresponding to two adjacent subunits, given in the inset of HRTEM image, is related to both <110> zone axis diffraction pattern. Such kind of decahedral nanoparticle, exhibiting a fivefold symmetry, is generally explained in detailed via the composition of 5 individual crystals oriented along a common <110> direction (*See Chapter IV for detailed explanation*) [2,15–17].

In Figure II.5e HRTEM image of a rounded nanoparticle obtained via reverse Turkevich method (Type 3 seed) is given with its corresponding FFT. Particle size is measured as 10.8 nm. The structure bears various twining fault (*See Appendix 2 for additional images*). Even though we are able to identify the crystal orientation of one sub-unit as <100>, extracting the real morphology of such nanoparticle is challenging task since the orientation of other sub-units are not definite. All individual crystals contribute in FFT making it harder to analyze morphology [18].

For Type 4, Han et al [13] crystal structure of observed nanoparticles is partitioned between two different morphologies; single crystalline (*See Appendix II*) and penta-twinned (Figure II.5g) resembling to Seed 2. Overall FFT of the particle (Figure II.5h) can again be interpreted as sum of FFT of 5 individual crystals with <110> orientation.

In Table II.5 we have summarized the reducing conditions and the capping agent used during preparation of seeds and its effect on size and internal crystal structure of nanoparticle. We have obtained small nanoparticles (sub-5 nm) only when CTAB is used as capping agent and $NaBH_4$ as reducing agent. Also mainly single crystal structures are observed for Type 1 seeds with CTAB (*See Appendix 2*) rather than twinned morphologies. For all other presented seeds (Type 2, 3 and 4), TEM observations revealed that particles exhibit multiple twining faults with mainly penta-twinned structures and size larger than 4 nm.

Table II. 5 *Chemical Reagents used in the preparation of different types of seeds and their average size issued from TEM*

Seed	Reducing Agent	Capping Agent	Average Size (d.nm)	***σ/<r>	Crystal Structure
[1]	$NaBH_4$	CTAB	2.0	-	SC*
[2]	$NaBH_4$	Trisodium citrate	4.9 ± 1.5	0.706	PT**
[3]	Trisodium Citrate T=90°C	Trisodium Citrate	8.7 ± 3.0	0.344	MT*
[4]	Ascorbic Acid (pH=11)	(-) Charge	5.6 ± 1.6	0.285	SC+PT

* SC = Single Crystalline

** PT = Penta-twinned

***MT = Multi-twinned

- **Estimation of overall number of added seeds**

To adapt the experimental protocol for comparison of growth from individual seeds, we have estimated the number of particle added in each experiment in function of the average size and the volume of seed solution (V_{seeds}) used (*NP is assumed to be spherical with a radius, r).*

With given estimation, N_{seed} (Eq 2.2) can be deduced from the volume fraction ($\Phi_{0-seeds}$) of the gold (Eq 2.1), incorporated into the nanoparticles considering the face centered cubic crystal structure of bulk gold with an initial salt concentration ($[Au^{3+}]$) of 0.25 mM (M_{Au} = 197g/mol, d_{Au} = 19.32 g/cm^3).

$$\Phi_{0-seeds} = [Au^{3+}]^0 \times {M_{Au}}/{d_{Au}} \quad (2.1)$$

$$N_{seeds} = \frac{\Phi_{o\,-seeds} \times V_{seeds}}{{4}/{3}\pi r^3} \quad (2.2)$$

By given relation, we can easily see that as the size of the seed increases, total number of gold atoms required per seed particle also increases. For same gold concentration (0.25 mM), this indicates a decrease in the number of seed per unit volume with increasing particle size.

To avoid high difference in the added number of particles during growth for different types of seeds, we have modified the volumes of the seed solution added in the growth media for different sets of experiences. It should be noted that any attempt of concentration of the as-prepared seeds, to adjust the similar number for each case, has a strong influence on the size distribution (*for instance, small size particles tend to aggregate when subjected to concentration*). Therefore, we have chosen to regulate the number of seeds in growth media via volume control of added particles. Reference conditions for each seeds are given in Table II.6 with volume fraction of gold. Size given by DLS was used to obtain the number of added seed. The order of magnitude is larger for Seed 1 than other precursors due to small size of given nanoparticle.

Table II. 6 *Calculation of number of different sized seeds in a given volume and volume fraction* ($\boldsymbol{\Phi_{0-seeds}}$= 2.55 10^{-6})

Seed	d_{DLS} (nm)	V_{seed} (µL)	N_{seed} **	N_d **(part/cm3) DLS	N_d ** (part/cm^3) SAXS
[1]	2.0	120	7.30 10^{13}	6 .1 10^{14}	4.6 10^{14}
[2]	4.9	60	2.48 10^{12}	6.6 10^{13}	2.0 10^{13}
[3]	8.7	400	2.95 10^{12}	7.3 10^{12}	5.0 10^{12}
[4]	5.6	400	1.10 10^{13}	2.0 10^{13}	8.0 10^{13}

* d= average diameter of particles obtained by DLS

**N_{seed} = Number of seeds in corresponding volume

***N_d = Number density

2.2.2 Characterization of Final States by TEM

TEM images of final NP (*after termination of growth and purification of excess CTAB*), obtained with addition of different seeds within the same growth media (*See Table II.2*), is represented in Figure II.6. Initial results indicate that every seed is associated to a different final form.

For Type 1 seeds, the Figure II.6a represents a TEM image of nanorods. Additional cubic shapes other than nanorods are also observed as by-products in few quantities. Corresponding length (*L*) versus width (*W*) plot is shown in Figure II.6b. A bifurcation point can be seen between nanorods and isotropic particles around 6 nm in an agreement with previous studies on seedless synthesis [19]. Average dimensions of nanorods is estimated as *L* = 35nm ± 7 nm and *W*= 13 nm ± 8 nm with an average aspect ratio of 2.7 (*detailed crystal structure of these single nanorods will be given in Chapter IV with HRTEM electron tomography and analysis).*

In growth of Type 2 seeds, the dominant morphology is found as bean shape nanoparticles coexisting with spherical NPs (Figure II.6c). From *L, W* plot (Figure II.6d), it appears that three kind of particles are coexisting;

- Spherical particles with average diameter of 20 nm
- Nanobeans with <*L*>=26 nm, <*W*>=16 nm, AR=1.6 nm
- Larger nanobeans with similar AR as previous, <*L*>=42 nm, <*W*>=26 nm

For Type 3 seeds, the TEM images of final nanoparticles show a majority of isotropic NPs exhibiting systematically numerous defects (Figure II.6*e*). On *L,W* plot, even though the main population is occupied by spherical particles, small anisotropy between AR 1-1.5 means that some particles have spheroid shapes (Figure II.6*f*). Average size of spherical nanoparticles nanoparticles are estimated around 35 nm.

For Type 4 seeds, the TEM image of resulting nanoparticles is shown in Figure II.6*g*. Again, final nanoparticles show isotropic morphologies with average size of 17 nm. Even though low resolution micrograph is not quantitative to indicate the crystal structure of NPs, TEM images show that nanoparticles bear various crystal defects and twining faults.

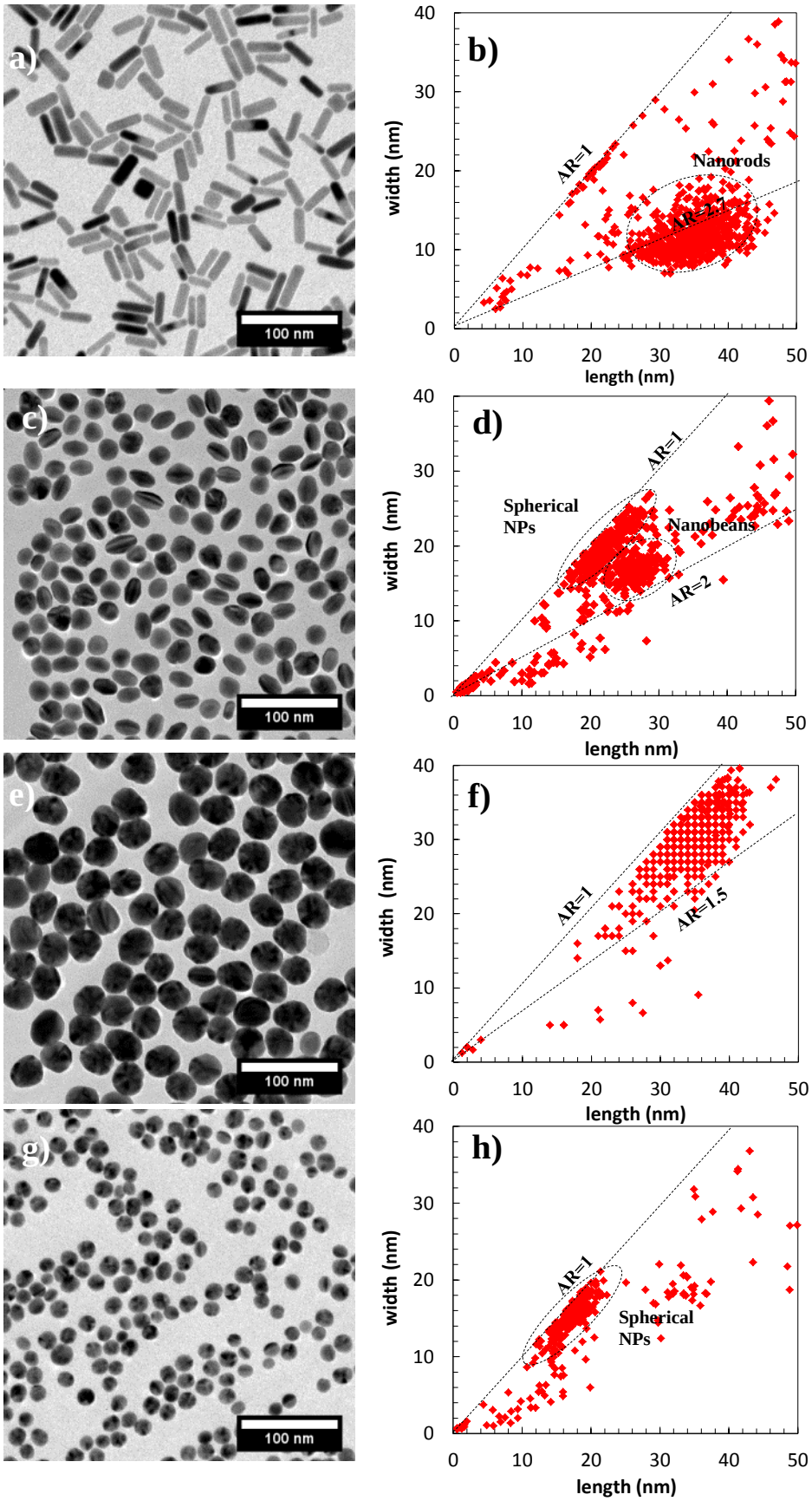

Figure II. 6 *TEM images of final NPs obtained with (a, b)120 µL of Type 1 Seeds stabilized with CTAB (c, d) 400 µL of Type 2 Seeds stabilized with citrate (e, f) 400 µL of Type 3 seeds stabilized by citrate (g, h) 400 µL of Type 4 seeds stabilized by AA with corresponding size analysis obtained from TEM data*

Results on obtained final nanoparticles synthesized with variable seeds are summarized in Table II.7 with corresponding dimensions of dominant morphologies.

Table II.7 *Comparison of final NP morphology and dimension with respect to initial seed*

Seed	Capping Agent	Final NP	Avergae Dimensions (nm)	
			<length>	<diameter>
[1]	CTAB	Nanorods	35	12
[2]	Citrate	Nanobeans spheres	27 -	17 20
[3]	Citrate	Spheroids (*small anisotropy*)	-	35
[4]	L-Ascorbic Acid	Spheres	-	17

2.2.3 Following the Growth Kinetics by UV-Vis Spectroscopy

2.2.3.1 Growth from Type 1 Seeds

It is already known that by using CTAB capped seeds (Type 1), it is possible to produce high yield of nanorods, up to 95%, with traditional growth conditions given in Table II.2 [20–22]. Here, the kinetic studies on the growth from such type of seeds into nanorods, for this traditional growth conditions are presented.

Figure II.7 represents temporal evolution of the absorption spectra, monitored during the growth (*spectra's are recorded with delay of 10 s starting from the moment of addition of seeds into growth media*). The continuous increase in absorbance of both transverse ($\lambda_{T\text{-}SPR}$) and longitudinal surface plasmon peaks ($\lambda_{L\text{-}SPR}$) are clearly visible. Overall growth of nanoparticles is completed in 15 minutes.

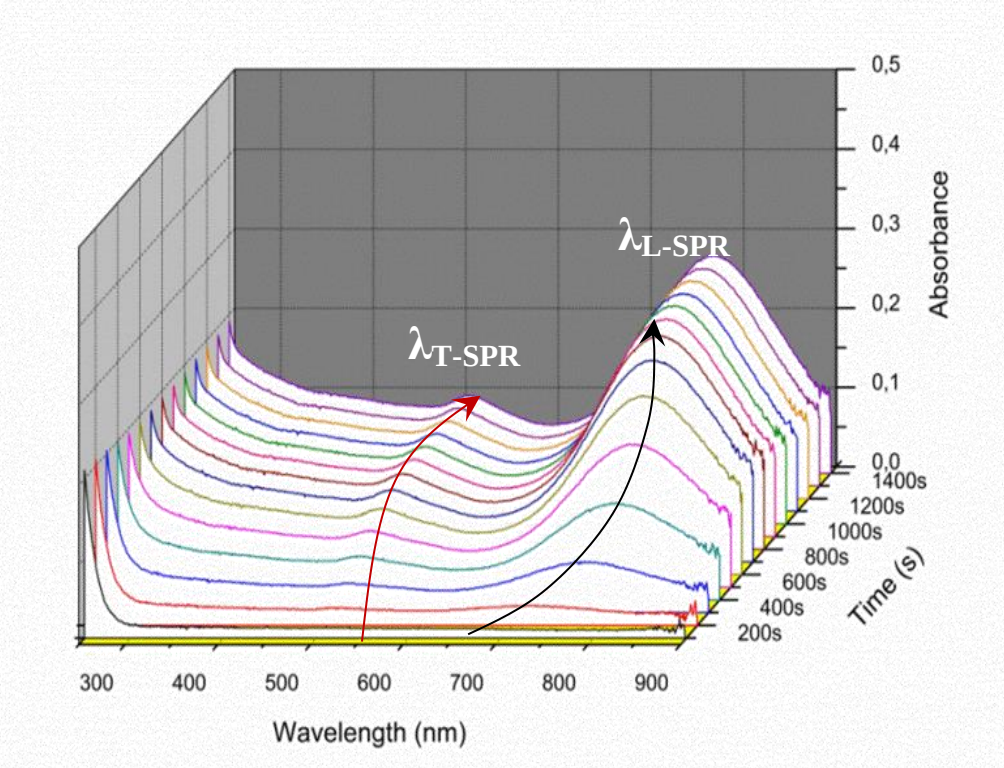

Figure II. 7 *UV-Vis Spectrum of growth solution right after addition of 120 µL of Type 1 seed in growth solution ([CTAB] = 0.1M, [$HAuCl_4$] = 0.5mM, [AgNO3] =0.045mM, [AA] =0.75mM)*

Variation of absorbance as a function of time for both characteristic surface plasmon peaks ($\lambda_{T\text{-}SPR}$ and $\lambda_{L\text{-}SPR}$) and the one corresponding to 400 nm (λ_{400}) is plotted in Figure II.8a. Basically, absorbance increases steadily for all given wavelengths with different rates. Growth rate of characteristic plasmon peaks ($A_{L\text{-}SPR}$ and $A_{T\text{-}SPR}$) can be identified by the slope of the initial section of the Absorbance (A) vs time (s) plot. To be more specific, from the slope of Absorbance = $f(t)$, it can be deduced that $A_{L\text{-}SPR}$ is increasing 3 times more than $A_{T\text{-}SPR}$ (*the difference can also be seen, if we plot the temporal evolution of the ratio of* $A_{L\text{-}SPR} / A_{400\ nm}$ *and* $A_{T\text{-}SPR} / A_{400\ nm}$ *as demonstrated in Figure II.8d*).

The $\lambda_{\text{-}SPR}$ reaches its maxima at about 540 seconds, at the resonance wavelength of 795 nm, achieving relative absorbance of approximately 0.3 (Figure II.8b). As the growth time increases a significant decrease in $\lambda_{L\text{-}SPR}$ starts to appear after 540 seconds, after 790 nm, which is the result of reshaping of gold nanorods into less anisotropic nanoparticles with time (Figure II.8b). Such trend of reshaping is often observed in classical wet seed mediated growth synthesis of nanorods and generally explained by etching at the tips of nanorods [1,14,23].

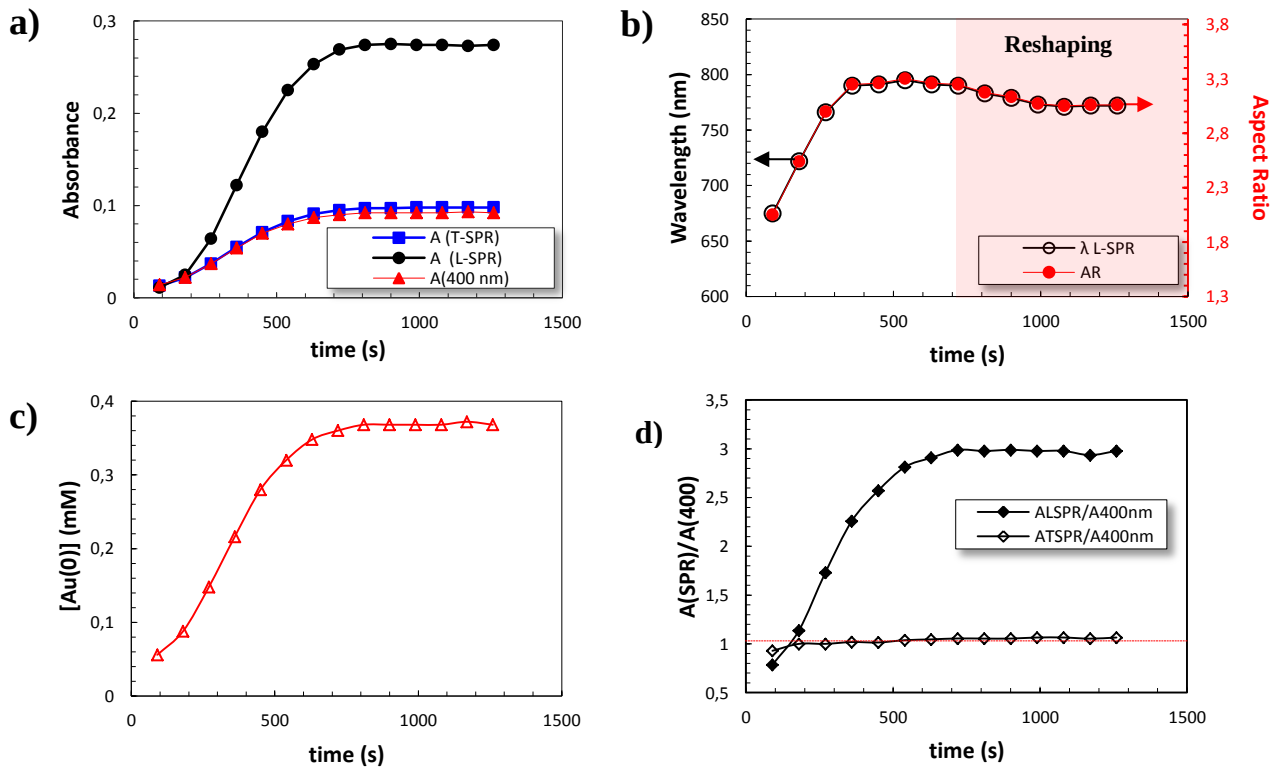

Figure II. 8 *(a) Evolution of absorbance for longitudinal, transverse LSPR and at 400 nm with time (b) evolution of localized plasmon resonance wavelength with time (c) Change in final Au(0) concentration and aspect ratio of nanorods in function of time (d) Ratio of* $A_{(SPR)}/A_{400nm}$ *for both T-SPR and L-SPR as a function of time*

Even though various models have been described in the literature to predict the optical response of different gold nanoparticles structures in solution, there are still some difficulties in reproducing quantitatively the total experimental spectra like previously presented in Figure II.7. Both, the scattering and absorption components of the spectra depends on volume, size and aspect ratio of the nanoparticles present in the solution, making difficult to extract the size distribution of nanoparticles in solution from UV-Vis spectra [24,25]. However, since $\lambda_{L\text{-}SPR}$ is more sensitive to shape rather than $\lambda_{T\text{-}SPR}$, $\lambda_{L\text{-}SPR}$ can be used to estimate the aspect ratio of the nanorods. A simple relationship between the absorption maximum of $\lambda_{L\text{-}SPR}$ (λ_{max}) and the aspect ratio of the nanorods may be used to extract information on evolution of AR in time (Eq 2.3) [26–28]:

$$AR = \frac{\lambda_{max} - 478}{96} \quad (2.3)$$

Results on temporal evolution of AR, are given in Figure II.8b. Initially formed seeds start to elongate rapidly and reaches the aspect ratio of 3.25 in the first 360 second of the reaction. After fast growth stage, increase of AR continues with slow speed followed by steady decrease. In this stage nanorods rearrange their aspect ratios to lower values. This final stage of gold nanorod growth is followed by the stabilization of AR. This tendency is in perfect agreement with the results obtained by Henkel et al. [29] where maximum aspect ratio is attained around 360 s for similar chemical conditions.

Another information, that could have been extracted from given kinetic spectra, is following the variation of absorbance value at 400 nm to study the rate of conversion of ionic gold, Au(I), into metallic gold, Au(0), at different time spans via Eq 2.4;

$$A_{400\,nm} = \varepsilon b c_{Au(0)} \quad (2.4)$$

where ε is the absorption coefficient ($2500 M^{-1}cm^{-1}$ [30,31]), b is the path length of the cell (1 mm) and $c_{Au(0)}$ is the concentration of metallic gold. Results are presented in Figure II.8c. Rapid increase in colloidal gold concentration with time indicates a rapid increase in Au(0) concentration indicating that yield of monomer formation is quite rapid till 630 seconds. Therefore reshaping (*Figure II.8.b*) occurs after the completion of the reduction of Au(I) into Au(0). After termination of growth, total Au(0) amount is found as 0.368 mM with yield of 73.6% in the final solutions before purification step.

In the following section, similar analysis will be explained for growth of Type 2 (citrate capped) seeds.

2.2.3.2 Growth from Type 2 Seeds

Figure II.9 represents the absorbance plot of the growth solution after addition of 60 µL Type 2 seeds. As in the previous case, two distinct plasmon bands are visible similar to the ones observed for nanorods. Main the difference between both spectrums is that, for nanobeans, the absorbance value for $\lambda_{L\text{-}SPR}$ is lower than for $\lambda_{T\text{-}SPR}$. This may result from the fact that, high yield of isotropic nanoparticles are simultaneously formed during the growth of anisotropic nanobeans.

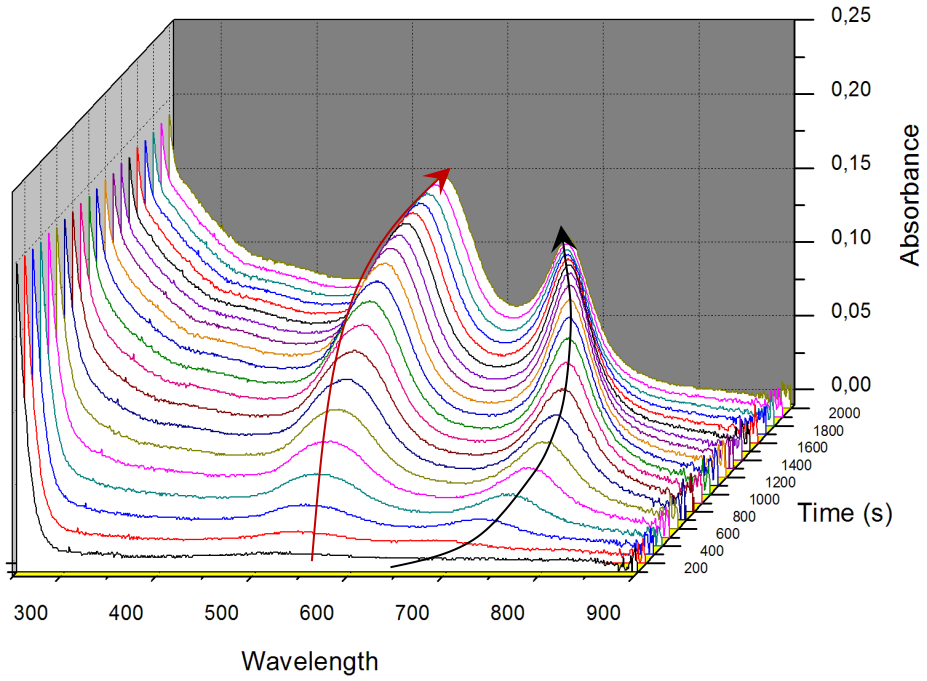

Figure II. 9 *UV-Vis Spectrum of growth solution recorded right after addition of 60µL of Type 2 seed in growth solution ([CTAB] = 0.1M, [$HAuCl_4$] = 0.5mM, [$AgNO_3$] =0.045mM, [AA] =0.75mM)*

Because the $\lambda_{T\text{-}SPR}$ signal is the result of the superposition of two different signals (*from high yield spherical nanoparticles and nanobeans*), no straight forward information on the growth rate of different morphologies, by using slope of the Absorbance(t) curve, can be deduced for given signal. We may only state that, in the Figure II.10a, both $A_{T\text{-}SPR}$ and $A_{L\text{-}SPR}$ increases steadily tills its saturation point.

Plot of the evolution of $\lambda_{L\text{-}SPR}$ with time indicates a red shift from 678 nm to 750 nm in the early stages of growth (Figure II.10b). After reaching its maximum value (765 nm), a strong decrease is observed down to 660 nm after 30 minutes. This variation in $\lambda_{L\text{-}SPR}$ position

prevents us to predict of the AR of final nanobeans with previously given equation (Eq. 2.4) for given growth conditions.

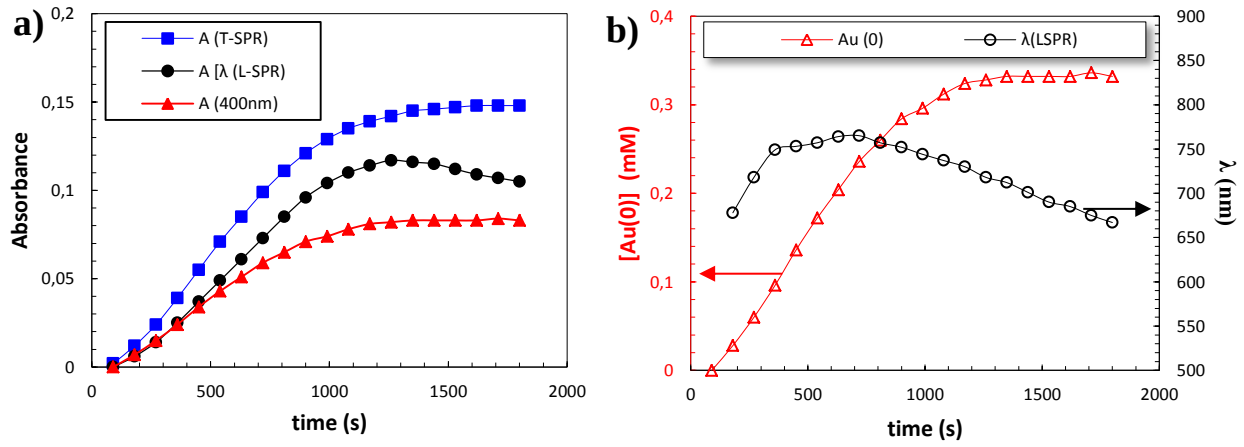

Figure II. 10 *Evolution of a) absorbance at 400 nm, longitudinal and transversal surface plasmon band b) position of L-SPR and T-SPR c) Colloidal gold concentration with time*

As previously done, the formation of colloidal gold is quantified over time by using magnitude of absorbance at 400 nm. After 1350 s, colloidal gold concentration remains constant at 0.320 mM. By the end of the reaction, 67.2% of initial ionic gold is reduced. Contrary to nanorods case, the reshaping starts before the completion of the reduction of Au(I) into Au(0).

- ***Comparing the Kinetics of Au(0) Formation for Both Nanorods and Nanobeans***

Kinetic of conversion of Au(I) into Au(0) for both nanorods (Fig II.8c) and the bean shape nanoparticles (Fig II.10b) can be compared from the slope of the $Absorbance_{400nm}(t)$. For nanorods absorbance is increasing about 2 times faster than nanobeans at 400 nm. This means that the rate of ionic gold conversion is slower for nanobeans. The reason can be explained by using the number of seeds given in Table II.6. During the formation of nanobeans, lower numbers of Type 2 ($2.48\ 10^{12}$) seeds are added in comparison to Type 1 seeds ($7.30\ 10^{13}$), for the same growth solutions. In seeded growth method it has been proved that the Au(I) to Au(0) transformation proceeds through surface catalyzed reduction [32]. The transformation is thus favored by a larger available surface of gold seed (*due to large number*), in this case Type 1 seeds, in the solution.

2.2.3.3 Growth from Seed 3

Kinetic experiments regarding Type 3 seeds (*prepared by changing the order of reactants in classical Turkevitch synthesis*), has been realized by adding 400 µL of seed solution to the reference chemical conditions (0.1 M CTAB, 0.5 mM $HAUCl_4$, 0.045 mM $AgNO_3$ and 0.75 mM AA). A representative spectrum of growth kinetics for such condition is given in Figure II.11a.

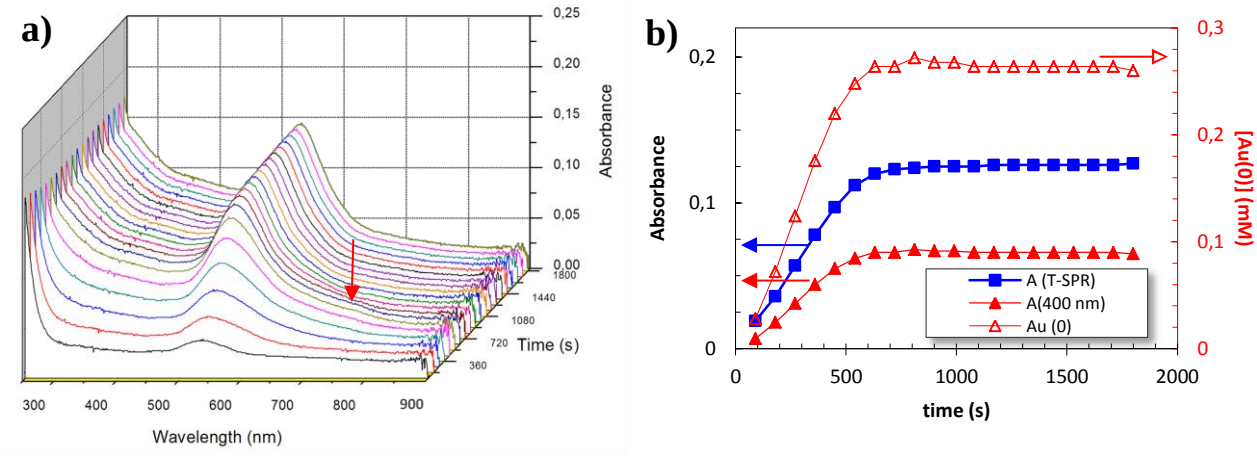

Figure II. 11 *a) UV-Vis Spectrum of growth solution right after addition of Type 3 seed b) Evolution of absorbance at transverse surface plasmon band with time*

A small trace of secondary plasmon band at higher wavelengths (~736 nm) can be seen at early stages of growth and vanishes quickly in time. This means that, small elongated nanoparticles forming at the beginning of the reaction transform into isotropic shapes rapidly. At the end of the reaction, SPR band appearing around 536 nm indicates that particles adopt only isotropic morphologies.

The absorbance related to the transversal peak ($A_{T\text{-}SPR}$) subsequently increases with time until a saturation point at 0.126, revealing that reaction is finished around 720 seconds (Figure II.11b). Concentration of Au(0) at the end of the reaction is estimated around 0.264 mM, meaning that only 53% of the initial Au(I) (0.5 mM) is reduced.

No sign of high anisotropic shapes (*rods or beans*) in case of growth from Type 3 seeds can be seen. The reason can be related to the large size of the seeds (*8.7 nm*).

2.2.3.4 Growth from Type 4 Seeds

In this section, the seeds prepared by microfluidic set-up [6] have been used as precursors in our reference growth solution. Absorption spectra of the growth from such type of seeds exhibit one strong transverse plasmon band at 529 nm (Figure II.12a). As previously seen (*in Figure II.11*), small peak appearing at higher wavelengths (~650 nm) fades quickly with increasing time, as in the case of Type 3 seeds, meaning that initially formed elongate particles reshapes into isotropic NPs.

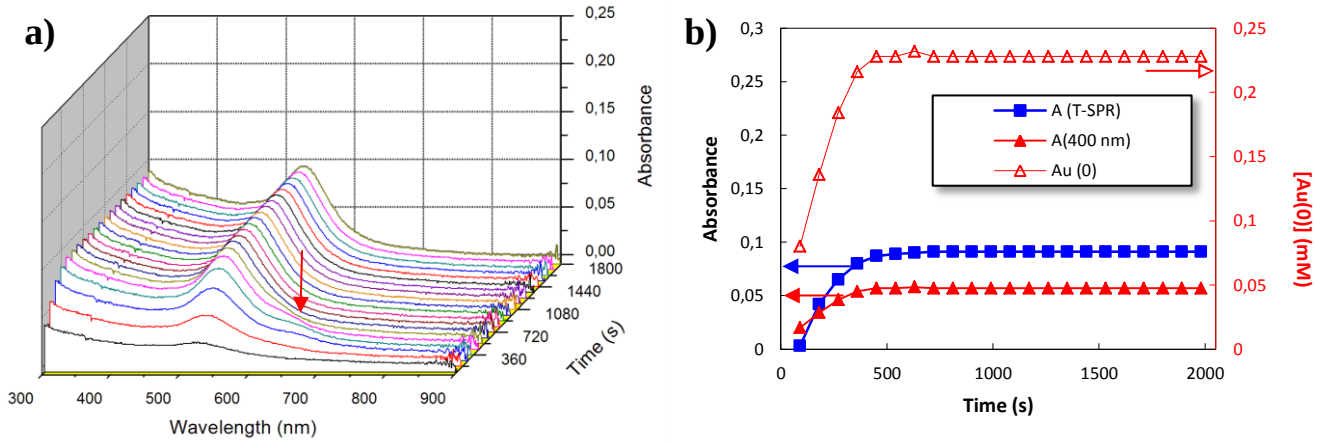

Figure II. 12 *(a) UV-Vis Spectrum related to the growth solution right after addition of Type 4 seed (b) Evolution of absorbance at transverse surface plasmon band with time*

Overall reaction is completed around 500 seconds (Fig II.12b). A weak yield of ionic gold reduction % 45.6 at the end of the reaction means that nearly half of the gold precursor is not converted to colloidal gold.

2.2.4 Size Tuning of Anisotropic Gold NPs

Aspect ratio of elongated NP (*in this case nanorods and nanobeans*) may be controlled by;

- varying the seed volume injected to the growth solution [1,33]
- optimizing the concentration of $AgNO_3$ in the growth solution [17]
- controlling the pH of the growth solution.

In this section, the results obtained concerning the optimization of the AR of anisotropic nanoparticles (nanorods and nanobeans), by simple variation in reaction parameters, is presented. Additional study on given parameters and many others (*effect of CTAB concentration, influence of external additives such as NaBr, etc.*) responsible for the anisotropy are analyzed in the next chapters in detail (*See Chapter IV*).

2.2.4.1 Tuning the AR of Final NPs by Varying the "Seed Volume" during the Growth from Type 1, Type 2 and Type 3 Seeds

A comparative study of the effect of seed volume on the final shapes, has been performed respectively for Type 1, 2 and 3 seed by decreasing the volume, for Type 1 seeds from 120 µL to 60 µL, for Type 2 seeds from 150 µL to 60 µL and for Type 3 seeds from 400 µL to 50 µL (*additional pH control was mandatory to promote the anisotropy during the growth of Type 3 seeds*). Resulting UV-Vis spectra's are summarized in Figure II.13.

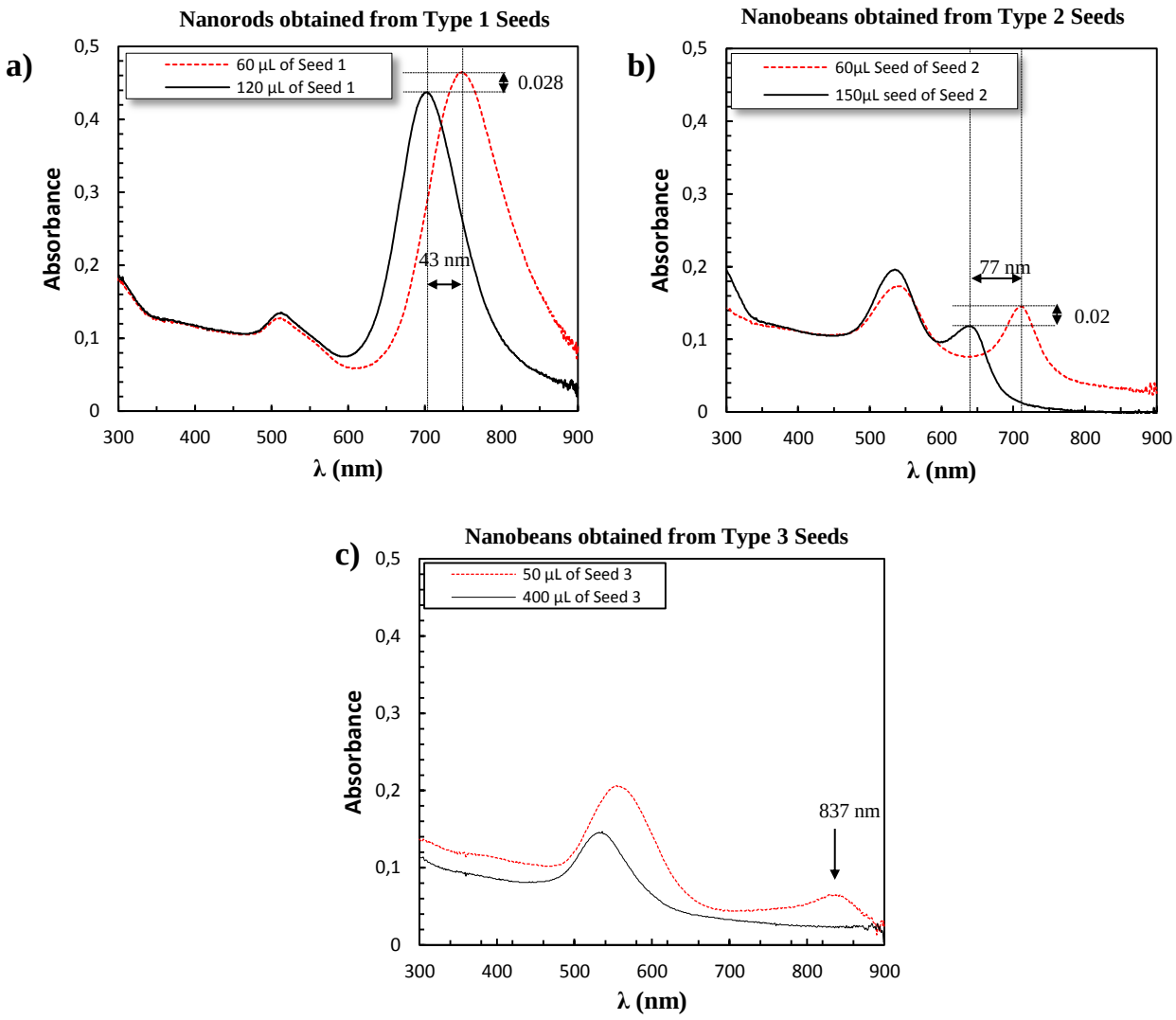

Figure II. 13 *UV-Vis spectrum corresponding to final nanoparticles obtained with a) Seed 1 (60-120 µL) 1 and b) Seed 2 (60-150µL) with growth solution composition of 0.1 M CTAB, 0.5 mM $HAuCl_4$, 0.14 mM $AgNO_3$, 0.75 mM L-Ascorbic Acid and c) Seed 3 (50-400 µL) 0.01 M HCl is used in addition to similar growth solution*

Final nanoparticles obtained from Type 1 and 2 seeds exhibit higher $\lambda_{L\text{-}SPR}$ values (*for nanorods obtained from Type 1 seeds, $\lambda_{L\text{-}SPR}$ increases from 697 nm to 740 nm; for nanobeans obtained from Type 2 seeds, $\lambda_{L\text{-}SPR}$ increases from 630 nm to 707 nm*) when the volume of the seeds are decreased in both cases (Figure II.13a,b). This indicates that AR of both anisotropic particles (nanorods and nanobeans) increase with decreasing seed volume. For nanorods the increase in the AR from 2.3 to 2.7 can be calculated by using the simple relation between the absorption maximum and the aspect ratio, given previously in Eq.2.3.

Additionally, for both cases, the $A_{L\text{-}SPR}$ increases when the volume of the seed is decreased, indicating that the fraction of anisotropic nanoparticles increases. The amplitude of the plasmon band at 400 nm stays constant with decreasing seed volume, for both spectra's given in Figure II.13a,b and they exhibit similar values (A_{400} *=0.117 for nanorods,* A_{400} *=0.111 for nanobeans obtained by Type 2 seeds)* meaning that the amount of seeds do not affect directly the total Au (0) concentration ([Au(0)]~0.45 mM). This is in agreement with former studies, by in situ SAXS, showing that final yield is controlled by the ascorbic acid concentration in the growth media [32].

In Figure II.13c, given UV-Vis Spectra's corresponds to the samples, where two different volumes of (50 µL and 400 µL) Type 3 seeds are added in a growth solution with controlled pH (1.9). The pH control was performed for given samples to promote the growth of small longitudinal plasmon band observed during the kinetic experiments, which vanishes quite rapidly in time (See 2.2.3.3). When volume of Type 3 seeds used during growth is decreased from 400 µL to 50 µL, small $\lambda_{L\text{-}SPR}$ at 837 nm appears with an absorbance intensity of 0.067. This number is quite low in comparison to the absorbance intensity of $\lambda_{T\text{-}SPR}$, 0.206, meaning that yield of anisotropic NPs are considerably low. In this sample, variation in the seed volume clearly induce an effect in the absorbance value at 400 nm (*values is increased from 0.086 to 0.113*) meaning that the final colloidal gold concentration is increased from 0.344 mM to 0.452 mM with decreasing seed volume. This result is however, in contradiction with the statement that the colloidal gold concentration is increased when the surface of the seeds are increased (*because the reduction of Au(I) to Au(0) is catalyzed on seed surface),* since in our case, at 400 µL the average number of seed particle (*calculated via Eq. 2.2*) is around $3.0\ 10^{12}$ and for 50 µL this number decreases to $3.6\ 10^{11}$.

The TEM image of this sample, given in Figure II.14, shows that the morphology is a mixture between the spherical NPs ($d_{average}$ *= 55 nm*) and the small elongated nanobeans (*<L>=72 nm, <W>= 43 nm*).

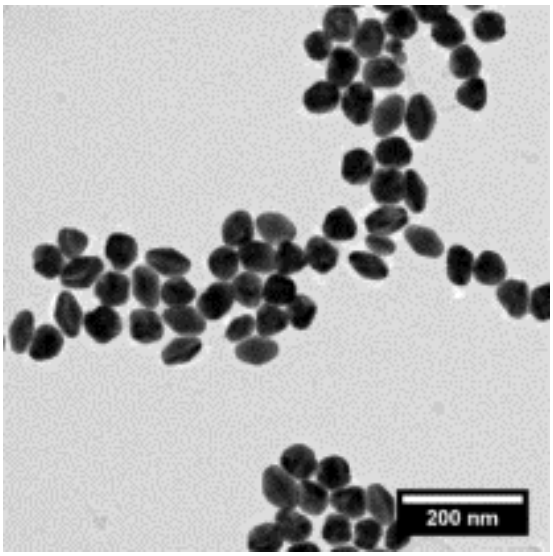

Figure II. 14 *TEM image of the final nanoparticles obtained when 50 µL of Type 3 seeds are added in a growth solution containing, 0.1 M CTAB, 0.5 mM $HAuCl_4$, 0.045 mM $AgNO_3$, 0.75 mM AA and 0.01 M HCl*

2.2.4.2 Tuning the AR of Nanobeans obtained by Type 2 seeds by Varying the Silver Nitrate Concentration

UV-Vis spectra's corresponding to the final nanoparticle solutions, obtained by Type 2 seeds, at two different $AgNO_3$ concentrations (*0.045 mM and 0.14 mM*) are shown in Figure II.15a.

When the silver amount is increased to 0.14 mM, $\lambda_{L\text{-}SPR}$ shifts to higher values (*from 673 nm to 707 nm*) meaning that the aspect ratio is increased for elongated nanobeans. Colloidal gold concentration for both samples, prepared with 0.045 mM $AgNO_3$ and 0.14 mM $AgNO_3$, is calculated as 0.46 mM and 0.42 mM respectively (*by using the absorbance at 400 nm*). This means that Au(0) concentration decreases with increasing silver concentration. Additionally, the absorbance, corresponding to the $\lambda_{L\text{-}SPR}$, decreases from 0.112 to 0.098, with increasing silver concentration showing that the yield of anisotropic particles is decreased. The reason may be the result of the decrease in the colloidal gold concentration as previously stated.

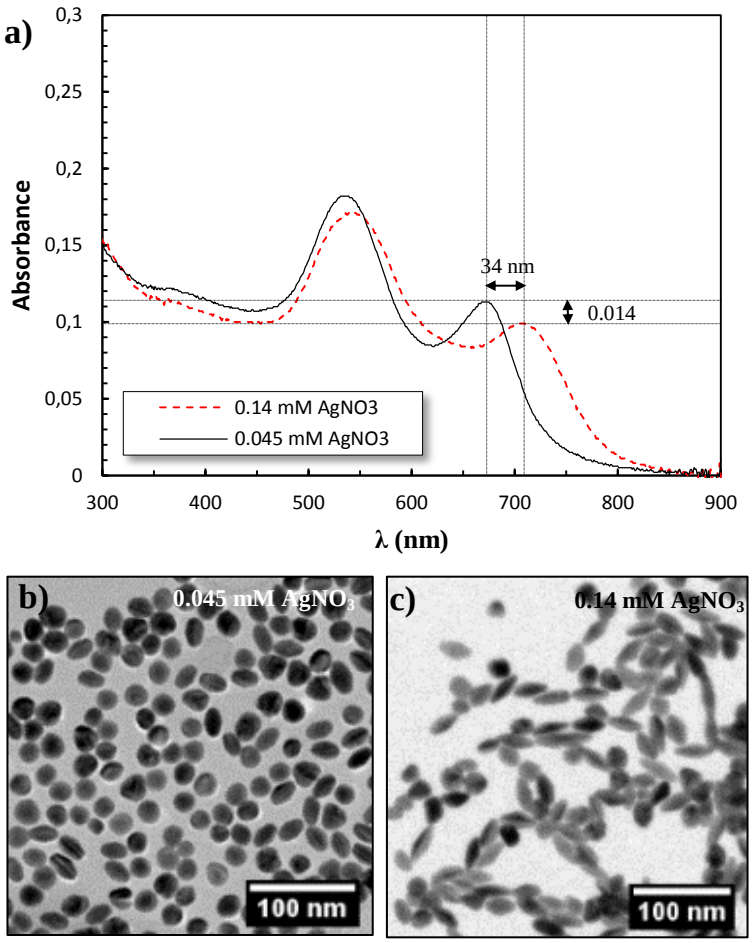

Figure II. 15 *a) UV-Vis Spectra's relating to the samples prepared with addition of 400µL of Type 2 seed into a growth solution containing 0.045 mM and 0.14 mM of $AgNO_3$. Representative TEM images of final nanoparticles obtained at b) 0.045 mM Ag(I) and c) 0.14 mM Ag(I) concentration*

By the analysis of the TEM images of final nanoparticles (*corresponding images are given in Figure II.15b,c*), the average aspect ratio of 1.6 is assigned to the nanobeans obtained in the presence of 0.045 mM silver nitrate and 2.0 for the final nanoparticles, resembling more to bipyramids due to their sharper tips, obtained with 0.14 mM of silver nitrate.

Although the mechanism of silver on promotion of higher aspect ratio particles is not fully understood, evidently it is involved in the shape control of final nanoparticles as indicated in our results which are in agreement with previous studies [1,2,17].

In the next part, the same type of analysis is performed, to study the effect of silver concentration on the final nanoparticles in a pH controlled growth solution (*again two different silver concentrations are studied 0.045 mM and 0.14 mM*).

- **Tuning the AR of Nanobeans obtained by Type 2 seeds by Varying the Silver Nitrate Concentration at low pH (1.9)**

In the previous experiments, given in 2.2.4.1, we have demonstrated that the AR and the yield of anisotropic nanoparticles increase when the volume of seed solution (Type 2) decreases. Additionally in 2.2.4.2, we have revealed that the anisotropy is highly promoted with increasing $AgNO_3$ concentration during the growth of nanobeans when 400 µL of Type 2 seeds are used. The following experiments are designed to have a similar kind of study on the influence of silver, however this time the pH of the growth solution is controlled around 1.9 (*by the addition of 1 M HCl (50 µL) into the reference growth solution given in Table II.2*) and lower volume of Type 2 seeds are used in comparison to Figure II.15 (*60 µL instead of 400 µL*). In other words, 60 µL of Type 2 seeds are added in acidic growth medias with variable $AgNO_3$ concentrations (*0.045 mM and 0.14 mM*).

Figure II.16a summarizes the UV-Vis Spectra's of these experiments. Both spectra's exhibit high $\lambda_{L\text{-}SPR}$ peaks (*806 nm and 861 nm respectively*) indicating the formation of high AR nanoparticles. Large shift in the $\lambda_{L\text{-}SPR}$ to higher wavelengths means that anisotropy is increased with the increase of $AgNO_3$ concentration.

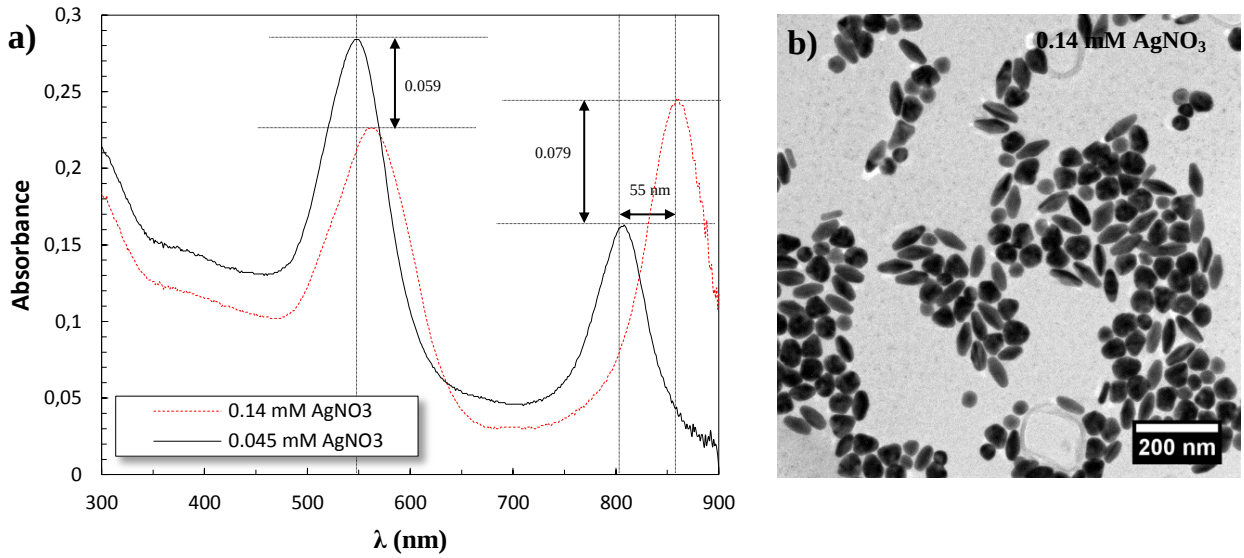

Figure II. 16 *a) UV-Vis Spectrums of experiments realized via addition of 60µL Type 2 seed in growth solution where pH is regulated via addition of 50 µL of 1 M HCl, at two different $AgNO_3$ concentrations (0.045 mM and 0.14 mM) b) TEM image of nanoparticle synthesized at 0.14 mM silver nitrite concentration*

The increase of the $A_{L\text{-}SPR}$ / $A_{T\text{-}SPR}$ ratio from 0.56 to 1.1 is probably due to the fact that, anisotropic particles increase their yield over isotropic shapes. Again the decrease in the absorbance at 400 nm with increasing silver amount, reveals that less Au(I) is reduced as previously seen in Figure II.15a. We retrieve the poisoning effect of added silver in growth solution already observed in silver(I) assisted seed mediated growth of nanorods [32].

Additionally, both spectra's exhibit sharper longitudinal plasmon peaks with respect to previously seen nanobeans. The TEM image of the final nanoparticles obtained at 0.14 mM $AgNO_3$ concentration, given in Figure II.16b, shows that previously obtained nanobeans leave their place to higher aspect ratio bipyramids (2.7) bearing sharper tips.

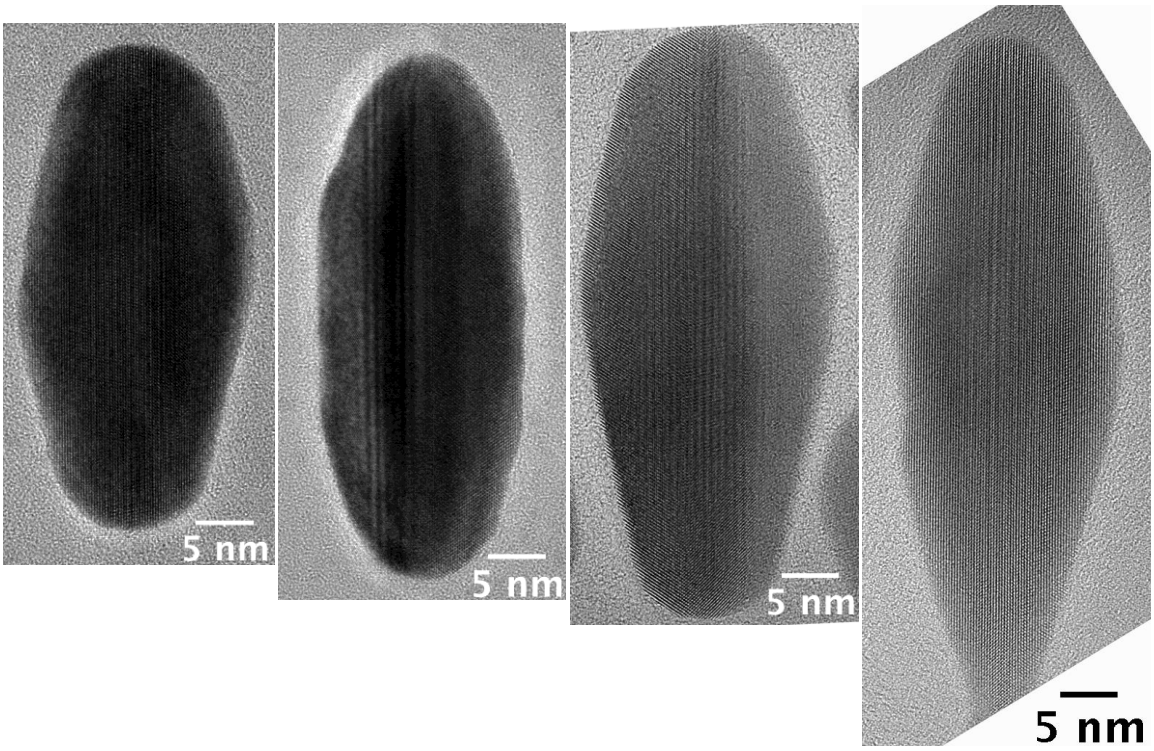

Figure II. 17 *HRTEM images showing the evolution of nanobeans into bipyramids*

In Figure II.17, given HRTEM images demonstrates the evolution of low AR nanobeans into high AR bipyramids by elongating their size and sharpening their tips through the twining axis. In Chapter IV, by combining HRTEM images and selected area diffraction pattern (SAED) analysis we will demonstrate that both nanobeans and bipyramids have the same type of crystal structures.

To sum up, both low pH and high silver nitrate concentration promotes the formation of highly anisotropic bipyramids from low AR nanobeans.

2.3 Discussion

2.3.1 Comparing Type 1 and Type 2 Seeds

The use of distinct seeds, varying in size and crystal structure, has a strong influence on the final shape of the nanoparticles obtained by seeded mediated method in liquid phase. With CTAB Capped Seeds (Type 1) we are able to obtain monocrystalline nanorods, whereas with citrate capped seeds (Type 2) obtained nanoparticles exhibit bean alike structures or bipyramidal shapes (*when the chemical conditions are optimized*) with large number of crystal defects.

Although both seeds exhibit initial size under the bifurcation point [19], we can say that Type 2 seeds will hardly yield to single crystalline nanorods in the presence of $AgNO_3$. This is in agreement with the observation made by various authors on final bipyramidal shapes. To be specific, Guyot-Sionnest et al. have demonstrated that for silver supported seeded growth method; CTAB seeds give in majority monocrystalline nanorods while citrate seeds lead in majority to bipyramids [16]. Kou et al. have obtained similar results to synthesize high yield of bipyramids (50-60%) with citrate capped seeds (Type 2) by replacing CTAB with CTBAB in the growth solution [34,35]. Here, contrary to former studies on similar case, our conclusions are supported by a complete quantitative analysis of the seeds (*size, shape and internal structure*) prior to their growth.

Both highly anisotropic bipyramids and nanorods will be the focus of interest throughout this thesis; therefore, to visualize the distinct difference in optical response of both morphologies we have superposed the representative UV-Vis spectrum of the nanorods with the one for bipyramids and summarized the result in Figure II.18 ($\lambda_{L\text{-}SPR}$ *absorbance of bipyramids is normalized to with respect to nanorods*).

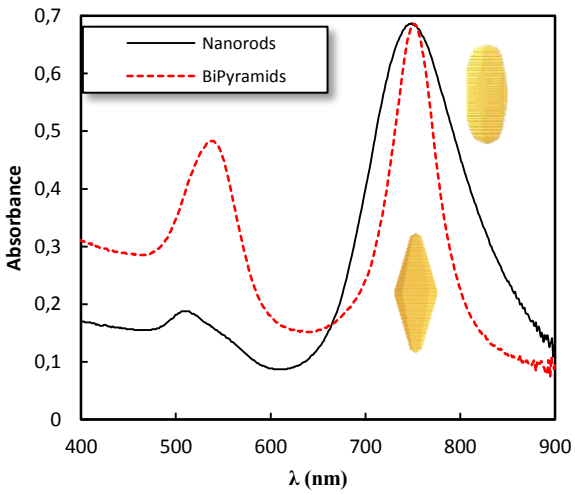

Figure II. 18 *Comparison of UV-Vis Spectra's of Bipyramids and Nanorods*

The clear difference between the shape of $\lambda_{L\text{-}SPR}$ for nanorods and bipyramids is due to the fact that, bipyramids exhibit thinner and sharper longitudinal plasmon peaks in the wavelength range of 600-1000 nm (*in function of the aspect ratio*) because of their sharp tips whereas in nanorods UV spectrum is much more broader due to their rounded tips in similar wavelength range given for bipyramids. Higher absorbance value of $\lambda_{T\text{-}SPR}$, for the representative UV-Vis spectrum of bipyramids, can be explained by the fact that final bipyramids are excessively polluted by isotropic shapes. The yield of bipyramid formation never exceeds 30% [16,36] with current version of the seed mediated synthesis we have employed and the final particles are always polluted with isotropic analogues (*when no additive is used during formation*).

2.3.2 Comparing Type 2 and Type 3 Seeds

Although Type 2 and Type 3 seeds are prepared with same type of stabilizing agent (citrate), obtained final nanoparticles differ in partition of morphology (*Type 2 producing high yield of nanobeans and Type 3 yielding mainly spherical NPs*) when comparable number of particles are added (N_2*=3.94* 10^{12} *for seed 2 and* N_3*=2.95* 10^{12} *for seed 3*). For type 3 seeds, it is remarkable to see that, we end up with spherical NPs after an initial formation of a small amount of anisotropy that rapidly reshape when high number of seed is added in reference growth solution. This reshaping can be compared to the one observed in the case of Type 2 seeds even though the trace of reshaping is less significant for Type 3 seeds.

Another difference between both seeds is the concentration of Au(0) integrated in final nanoparticles. Lower Au(0) concentration in case of Type 3 can be explained by considering high polydispersity of size of this type of seeds. Mainly, due to high polydispersity, large sized Type 3 seeds grow rapidly into spherical shapes, consuming the Au(0) available for the small size particles that are able to grow into nanobeans. It is also possible that we are far away from bifurcation point for Type 3 seeds due to its larger size. However, both types of seeds have a tendency to produce more anisotropic nanoparticles when the numbers of seeds are decreased in an acidic environment containing high amount of Ag^{+}. This is because low pH (*acidic medium*) induces a strong modification in the redox properties of ascorbic acid and decreases the kinetic of nanoparticle formation. It is known that slow growth kinetics promotes the anisotropy [37].

2.3.3 Comparing Type 3 and Type 4 Seeds

In the growth of Type 3 and 4 seeds, identical isotropic shapes (*spherical*) are obtained in final when the similar volumes of seeds are used (400 µL). Unique difference between both cases is the size of the final spherical particles. Final nanoparticles synthesized from Type 3 seeds (8.7 nm) exhibit mean diameter of 35 nm, whereas this value decreases to 15 nm for the final NPs obtained with Seed 4 (5.6 nm). Such difference in the size can be related to the number of seeds present in the growth solution. To be specific, in a given volume (400 µL), low number of Type 3 particles (~2.9 10^{12}) ensures the formation of large sized final states in an environment rich with monomer, whereas in Type 4 seeds the situation is reversed, meaning that increased number of precursors (~7.8 10^{12}) grow to smaller final states in an environment depleted in monomer.

2.4 Conclusion

In this chapter we have studied the influence of seed size and crystal structure on the formation of final nanoparticles. It is clear that final nanoparticle shape and crystal structure depends strongly on the initial seed employed; meaning that crystal structure of seed is inherited during the growth and transferred to final material.

Growth of different stabilized seeds in a reference reaction condition result in different morphologies such as nanorods, bean shape particles, bipyramids as well as spherical morphologies. Generation of nanorods from CTAB capped seeds and elongated pseudo typed bean structures from citrate capped seeds give a hint that shape and structure of the seeds plays a crucial role in the growth kinetics and the crystal structure of final NP.

Difference in the rate of growth from individual seeds (*Type 1,2,3 and 4*) can be attributed to the difference in size and the crystal structure of each seed. Depending on the chosen seed to be grown, one can control kinetics of growth for the final NP and the final morphology. This argument raise the following question: What would be the outcome if two different crystalline structured or size seeds are added in the same reaction container? It will be the subject of the following chapter.

2.5 References

[1] N.R. Jana, L. Gearheart, C.J. Murphy, Adv. Mater. 13 (2001) 1389.

[2] B. Nikoobakht, M.A. El-Sayed, Chem. Mater. 15 (2003) 1957.

[3] A. Gole and C. J. Murphy, Chem Mater 16 (2004) 3633.

[4] S.K. Sivaraman, S. Kumar, V. Santhanam, J. Colloid Interface Sci. 361 (2011) 543.

[5] J. Kimling, M. Maier, B. Okenve, V. Kotaidis, H. Ballot, and A. Plech, J. Phys. Chem. B 110 (2006) 15700.

[6] Han J., Testard F., Malloggi F., Coulon P.E., Menguy N., and Spalla O., Langmuir 28 (2012) 15966.

[7] G.A. Rance, D.H. Marsh, A.N. Khlobystov, Chem. Phys. Lett. 460 (2008) 230.

[8] E. Cottancin, G. Celep, J. Lermé, M. Pellarin, J.R. Huntzinger, J.L. Vialle, M. Broyer, Theor. Chem. Acc. 116 (2006) 514.

[9] C. Louis, O. Pluchery, Gold Nanoparticles for Physics, Chemistry and Biology, Imperial College Press, London, 2012.

[10] T. Hendel, M. Wuithschick, F. Kettemann, A. Birnbaum, K. Rademann, J. Polte, Anal. Chem. 86 (2014) 11115.

[11] G. Wulff, Z.Kristallogr. 34 (1901) 449.

[12] J.L. Elechiguerra, J. Reyes-Gasga, J.M. Yacaman, J Mater Chem 16 (2006) 3906.

[13] H. J., T. F., M. F., P.E. Coulon, M. Nicolas, S. Olivier, Langmuir 28 (2012) 15966.

[14] C. Lofton, W. Sigmund, Adv. Funct. Mater. 15 (2005) 1197.

[15] C. J. Johnson, E. Dujardin, S. A. Davis, C. J. Murphy and S. Mann, J Mater Chem 12 (2002) 1765.

[16] M. Liu, P. Guyot-Sionnest, J. Phys. Chem. B 109 (2005) 22192.

[17] M. Grzelczak, J. Perez-Juste, P. Mulvaney, L.M. Liz-Marzan, Chem Soc Rev 37 (2008) 1783.

[18] J. Reyes-Gasga, S. Tehuacanero-Nuñez, J.M. Montejano-Carrizales, X. Gao, M. Jose-Yacaman, Top. Catal. 46 (2007) 23.

[19] F. Hubert, F. Testard, G. Rizza, O. Spalla, Langmuir 26 (2010) 6887.

[20] Z.L. Wang, M.B. Mohamed, S. Link, M.A. El-Sayed, Surf. Sci. 440 (1999) 809.

[21] J. Rodríguez-Fernández, J. Pérez-Juste, P. Mulvaney, L.M. Liz-Marzán, J. Phys. Chem. B 109 (2005) 14257.

[22] C.J. Murphy, T.K. Sau, A.M. Gole, C.J. Orendorff, J. Gao, L. Gou, S.E. Hunyadi, T. Li, J. Phys. Chem. B 109 (2005) 13857.

[23] C. Bullen, P. Zijlstra, E. Bakker, M. Gu, C. Raston, Cryst. Growth Des. 11 (2011) 3375.

[24] N. Xu, B. Bai, Q. Tan, G. Jin, Opt. Express 21 (2013) 21639.

[25] K. Park, S. Biswas, S. Kanel, D. Nepal, R.A. Vaia, J. Phys. Chem. C 118 (2014) 5918.

[26] A. Brioude, X.C. Jiang, M.P. Pileni, J. Phys. Chem. B 109 (2005) 13138.

[27] H. Omi, in:, Transm. Electron Microsc., InTech, 2012.

[28] S. Link, M.A. El-Sayed, J. Phys. Chem. B 109 (2005) 10531.

[29] J. Becker, A. Trügler, A. Jakab, U. Hohenester, C. Sönnichsen, Plasmonics 5 (2010) 161.

[30] P.K. Jain, K.S. Lee, I.H. El-Sayed, M.A. El-Sayed, J. Phys. Chem. B 110 (2006) 7238.

[31] S. Gómez Graña, Colloidal Synthesis, Structural Characterization and Assembly of Plasmonic Metal Nanorods, Universidad de Vigo, 2013.

[32] F. Hubert, F. Testard, A. Thill, Q. Kong, O. Tache, and O. Spalla, Cryst. Growth Des. 12 (2012) 1548.

[33] N.R. Jana, L.A. Gearheart, S.O. Obare, C.J. Johnson, K.J. Edler, S. Mann, C.J. Murphy, J. Mater. Chem. 12 (2002) 2909.

[34] X. Kou, S. Zhang, C.-K. Tsung, M.H. Yeung, Q. Shi, G.D. Stucky, L. Sun, J. Wang, C. Yan, J. Phys. Chem. B 110 (2006) 16377.

[35] X. Kou, W. Ni, C. Tsung, K. Chan, H. Lin, G. D. Stucky, J. Wang, Small 3 (2103) 2007.

[36] J. Burgin, I. Florea, J. Majimel, A. Dobri, O. Ersen, M. Treguer-Delapierre, Nanoscale 4 (2012) 1299.

[37] S. Köppl, Seed-Mediated Synthesis of High Aspect Ratio Nanorods and Nanowires of Gold and Silver, Univ., Technische Universität München, 2011.

CHAPTER III

The Competitive Growth of Different Type of Seeds

CHAPTER III

Chapter 3

Competitive Growth of Different Type of Seeds

In wet chemical synthesis of gold nanoparticles, the structure of the final NP is determined by various factors. Our initial results revealed that, the crystalline structure and the size of the starting precursor are dominantly the most influential ones during the determination of the morphology of the final NP. To be specific, we have demonstrated that by using seeds different in their size and their structure, it is realizable to promote the growth of spherical NPs, single crystalline nanorods, elongated nanobeans or bipyramids using exactly the same growth solution. One of the major results from Chapter 2 is that the initial structure of seeds orientates the nature of the possible anisotropic shape. While nanorods are obtained from single crystalline CTAB capped seeds (Type 1), nanobeans or bipyramids can only be developed from multi-twinned nanoparticles. For these syntheses, the anisotropic shapes are never obtained in 100% yield due to the pollution by isotropic nanoparticles.

In order to highlight the importance of the initial precursor on the final nanoparticle morphology, we have developed an original competitive approach. This study consist in the simultaneous addition of two different kinds of seeds into the same growth solution, in order to see which seed will rule the final morphology: Will they grow simultaneously in the same reaction container or will there be an unbalanced partition between both? This method enables us to demonstrate the importance of the nature of defects in the initial seeds.

3.1 Methodology

3.1.1 Competitive Approach

As indicated previously, the competitive approach includes the addition of two seeds, prepared with different methods, into the same growth solution. In contrary to the single seed oriented growth (Figure III.1a), in our competitive growth system, both seeds will compete for the same gold source in a surfactant rich medium (Figure III.1b).

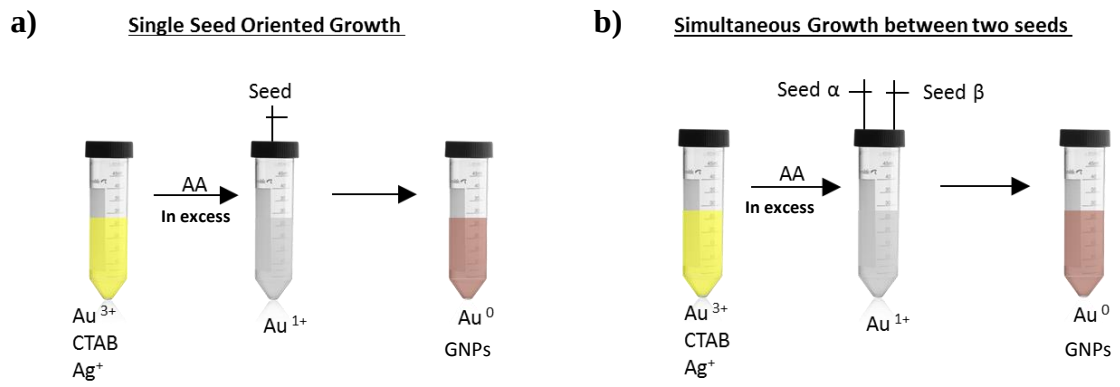

Figure III. 1 *Generation of gold nanoparticles via seed mediated synthesis of a) single seed oriented growth b) simultaneous growth between two as-prepared seeds*

The preparation and the characterisation of the seed solutions, which have been utilized in this section, have already been presented previously in Chapter II (*See 2.1.1.1*). Summary of the size and the crystalline structure of all type of seeds are given in Table III.1.

Table III. 1 *Average size of prepared seeds with structural information*

Seed Type	**Average Diameter (DLS) (nm)**	**Crystal Structure**
[1]	2.0	Single Crystalline
[2]	4.9	Poly crystalline
[3]	8.7	Poly crystalline
[4]	5.6	Poly crystalline

The principal idea is, to follow the competitive growth of seeds in the same reaction container, known to give different final states. In other words, two competitive systems have been chosen to study:

i. Type 1 & Type 2 seeds known to yield different final morphologies; former producing nanorods and latter producing nanobeans or bipyramids

ii. Type 3 & Type 4 seeds known to produce different sized spherical nanoparticles

Since the sizes of different seeds vary greatly, the total number of each added precursor was calculated before its injection into the growth solution. The calculation method, used to

obtain the average number of seeds in a given volume, has been explained in detail in previous chapter II.

The same growth solution is used for all competitive growth experiments. The chemical composition of the growth solution is reminded in Table III.2.

Table III. 2 *Synthetic conditions for the reference growth solution*

Reagents	**Quantity (mL)**	**[C_{final}] (mM)**
0.05M $HAuCl_4 \cdot 3H_2O$	0.1	0.5
0.1 M CTAB (cetyltrimethylammonium bromide)	10	10
0.01 M $AgNO_3$	0.045	0.045
0.1 M Ascorbic Acid	0.075	0.75

Kinetic spectra's are performed right after the addition of seeds without any centrifugation step. Final nanoparticles are purified from the excess surfactant and the remaining reactants with similar process of purification given in previous chapter (*see Chapter II.2*). TEM images correspond to the purified samples.

3.2 Results

Following experiments are performed as a complementary study to our initial results, which reveal that in wet chemical synthesis of gold NPs, the structure and the amount of seeds play important role in the growth kinetics (*See Chapter II*). To disclose the real role played by the seeds, in this part we went further toward the competitive growth.

3.2.1 Competitive Growth between Type 1 and Type 2 Seeds

- **Estimation of the Number (N_α) and the Surface Area (Σ_α) of Seeds in a Corresponding Volume (V_α)**

Table III.3 summarizes the first set of competitive experiments performed at different seed volumes, V_α (V_1 *corresponding to the volume of type 1 Seed and* V_2 *to type 2 seed)*. In the

table, N_α represents the total number of each seeds in the corresponding volume, V_α. We give an estimation of number percentage of each seed ($\%\ N_\alpha$) and relate those values to surface area percent ($\%\ \Sigma_\alpha$) (*assuming that the particles are spherical*).

Results of the competitive growth experiments will be explained by using the total number and the surface area of each seeds, later on. It has to be noticed that, for experiments given in Table III.3, in all three scenarios the number of Seed 1 (N_1) is always higher than the number of Seed 2 (N_2).

Table III. 3 *Comparison of different experimental conditions with respect to added seed volume, number of seed in corresponding volume and the surface area for two kinds of seeds CTAB seed 1 and Citrate seed 2 characterized in the Chapter II*

Sample	$V_1^{(1)}$ **(µL)**	$N_1^{(2)}$ **(x10^{13})**	$V_2^{(1)}$ **(µL)**	$N_2^{(2)}$ **(x10^{13})**	$N_T^{(3)}$ **(x10^{13})**	**(%)** $N_1^{(4)}$	**(%)** $N_2^{(4)}$	$\Sigma_1^{(5)}$ **(nm^2)**	$\Sigma_2^{(5)}$ **(nm^2)**	**%** $\Sigma_1^{(6)}$	**%** $\Sigma_2^{(6)}$
C1	100	6.08	20	0.082	6.17	98.6	1.4	$7.64\ 10^{14}$	$6.24\ 10^{13}$	92.5	7.5
C2	60	3.66	60	0.24	3.90	93.6	6.4	$4.58\ 10^{14}$	$1.87\ 10^{14}$	71.0	29
C3	96	5.84	192	0.79	6.63	88.0	12.0	$7.34\ 10^{14}$	$5.99\ 10^{14}$	55.0	45

$^{(1)}V_\alpha$ = Volume of added seed
$^{(2)}N_\alpha$ = Number of seed in added volume (V_α)
$^{(3)}N_T$ = Total number of seeds added in overall volume ($V_1 + V_2$)

$^{(4)}\%\ N_\alpha$ = Number percentage
$^{(5)}\sum_\alpha$ = Surface area of seeds
$^{(6)}\%\ \sum_\alpha$ = Surface area percentage

3.2.1.1 Characterization of Final States by UV-Vis Spectroscopy and TEM

UV-Vis Spectra's and the corresponding TEM images of samples, is summarized in the Figure III.2. Initially analysis is dedicated to UV-Vis Spectrums whereas to explain some results we will refer to corresponding TEM images. However, detailed TEM analysis is given in the second part.

- **Analysis of UV-Vis Spectrums**

Since the UV-Vis Spectra's of competitive growth experiments include the information from two different final nanoparticles, obtained from two different seeds, during the analysis of all spectra's, the longitudinal surface plasmon peaks corresponding to wavelengths larger or smaller than 600 nm, will be designated as $\lambda_{L\text{-}SPR\ (1)}$ and $\lambda_{L\text{-}SPR\ (2)}$ respectively. Here, the transversal plasmon resonance band, $\lambda_{T\text{-}SPR}$, contains the signal of both isotropic nanoparticles and the anisotropic nanoparticles (*contribution from the diameter of the particle*).

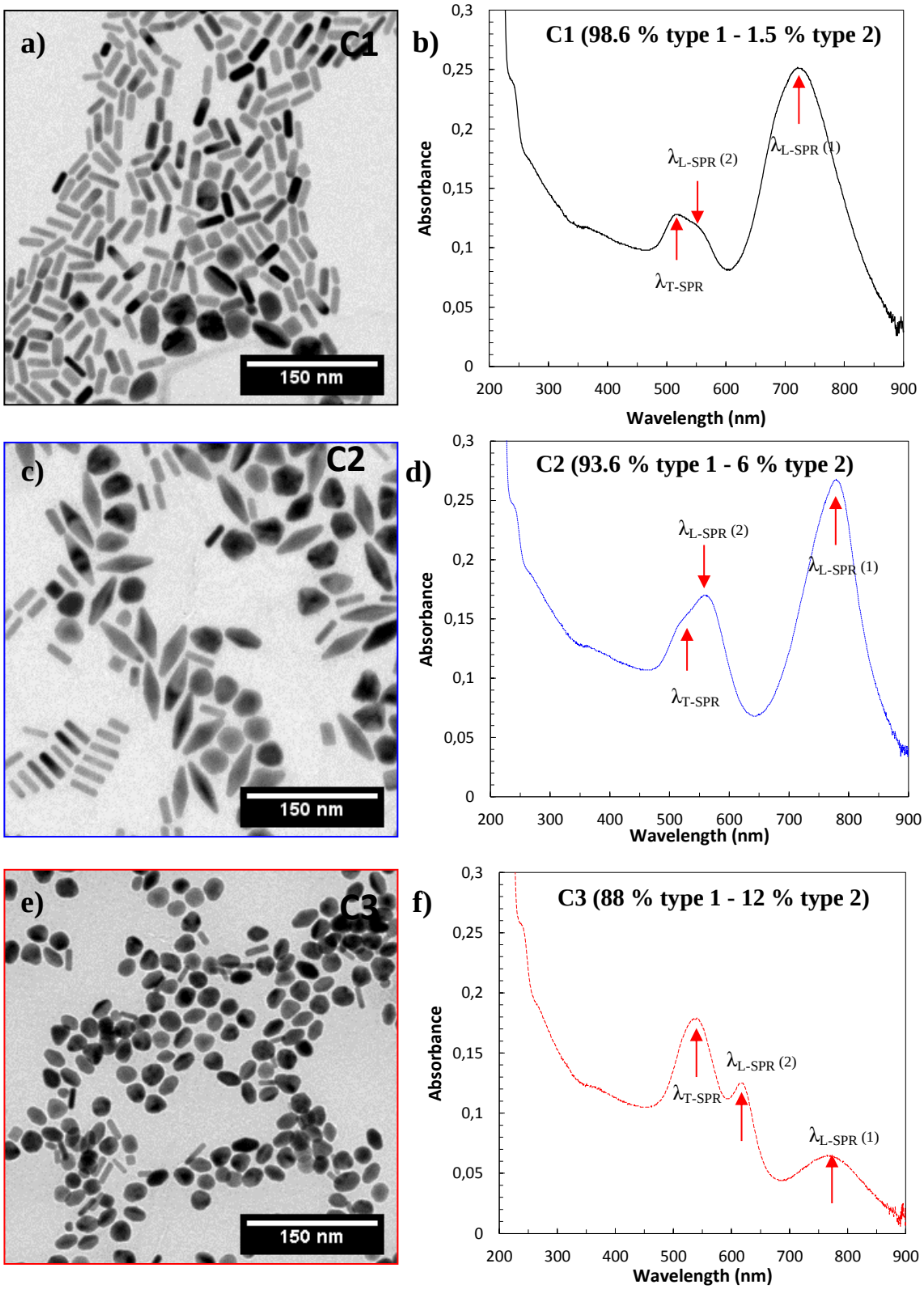

Figure III. 2 *UV-Vis Spectra and corresponding TEM images of samples obtained by competitive approach at different volumes of Type 1 and Type 2 seeds a) 100µL-60µL b) 60µL-60µL c) 96µL-192µL*

To explain the evolution of the wavelength and the absorbance in characteristic plasmon peaks ($\lambda_{T\text{-}SPR}$, $\lambda_{L\text{-}SPR\ (1)}$ and $\lambda_{\ L\text{-}SPR\ (2)}$), for the samples given in previous figure, we have summarized the values for the three different cases in Table III.4.

Table III. 4 *Comparison the position of distinct plasmon peaks with corresponding absorbance values*

	$\lambda_{T\text{-}SPR}$ [(1)]	$\lambda_{L\text{-}SPR\ (1)}$ [(2)]	$\lambda_{L\text{-}SPR\ (2)}$ [(3)]	$A_{T\text{-}SPR}$	$A_{L\text{-}SPR\ (1)}$	$A_{L\text{-}SPR\ (2)}$	$A_{L\text{-}SPR\ (1)}/A_{T\text{-}SPR}$ [(4)]	$A_{L\text{-}SPR\ (2)}/A_{T\text{-}SPR}$ [(5)]
C1	520	720	560	0.13	0.25	0.11	1.97	0.88
C2	520	780	560	0.15	0.27	0.17	1.81	1.15
C3	540	765	620	0.18	0.06	0.12	0.36	0.69

[(1)] $\lambda_{T\text{-}SPR}$ = SPR of transversal band
[(2)] $\lambda_{L\text{-}SPR\ (1)}$ = SPR of longitidunal band due to long axis of NRs
[(3)] $\lambda_{L\text{-}SPR\ (2)}$ = SPR of longitidunal band due to long axis of nanobeans and bipyramids
[(4)] $A_{L\text{-}SPR\ (1)}$ / $A_{T\text{-}SPR\ =}$ ratio of absorbance value of $\lambda_{L\text{-}SPR(1)}$ resulting from NRs to $\lambda_{T\text{-}SPR}$
[(5)] $A_{L\text{-}SPR\ (2)}$ / $A_{T\text{-}SPR\ =}$ ratio of absorbance value of $\lambda_{L\text{-}SPR\ (2)}$ resulting from nanobeans (bipyramids) to $\lambda_{T\text{-}SPR}$

The same absorbance value (0.113) at λ_{400} states that the concentration of colloidal gold integrated into nanoparticle are same and equal to 0.45 mM for all listed samples (C1,C2,C3).

In the UV-Vis spectrum of the first sample, C1, in which 98% of the seed population is occupied by Type 1 seeds, the large $\lambda_{L\text{-}SPR\ (1)}$ at 720 nm is due to the large number of nanorods coming from Type 1 seeds (Figure III.b). The high absorbance value of the longitudinal plasmon band, $A_{L\text{-}SPR\ (1)}$ in compared to the other peaks, means that high yield of nanorods are formed. In the same spectrum, we can distinguish a second maximum ($\lambda_{L\text{-}SPR\ (2)}$) around 560 nm. The source of this plasmon peak is probably the short aspect ratio nanobeans. In the same spectrum, transversal peak ($\lambda_{T\text{-}SPR}$) is positioned at 520 nm with an absorbance intensity of 0.13.

UV-Vis Spectrum of second sample, C2, in which 94% of the population is occupied by Type 1 seed, given in Figure III.3d, again displays three distinct plasmon peaks, at 520 nm, 560 nm and 780 nm ($\lambda_{T\text{-}SPR}$, $\lambda_{L\text{-}SPR\ (2)}$ and $\lambda_{L\text{-}SPR\ (1)}$). To explain the results of this sample, we have compared its corresponding UV spectrum with the one explained for the previous sample. Basically, the increase in the $\lambda_{L\text{-}SPR\ (1)}$ towards higher wavelengths, in comparison to C1, indicates that the aspect ratio of anisotropic nanoparticles is increased. The absorbance

values for all distinct plasmon peaks ($\lambda_{T\text{-}SPR}$, $\lambda_{L\text{-}SPR\ (2)}$ and $\lambda_{L\text{-}SPR\ (1)}$) increases in comparison to previous sample, C1. Such increase in the ($A_{L\text{-}SPR\ (2)}$ and $A_{L\text{-}SPR\ (1)}$) can be explained by the increase of anisotropy in the elongated nanoparticles. Additional increase in $\lambda_{T\text{-}SPR}$ means that the spherical nanoparticles also increase their yield. The main difference between C1 and C2, is the change in the ratio of absorbance values between;

- The first longitudinal SPR resulting from nanorods to transversal SPR ($A_{L\text{-}SPR\ (1)}$ / $A_{T\text{-}SPR}$). One can detect, the high yield of nanorods as in C1, by the high ratio of $A_{L\text{-}SPR\ (1)}/A_{T\text{-}SPR}$ as 1.97, whereas this number decreases to 1.81 for C2.

- The second longitudinal SPR originating from nanobeans (and bipyramids) to transversal SPR ($A_{L\text{-}SPR\ (2)}/A_{T\text{-}SPR}$). In case of C2, increase in the number of Seed 2 results in an increase of $A_{L\text{-}SPR\ (2)}/A_{T\text{-}SPR}$ ratio from 0.88 to 1.15, meaning that elongated nanobeans increases their yield. Additionally, increase of Seed 2 causes an increase in the absorbance of transversal SPR peak ($A_{T\text{-}SPR}$). This can be related to a larger amount of coexisting nanospheres in agreement with the TEM distribution (Fig III.3d).

In case of C3, in which 88% of the total seed number is occupied by Type 1 seed, $\lambda_{T\text{-}SPR}$ and $\lambda_{L\text{-}SPR\ (2)}$ are shifted to higher values (540 nm and 620 nm) in comparison two first two conditions (Figure III.f). The significant decrease of $A_{L\text{-}SPR\ (1)}$ from 0.25 to 0.06 with the large increase in $A_{T\text{-}SPR}$ to 0.18, in comparison to C1 and C2, leaves the conclusion that yield of nanorods is diminished drastically. Moreover, the $\lambda_{L\text{-}SPR\ (1)}$ is shifted to lower wavelengths with respect to C2 due to the decrease in the AR of nanorods.

- **Analysis of TEM images**

For each sample, by using TEM images given in Figure III.2, about 900 nanoparticles were counted to have estimation about the number percentage between the different morphologies. Results are presented in the *L,W* plot Figure III.3. In all experiments, two populations are visible; with distinct variation in the number of occupants in each population.

In C1, most of the population is occupied by nanorods (82%) with small number of elongated nanobeans (7%) and spherical particles 11%. Large nanorod population prevents to visualize the nanobeans in *L,W* plot since both populations are superimposed (Fig. III.3a).

TEM images of C2 (Figure III.2c) show that, even though the nanorods keep their structure, the nanobeans transform into bipyramidal shapes when the relative number of Type 2 seeds is increased from 1.5% to 6%. In this case, *L,W* plot, given in Figure III.3b, shows that both nanorods and bipyramids lay on the same line with an average aspect ratio of 3. It is clear that the population of nanorods decreases, with respect to C1, from 82% to 53% while the bipyramidal particles increase their number (13%) as well as the spherical nanoparticles (34%).

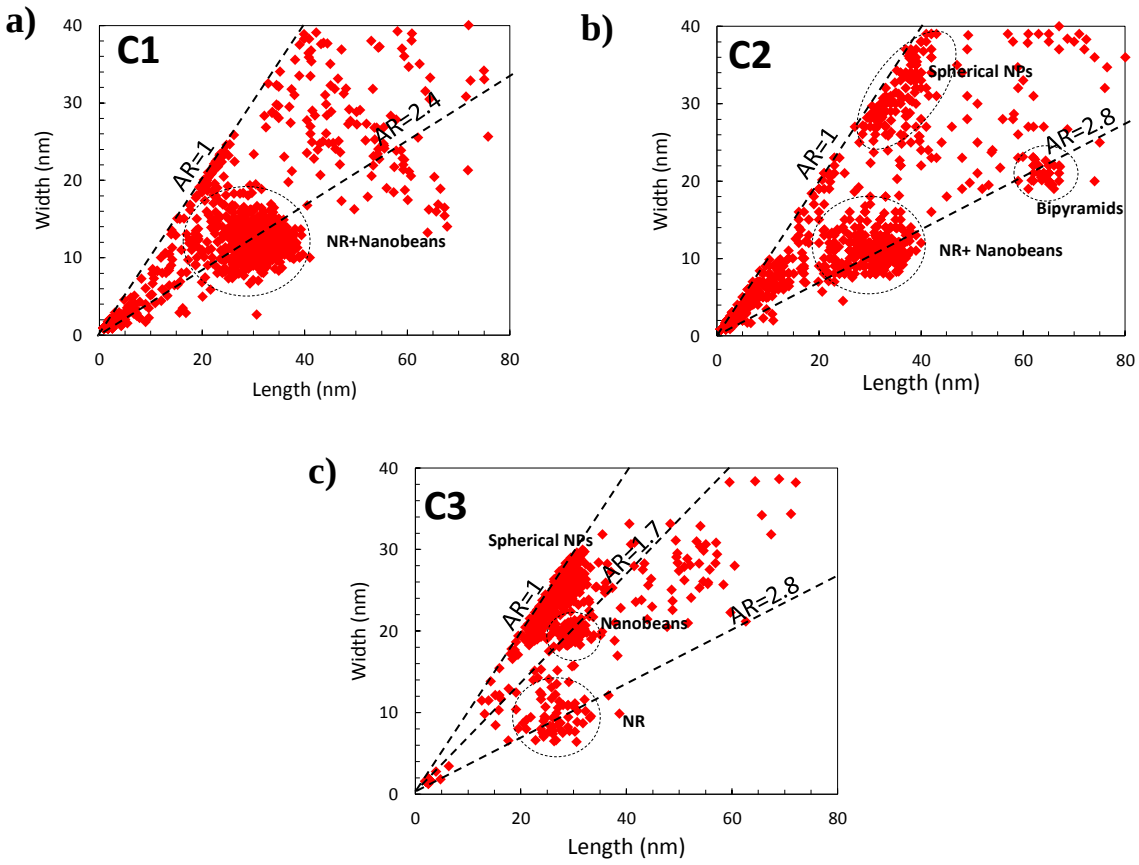

Figure III. 3 *Size analysis on sample obtained from TEM data a) C1-98% Seed 1-2% Seed 2 in numbers b) C2-89% Seed 1-11% Seed 2 in numbers c) C3-80% Seed 1-20% Seed 2 in numbers*

For C3, TEM results, given in Figure III.2a, are in agreement with the UV-Spectrum and size analysis results (Figure III.3c) showing slight number of nanorods (20%) and high concentration of bean shape nanoparticles (42%) coupled with spherical shapes (38%). This means that, due to further increase of the number of Type 2 seeds to 12%, the population of the nanorods decreases to a critical point C3 even though the large number of initial seed

actually contains Type 1 seeds (88%). Also, no bipyramidal shapes (*i.e. with sharp tips*) are observed on this type of samples.

Intermediate Discussion

In general, the total numbers of nanobeans, bipyramids and nanospheres increase drastically in comparison to nanorods when the number percent of the Type 2 seed is increased from 1.5% to 12%.

Even though, when this number is only around 6% for Type 2 seeds (*meaning that 94 % is Type 1 seeds*), a majority of particles are nanobeans/bipyramids and spherical shapes. At the end, nearly no nanorods are formed when total seeds contain 12% of Type 2 seeds (number percent). The reason of such tendency can be explained by using the surface area percent calculated for both seeds (*Table III.3*). For anisotropic nanoparticles, the percentage of nanobeans over nanorods is increasing from 7 % to 42 % when the total surface area of Type 2 seeds is increased from 8% to 45%. Even though the surface area of both type of seeds are comparable in the final sample, C3 (55% Type 1 - 45% Type 2), formation of nanobeans are favoured over nanorods meaning that the growth of citrate seeds is favorable over the CTAB capped seeds for chosen growth conditions.

To sum up, the competitive growth experiments between Type 1 and Type 2 seeds, results with a partition between two dominant morphologies; nanorods and nanobeans. As the number percent of Type 2 seed increases to 6%, the yield of nanorods gradually decreases and the nanobeans start to elongate and exhibit sharper tips to form bipyramids. Further increase in the number to 12% (*i.e. increase in surface area percent*) of Type 2 seeds result with the disappearance of most of the gold nanorods, and simultaneously, this increase in the number of Type 2 seeds promote the formation of nanobeans instead of bipyramids. The reason of such promotion can be related to the higher number of citrate capped seeds in an environment deficient of monomer, yielding small anisotropic NPs, rather than large sized high aspect ratio NPs (Table III.3).

In the following part (3.2.1.2) temporal evolution of the UV-Vis Spectrum for the sample C2 will be analysed both for same growth conditions and additional pH controlled growth conditions.

3.2.1.2 Kinetic Studies on Competitive Growth

The temporal evolution of the UV-Vis spectrum, given in Figure III.4, corresponds to the same chemical compositions used previously for the sample C2 (*presented previously in Figure III.2d*) in which 94 % of the initial added seed is from Type 1 and the 6% is from Type 2. The final spectrum, however, resembles more to the one observed for sample C3 rather than the one for sample C2 after 30 minutes. Same tendency is observed for all other experiments when we tried to reproduce C2. The reason can be explained by the fact that, it is rather difficult to control the yield and the AR of the bipyramids which is directly related to the position and the intensity of $\lambda_{L\text{-}SPR\ (2)}$. Such control of AR in multi-twinned NPs is even harder when the initial pH is not imposed during the growth. Namely, when pH is not well controlled, chloride ions and dissolved oxygen, present in the solution, leads to strong etching on the tips of the nanobeans and the bipyramids transform their morphology into thermodynamically stable spherical shapes. Such morphological transformation can explain the shift of $\lambda_{L\text{-}SPR}$ (*both for nanobeans and bipyramids*) to lower wavelengths to merge with $\lambda_{T\text{-}SPR}$.

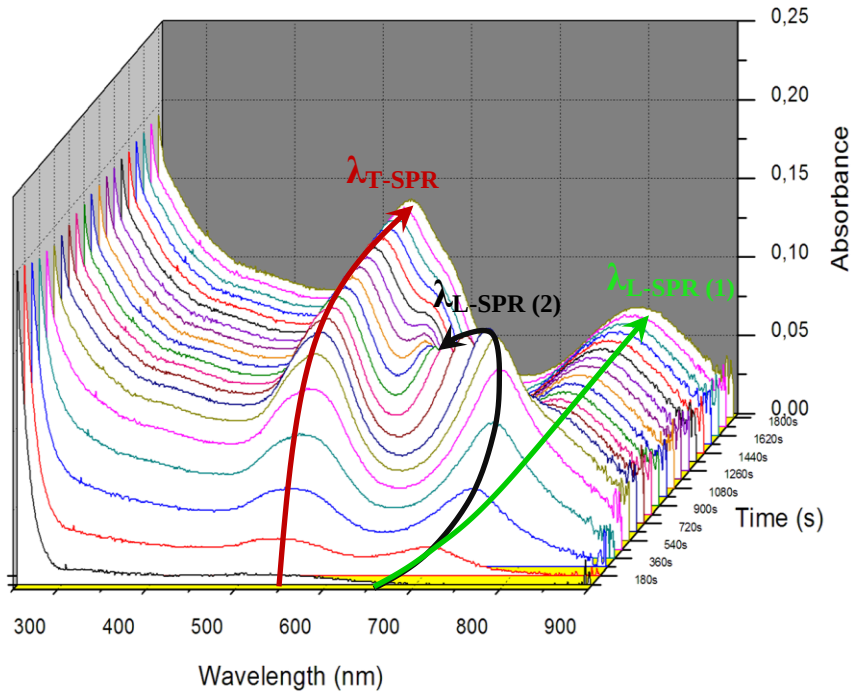

Figure III. 4 *Time resolved UV-Vis Spectra of gold NP growth obtained via simultaneous addition of two different types of seeds in growth solution composed of 0.1 M CTAB, 0.5 mM $HAuCl_4$, 0.045 mM $AgNO_3$ and 0.75 mM L-Ascorbic Acid*

The facile etching of nanobeans and bipyramids, induces strong difficulties in the reproducibility and prevents the predictions of the AR of twinned NPs with previously given equation (*See Chapter II, Eq. 2.3*) for given growth conditions.

The temporal evolution of each characteristics plasmon peaks is given in Figure III.5b. A single $\lambda_{L\text{-}SPR}$ is visible in the early stages with the associated wavelength evolving from 710 nm to 760 nm. After 350 seconds, with the separation of the large signal of nanobeans, plasmon band of nanorods, $\lambda_{L\text{-}SPR\ (1)}$, become visible at 760 nm and remains constant at position. The broad signal of nanobeans $\lambda_{L\text{-}SPR\ (2)}$, starting at 721 nm shows a strong decrease to lower wavelengths, to finally merge with $\lambda_{T\text{-}SPR}$ around 583 nm.

To conclude, given longitudinal plasmon peaks, formed at the early stage of growth, corresponding to the two modes for two different anisotropic structures; one being for nanorods ($\lambda_{L\text{-}SPR\ (1)}$) and the other for bipyramids ($\lambda_{L\text{-}SPR\ (2)}$) do not show same stability against reshaping. Mainly, in competitive experiments different seeds grow independently form each other from the very beginning of the reaction.

The evolution of absorbance in time is presented again for $A_{T\text{-}SPR}$, $A_{L\text{-}SPR(1)}$ and $A_{L\text{-}SPR\ (2)}$ in Figure III.5a. For $A_{T\text{-}SPR}$ the continuous increase stops around 1170 seconds reaching to a saturation point in absorbance at 0.132. Decrease of the absorbance in longitudinal modes ($A_{L\text{-}SPR(1)}$ and $A_{L\text{-}SPR(2)}$) after 450 second can be attributed to the separation of the superposition of both signals, removing the contribution from each other. The number of final colloidal gold concentration integrated in nanoparticles at the end of the reaction is found as 0.35 mM (via $\varepsilon = 2.5\ 10^3\ L\ mol^{-1}cm^{-1}$) by using the final absorbance value obtained at 400 nm after termination of reaction in 30 minutes.

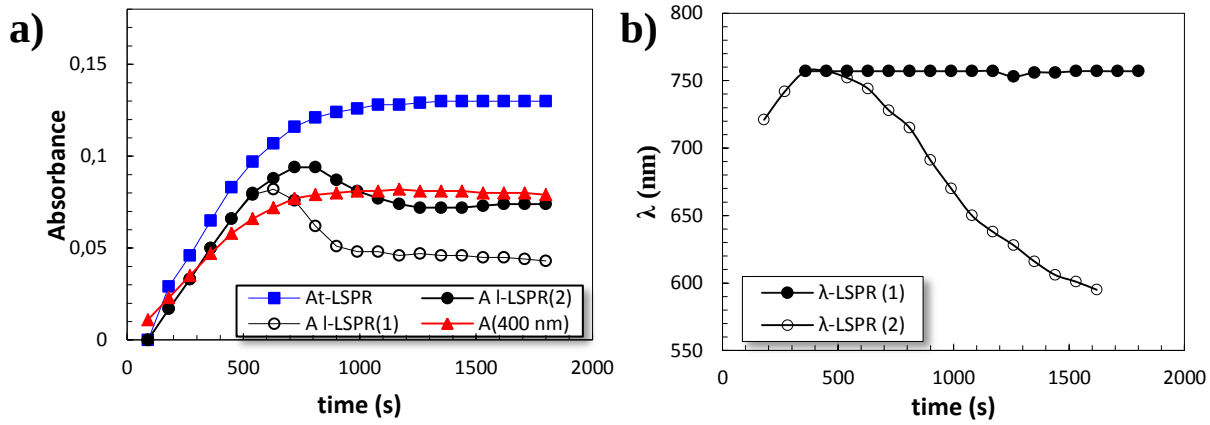

Figure III. 5 *Relationship between a) absorbance's at 400 nm, transversal and longitudinal plasmon peaks b) maximum L-SPR values for nanorods (1) and nanobeans (2)*

Our previous experiments related to the growth of gold nanorods (*Chapter II.2.2.3.1*) have shown that the growth takes 700 seconds. In competitive growth experiments, the kinetic is slightly increased meaning that for $\lambda_{L\text{-}SPR\ (1)}$ growth is completed below 350 seconds (Figure III.5b). Stable $\lambda_{L\text{-}SPR\ (2)}$ observed during the single growth nanobeans, given in *Chapter II.2.2.3.1*, means that anisotropic nanoparticles preserve their shapes and do not evolve into isotropic nanoparticles. However, for competitive growth experiments, this stability is rather lost for $\lambda_{L\text{-}SPR\ (2)}$ meaning that elongated structures loses their anisotropy easily. To reveal the source of this reshaping, we have imposed the initial pH in the following experiments to slow down the kinetic and have better control in the AR.

- **Effect of pH on Kinetics of NP Growth**

To observe the direct influence of the pH on the kinetics of competitive growth, we have introduced small amount 0.1 M HCl (50 µL) in the reference growth solution. Considering our initial results and literature over gold NPs, it appears that imposing the pH of the growth solution to lower values (1.9) before the addition of seeds, causes a significative increase in reaction time and yields more elongated structures [1–4]. The reason of this increase can be explained by the fact that, reducing the pH of the reaction media causes a decrease in the reducing power of ascorbic acid; which induces an increase in reaction time favorable to elongated shape. The time resolved UV-Vis spectrum obtained at low pH (1.9), is indicated in Figure III.6.

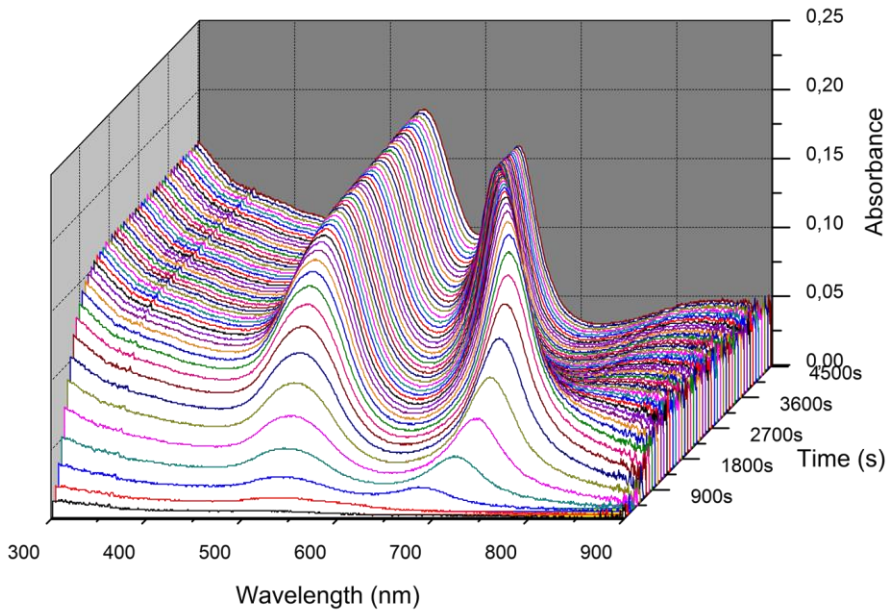

Figure III. 6 *Time resolved UV-Vis Spectra of nanoparticle growth at pH 1.9*

It appears that in pH controlled experiments, UV-Vis spectrum of the corresponding sample, exhibit relatively more stable $\lambda_{L\text{-}SPR(2)}$ peak than the previous experiment where $\lambda_{L\text{-}SPR(2)}$ was joining into transversal mode in 30 minutes (Figure III.4). Additionally $\lambda_{L\text{-}SPR(2)}$ exhibits sharper structure than before. This is due to the formation of bipyramids with sharper tips rather than nanobeans.

The evolution of $\lambda_{L\text{-}SPR\ (2)}$ as a function time, given in Figure III.7b, indicates relatively slower reshaping towards lower wavelengths (Figure III.7b) after 810 seconds. Major effect of pH on reaction time can clearly be observed by following the evolution of $\lambda_{L\text{-}SPR(2)}$. In previous conditions (Figure III.5), $\lambda_{L\text{-}SPR(2)}$ decreases from 750 nm to 600 nm in 1500 seconds, whereas with HCl, this time increases to 4000 seconds for the interval of 750 nm to 630 nm.

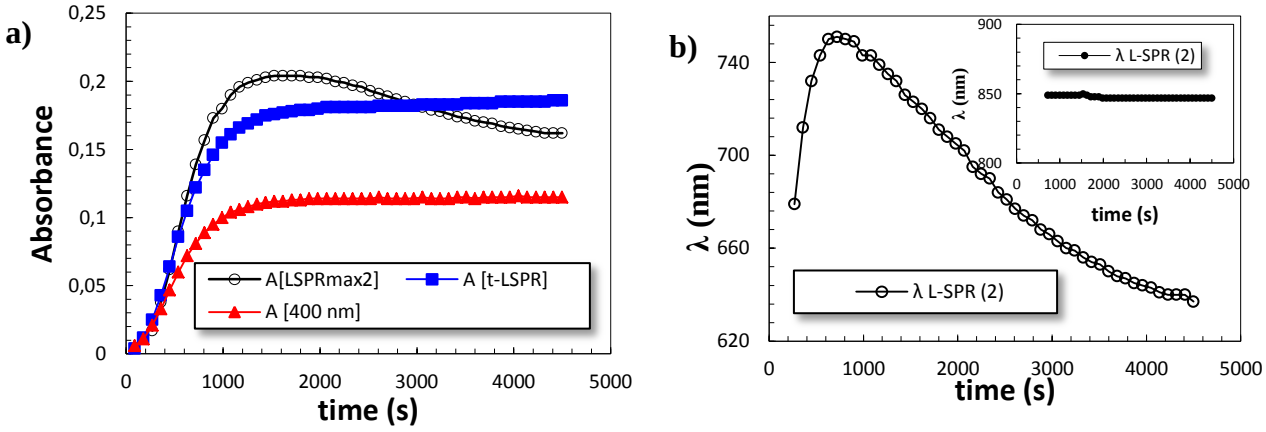

Figure III. 7 *Temporal Evaluation of (a) absorbance at 2nd longitudinal mode and 400 nm (b) $\lambda_{l\text{-}SPR(1)}$ at elevated pH*

The plasmon peak of nanorods, $\lambda_{L\text{-}SPR\ (1)}$, is hidden under the broad signal of nanobeans/bipyramids ($\lambda_{L\text{-}SPR(2)}$) and as soon as $\lambda_{L\text{-}SPR(2)}$ shifts to lower wavelengths around 810 seconds, $\lambda_{L\text{-}SPR\ (1)}$ becomes visible and remains constant at 849 nm (Figure III.7b, inset). This means that nanorods already completed their growth under 810 seconds.

- ***<u>Comparison between Reference Experiment given in Figure III.4 (no pH is imposed) and the Experiment given Figure III.6 where the initial pH of the Growth solution is adjusted at 1.9</u>***

The slope of the Absorbance=*f*(*t*), for distinct plasmon peaks ($\lambda_{T\text{-}SPR}$ and $\lambda_{L\text{-}SPR\ (2)}$) and also for λ_{400}, for both of the experiments where *i*) no pH is dictated during the growth (*given in Figure III.5a* and *ii*) pH of the growth solution is imposed to 1.9 before the growth stage, (*given in Figure III.7a*).

Table III. 5 *Comparison of slope of distinct plasmon peaks (a.u./s) for two different set of experiments*

Sample	**$\Delta A_{T\text{-}SPR}/\Delta t$ (s^{-1})**	**$\Delta A_{L\text{-}SPR\ (2)}/\Delta t$ (s^{-2})**	**$\Delta A_{400nm}/\Delta t$ (s^{-1})**
*Refence Growth Soln	$2.67\ 10^{-4}$	$2.89\ 10^{-4}$	$1.83\ 10^{-4}$
** $pH_{initial}$ 1.9	$1.82\ 10^{-4}$	$1.84\ 10^{-4}$	$1.15\ 10^{-4}$

* Reference Growth= Spectrum is given in Figure III.4
** $pH_{initial}$= Spectrum is given in Figure III.6. It corresponds to the sample with the addition of 50 µL 0.1 M HCl into growth media (pH=1.9)

From the slope of Absorbance$_{400nm}$=*f(t)*, it can be deduced that, reaction speed decreases 1.6 times when pH is decreased. Again by the direct relation, between absorbance at 400 nm and colloidal gold concentration (*given previously in chapter II (Eq.2.4)*), it can be deduced that the rate of Au(1+) conversion is lowered for the experiments where initial pH is imposed to 1.9. For low pH experiments, at the end of the reaction (~2000 s), A_{400} nm has been found as 0.114 with the final Au(0) concentration of 0.46 mM . If we compare this value with the one obtained from reference growth solution, we can see that the yield of Au(0) produced during the reaction is increased from 0.35 mM to 0.46 mM when the initial pH of the growth solution is fixed at 1.9.

The results given in Table III.5 can be summarized as the following; the addition of HCl (starting with more acidic growth solution) decreases the kinetic by a factor 1.5 for all other plasmon peaks peaks ($\lambda_{T\text{-}SPR}$ and $\lambda_{L\text{-}SPR\ (2)}$) with the clear evidence that slope is decreasing in all cases.

3.2.2 Competitive Growth between Type 3 and Type 4 Seeds

We have shown how competitive experiments can bring some information on the growth orientation for anisotropic nanoparticles. With the work of Hubert et al. [5], we know the important role played by the size of initial seed during the formation of anisotropic nanoparticles. Here, we have used the similar competitive approach as before, to compare the growth kinetics of two other kinds of seeds, possessing large difference in initial size (*Type 3 seed, 8.7 nm and Type 4 seed, 5.6 nm*) and the final nanoparticle size that they yield (*Type 3 seeds yielding spherical NPs with average diameter of 35 nm and Type 4 seeds 17 nm*) when equal volume of each is added in the reference growth solution (*Chapter II.2.2.2*).

Our previous research has demonstrated that both for larger sized seeds (*Type 3 and Type 4*) the anisotropy is hard to attain by using our conventional growth solution. Even though small trace of anisotropy is observed in early stages of growth for both seeds, it fades quickly and results into the formation of spherical nanoparticles characterized by single plasmon peak (*Chapter II.2.2.3*). One reason could be related the large size of both seeds.

To compare the efficiency of both seeds in the same reaction environment, we have injected 200 µL from each seed simultaneously and recorded the UV-Vis Spectra. It should

have been noted that both seeds have been used one day after their preparation to make sure excess reactants are eliminated particularly for the Type 4 seeds prepared with AA.

The number percentages of the each seeds in corresponding volume are summarized in Table II.6. It should be also noted that, the total number of seeds (N_T=6.4 10^{12}) in this competitive growth experiment, is one order of magnitude smaller than the previous competitive growth experiments between Type 1 and Type 2 seeds (N_T~10^{13}).

Table III. 6 *Comparison of Seed Numbers in a Given Volume for Competitive experiments between Type 3 and Type 4 Seeds*

Code	V_3* (µL)	N_3**	V_4 (µL)	N_4	N_T***	% N_3****	% N_4
C4	200	1.9 10^{12}	200	4.5 10^{12}	6.4 10^{12}	29.0	71.0

*V_α = Volume of added seed
**N_α = Number of seed in added volume (V_α)
***N_T = Total number of seeds added in overall volume (V_3 + V_4)
****% N_α = Number percentage

The resulting temporal UV-Vis spectrum and corresponding analysis is given in Figure III.8a,b. Small plasmon peak ($\lambda_{L\text{-}SPR\ (1)}$) around 700 nm increases its wavelength to 720 nm in the earlier stages of growth. After 360 s $\lambda_{L\text{-}SPR\ (1)}$ is shifting to lower wavelengths and joins to the transversal mode at 540 nm, leaving no sign of anisotropy.

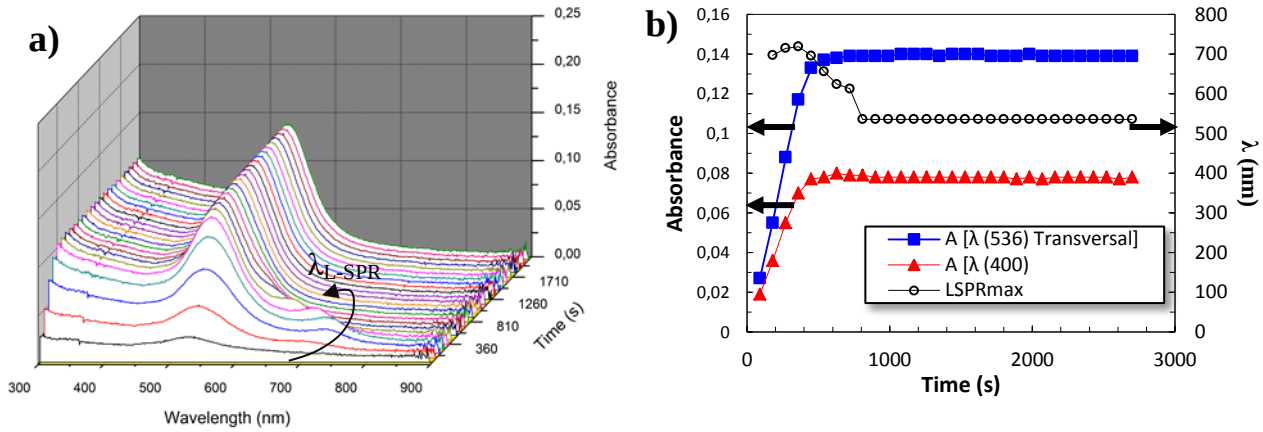

Figure III. 8 *a) UV-Vis Spectra of Competitive growth between Type 3 and Type 4 seeds b) Evaluation of (♦) absorbance at 536 nm (■) absorbance at 400 nm (•) LSPR mode with time*

The absorbance at 540 nm (transversal mode) and at 400 nm ([Au(0)]) increase constantly until 800 seconds and are constant after; indicating the completion of the reaction. This result is consistent with our previous results on kinetics of growth from Type 4 seeds, which is feasible since large number of seeds is occupied by them.

TEM observations related to this sample reveal the formation pf spherical nanoparticles (Figure III.9a) with variable size ranges. Even though, some elongated spheroid NPs can be found on the TEM grid, large population is composed from spheres.

The size analysis of single growth from Type 3 and Type 4 seeds, as well as competitive growth from each is integrated in same *L,W* plot in the same figure (Figure III.9b). When 200µL from each precursor is added in the same reaction container, final size is found as 25 nm, whereas this number changes to 17 nm in single growth of Type 4 seeds and 35 nm for growth of Type 3 seeds. Figure III.9 clearly shows that competitive growth lead to intermediate size of respectively growth of Type 3 and Type 4. These two seeds both exhibiting larger sizes (> 5 nm) are growing in parallel without any preference for one of the used seeds. This result is opposite to the one found in Type 1/Type 2 competitive growth where the multi-twinned seed have shown a preferential growth over monocrystalline seeds.

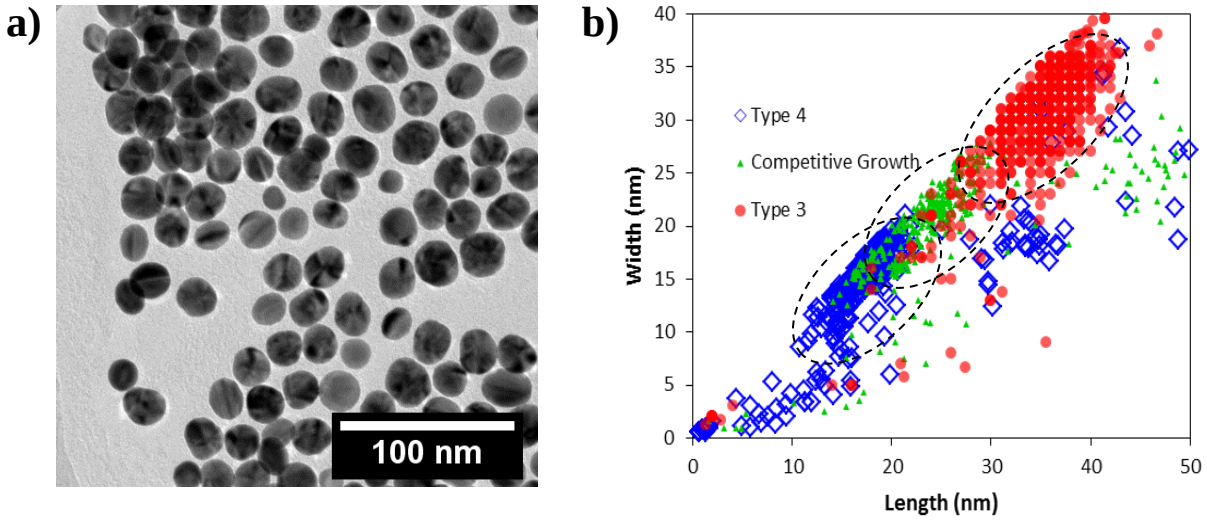

Figure III. 9 *a) TEM micrograph of sample presented in Fig III-8 b)* L, W *plot of size for Single growth from Type 3,4 and Competitive Growth from both*

3.3 Discussion

3.3.1 Competitive Growth of Type 1 and Type 2 Seeds

The final morphology of nanoparticles depends strongly on the initial morphology of seeds. Mixing single crystalline seeds (Type 1), known to produce single crystalline nanorods plus spherical particles and decahedral seeds (Type 2), known to produce nanobeans/bipyramids also spherical particles, apparently lead to a mixture between all listed morphologies. We can control the partition between these morphologies by imposing the number percentage of two seeds (Type 1/Type 2).

When the number percentage of Type 1 seeds is higher than 98 %, high amount of nanorods are obtained, whereas slight number of nanobeans are formed due to the low amount of Type 2 seeds. As soon as the number of Type 2 is increased to 6%, the proportion of nanobeans/bipyramids and spherical particle increases with respect to the nanorods even though the growth solution includes large number of Type 1 seeds. Same tendency is observed even when the pH of the growth solution is lower around 1.9, which is known to promote the formation of high yield anisotropic nanorods. By these results, we can estimate that the reduction of Au(I) to Au(0) is thus favored primarily on the surface of Type 2 seeds (citrate seeds) rather than Type 1. In this case favored Type 2 seeds, consume most of the available Au(I) during the growth and starts to promote the formation of high AR bipyramids. This argument is supported by the presence of high population of low AR of nanorods and small sized spherical nanoparticles in the L,W plot when initial seed contains 94% of Type 1 seed and 6% of Type 2 seed. The reason of such preferential favoring, may be explained by the presence of large numbers of twinning planes and highly reactive edges on the surfaces of Type 2 seeds [4]. This is a strong indication that the initial structure of the seed also has vital importance to control the kinetics of growth of final shapes.

Further increase in the number percentage of Type 2 seeds to 12%, increases the active surface area of this type of seeds from 29% to 55% and decreases the one for Type 1 seeds from 71% to 45% (Table III.3). In this case, only favored Type 2 seeds grow into nanobeans without any chance for Type 1 seeds to attain the bifurcation size. Since, the kinetic here is mostly controlled by Type 2 seeds, high amount of small AR nanobeans are obtained rather

than high AR bipyramids. Bipyramids could not be formed in this case because of the large number of citrate seed creating an environment deficient of monomer.

This competitive growth permits us to explain why the yield of nanorods is never 100% for single growth from CTAB capped seeds. Namely, these types of seeds are in majority monocrystalline, but they also contain a few proportions of multi-twinned seeds (*similar to Type 2 seed*). This creates a situation, resembling to the competitive growth conditions, like a fast consumption of gold monomer by the slight number of polycrystalline seeds to produce either spherical shapes or nanobeans as side products during synthesis of gold nanorods.

3.3.2 Competitive Growth of Type 3 and Type 4 Seeds

During the competitive growth of Type 3 and Type 4 seeds, obtained final nanoparticles always observed as exhibiting isotropic shapes rather than elongated structures. The reason why anisotropy is never promoted for given seeds can be related to the poly crystalline structure of both seeds. As we demonstrated in Chapter II, both seed bear complex twining faults. In case of Type 4 seeds, prepared with milifluidic set-up, these faults are sometimes organized around a common twining axis to form decahedral structures at large particle sizes (~ 5nm). For Type 3 seeds, prepared, by reverse turkevich method, crystal structure of the particle, with multiple twinning faults, is much more complex and not well identified.

If the previously given situation given for CTAB capped seeds (*3.3.1*) is also considered for the competitive growth of Type 3 and Type 4 seeds, we can assume that the large sized NPs, bearing multiple twining faults, consume all the monomer in the environment due to its highly active surface so small sized NPs do not grow into anisotropic shapes due to lack of monomer. Both type of seeds in this situation, continuous to increases their sizes simultaneously, without any one of them being favoured (*since both contain multiple twining faults*), forming final nanospheres with intermediate sizes.

3.4 Conclusion

In this study, by combining TEM and time resolved UV-Vis Spectroscopy, growth kinetics of gold nanoparticles obtained by addition of two as-prepared seeds has been investigated. When nanoparticles smaller than 5 nm competes for the same gold source, the partition between two unique anisotropic structures (nanorods and bipyramids) is observed. Individual seeds continue their growth separately in the same reaction container, even though growth kinetics for both morphologies differs from each other. Number and surface area of both seeds seemed to be important parameters to rationalize the final number of obtained anisotropic NP. Increasing the number of one seed causes a rise in the number of final anisotropic NP that it is responsible for. Namely, increase in Type 2 seeds will cause a growth in the yield of spheroid NPs. At a certain critical number of Type 2 seeds, we end up with high aspect ratio bipyramids rather than nanobeans.

By competitive growth, we have demonstrated an effective approach to understand the dependency of initial structure of seeds in the formation of final gold nanoparticles. Our competitive approach can be used as an efficient tool to understand the mechanistic of growth for various type of structured and can be also extended to various materials.

3.5 References

[1] M. Liu, P. Guyot-Sionnest, J. Phys. Chem. B 109 (2005) 22192.

[2] J. Yang, S. Lohse, S. Boulos, C. Murphy, J. Clust. Sci. 23 (2012) 799.

[3] G. Oza, S. Pandey, R. Shah, M. Vishwanathan, R. Kesarkar, M. Sharon and M. Sharon, Adv. Appl. Sci. Res. 3 (2012) 1027.

[4] M. Grzelczak, J. Perez-Juste, P. Mulvaney, L.M. Liz-Marzan, Chem Soc Rev 37 (2008) 1783.

[5] F. Hubert, F. Testard, A. Thill, Q. Kong, O. Tache, and O. Spalla, Cryst. Growth Des. 12 (2012) 1548.

CHAPTER IV

Synthesis and Characterization of Gold Nanorods and Bipyramids

CHAPTER IV

PART A: GOLD NANORODS

PART B: GOLD BIPYRAMIDS

Chapter 4

Synthesis and Characterization of Gold Nanorods and Bipyramids

During the formation of gold nanorods, as previously discussed in Chapter II, small sized seeds without any crystal defects (*such as CTAB capped seeds*) needed to be used, whereas to obtain bipyramids more complex internal structured seeds had to be employed (*such as citrate capped seeds*). In previous chapters, the constant growth conditions were remained for both cases, to focus and evaluate only the influence of the structure of seeds on the development of anisotropy. In Chapter III, the competitive growth method revealed the strong influence of the crystal structure of the seeds during determination of the final morphology.

Since seed mediated growth is governed by an intricacy between the structure of seeds and the growth conditions (*See Chapter I*), in this chapter, we have studied the impact of the growth solution composition during the formation of chosen anisotropic nanoparticles; nanorods and bipyramids. In other words, the influence of the growth solution over the seed structure has been examined for both CTAB (*Type 1 seeds with average diameter of 2 nm*) and citrate (*Type 2 seeds with average diameter of 4.9 nm*) capped seeds.

The first part (*Part A*) includes the study of the resulting final nanoparticles, when *Type 1* seeds are added in growth solutions with varied compositions. Final particle structure was analyzed in detail by combining both the HRTEM and the electron tomography. In comparison to the batch synthesis, we have offered an alternative way; *microfluidic device*, to mix the small volume of seed solution with the large volume of growth solution during nanorod synthesis. Even though, obtained results represent the preliminary experiments, the procedure used during the adaptation of the batch chemical conditions to the microfluidic set-up offers promising applications. Second part is dedicated to a similar type of survey on the formation of bipyramids from citrate capped seeds (*detailed in Chapter II*). Since both seeds and final nanoparticles bear complex internal structures, we have analyzed the combined HRTEM and electron tomography results in the framework of an atomistic model, developed for multi tinned particles.

Part A: Gold Nanorods

A.4.1 State of Art

It is known that for seed mediated synthesis of gold nanorods in liquid phase, the high surfactant concentration ([CTAB] = 100 mM) and the presence of small amount of $AgNO_3$ (0.05 mM) is mandatory for the formation of high yield of single crystalline nanorods from CTAB capped seeds [1]. In the previous chapters, the atomic resolution images and the FFT analysis have revealed that such seeds exhibit mainly single crystalline structures (*See Chapter II*). This result shows an agreement with the single crystalline structure envisaged for given seed by Guyot-Sionnest [1].

Size tuning of gold nanorods, obtained from CTAB capped seeds, can be achieved by varying different chemical parameters, such as; varying the concentration of the shape directing agent (*$AgNO_3$),* controlling the reaction kinetics via control of the initial pH of the growth solution or by the modification of the packing parameter of the surfactant via external additives, *i.e.* NaBr, 5-Bromo Saliclic acid, etc. [2–6] (*Chapter I 1.2.1.2*). Even though it is known how to tune the aspect ratio of the gold nanorods with the given parameters, a complete study including the effect of all variables, on the size and the crystal structure of final nanorods is necessary to optimize the experimental conditions for *in-situ* TEM experiments (Chapter V). Additionally, the concentration of chemical reagents used during seed mediated synthesis of gold nanorods [7,8] are quite low with respect to the seedless synthesis, in which large amount of reagents are used for gold nanorod production [9,10]. Reason of this minimization in concentration of chemical reagents, has not been well explained for the seed mediated synthesis.

Here, we have focused on some chosen parameters of the growth solution, to evaluate their impact on the development of anisotropy. Particularly the flowing analyzed conditions are selected with respect to the reference conditions described in Chapter II (Table II.2) where 100 mM of CTAB is used:

i. decrease of CTAB concentration (< *below 10 mM*) with the addition of external Br^- source to complete total bromide concentration to 0.1 M
ii. decrease of CTAB concentration to 10 mM without any additives

iii. increase of $[Au^{3+}]/[Ag^{+}]$ ratio from the value traditionally used for seed mediated synthesis (11) to the one used for seedless synthesis of gold nanorods (3.5)

iv. increase of concentrations of all chemical reagents by excluding the surfactant one

A.4.2 Materials and Methods

Preparation of CTAB Capped Seeds (*Type 1*) is already presented in detail in Chapter II. Basically, 0.1 mL of 0.0264 M ice cold solution of $NaBH_4$ is added into the 5 mL mixture of 0.25 mM $HAuCl_4$ and 0.1 M CTAB. Prepared seed solution is let undisturbed for an hour to eliminate excess $NaBH_4$.

Obtained seeds are mixed with growth solutions by employing two different methods; batch mixing and microfluidic mixing. Whatever the way to mix both solutions, excess surfactant was purified by using similar type of purification given in Chapter II and III, after termination of growth. UV-Vis Spectrums of all samples, without any purification, are given in Appendix 3.

A.4.2.1 Batch Synthesis of GNRs

In Table IV.1, the reference chemical conditions employed in previous chapters, during the preparation of the growth solution, are reminded.

Table IV. 1 *Chemical composition of reference growth solution*

Sample	**CTAB [mM]**	**$HAuCl_4$ [mM]**	**$AgNO_3$ [mM]**	**AA [mM]**	**Seed µL**
Reference	100	0.5	0.045	0.75	120

A.4.2.1.1 Reducing the Concentration of CTAB

The experiments on reducing the concentration of CTAB, is actually designed for *in-situ* scanning transmission electron microscopy (STEM) experiments given in Chapter V,

since high surfactant concentration generates multiple problems for liquid state microscopy observations (*rapid crystallization of surfactant under e beam, facile contamination, etc.*).

i. With the Addition of External Br^- Source

Initial experiments, employed to reduce to concentration of CTAB below 20 mM, is inspired from the work of Garg et al.[4]. Principally, growth solutions were prepared by the addition of an external halide source (NaBr), to complete the final bromide ion concentration to 0.1 M while CTA^+ concentration is reduced below 20 mM. Three different concentrations of CTAB are analyzed (2 mM, 5 mM and 20 mM). The chemical conditions, used during the preparation of growth solutions and the volumes of the seed added, are given in detail in Table IV.2.

Table IV. 2 *Chemical compositions of growth solutions, prepared with [$HAuCl_4$] = 0.5 mM, [$AgNO_3$]= 0.12 mM and [L-Ascorbic Acid] = 1.05 mM*

Sample	CTAB [mM]	*NaBr [M]	Seed µL
N_1	20	0.08	25
N_2	5	0.09	25
N_3	2	0.10	25

*NaBr=Sodium Bromide is used as an external halide source

ii. Without External Additives

During our attempts to reduce the amount of CTAB, we have also tried to decrease the concentration from 100 mM (reference) to 10 mM with keeping the other chemical reagent concentrations constant with reference conditions (Table IV.1). No external additive is used in this experiment (Sample Name: N_4).

A.4.2.1.2 Effect of Silver Concentration

Initial ratio between $[Au^{3+}]/[Ag^{+}]$ is decreased from 11 (*Reference sample where concentration ratio corresponds to 0.045 mM of silver salt*) to 3.5 (*ratio corresponds to 0.14 mM of silver salt*) for the next set of following experiments. Concentrations of other chemical reagents and the added seed volume are kept constant, with respect to the reference conditions, for given sample-N_5 (*Conditions are as follow; 0. 1 M CTAB, 0.5 mM $HAuCl_4$, 0.14 mM $AgNO_3$, 0.75 mM AA and 120 µL Seed*).

A.4.2.1.3 Effect of Concentrations of All Chemical Reagents

Final experiment in this section includes the addition of 120 µL of classical seeds into a growth solution concentrated by factor of 5 for all chemical reagents except surfactant. For this sample (N_6), the conditions are as follows; 0.1 M CTAB, 2.5 mM $HAuCl_4$, 0.22 mM $AgNO_3$ and 3.75 mM AA.

A.4.2.2 Microfluidic Synthesis of Gold Nanorods

Gold nanorods are generally obtained by mixing very small volume of seeds (typically 120µl) with higher volume of growth solution (10ml). To achieve the well mixing of both solutions , in a microfluidic set-up, given small volume seeds (120 µL) were diluted, with 0.1 M CTAB, to 1 mL. Same dilution factor (1.1) is used to concentrate the growth solution to 9 mL. After mixing the total volume (10 mL) remains constant as in batch synthesis conditions given in Table IV.1. This condition is adapted from the work of Murphy et al. for batch synthesis of gold nanorods from large sized seeds [8].

Both solutions were mixed in a PDMS based microfluidic device. Initial step of the preparation of such a device consist of production of a wafer by photolithography. In the second step, the elastomer base and the elastomer curing agent (*Sylgard 184 Silicone Elastomer Kit, Dow Corning, Midland, MI*) were mixed at a ratio of 10:1. Resulting mixture was poured on top of the initially prepared wafer. Vacuum treatment was applied to remove all air bubbles produced during rapid mixing. Prepared PDMS mold is cured in an oven at 70 °C for a night to have hydrophobic channels and to achieve polymerization. After this procedure the PDMS was peeled off from the wafer containing the micro-channel and bonded on a glass slide (*both PDMS and glass treated with plasma cleaner to achieve strong binding of two surfaces*).

For the synthesis of nanoparticles, PDMS device containing 20 mixers is used. Representative image the microfluidic mixer is shown in Figure IV.1a. In the next figure (Figure IVb), the geometry and the dimensions of the device used for the synthesis of gold nanoparticles is given. Basically, the dimension of a single mixer is set as 500 µm x 300 µm x 50 µm to maintain the homogeneous mixing of two solutions at reactant speeds of 10 µL/min and 90 µL/min, for the seed and the growth solution. These flow rates have been chosen as results of the fluorescence experiments, performed in water, to ensure the homogeneity of the mixing in given flow rates.

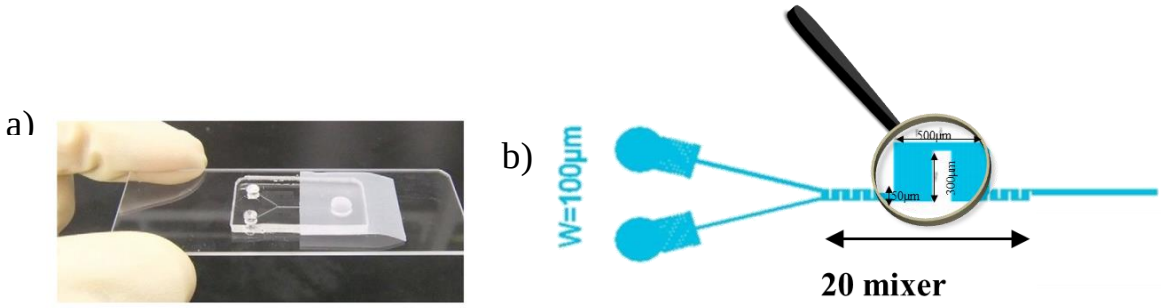

Figure IV. 1 *a) The picture of the short length microchip prepared with PDMS [11] b) The design and the dimensions of the micro channels (corresponds to a longer length microchip than the one given in picture)*

A schematic illustration of the microfluidic synthesis is shown in Figure IV.2. Mainly, the seed solution and the growth solutions were introduced into the micro-channels by using two micro syringe pumps at different flow rates (Q_{seed} = *10µL/min and* $Q_{growth\text{-}soln.}$ = *90µL/min*). Mixing of both solutions is attained thanks to the geometry of the chips, although the conditions are the ones of laminar flow. Resident time is prolonged by the addition of 3 meter Teflon tubing (1/16 inch, 0.8 mm) at the end of mixer to ensure that the reaction is finished before collecting the solution. Final nanoparticles were collected in 1 mL Eppendorf tube.

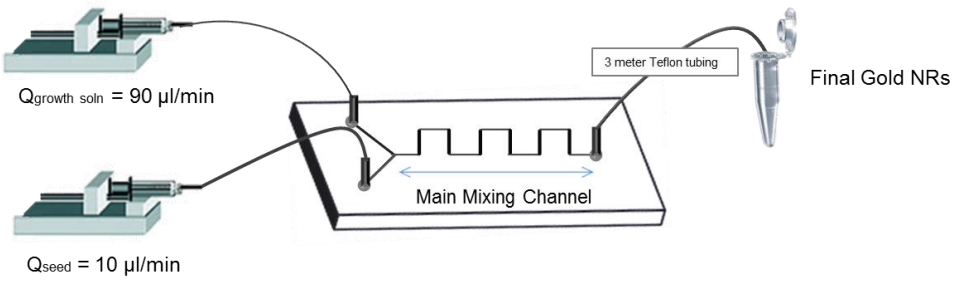

Figure IV. 2 *Microfluidic Set-up used for mixing seed and growth solution*

A.4.3 Results

The results of the growth experiments are presented under two different sections, depending on the method used for mixing the seed and the growth solution: *i*) Batch Mixing and *ii*) Microfluidic mixing.

A.4.3.1 Batch Synthesis of Nanorods with Variable Aspect Ratios

During the batch synthesis of gold nanorods, the growth condition was systematically changed for constant seed (*Type 1*) to observe the direct effect of varied parameters on the final products. UV-Vis Spectrums of all listed experiments with detailed spectrum analysis is given in Appendix 3. In the next sections we have focused on the analysis of final nanoparticles (*after purification step*) via TEM.

A.4.3.1.1 Reducing the Concentration of CTAB

As we stated previously in Materials and Methods part (*section A.4.2.1.1*), multiple methods have been tried to reduce the surfactant concentration, in purpose of adopting the chemical conditions of gold nanorod synthesis to *in-situ* STEM method. We will see in the next chapter that, minimization of surfactant concentration for such method, is a crucial importance to obtain better resolution during observation of nanoparticle growth in liquid state.

i. With an external Br^- ion source

The initial attempt, to lower the concentration of surfactant, is inspired from the work of Garg et al.[4], stating that the gold nanorods can still be obtained in a growth solution containing CTA^+ amount close to critical micelle concentration, only if the final Br^- ion concentration is completed to 0.1 M with an external halide source.

To be specific, achieved the large decrease of surfactant concentration below 10 mM (*2 mM for sample N_1 and 5 mM for Sample N_2*), in comparison to the reference value (*100 mM*), is compensated for halide concentration by the addition of an external Br^- ion source (*NaBr*). Additional study including higher surfactant concentration (*20 mM*) is introduced to compare the final states obtained by two large extremities on the surfactant amount (*2 mM to 20 mM*).

TEM images and the corresponding *L,W* plots of the samples N_1 and N_2, given in Figure IV.3b-d, indicate that the nanorods obtained in these samples bear lower ARs (1.50 for N_1 and 1.55 for N_2). In *L,W* plots of these samples, the separation of isotropic and anisotropic NP population is not well established. Increasing the CTAB amount from 2 mM to 5 mM; however, induces an increase in the proportion and the AR of nanorods.

The TEM image of the sample, in which CTAB amount is increased to 20 mM (N_3), is shown in Figure IV.4e. Clear separation between two populations (*isotropic and anisotropic*) is visible in the *L,W* plot, meaning that obtained nanorods are less polydisperse in size rather than first two conditions, 2 mM and 5 mM (Figure IV.3f). AR of the nanorods obtained with 20 mM CTAB and 0.08 M of NaBr, has been found as 2.1. This value shows a slight decrease from the one obtained by Garg et al. [4] (AR = 2.3) even though, the proportion of nanorods seen in TEM images is increased in our case.

To conclude, these experiments indicate that the AR of gold nanorods shows strong dependence to the concentration of surfactant as well as the counter ion. When the concentration of CTAB is reduced, below 20 mM, to increase the anisotropy addition of an external halide source is a reliable source to compensate the decrease in surfactant concentration. But further decrease below 10mM, even with an external Br^- source, does not permit to obtain high aspect ratio nanorods.

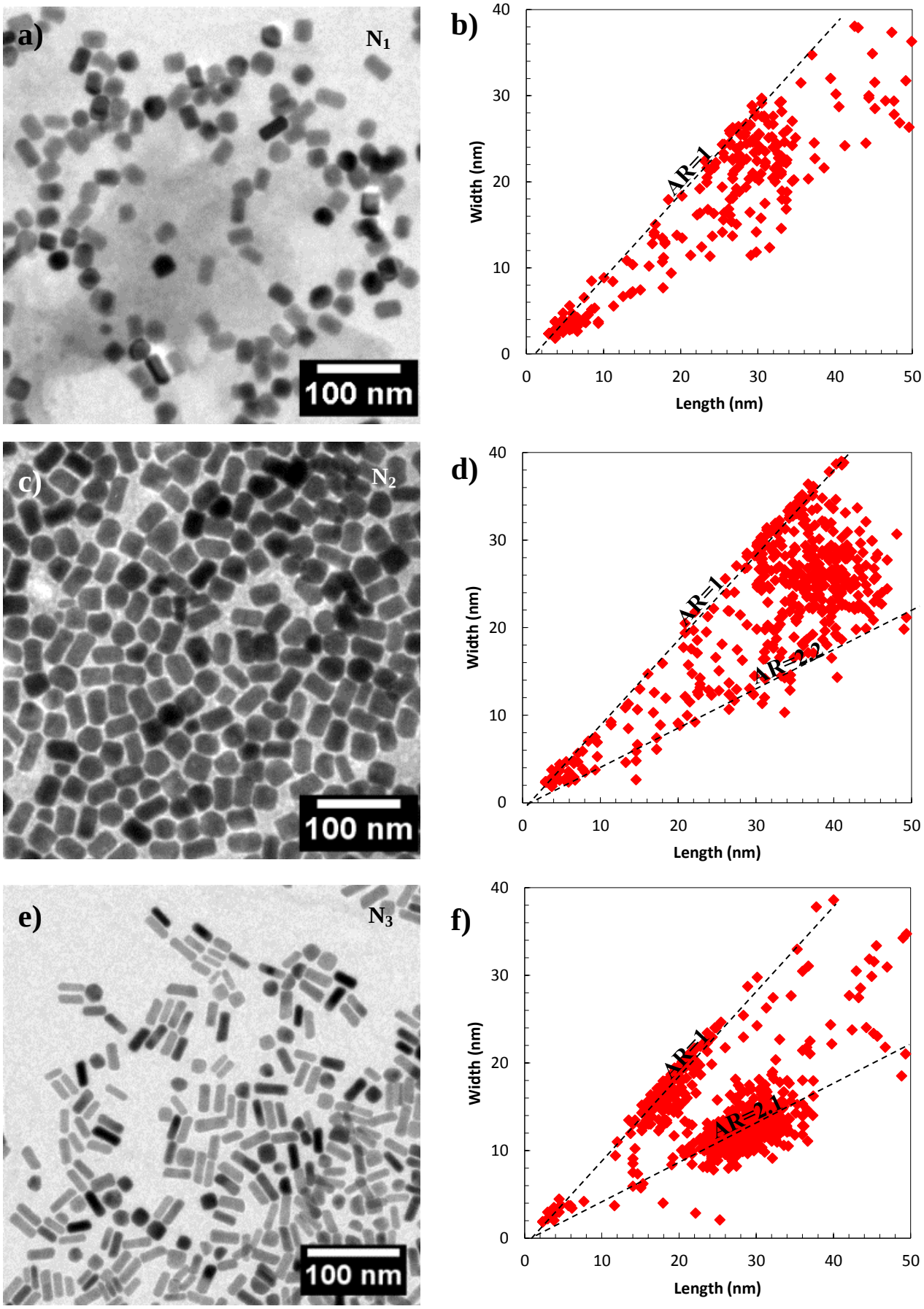

Figure IV. 3 *(a, c, e) TEM images of final nanoparticles obtained with growth solutions presented in Table IV.2 (b, d, f) L,W representation of size*

ii. Without any external additives

Next attempt to increase the concentration of surfactant is achieved by much more simple way. Basically, the CTAB amount is decreased to 10 mM in the reference growth solution without playing any other parameters (Table IV.1).

The TEM image of the final nanorods, obtained at reference growth conditions (*100 mM CTAB*), is given in Figure IV.4a with the TEM image of nanorods obtained at reduced CTAB concentration (10 mM), given in Figure IV.4b.

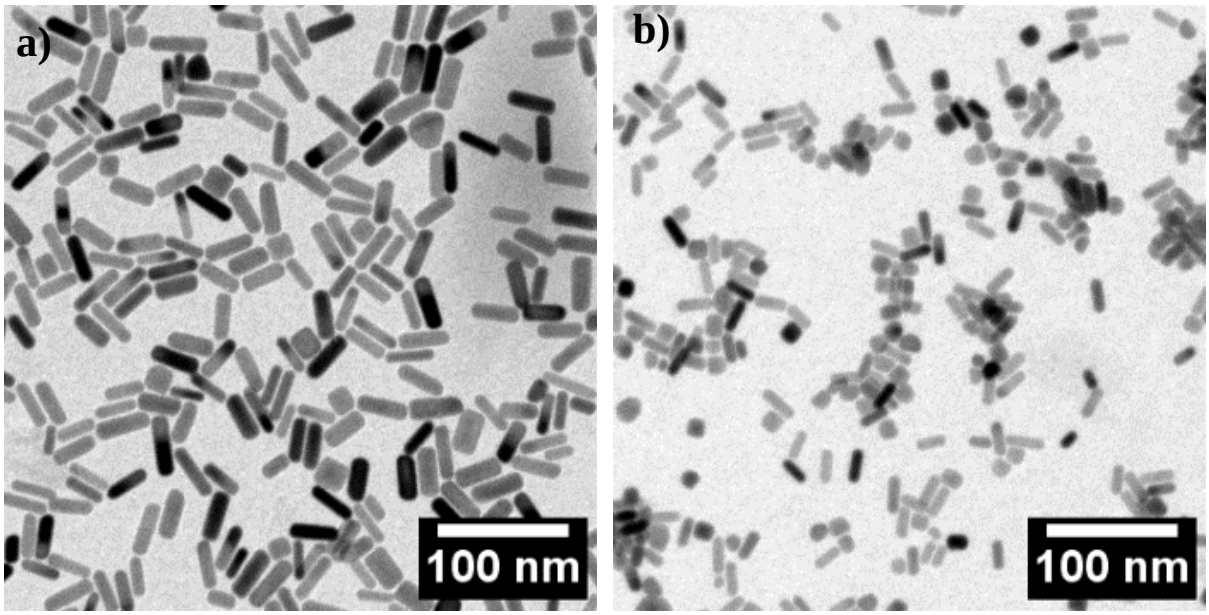

Figure IV. 4 *TEM images of gold nanorods obtained at a) 100 mM CTAB and b) 10 mM CTAB*

Between both images, we see that the percent and the AR of the nanords are decreased when CTAB concentration is reduced from 100 mM to 10 mM. Both final states are polluted by isotropic morphologies and for 10 mM the pollution is increased with respect to the reference sample.

Average aspect ratios of the final nanorods have been calculated as 2.7 for the reference conditions (100 mM CTAB) and 2.3 for low surfactant experiment (10 mM), by using TEM data. Such a decrease in the AR can be visualized easily when the size analysis were represented is superimposed in the same *L,W* plot (Figure IV.5).

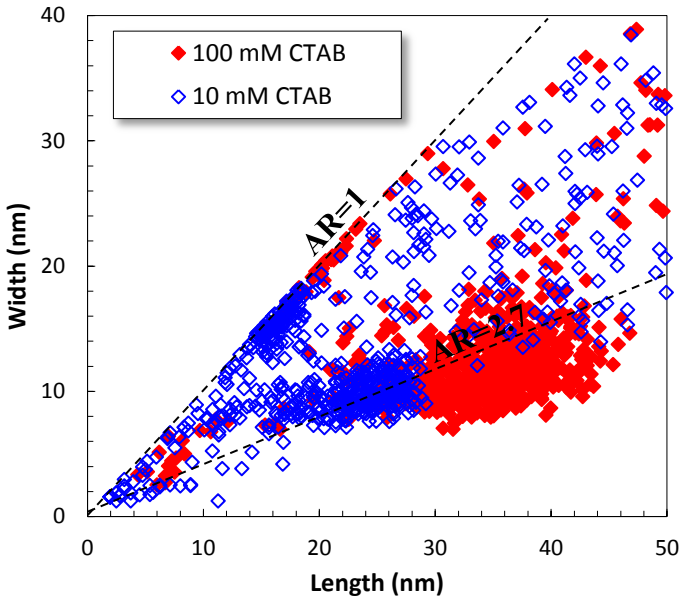

Figure IV. 5 *2D L,W Plot of samples prepared with 100 mM CTAB concentration (Reference sample) and 10 mM CTAB concentration, Sample N_4*

Our results obtained with 10 mM CTAB is in contradiction with the ones obtained by Garg et al. [4] claiming that only spherical particles can be obtained when CTAB concentration is decreased below 20 mM without external additives.

The AR (2.3) of the nanorods obtained when 10 mM CTAB is used (*without any NaBr*) was compared with the results of Garg et al. [4]. Basically, they needed 0.08 M NaBr and 0.02 M CTAB to achieve similar AR nanorods. Although, the lower volume of seed (25 µL) and the higher concentration of $AgNO_3$ (0.12 mM) used by Garg et el. [4] should promote the formation of higher AR nanorods than our case (*where 120µL seed of seed is added in a growth solution containing 0.045 mM $AgNO_3$*), at the end the larger amount of AA (1.05 mM) used in their condition can induce the difference in the final nanorods. Hubert et al., [12] has demonstrated that for seedless synthesis of gold nanorods, the concentration of ascorbic acid is also an important parameter to be considered, hence, after a saturation point the formation of isotropic NPs are promoted rather than anisotropic shapes. Finally, the purity of CTAB is also an important parameter to be considered. It is known that unpurified CTAB usually produces growth solution with higher pH than desired and yield lower amount of nanorods. In our study, we have systematically used CTAB with high purity (> 99%).

To conclude, we retrieve that high CTAB concentration is preferable to promote anisotropy. But interestingly, nanorods can also be obtained at low CTAB concentrations (10 mM) with lower aspect ratios but without need of an external Bromide source.

A.4.3.1.2 Effect of Silver Concentration

Additional experiments to study the effect of the growth conditions over final nanoparticles, is performed by increasing the concentration of $AgNO_3$ (*with respect to the reference sample where only 0.045 mM silver is used*) to 0.14 mM. The corresponding TEM images of these samples are given in Figure IV.6.

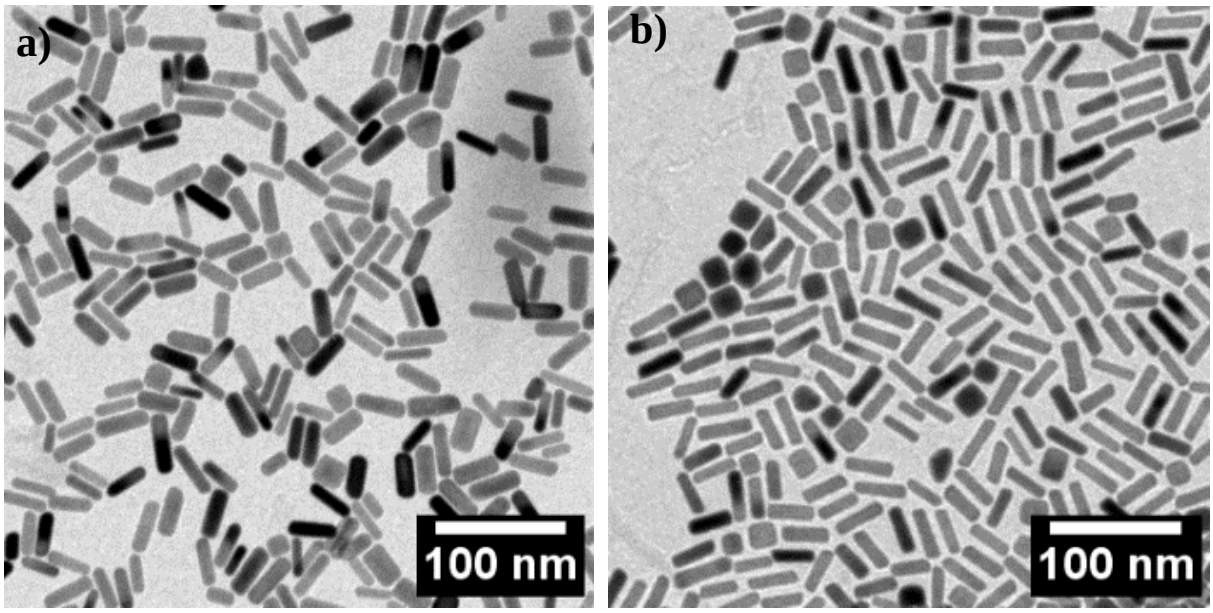

Figure IV. 6 *Final nanorods obtained at a) 0.045 mM of $AgNO_3$ b) 0.14 mM of $AgNO_3$*

The nanorods obtained with 0.14 mM silver salt (sample N_5), given in Figure IV.6b, show better alignment on the TEM support, in comparison to the reference sample (Figure IV.6a). Again the final state, obtained at higher $AgNO_3$ concentration is polluted by sub-20 nm cubic shape nanoparticles as in the reference sample.

The *L,W* plot, given in Figure IV.7, shows that the nanorods obtained at 0.14 mM of $AgNO_3$ are less polydiperse in diameter than 0.045 mM of $AgNO_3$. Average AR of nanorods is slightly increased from 2.7 to 2.75 in this case for 0.14 mM of silver.

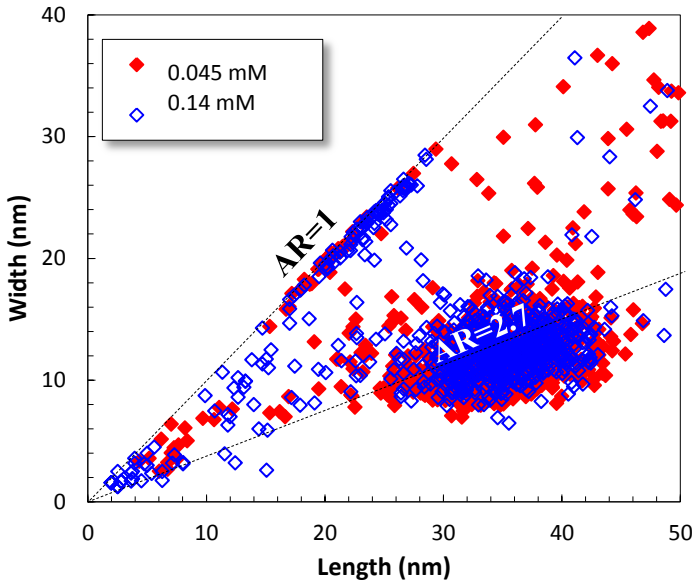

Figure IV. 7 *2D L,W plot of size of final nanoparticles obtained for reference sample including 0.045 mM silver salt and sample N_5 including 0.14 mM of silver salt*

As a result, we retrieve the observation of seedless synthesis where AR is increasing with silver nitrate concentration, but in the present case no further concentration have been studied to verify the saturation limit [12].

A.4.3.1.3 Increasing Concentration of All Chemical Reagents except CTAB

Another experiment, to study the overall effect of concentration of the chemical reagents in the growth solution, was performed with growth solutions concentrated by a factor of 5 for all chemical reagents except surfactant. This study is inspired from seedless synthesis of gold nanorods where concentrations of reagents are considerably high [9,10] than the classical seed mediated synthesis [7,8,13]. Results are shown in Figure IV.8.

The TEM image of the nanorods, prepared with 5 times concentrated growth solution than the reference conditions, shows that the final state is composed mainly by nanorods rather than isotropic by-products. The *L,W* plot reveals that the AR is diminished largely from 2.7 (reference sample) to 2.1 for given sample. Nanorods appear to be longer and thicker than the one obtained in reference conditions.

Given experiment states that, it is feasible to synthesize gold nanorods in growth solutions, with higher concentration of chemical reagents with respect to reference seed mediated synthesis conditions, however, the anisotropy is reduced for given conditions.

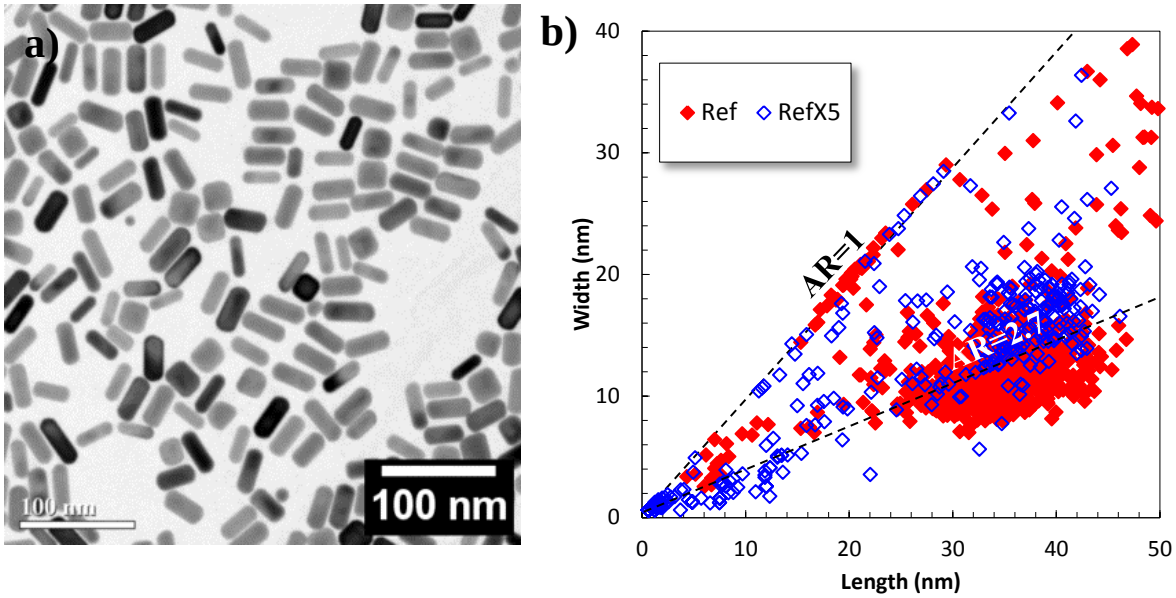

Figure IV. 8 *a) TEM images of GNRs prepared by the addition of 120 µL seed solution into growth solution containing 0.1 M CTAB, 2.5 mM $HAuCl_4$, 0.22 mM $AgNO_3$ and 3.75 mM AA b) Corresponding size analysis on particle represented in 2 D L,W plot with reference sample*

To sum up, with all given growth conditions, we have systematically obtained gold nanorods with different aspect ratios (Table IV.5) and additional isotropic shapes (nanocubes and spheres) rather than other anisotropic morphologies (*i.e. bipyramids, nanobeans, etc*.).

Large decrease of the concentration of surfactant (below 10 mM), is only achieved by the addition of an external halide source to attain the anisotropy even though final products bear small elongation.

We have clearly seen that the synthesis of large proportion of gold nanorods, with an AR of 2.3, is feasible with the CTAB concentration of 10 mM, without any external additives. To attain similar AR value, 0.08 M of Br^- (NaBr) can be used in a growth a solution containing 20 mM of CTAB.

Lastly, highest AR nanorods are obtained in the experiments performed with the traditional concentration of CTAB (100 mM). Reasons of provocation of anisotropy for given experiments have been discussed in next sections in comparison to literature.

Table IV. 3 *Average dimensions and aspect ratios obtained by TEM images for analyzed samples*

Sample	Average length (nm)	Average width (nm)	AR
Ref	38.0	14.0	2.70
N_1	35.0	23.5	1.50
N_2	50.0	33.0	1.55
N_3	30.0	14.0	2.10
N_4	30.0	13.0	2.30
N_5	37.0	13.5	2.75
N_6	30.0	12.5	2.10

Analysis of the crystal structure of different aspect ratio nanorods is presented in the next section.

4.2.1.1 Morphology of Nanorods Obtained via Seed Mediated Synthesis

In this section, we presented a closer look to the crystal structure of different aspect ratio nanorods prepared by reference growth conditions (*particles are found on the same grid*). Figure IV.9 represents high resolution images of single nanorods with variable aspect ratios lying on a carbon support.

By using Fast Fourier transform analysis, we have found that each nanorod bear single crystalline structure and [100] elongation direction (*except for small aspect ratio nanorod, given in Figure IV.9a, where only one crystal orientation is accessible in FFT of HRTEM image*). For given protocol (*reference sample, Table IV.1*), the tips of all nanorods bears smooth external facets rather than sharp sections.

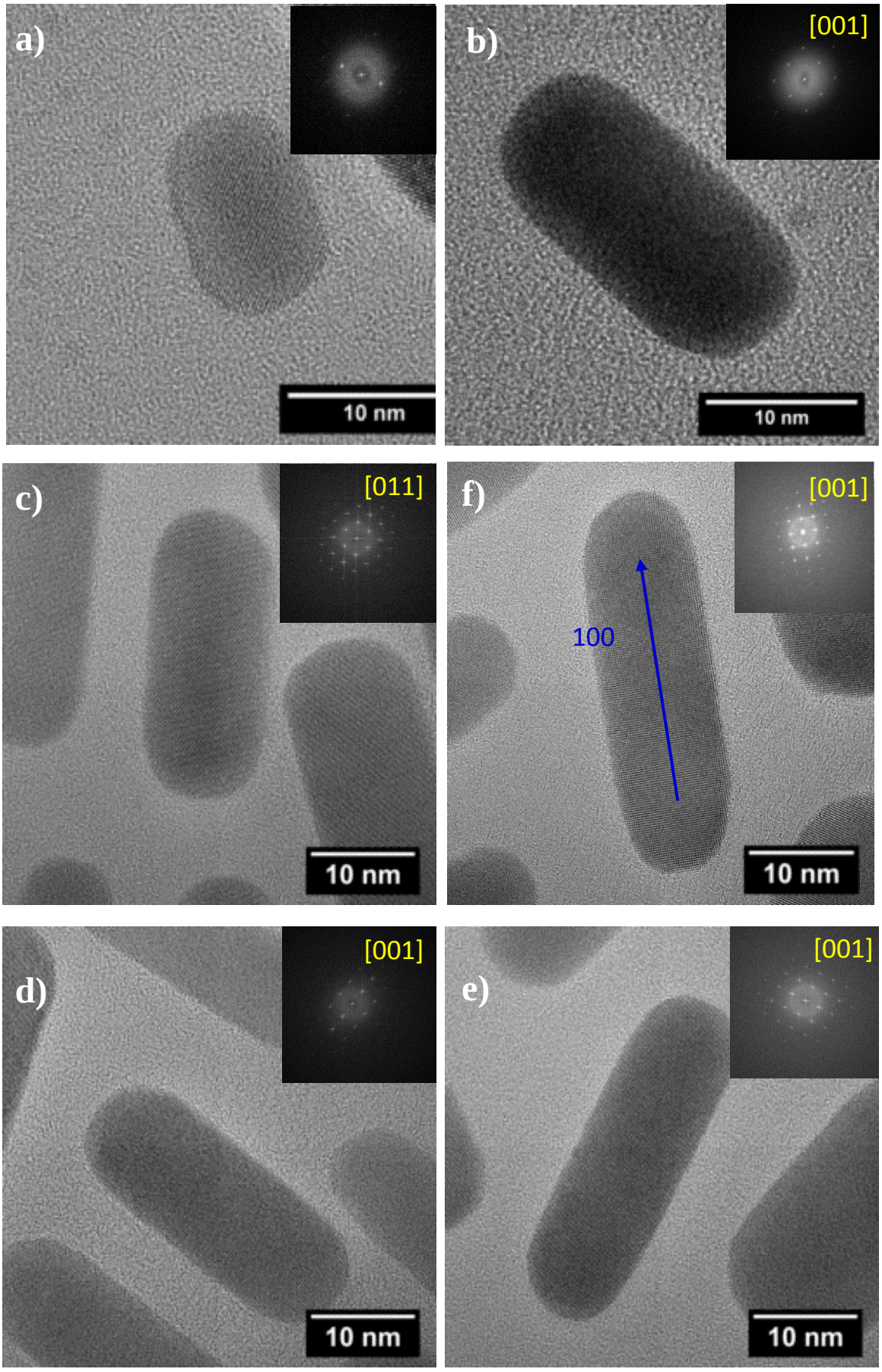

Figure IV. 9 *HRTEM image of single Au nanorods at varied aspect ratios a) 1.5 b) 2.0 c) 2.3 d) 2.7 e) 3.1 f) 3.3. The inset shows the corresponding SAED pattern*

To obtain clear information on the morphology of small size nanorods (*after development of anisotropy*), we have tried to employ the electron tomography for nanorods <10 nm. However, it was extremely difficult to acquire tilt series images on a single nanoparticle at this size without inducing any contamination. For such reason, electron tomography was only used for a high aspect ratio nanorod (3.1).

In figure IV.10a, given projected volume of a single nanorod includes the cross section of the particle at different positions, along the longitudinal axis. Even though, limited resolution of 3D model given in Figure IV.10b (*down*) restricts us to obtain details on external crystallographic faces of the nanoparticle, we can say that we deal with a nanorod possessing an octahedral symmetry. Our results are in correlation with the previously published data's from other groups [13–15], who suggest that CTAB capped seeds produces single crystalline nanorods with an octahedral symmetry**.**

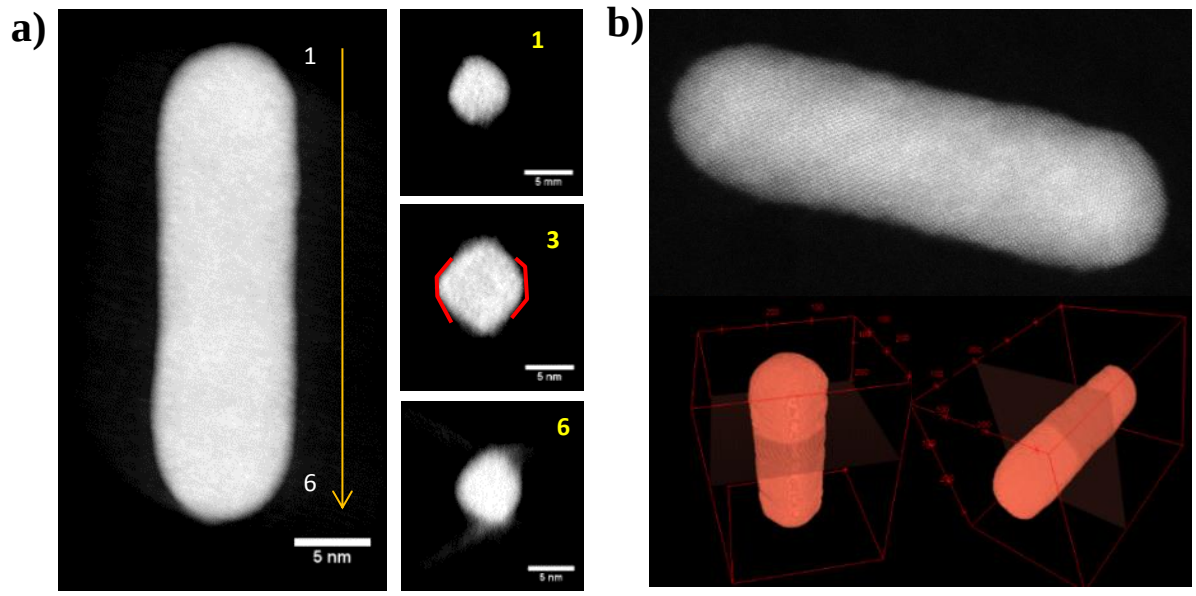

Figure IV. 10 *(a) Projected volume of nanorod with slices extracted from variable positions along the elongation axis (b)up-High Resolution STEM HAADF image of the same object taken at tilt angle 0° -down- 3D model of the nanoparticle obtained from a reconstructed HAADF-STEM tilt series*

The HRTEM images of two isotropic nanoparticles; (a) spherical and (b) cubic nanoparticles, found in the reference sample are given in Figure IV.11. The corresponding FFTs of both shapes show that the particles bear single crystalline structures as nanorods.

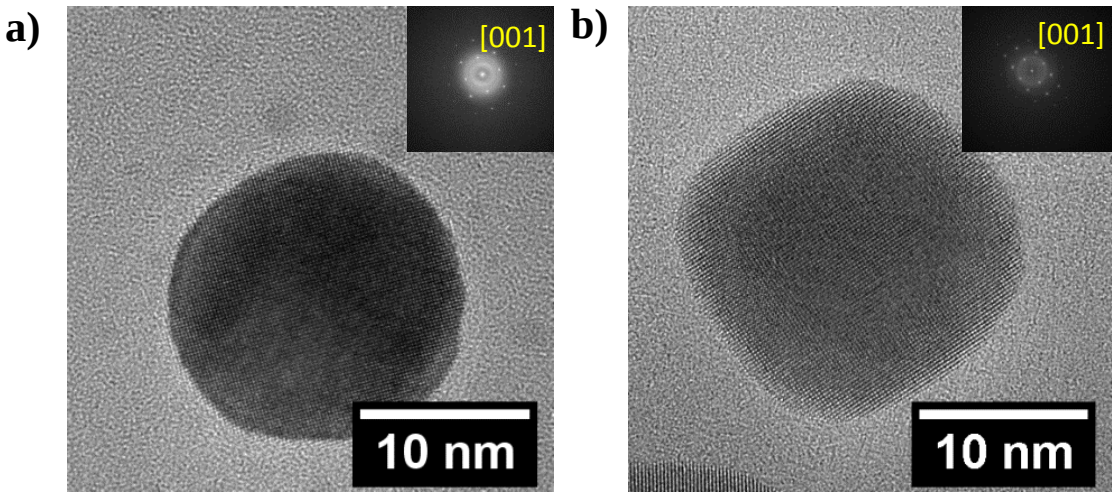

Figure IV. 11 *HRTEM images of a) spherical NPs b) cubic nanoparticles with corresponding FFT in the inset of the images*

To conclude, during the silver assisted wet chemical synthesis of gold nanorods, from CTAB capped seeds bearing single crystalline structures, the structure of the seed is preserved through the growth (*either isotropic or anisotropic growth*) and inherited into final nanoparticles. To be specific, final nanorods, at different aspect ratios and the isotropic shapes (*spherical and cubic*) exhibit single crystalline structures like the initial precursors.

A.4.3.2 Characterization of Gold Nanorods Obtained by Microfluidic Set-up

Continuous flow synthesis of nanoparticles is applied by various researchers to large number of materials [16–19]. One of the benefits of using a microfluidic device is to achieve better control on mixing of precursor and growth solution under continuous flow. Recently Lohse et al. [19] demonstrated the growth of gold nanorods (*with similar type of approach that we have adopted on dilution on seed solution*), by using milifluidic devices at variable aspect ratios (AR ~ 2-3). They have employed high flow rate (*50mL/min*) for mixing both reactant solution inside 50 mL conical tube. In this section we have used similar type of approach to mix seed solution and growth solution inside microfluidic devices rather than milifluidic set-up. Presented results are representative of preliminary experiments on production of nanorods in micro channels by using custom made microfluidic device.

Namely, the residence time of nanoparticles in the channels was estimated around 15 minutes with the following equation Eq. 4.1 (*for diameter of the tube (r)= 0.4 mm, length of the tube (l)=3 m, Q_{Seed}=10 µL/min, $Q_{Growth\ Soln.}$= 90µL/min*) ;

$$t_{residence} = \frac{\pi r^2 l}{Q_{seed} + Q_{growth\ sln}} \quad (4.1)$$

The UV-Vis spectrum of this nanoparticles, obtained by microfluidic mixing of seed solution (*with speed of 10µL/min*) with the growth solution (*injected at 90µL/min*) in the set-up presented in experimental section (*Figure IV.2*), is shown in Figure IV.12,. At this speed of reagents, mixing of both solutions is performed at controlled temperature (30°C). Mainly, the spectrum exhibits an intense, $\lambda_{L\text{-}SPR}$ around 700 nm with an absorbance value of 0.3. The AR of nanorods is calculated as 2.3 with previously given relationship between the absorption maximum of $\lambda_{L\text{-}SPR}$ and the AR (Chapter II, p53, Eq.2.3). High ratio between the absorbance maxima's of $\lambda_{T\text{-}SPR}$ and $\lambda_{L\text{-}SPR}$ is an indication that large numbers of isotropic particles are formed as by-products.

The colloidal gold concentration is estimated as 0.5 mM which means a 100% yield of Au(I) to Au(0) transformation. This surprising value (*in regard to former study*) can be linked to a slight deviation in the absorption coefficient of nanorods (*than the value we used in previous experiments, 2500$M^{-1}cm^{-1}$* [20]). This deviation is generally related to the AR of nanorods [20,21], since, the absorption coefficient strongly depends on the AR for large values whereas it varies slightly when AR<2.5.

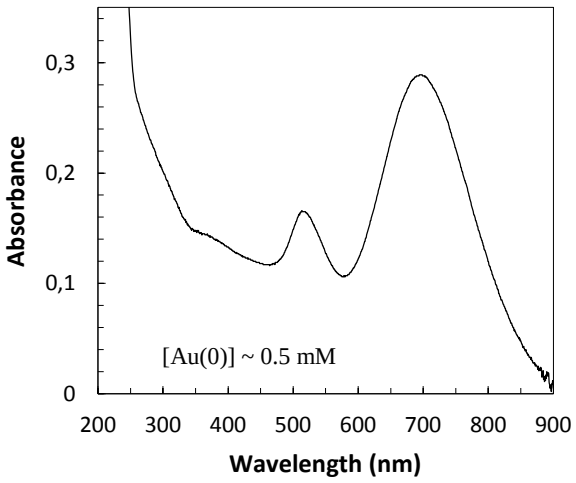

Figure IV. 12 *UV-Vis Spectroscopy of nanorods synthesized via microfluidic mixing*

The TEM image of the sample, given in Figure IV.13a, displays high number of spherical particles as expected from UV results. Quantitative size analysis, presented in Figure IV.13b, shows that the separation of nanorod and spherical particle population is not well achieved. The large distribution of the dimensions for nanorods is a representative that the particles are highly polydisperse. We have estimated an average AR of 1.9 for the gold nanorods, by TEM analysis, which is in lower than the value obtained by UV (2.3). Such difference can be explained by the etching of gold nanorods during the purification process after the acquisition of UV-Vis spetra.

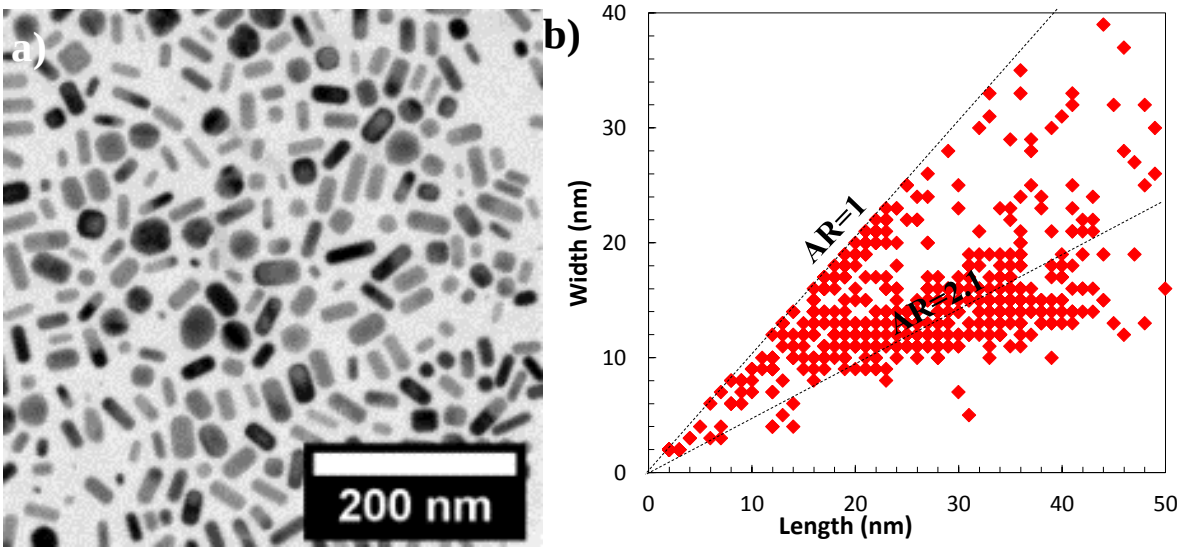

Figure IV. 13 *TEM images of GNRs obtained via microfluidic mixing of seed and growth solution with flow rates of 10 µL/min and 90 µL/min respectively (b) Corresponding size analysis represented in L,D plot*

The reason of high polydispersity, seen in *L,W* plot (Figure IV.13b), may be explained by the fact that the reaction is not completed inside microfluidic channels. Namely, the estimated residence time ($t_{residence}$*=15 min*) does not directly correspond to the kinetics of nanorod growth as we have seen previously in Chapter II, where the growth of nanorods is terminated in 17 minutes in batch conditions. If the reaction is not fully completed for microfluidic synthesis (*meaning total gold precursor is not consumed*), growth of NPs continues after the collection of the solution in the reaction container. Uncontrolled growth in this case, can explain high polydispersity. Jun et al. [22] has shown that, for spherical nanoparticles, monodispersity increases largely when the reaction is completed in the

millifluidic tube in comparison to the batch synthesis or incomplete reaction in the tube, before collection.

Another possible explanation could be an inhomogeneity in the mixing part due to high CTAB concentration and low Kraft temperature of the surfactant. Fluorescence has been used to ensure the homogeneity of the mixing in water solution only, while CTAB viscosity can change drastically the mixing conditions. At the end, during the test we have encountered some problems with blocking of channels.

Even though, mixing conditions need to be optimized for microfluidic technique in the way to obtain more monodisperse nanorods, this experiment is an evident that microfluidic mixers can be used as an alternative method of mixing to produce nanorods by changing the ratio between seeds and growth proportion. Further amelioration to the technique should be done to prevent the irreversible blocking of micro channels by alimentation of newly formed nanoparticles and to adopt the temperature control inside the device to prevent crystallization of CTAB.

A.4.4 Discussion

In this section, we have prepared gold nanorods with different aspect ratios by employing a classical seed mediated growth of CTAB capped seeds. For batch mixing we have analyzed variable range of reaction parameters responsible for the formation of anisotropy in surfactant based synthesis of gold nanorods. For given single crystalline seed, we have obtained systematically single crystalline nanorods for analyzed growth conditions.

By combining our results obtained in Chapter III with given experiments in this chapter, we have seen that the key factors on the fabrication of nanorods in solution, with controlled aspect ratio and controlled crystal structures, is one's ability to control the size and the morphology of the seeds as well as optimizing the chemical parameters in growth solution. We can conclude on the primordial role played by the structure of seeds in anisotropic development. The effect of each parameter will be discussed separately in following paragraphs.

- *The role of CTAB*

The precise role played by the surfactant is still ambiguous point during genesis of anisotropy [2] since the chemical reagent undertake multiple roles simultaneously. Some of the complex roles of CTAB have been explained in detail in Chapter I.

The important discussion is the reason of the necessity of such high concentration of surfactant (0.1 M) to obtain high yield and AR nanorods, even though the bilayer around the particles can be attained at lower CTAB concentrations [2,23,24]. The explanation that high concentration of CTAB is not directly needed for CTA^+ ions (*which forms the bilayer around the nanorods for the stabilization*), but related to the need for high concentration of bromide ions, Br^- as shape directing agents [4] is not convincing since we have demonstrated that nanorods with good AR and proportion can be obtained when only 10 mM of CTAB is used. This means that, even at low concentration (10 mM), CTAB can promote the development of anisotropy from isotropic seeds. Our result shows that high Br^- concentration is not essential to control the AR of nanoparticles and similar AR nanorods can be obtained even at low halide concentrations.

Even though it is possible to form nanorods by reducing the surfactant concentration, with or without additives, such a decrease generally compensates its worth by decreasing the aspect ratio of the nanoparticles largely with respect to reference conditions where 2.7 AR nanorods are obtained with 100 mM surfactant.

- *The role of $AgNO_3$*

In Chapter II, we have introduced small discussion on the role of silver during growth of citrate capped seeds and state that even though the mechanism of silver in promotion of aspect ratio is not fully understood, it helps better control on shape of final NP [23–25].

For nanorods, we retrieve that increasing the $AgNO_3$ concentration promote the anisotropy like in seedless synthetic conditions [24]. This effect has to be related to the formation of $AgBr_2^-$ ions, as a counter ions of CTA^+ known to adsorb on some facet of the nanoparticles during formation [26,27].

- *The role of Overall Concentration of Chemical Reagents in Growth Solution*

Synthesis of gold nanorods is also probable when the growth solution is concentrated by the factor of 5 with respect to classical seed mediated approach. Mainly, this high concentration of chemical reagents, used for seedless synthesis [9,28], and first time applied

to seed mediated growth yields formation of gold nanorods with aspect ratio of 1.94. Given conditions can be used easily for further studies requiring high chemical concentration due to low detection limit (*e.g. in-situ SAXS/WAXS studies*).

Structure analyses on different aspect ratio nanorods reveal that particles are single crystalline for different aspect ratios. Octahedral cross section is evidenced for high aspect ratio nanorods with electron tomography analysis supporting the results obtained by various groups [15,29]. Spherical and cubic by-products also bear single crystalline structures.

To conclude, whatever the chemical conditions of the growth solution, the crystal structure of seed is inherited during the growth and transferred to final material.

Part B: Gold Bipyramids

B.4.1 State of Art

First considered as a byproduct, bipyramids appear to be very promising with the high plasmon enhancement properties related to their sharp tips [30]. In previous chapters we have shown that, gold bipyramids can be obtained preferentially over monocrystalline Au nanorods by changing the crystal structure of the seeds to more complex morphologies rather than single crystalline seeeds added in silver(I)-CTAB growth solution. These results are supported by Liu and Guyot-Sionnest [1] via comparison of the HRTEM images of seeds and final nanoparticles. They have identified that the seeds produced in CTAB are mostly single crystalline which grows preferentially into single crystal nanorods while seeds produced in citrate solution are multi-twinned and grows preferentially into bipyramids. Even if the resolution of the images obtained was not sufficient to clearly identify the precise crystal structure of the nanoparticles and particularly the seeds one, these experiments have shown the crucial importance of the structure of the seeds prior to their growth.

Additionally during formation of bipyramids, the nature of the growth solution also plays a key role. Multi-twinned seeds (stabilized by citrate) can grow into penta-twinned nanorods in the absence of silver in the growth solution [31] while multi-branched nanoparticles can be obtained if the seed to gold precursor ratio is increased in silver (I) assisted growth [32]. Again, the anisotropic shape is clearly dictated by an intricacy between the initial structure of seeds and the nature of the capping agent used in the growth solution.

Recently, Zhou et al [33] took benefit of the high chemical and colloidal stability of large decahedral seeds (> 25 nm), synthesized by complex procedures at high temperatures (220 °C) , to follow their growth into bipyramids with a good control over shape and size in an aqueous solution with added polymers. The reason that bipyramids were not obtained from large sized decahedral seeds (Type 3) in previous chapters can be related to the difference in the growth conditions employed. They demonstrated that bipyramids are derived from penta-twinned decahedra through a step growth of the seeds. The strategy used, is however difficult to be realized in classical conditions where the small size of seeds (< 3-5 nm) make them difficult to characterize and stabilize in water.

Furthermore, the structure of the bipyramid is still a matter of debate. Liu and Sionnest [1] were the first to give a detailed analysis on final bipyramids particles. From analogies with copper penta-twinned nanorods [34], they stated that bipyramids (D ~ 30 nm, L ~ 110 nm) has penta-fold twinned structures around their growth axis with probably high order side facets. Such penta-fold twinned model has been supported for bipyramids by various groups [1,35,36]. Recently, Burgin et al., [37] used electron tomography in order to investigate the structure of gold bipyramids and they reveal an irregular six fold twinning structure with highly stepped dominant {151} side facets without any detail concerning the type of twinning. This surprising hexagonal section is also mentioned by Yoo et al [38] in their study on bypiramids obtained with silver (I) assisted growth using CTAC and salicylic acid as surfactant. The versatility of the seeded growth synthesis and the difficult control over the stability of the seeds solution (size < 3nm) can explain the different structure found for the bipyramids and their precursors.

The goal of this chapter is to report a full characterization of gold bipyramids obtained by citrate capped seeds (*Type 2 presented in Chapter II*) and their associated formation mechanism starting from initial spherical decahedra. We used multiple techniques (HRTEM, electron tomography) to revisit the crystal growth of bipyramidal gold nanostructures with a theoretical approach modeling on the effect of the environment on gold facet stability. We have employed a faithful approach combining state of the art TEM and theoretical approach in order to investigate the growth mechanism from seeds to bipyramids.

B.4.2 Materials and Methods

B.4.2.1 Synthesis of Different AR Bipyramids

Type 2 seeds, prepared in the presence of citrate as ligand, (*Chapter II for more detail*), has been employed for the synthesis of bipyramids given in the next sections. Varied compositional growth solutions, summarized in Table IV.6, are used during the growth of Type 2 seeds to obtain different AR bipyramids.

Purification of the final products from excess reactants has been performed with similar type of method listed in previous sections. Namely, growth solutions (10 mL) were centrifuged at two cycles with speed of 8440 g for 20 minutes. After the first step of centrifugation,

supernatant was discarded and remaining sediment was re-dispersed in pure water to attain the same final volume of solution (10 mL). Following the second step of centrifugation nanoparticle solution is concentrated to 1 mL for microscopy observations.

Table IV. 4 *Compositions of growth solutions used for preparation of bipyramids with [$HAUCl_4$]=0.5 mM)*

Sample	Growth solution (10ml)					Seed Volume (µl)
	CTAB (M)	$AgNO_3$ (mM)	AA (mM)	5-bromo-salicylic acid (M)	HCl (M)	
N°1 (ref)	0.10	0.045	0.75	-	-	400
N°2	0.10	0.140	0.75	-	-	400
N°3	0.10	0.140	0.75	-	0 .01	50
N°4	0.05	0.100	0.25	0.01	-	60

B.4.3 Results and discussion

B.4.3.1 Synthesis of Different Aspect Ratio Nanobeans/Bipyramids

For the characterization of the final states UV-Vis Spectroscopy and TEM have been used in parallel as initial analysis tools. (*For detailed analysis of the corresponding UV-Vis Spectrums of the samples, given in Table IV.6, see Appendix 3*). The TEM images of the final nanoparticles after purification are summarized in the following Figure V.14.

Using the reference conditions given in Chapter II, a dispersion of nanobeans in coexistence with spheres can be obtained (Sample N°1) if 400 µL of seed is used. When such a large volume of seed is employed, obtained bean shapes particles bear small aspect ratios (1.6) as shown Figure IV.14a. Fortunately, in Chapter II (2.2.4) we have shown that, the aspect ratio of the nanobeans can be modified by either;

- increasing the $AgNO_3$ concentration (Sample N°2) to increase the AR to 2
- decreasing the pH [14,39] (Sample N°3) to obtain bipyramids with AR of 2.7

- adding 5-Bromosalicylic acid which is classically used for nanorods [40], employed here first time to produce bipyramids (Sample N°4) to increase the AR of the bipyramids to 2.9

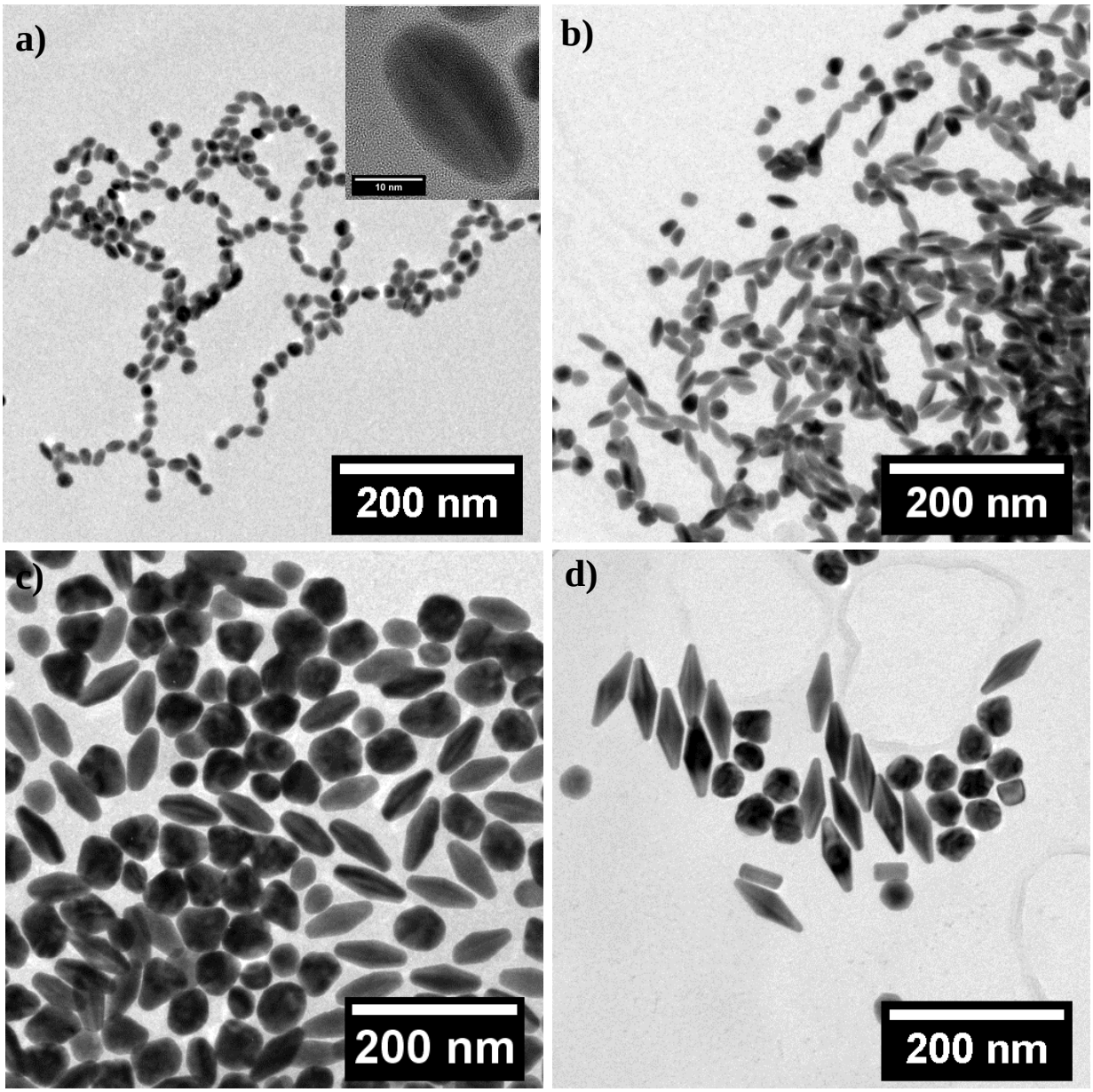

Figure IV. 14 *TEM image of a) N°1 (reference) b) N°2 c) N°3 d) N°4*

In the next section we have studied the crystal structure of different sized bipyramids to relate the complex internal structure of the final bipyramids, intermediate sized nanobeans and small sized decahedral NPs.

B.4.3.2 Morphology of the bipyramids

The morphology of the bipyramids has been derived from the analysis of HRTEM images and Selected Area Electron Diffraction (SAED). Bipyramids with aspect ratios greater than 2 and the size larger than 20 nm are most always observed with the elongation direction parallel to the carbon grid, *i.e.* perpendicular to the electron beam as given in Figure IV.15 (*See Appendix 3 for additional bipyramids*). They are always characterized by a non-uniform contrast and the presence of planar defect. From the analysis of several nanoparticles, it appears that the large bipyramids are always twinned and only two main observation directions separated by 18° are accessible (*Figure IV.15, See Appendix 3 for two other orientations*).

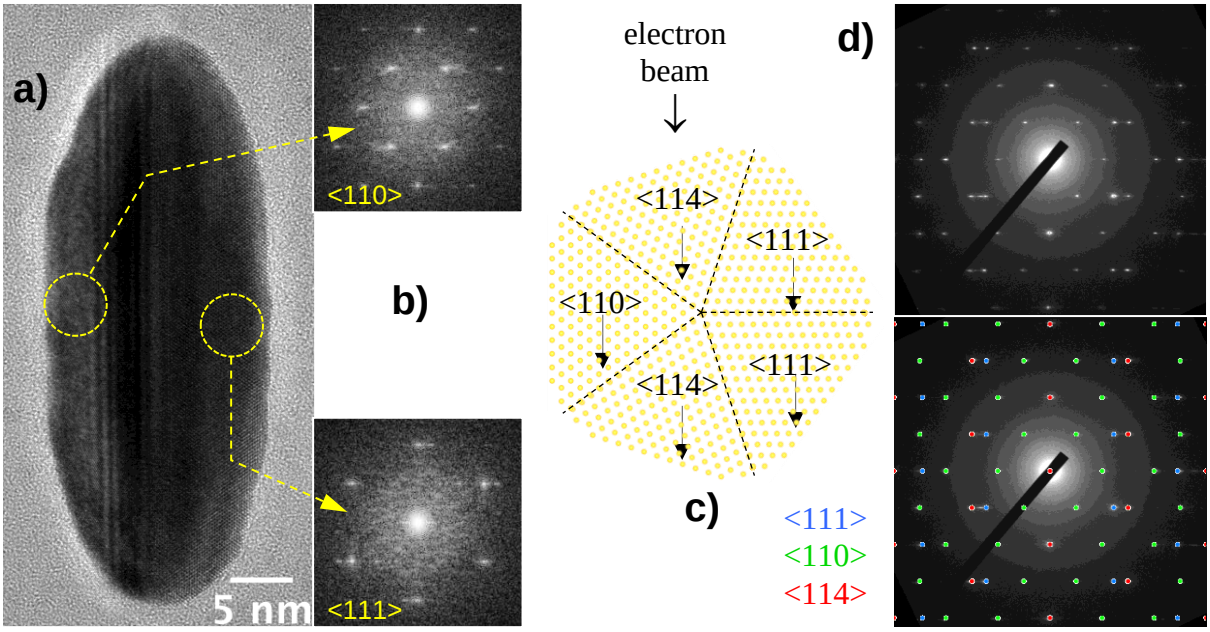

Figure IV. 15 *(a) HRTEM observation of a large bipyramid with elongation direction perpendicular to the electron beam. (b) Orientations of the crystals located on the sides of the bipyramid: <110> and <111> zone axis deduced from FFT analysis. (c) This result can be interpreted in agreement with a penta-twinned structure of the bipyramid. (d)The corresponding SAED pattern may be analyzed as the superimposition of <111>, <110>, <114> zone axis diffraction pattern.*

For the particle shown in Figure IV.15a (*L=45.7 nm W=17.1 AR=2.7*), two crystal orientations of the multi-twinned bipyramid can be easily deduced from Fast Fourier Transform (FFT) analysis: <110> and <111> (Figure IV.15b). The SAED pattern corresponds to a superimposition of three <111>, <110>, <114> zone axis diffraction pattern which is consistent with multiple twinning of a face-centered cubic structure.

This type of twinning, common in isotropic gold NPs with decahedral (D5h) morphology [41–44], has also been retrieved for nanorods in the case of gold [45] or copper [34]. We can

conclude that large bipyramids are based on a penta-twinned structure in agreement with initial observation from Guyot-Sionnest [1].

In contrast, smaller bipyramids (size ≤ 20 nm) with a more reduced aspect ratios offer a wider range of orientations. Thus, such kind of particle may be observed with an apparent fivefold axis quite parallel to the electron beam (*e.g. with an angular shift within the tilt capabilities of the double tilt specimen holder*) as in Figure IV.16a. Structural analysis of the particle reveal that the NP is constituted of 5 individual crystals oriented along a common <110> direction (*parallel to the electron beam*), exhibiting a fivefold symmetry. The overall Fast Fourier Transform can be interpreted as the superimposition of 5 <110> zone axis diffraction patterns.

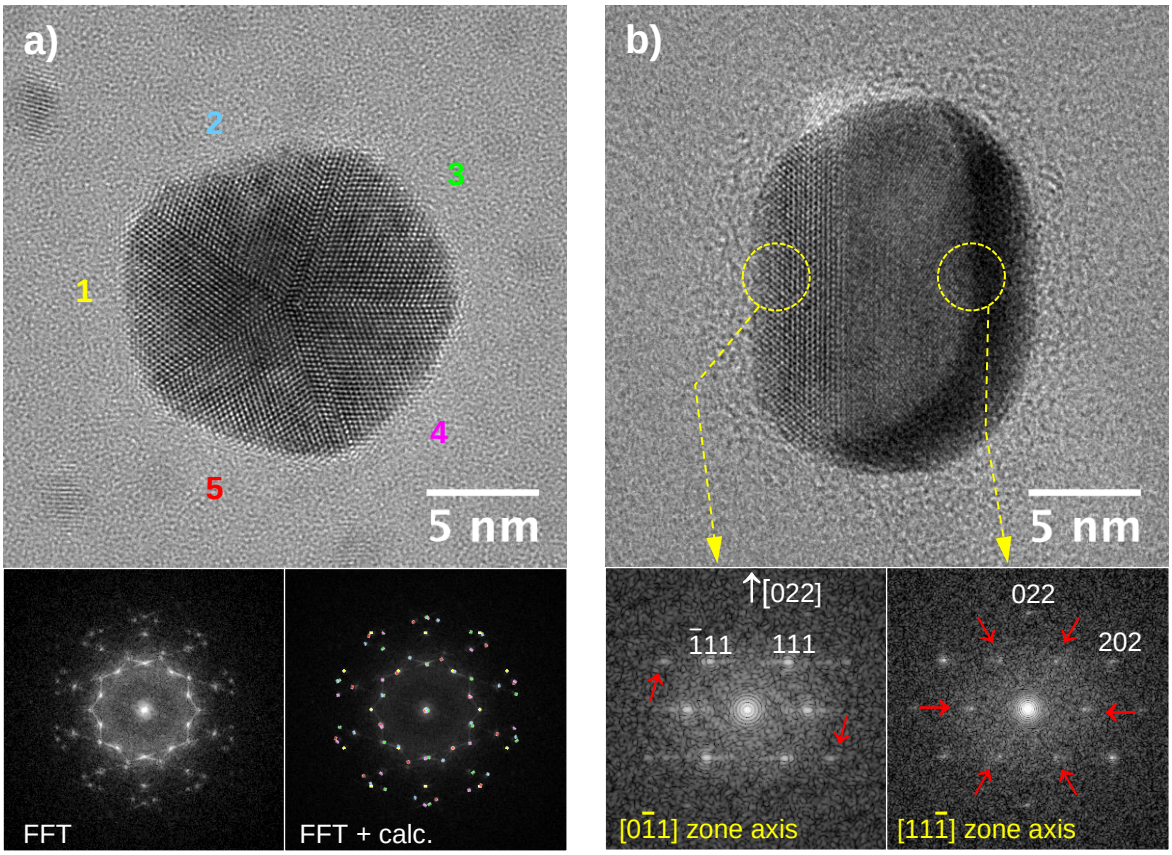

Figure IV. 16*(a) HRTEM image of an intermediate size penta-twinned particle (parallel to the electron beam), exhibiting a fivefold symmetry (the color of the calculated diffraction pattern is related to the corresponding labeled crystal. (b) HRTEM image a multi-twinned particle (perpendicular to the electron beam). Red arrows indicate supplementary reflections due to double diffraction and delocalization phenomena.*

Another intermediate sized bipyramid (*so-called nanobeans with an AR of 1.4*) observed perpendicular to the electron beam is given in Figure IV.16b. In this case, the particle constituted

of at least two crystals oriented along a common <110> direction. The FFT corresponding to the left part of the particle is related to a distorted <110> zone axis diffraction pattern whereas, the FFT corresponding to the right part of the particle is related to a <111> zone axis diffraction pattern. From FFT analysis, a penta-twinned structure can be unambiguously attributed to small bipyramids.

This typical twinning is therefore observed for different elongated nanoparticles with different aspect ratio going from nanobeans to bipyramids.

Further observations were achieved using STEM-HAADF electron tomography on a large bipyramid. The Figure IV.17 shows the 3-D morphology reconstructed from DART algorithms [46]. The bipyramids (*L = 64nm, D = 18 nm, AR = 3.55*) presents rounded tips with an angle of 27° between the side edges. Our results differ significantly from those obtained by Burgin et al. and Yoo et al. [37,38], for which a hexagonal section was observed. In our case, despite the fact that some angles may be rounded due to the missing wedge, a clear pentagonal section is observed.

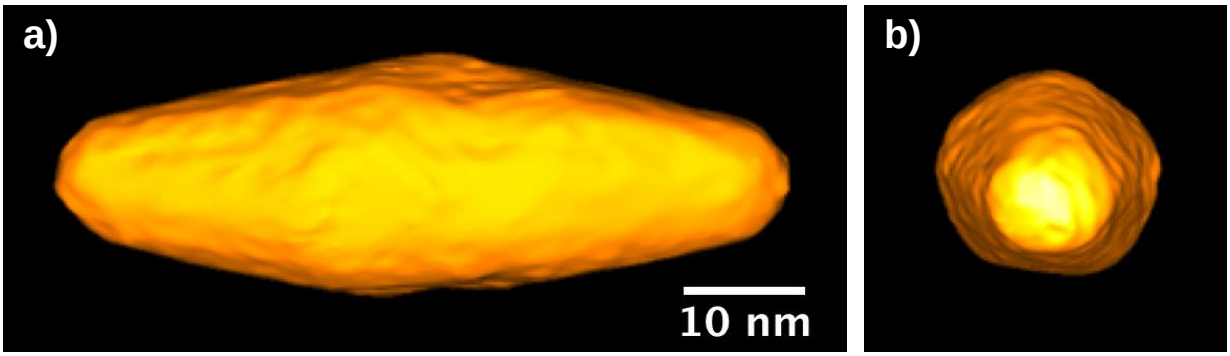

Figure IV. 17 *(a) Figure e-tomo 3D volume of a bipyramid obtained from a DART reconstruction procedure and bipyramid viewed along the elongation direction. (b) A clear pentagonal section is evidenced.*

To assess the complete internal structure of the bipyramid described above, a simulation of a penta-twinned bipyramids with stepped side faces of high index {11n} facets was obtained from the computational method described in materials and methods (for ~3000 atoms). The different view (See *Appendix 3*) from different orientation reproduces the classical TEM images observed for bipyramids. The variation of the twinning zone in the center of the particle with the orientation of the nanoparticles comes from the contribution of the different crystals along horizontal axis.

B.4.3.3 Characterization of Seeds and small size nanoparticles

As previously mentioned, low gold concentration in seeds associated with their small size, makes their shape and structure analysis more difficult (*Chapter II.2.2.1*). Contrary to Turkevich method [47] known to produce stable isolated nanoparticles (Type 3), these small seeds produced by borohydride addition (Type 2) are quite unstable. DLS, SAXS and UV-Vis spectroscopy employed on freshly prepared Type 2 seeds, evidence a large distribution (σ/R= 0.37) of nanoparticles with the average particle size around 4.8 nm (*Chapter II.2.2.1.1*). However, any attempts for direct TEM analysis just lead to the formation of large sized aggregates on TEM support (*TEM image is given in Appendix 2*). To overcome this problem, we have imaged the residual seeds unaffected by the reduction of additional metal salt in the growth solution [48] assuming that those small particles as representative of the seeds after their addition into CTAB solution (Figure IV.18).

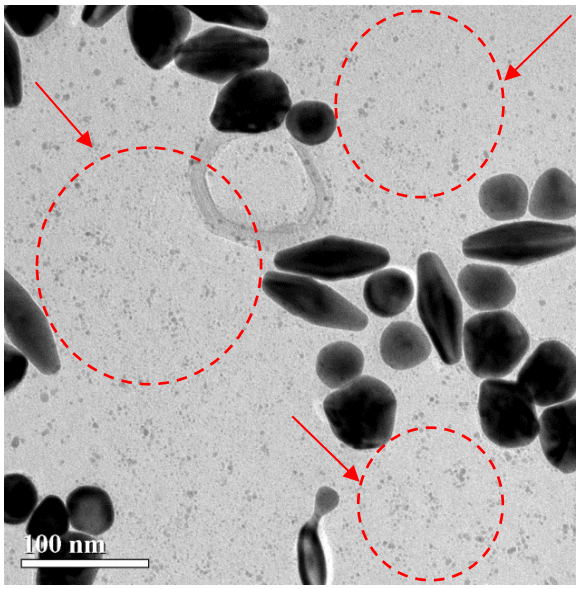

Figure IV. 18 *Coexistence of small and large particles in the final solution*

HRTEM image of sub-5 nm penta-twinned particle found in the final solution after the growth is demonstrated in Figure IV.19a. Particle is constituted in such a way that 5 individual crystals oriented along a common <110> direction (*parallel to the electron beam*) to exhibit a fivefold symmetry. Similarly, as shown in Figure 19b, a small multi-twinned nanoparticle exhibit the same structural feature, i.e. adjacent sub-units with the same relative crystallographic orientation, as the one described for large and small bipyramids (Figure IV.15 and 16). These small size nanoparticles have a larger {100} facets than classical decahedra.

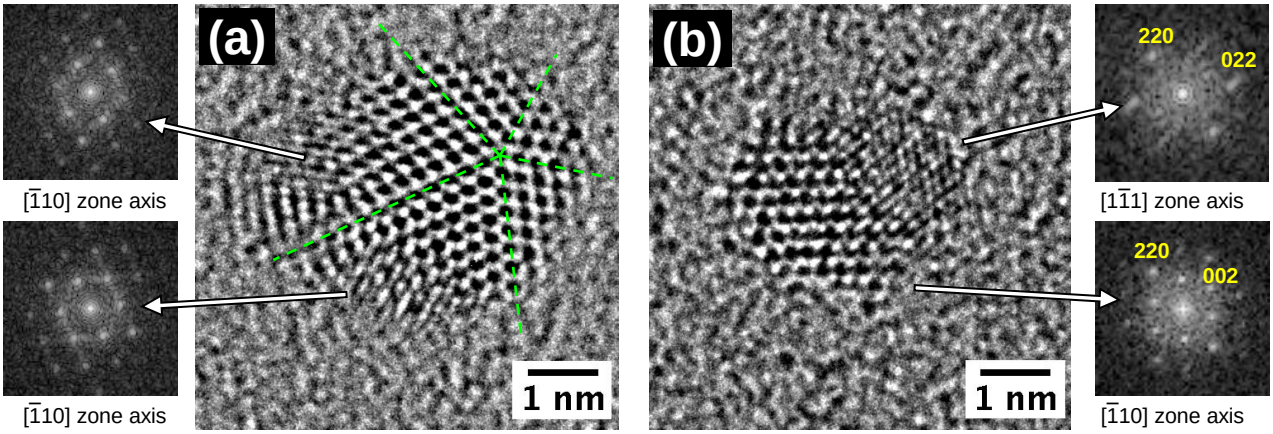

Figure IV. 19 *Structural analysis of twinned seeds, (a) Ultra HRTEM image of a 3.3 nm particle with FFT analysis on selected areas, (b) Ultra HRTEM image of a 2.7 nm seed particle with different orientation.*

HRTEM have shown penta-twinned structure for small size nanoparticles and elongated ones as being representative of the particles in formation. To investigate the link between the initial and the final structure of the nanoparticles, we have used a semi empirical approach to describe the effect of the environment on the stabilization of different shapes. Such kind of prediction is used instead of Wulff constructions since Wulff only predicts single crystalline structures rather than complex multi-twinned structures as we deal here [49].

B.4.3.4 Selection of Morphology Depending on Surface Energies

The model presented in this section was developed by Jacek Goniakowski, Claudine Noguera and Robin Cortes- Huerto in INSP, UPMC and represented in detail explaning the conditions of chosen environments in the article of Cortes et al. [50].

In the following part, three environments are chosen, corresponding to different (ε, p) parameters: A (ε = 0.05 eV/atom, p = 1.5), B (ε = 0.023 eV/atom, p = 1.9), and C (ε = 0.022 eV/atom, p = 2.0), for which the reduction of NP surface and edge energies due to interaction with the environment diminishes drastically the stability gap Δ-Δ_{Dh} between elongated particles and the spherical decahedral seeds (s-Dh).

In Figure IV.20 (upper panel), relative surface energies of three different elongated decahedral cross sectioned particles (with an average of 3000 gold atoms per particle) is reported with respect to the spherical decahedra (s-Dh) ones. The elongated penta twinned of type I, II, and III, depicted in the bottom panel, are the most stable NP in the environments A, B, and C, respectively.

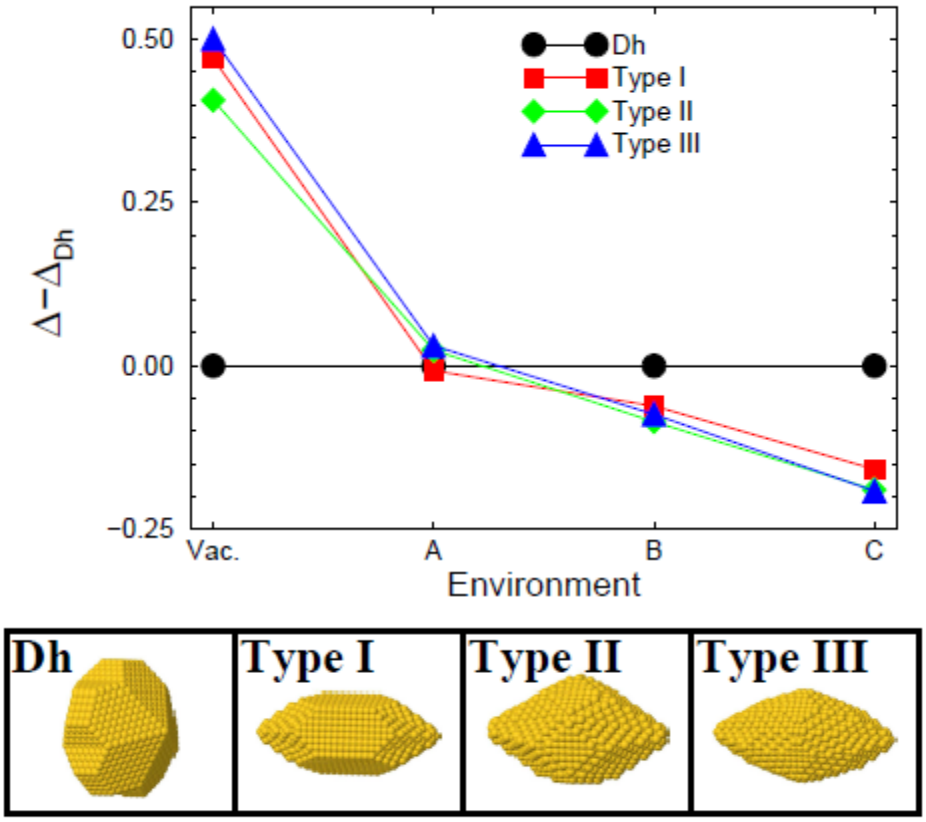

Figure IV. 20 *Top panel: Excess surface energies of the most stable elongated penta-twinned gold particles with respect to the spherical decahedral (s-Dh) ones Δ-Δ_{Dh} (eV/N$^{2/3}$). Bottom panel: s-Dh, Type I, II, and III particles correspond to the most stable structures in respectively vacuum and environments A, B, and C created with an average of 3000 gold atoms per particle.*

As expected, spherical Dh particles (aspect ratio 1.1), bordered by large {111} facets, are by far the most stable in vacuum (ε = 0.00 eV/atom), with Δ-Δ_{Dh} as large as 0.5 eV/ (number of atoms)$^{2/3}$. At variance, in the three chosen environments, Δ-Δ_{Dh} becomes negative, meaning that elongated penta twinned particles are more stable than s-Dh particles. Type I particles (aspect ratio 2.2) are the most stable in environment A. They are characterized by fairly long lateral

{100} facets and relatively small tips bordered by five {110} facets. This shape is similar to that of the penta-twinned nanorod structures observed by Johnson and coworkers [45].

In case of type II penta twinned (aspect ratio 1.6), stabilized environment B, the lateral {100} facets are much smaller, while the {110} facets at the two tips have increased in size.

Finally, type III particles (*aspect ratio 1.9*) are stabilized in environment C. While of an appearance similar to those of Type II, at their tips, they mostly expose {210} facets, somewhat more open than the {110} ones. These gold penta-twins resemble the so-called nanobeans (*low AR bipyramids*) given in Figure IV.14a. Depending on the environment (*i.e. on a chosen ligand added in the solution*), higher elongated decahedral cross sectioned particles can be stabilized.

B.4.4 Discussion

From HRTEM and SAED experiments, the structure of gold bipyramids obtained by silver(I)-seeded growth assisted processes have been determined. Analyzes have been performed on a final sample containing different size of representative growing nanoparticles. A penta-twinned structure was determined 1) for elongated nanoparticles with bipyramids shape for size superior to 5 nm and 2) for the smallest apparently isotropic nanoparticles with a size below 5 nm. Zhou et al [33] have shown strong evidences for growth of big decahedra seeds (25-49 nm) into bipyramids with the conservation of the five twinning internal planes, but for smaller size seeds, the direct evidence of conservation of the pentatwinned structure is difficult. For small size, the spherical Dh (s-Dh) particles is known to be the most stable in vacuum and has been largely described in the literature [43,51–53], however in solution, with ligands, experimental evidence of this structure is more tricky [1,54,55]. Using a low voltage (80 kV) for HRTEM allows extracting the structure of the small size seeds used in silver (I) assisted growth method even in the presence of CTAB surfactant. From these experiments, we can conclude to the conservation of the pentatwinned structure during the growth of the nanoparticles into bipyramids.

Regarding the different size of nanoparticles, the smallest size presents a penta-twinned structure with a larger {100} facet area in comparison to the initial s-Dh structure (Figure IV.19). It is known that for face centered cubic structure, the only way to obtain elongated shape is to break symmetry by either incorporating twin defects or stacking fault into the nanocrystal [48,56]. For nanoparticles in solution, the ligands can emphasize this process by inverting the energy of the facets through selective adsorption.

Simulations (Figure IV.20) obtained on a family of penta-twinned structure in different environment exhibit the possible inversion between stable isometric and elongated shapes. The differences between the three environments are representative of three different hypothetical ligands, environment being described by a set of parameters in a semi-empirical approach. The main result of this simulation is the evidence of a possible stabilization of elongated nanoparticles by changing the environment. In one case the {100} facets is stabilized (*i.e. this facet will be preferentially formed*) and nanorod shape is obtained (Figure IV.20, *type I*). This situation can be related to the experimental growth of citrate seeds in the absence of silver nitrate [57]. In the other case (Figure IV.20, *type II and III*), higher indexes facets are stabilized and

nanograins/ bipyramids are preferentially formed, like in the experience based on silver-(I) assisted growth of citrate seeds.

The two situations described above are differentiated by 1) experimentally, the presence or not of silver nitrate in the growth solution and 2) from simulation, a different order for the energy of the different facets. Establishing a relation between these two features implies a full description of the molecular analysis around gold nanoparticle and the shape orientation which is difficult to measure and either to simulate. Grochola et al. [58] have simulated explicitly the CTAB around gold nanoparticles to explain the growth of nanorods by preferential adsorption on chosen facet. Experimentally, the promotion of the anisotropy in the monocrystalline nanorods formation is supported by the combination of the face capping abilities of the complex between CTA^+ and $[Br\text{-}Ag\text{-}Br]^-$ ions [27,59] (*CTASB*) and the stabilization effect of a CTAX double layer [60]. Recently, Almora-Barrios et al. [61] go deeper in the atomistic description of the role played by silver to explain the increase of anisotropy in the formation of nanorods. Using Density Functional Theory simulations, they demonstrate the preferential adsorption of this complex on open facets {100} in comparison to {111} facets with at the end a strong stabilization effect for higher indexes facets {520} present on the lateral sides of the monocrystalline nanorods. This specific adsorption can be used to support the experimental differences of decahedra growth into either bipyramids or nanorods for respectively silver (I) containing or not growth solution.

When seeded growth is realized with silver nitrate: The first extension of the {100} facet observed for small size (Figure IV.19) can be supported by the strong value of energy gain of 3ev/CTASB calculated by Almora et al. [61] for a seed containing {111} and {100} facets. Further alimentation proceeds on along twinning axis along the tip of the nanoparticles (probably because of less compact surfactant layer [2]) leading to the creation of surface of higher indexes stabilized by the CTASB. These higher index facets being the most stable, it is more favorable for the system to grow these facets instead of the lateral {100} ones (Figure IV.16). Finally, Surface energies between {113} and {115} being similar, the small nanograins evolve towards higher aspect ratio bipyramids (Figure IV.15 and 16).

In an opposite way, it is known that in the absence of silver, even though attaining the anisotropy is same, growth of high energy {113} facets is not favored and not stabilized. Some pentagonal cross section nanorods with {100} side faces are formed in a very low yield (< 1%) [29]. From the calculation of Almora et al. [61], it appears that the adsorption of CTAB is less favored on {100} in comparison to the CTASB case (the gain in energy is only 0.3eV/CTAB).

Despite this small stabilization effect, few particles can be transformed into the small nanorods where the {100} is developed from the initial s-Dh seeds (Figure IV.19). As soon as the anisotropy is developed, gold nanorods continued to grow with increasing the (100) surfaces of the lateral facets by an autocatalytic process. In that case, higher indexes facets are not stabilized and the transition between small nanorods and bipyramids cannot be observed. These two growth directions are summarized in the Figure IV.21 for the growth of decahedron spheres into gold penta-twinned nanorods whithout silver or into bipyramids when silver is present.

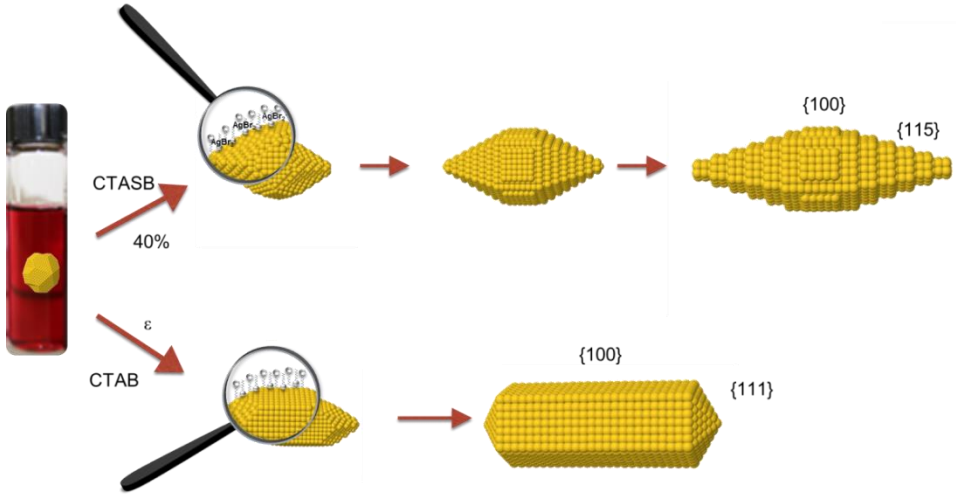

Figure IV. 21 *Formation mechanism of bipyramids and nanorods: In the present case, the bipyramids are formed by a silver (I) assisted process in CTAB solution, and we know from HRTEM that pentatwinned structured is maintained along the growth. For pentatwinned nanorods formation, they are obtained without silver from decaedra seeds in low yield.*

Conclusion

To conclude, for gold nanorods, during the modulation of the growth conditions for same type of single crystalline seed prepared with CTAB, two direct consequences are observed; *i*) variation of the proportion between the isotropic species (*nanospheres and cubic NPs*) and the anisotropic nanorods *and ii*) variation of the aspect ratio of the final nanorods. However, the final structure, imposed by the initial single crystalline seeds, is preserved through the variation of the growth parameters, meaning that the inherited structure does not directly varies for studied parameters. Importantly, gold nanorods can still be obtained even when the concentration of surfactant is reduced 10 times than the classical amount.

For bipyramids, HRTEM and tomography results demonstrate that, the internal structure of the bipyramids was fully determined and definitively attributed to a penta-twinned structure. If this structure was initially advanced in the literature, recent tomographic studies had opened the way to another possible section based on an hexagonal symmetry for bipyramid [37] . We ruled out this option for the gold bipyramids synthesized in CTAB solution from silver(I)-assisted growth process. Through a complete HRTEM, SEAD and tomography study, we also investigated the different sizes from initial decahedral seeds to final shape. The penta-twinned signature was clearly retrieved for all the different intermediate nanoparticles. This experimental approach could be combined to an atomistic model taking into account the environment of the gold nanoparticle that indeed showed that different kind of elongated nanoparticles (*either nanorods or bipyramids*) can be stabilized by changing the nature of the ligand used during the synthesis. This consolidates the importance of a fine tuning of surface chemistry for the control of (exotic) shape nanoparticles.

Additionally, we demonstrated that 5-bromosalycilic acid known to promote anisotropy in nanorods synthesis can also be used to promote anisotropy in bipyramids synthesis.

References

[1] M. Liu, P. Guyot-Sionnest, J. Phys. Chem. B 109 (2005) 22192.

[2] S.E. Lohse, C.J. Murphy, Chem. Mater. 25 (2013) 1250.

[3] S. Köppl, Seed-Mediated Synthesis of High Aspect Ratio Nanorods and Nanowires of Gold and Silver, Univ., Technische Universität München, 2011.

[4] N. Garg, C. Scholl, A. Mohanty, R. Jin, Langmuir 26 (2010) 10271.

[5] S. Si, C. Leduc, M.-H. Delville, B. Lounis, ChemPhysChem 13 (2012) 193.

[6] J.N. Israelachvili, D.J. Mitchell, B.W. Ninham, J. Chem. Soc. Faraday Trans. 2 Mol. Chem. Phys. 72 (1976) 1525.

[7] J. Rodríguez-Fernández, J. Pérez-Juste, P. Mulvaney, L.M. Liz-Marzán, J. Phys. Chem. B 109 (2005) 14257.

[8] A. Gole and C. J. Murphy, Chem Mater 16 (2004) 3633.

[9] F. Hubert, F. Testard, G. Rizza, O. Spalla, Langmuir 26 (2010) 6887.

[10] N.R. Jana, Small 1 (2005) 875.

[11] Sensors/MEMS, Http://www.eetasia.com/ (2014).

[12] F. Hubert, PhD Thesis: Nucléation et Croissance de Nanocylindres D'or : Mécanismes de Développement de L'anisotropie et Suivi in Situ Résolu En Temps, UPMC, 2009.

[13] N. Babak, M.A. El-Sayed, Chem. Mater. 15 (2003) 1957.

[14] M. Grzelczak, J. Perez-Juste, P. Mulvaney and L. M. Liz-Marzan, Chem Soc Rev 37 (2008) 1783.

[15] B. Goris, A. De-Backer, S. Van-Aert, S. Gomez-Grana, L.M. Liz-Marzan, G. Van-Tendeloo, S. Bals, Nano Lett. 13 (2013) 4236.

[16] C. Bullen, M.J. Latter, N.J. D'Alonzo, G.J. Willis, C.L. Raston, Chem. Commun. 47 (2011) 4123.

[17] Y. Song, J. Hormes, C.S.S.R. Kumar, Small 4 (2008) 698.

[18] J. Wagner, T.R. Tshikhudo, J.M. Köhler, Microreact. Technol. IMRET 9 Proc. Ninth Int. Conf. Microreact. Technol. IMRET9 Spec. Issue 135, Supplement 1 (2008) S104.

[19] S.E. Lohse, J.R. Eller, S.T. Sivapalan, M.R. Plews, C.J. Murphy, ACS Nano 7 (2013) 4135.

[20] S. Link, M.A. El-Sayed, J. Phys. Chem. B 109 (2005) 10531.

[21] P.K. Jain, K.S. Lee, I.H. El-Sayed, M.A. El-Sayed, J. Phys. Chem. B 110 (2006) 7238.

[22] Han J., Testard F., Malloggi F., Coulon P.E., Menguy N., and Spalla O., Langmuir 28 (2012) 15966.

[23] B. Nikoobakht, M.A. El-Sayed, Chem. Mater. 15 (2003) 1957.

[24] N.R. Jana, L. Gearheart, C.J. Murphy, Adv. Mater. 13 (2001) 1389.

[25] M. Grzelczak, J. Perez-Juste, P. Mulvaney, L.M. Liz-Marzan, Chem Soc Rev 37 (2008) 1783.

[26] X.-H. Liu, X.-H. Luo, S.-X. Lu, J.-C. Zhang, W.-L. Cao, J. Colloid Interface Sci. 307 (2007) 94.

[27] F. Hubert, F. Testard, O. Spalla, Langmuir 24 (2008) 9219.

[28] N.R. Jana, L. Gearheart, C.J. Murphy, Chem Commun (2001) 617.

[29] Z.L. Wang, M.B. Mohamed, S. Link, M.A. El-Sayed, Surf. Sci. 440 (1999) 809.

[30] M. Liu, P. Guyot-Sionnest, T.-W. Lee, S.K. Gray, Phys. Rev. B 76 (2007) 235428.

[31] C.L. Johnson, E. Snoeck, M. Ezcurdia, B. Rodriguez-Gonzalez, I. Pastoriza-Santos, L.M. Liz-Marzan, M.J. Hytch, Nat Mater 7 (2008) 120.

[32] D. Senapati, A.K. Singh, P.C. Ray, Chem. Phys. Lett. 487 (2010) 88.

[33] G. Zhou, Y. Yang, S. Han, W. Chen, Y. Fu, C. Zou, L. Zhang, and S. Huang, ACS Appl Mater Interfaces 5 (2013) 13340.

[34] I. Lisiecki and A. Filankembo, Phys. Rev. B 61 (2000) 4968.

[35] X. Kou, S. Zhang, C.-K. Tsung, M.H. Yeung, Q. Shi, G.D. Stucky, L. Sun, J. Wang, C. Yan, J. Phys. Chem. B 110 (2006) 16377.

[36] X. Kou, W. Ni, C.-K. Tsung, K. Chan, H.-Q. Lin, G.D. Stucky, J. Wang, Small 3 (2007) 2103.

[37] J. Burgin, I. Florea, J. Majimel, A. Dobri, O. Ersen, M. Treguer-Delapierre, Nanoscale 4 (2012) 1299.

[38] H. Yoo and M. H. Jang, Nanoscale 5 (2013) 6708.

[39] N.R. Jana, L. Gearheart, C.J. Murphy, J. Phys. Chem. B 105 (2001) 4065.

[40] X. Ye, L. Jin, H. Caglayan, J. Chen, G. Xing, C. Zheng, V. Doan-Nguyen, Y. Kang, N. Engheta, C.R. Kagan, C.B. Murray, ACS Nano 6 (2012) 2804.

[41] S. Iijima, T. Ichihashi, Phys. Rev. Lett. 56 (1986) 616.

[42] K. Koga, K. Sugawara, Surf. Sci. 529 (2003) 23.

[43] Z.Y. Li, N.P. Young, M. Di Vece, S. Palomba, R.E. Palmer, A.L. Bleloch, B.C. Curley, R.L. Johnston, J. Jiang, J. Yuan, Nature 451 (2008) 46.

[44] L D Marks, Rep. Prog. Phys. 57 (1994) 603.

[45] C. J. Johnson, E. Dujardin, S. A. Davis, C. J. Murphy and S. Mann, J Mater Chem 12 (2002) 1765.

[46] G.T. Herman, A. Kuba, Discrete Tomography: Foundations, Algorithms, and Applications Series: Applied and Numerical Harmonic Analysis, Birkhäuser Basel, 1999.

[47] B.V. Enustun, J. Turkevich, J. Am. Chem. Soc. 85 (1963) 3317.

[48] C. Lofton, W. Sigmund, Adv. Funct. Mater. 15 (2005) 1197.

[49] G. Wulff, Z.Kristallogr. 34 (1901) 449.

[50] R. Cortes-Huerto, J. Goniakowski, C. Noguera, J. Chem. Phys. 138 (2013) 244706.

[51] H. Hofmeister, Z.Kristallogr 224 (2009) 528.

[52] J. Reyes-Gasga, J.L. Elechiguerra, C. Liu, A. Camacho-Bragado, J.M. Montejano-Carrizales, M. J. Yacaman, J. Cryst. Growth 286 (2006) 162.

[53] A. Howie, L.D. Marks, Philos. Mag. A 49 (1984) 95.

[54] X.J. Xu, Z. Saghi, B.J. Inkson, G. Möbus, J. Nanoparticle Res. 12 (2010) 1045.

[55] J.L. Elechiguerra, J. Reyes-Gasga, J.M. Yacaman, J Mater Chem 16 (2006) 3906.

[56] Y. Xia, Y. Xiong, B. Lim, S.E. Skrabalak, Angew. Chem. Int. Ed. 48 (2009) 60.

[57] C.J. Johnson, E. Dujardin, S.A. Davis, C.J. Murphy, S. Mann, J Mater Chem 12 (2002) 1765.

[58] G. Grochola, S.P. Russo, I.K. Snook, J. Chem. Phys. 126 (2007) 164707.

[59] Y. Niidome, Y. Nakamura, K. Honda, Y. Akiyama, K. Nishioka, H. Kawasaki, N. Nakashima, Chem. Commun. (2009) 1754.

[60] S. Gómez-Graña, F. Hubert, F. Testard, A. Guerrero-Martínez, I. Grillo, L.M. Liz-Marzán, O. Spalla, Langmuir 28 (2011) 1453.

[61] N. Almora-Barrios, G. Novell-Leruth, P. Whiting, L.M. Liz-Marzán, N. López, Nano Lett. 14 (2014) 871.

CHAPTER V

In-Situ Transmission Electron Microscopy Analysis of Gold Nanoparticles to Understand Nucleation and Crystal Growth

CHAPTER V

Chapter 5

In-Situ TEM Analysis of Gold Nanoparticles to Understand Nucleation and Crystal Growth

In previous chapters we have demonstrated that the initial structure and the size of the seeds have vital importance on the determination of the structure of final nanoparticles. In batch synthesis of seeds depending on the surrounding ligand and the reducing agent, one can prepare single or polycrystalline particles at variable size limits which then can grow into single crystalline nanorods or penta-twinned bipyramids. To visualize directly the intermediate stages between the seeds and the final nanoparticles, we take benefit of the recent advances in transmission electron microscopy; liquid environmental cell (e-cell) specimen holder developed for TEM. Liquid cell TEM offers the possibility to probe nanoparticles *in-situ* and to obtain detailed information on how nanoparticles grow in solution.

However, under electron beam, radiolysis of water produces radicals which can interact with the reactants and modify the chemical processes. Such phenomenon has to be considered during *in-situ* TEM analysis. In case of gold, this priori drawback can also be used to control the reaction.

In this chapter, formation of gold nanoparticles has been studied by using *in-situ* STEM. The incident electron beam was chosen to achieve two tasks simultaneously; first, as a radiation source to induce the radiolysis of water (which is responsible for the reduction of gold precursor) and the second, it allows the real time imaging of particles of interest in a thin layer of liquid. In the first part, the influences of the beam parameters and the chemical conditions on the final shape of the particles were described. In the second part, the structure of final nanoparticles obtained by *in-situ* STEM and by γ irradiation source (*at similar chemical compositions*) is compared.

5.1 State of Art

In-situ TEM/STEM, developed over the years, is proposed as a solution to other *ex-situ* methods that limits researchers to visualize the nanoparticle formation in liquid state [1–4]. Even though conventional electron microscopy is used continuously for nanoparticle research, liquid state method was recently developed and applied to many different nanoparticle systems with the production of liquid sample holders for electron microcopy [5–10].

Initial use of the liquid cell windows, for material research, has started with the work of Marton et al. in 1934 with the observation of biological samples between two aluminum foils [11]. Later on technique was adapted to nanoparticle research by Williamson et al. in 2003, with the dynamic observations on growth of copper clusters, trapped between two silicon nitride membranes [12]. Limited resolution of the technique due to large thickness of the membrane window (~100 nm) was improved by Zheng et al. with the development of thinner membranes (~25 nm) which allow researchers to study the growth of platinum nanoparticles in solution [13]. Later, they have used the TEM mode to visualize the complex movements of both spherical (5-15 nm) and rod shape gold nanoparticles (5x10 nm) trapped between thin layer of water (~20-30 nm thickness) +15% glycerol liquid [14]. Additionally, they have studied the growth of Platinum nanoparticles via coalescence and monomer attachment to reveal that initial coalescent growth results in shape re-arrangement in the particle. Such re-arrangement causes a pause in coalescence growth allowing monomer attachment growth to be initiated [13]. Later on, the resolution on this kind of growth observations, was ameliorated by the use of high angle annular dark field scanning TEM mode (HAADF-STEM) by Liao et al. for real time imaging of Pt_3Fe nanorod growth in solution [15]. Latest upgrade to the technique was of course the introduction of the flow cells; allowing to inject the chemical reactants directly in liquid cell to study reaction kinetics [16].

Even though, in-situ TEM technique has various limitations such as potential contamination on sample due to electron beam [10], it also offers multiple advantages over other in-situ methods (*in-situ optical spectroscopy, in-situ AFM and STM*) such as direct observation of structural and morphological transition of nanoparticle in liquid solution. One main interest is certainly the direct observation of the intermediate stages in the solution without any drying stages. For the particular case of anisotropic gold nanoparticles, it can help to obtain experimental data on the isotropic/anisotropic transition directly in the growth media even in the presence of numerous additives.

5.1.1 Radiolysis of Water under Electron Beam

It is already known that, interactions of high energy radiation beam with metal ions are the excitation and ionization of the solvent followed by the formation of various species [17]. When aqueous media is used during the preparation of nanoparticles, the primary reaction is radiolysis of water which generates solvated electrons (e_h^-), hydroxyl radicals ($OH^\bullet$) and hydrogen radicals ($H^\bullet$) [18]:

$$H_2O \longrightarrow e_h^- , H_3O^+ , H^\bullet , H_2 , OH^\bullet , H_2O_2 \qquad (5.1)$$

Among the radicals induced by solvent excitation, e_h^- and $H^\bullet$ are known to be strong reducing agent which may reduce metal ions whereas, $OH^\bullet$ and H_2O_2 are known as strong oxidative species that may trigger the reverse reaction. As the concentrations of radiation products are dose-dependent, relevant interpretation of the complex phenomena observed by liquid-cell microscopy requires a fine control over the electron irradiation.

5.1.2 High Angle Annular Dark Field (HAADF) Scanning Transmission Electron Microscopy (STEM) and Dose Rate

Following experiments have been acquired in scanning mode (STEM) by using the high angle annular dark field detector (HAADF). To be explicit, in conventional STEM mode, the sample is scanned with an extremely convergent electron probe and electrons are collected by different detectors. STEM detectors are generally positioned above the observation screen, collect and amplify the signal generated in any point of the zone scanned by the beam. A computerized acquisition system can reproduce the image point by point. According to its position, a detector can acquire the transmitted beam (*bright field detector*), the scattered beams (*dark field detector*), or the beams scattered at high angles (*HAADF*). The intensity of HAADF images is proportional to $\rho.t.Z^{\alpha}$, where α is a constant ranging between 1.5 and 2; ρ, t and Z, are the density, thickness and atomic number of the material respectively. STEM-HAADF, also known as Z-contrast imaging, is a chemically sensitive imaging which is highly

exciting for the study of the growth of monometallic nanoparticles, since their contrast is then proportional to their thickness.

In electron microscopy, the dose rate (*d*) can be calculated via following equation 5.2 [6,7]:

$$d = \frac{i_e}{eA} \tag{5.2}$$

Here, i_e is the beam current in ampere ($A = C/s$) that can be measured on the phosphorescent screen of the microscope. *A* is the area of the STEM scan ($Å^2$), which in STEM mode advantageously corresponds to the imaged area. e^- is the elementary charge (C/electrons). Then, electron microscopists define the dose rate in *electrons/Å²s*. When STEM-HAADF imaging is performed by using the smallest probe size and the condenser aperture (*in order to minimize and to maintain the constant beam current (i_e) focalized on the liquid-cell*), the dose rate can be easily controlled since it is then inversely proportional to the square of the magnification. Indeed, at lower magnifications the area scanned by the electron beam becomes larger generating a low dose rate in this large area (Figure V.1). In reverse case, when magnification is increased the scanning area is decreased yielding a higher dose regime in a smaller volume. For example, with a beam current of 20 *pA*, the dose rate varies from 0.055 to 1.38 *electrons/Å²s*, with a magnification ranging from 50*k* to 250*k*.

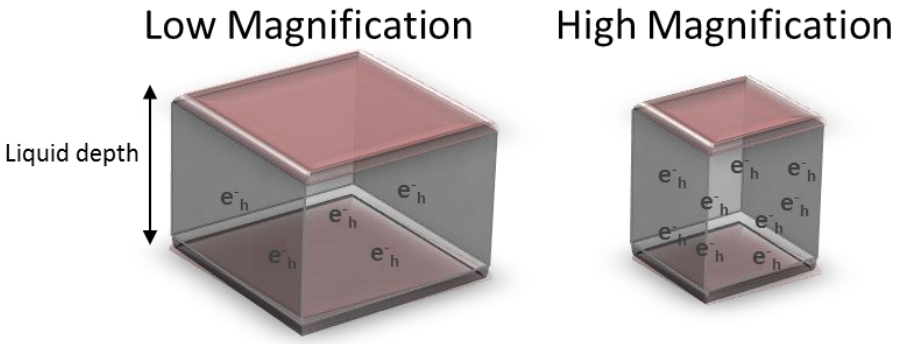

Figure V. 1 *Schematic description of the change in dose rate when changing the magnification*

In comparison to conventional studies on radiolysis (*nuclear reactor, medicine*), the conditions of transmission electron microscopy are quite different. Indeed, the conversion of the dose rate in *Gy/s* (*units commonly used in the field of radiation chemistry*), simply

requires multiplying the dose rate in *electrons/Å^{2}s* by the density normalized stopping power of water (*2.798 10^5 eV.m^2/kg, at 200kV*). This conversion allows realizing the drastic effects of the beam confinement on ionizing radiations. The dose rate associated to the TEM electron beam (*10^6-10^7 Gy/s in our case*) is in average 6 to 7 orders of magnitude higher than the typical dose generated by a common radiation source (*~1 Gy/s*). Recently, Schneider et al. [19] have proposed a kinetic model to calculate the time evolution of the concentration of the radicals produced by water radiolysis under the high dose rate regime of the liquid cell electron microscopy. They have established that the radiolysis products reach a steady state concentration which increase with the dose rate (Figure V.2). We can then conclude that the concentration of radiolysis radical in a liquid-cell TEM experiments is much higher than in conventional radiolysis synthesis.

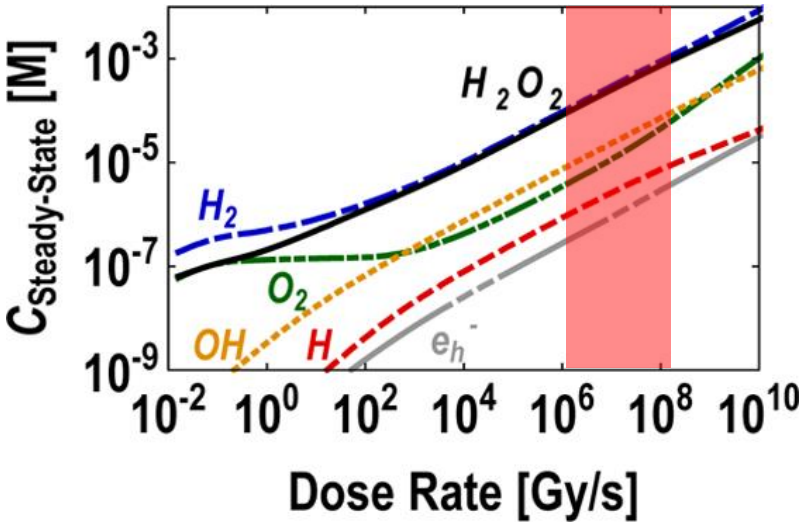

Figure V. 2 *Steady state concentrations of eh$^-$, H•, H_2, H_2O_2, OH•, and O_2 as functions of dose rate (re-produced from [19]). Red highlight is indicating the interval of the dose rate associated in our experimental conditions (*~10^6-10^7 Gy/s*)*

From their model, Schneider et al. [19] have rationalized the effect of the solution composition (*pH and oxygen concentration*), prior to irradiation, on the steady state concentration of the radiolysis product. The particular case of oxygen, known to be a scavenger for hydrated electron, has been fully studied. The Figure V.3 reproduced from their article, illustrates the variation in the ratio of the concentration of different species for aerated and deaerated solution as a function of the dose rate. The important conclusion is the strong dose rate dependence of the molar ratio of radiolysis species below *10^8 Gy/s*. Above *10^8 Gy/s*, this ratio is equal to 1 because the steady state concentration of produced O_2 is higher than

initial saturated O_2 concentration. For such high dose rate ($\geq 10^8$ *Gy/s*), the initial oxygen concentration doesn't have significant impact on the species produced by radiolysis.

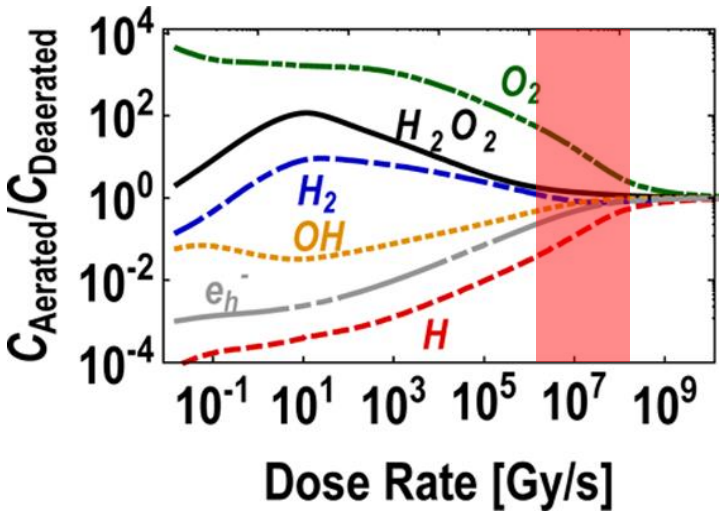

Figure V. 3 *Ratio of aerated to deaerated steady state concentrations of e_h^-, $H^\bullet$, H_2, H_2O_2, $OH^\bullet$ and O_2 (re-produced from [19]). Red highlight is indicating the interval of the dose rate associated in our experimental conditions (*~10^6-10^7 Gy/s*)*

5.1.3 Application to the system of interest: Anisotropic AuNPs

In the following, we have demonstrated the preliminary results on the study of the influence of magnification (*i.e.* dose rate) on the growth of gold nanoparticles in liquid STEM, realized both in aerated and deaerated surfactant media. Given results are obtained in collaboration with Damien Alloyeau at Matériaux et phénèmènes quantiques (*MPQ Laboratory, Université Paris Diderot*). Listed results than compared to conventional radiolysis synthesis of gold nanoparticles, realized in collaboration with Hynd Remita at Laboratoire de Chimie Physique (*LCP, Université Paris-Sud*).

Using the liquid STEM method, for the first time to our knowledge, we were able to image the formation of gold nanoparticles in a CTAB solution. Because of the risk of crystallization of CTAB, in the microfluidic system of the sample holder, we worked with static liquid cells containing the growth solution with the reducing agent L-Ascorbic Acid, known to reduce Au(I) into Au(0) only in the presence of gold surface (*See Chapter I for further explanation*). We take benefit of the high dose rate delivered by the electron beam to

generate gold seeds and follow their formation into larger isotropic or anisotropic nanoparticles.

During the synthesis of nanoparticles in liquid cell two reduction mechanisms occurs in analyzed chemical system:

- *Excess reducing agent (L-Ascorbic acid)*
- *Reduction due to radicals* (e_h^- *and* $H^\bullet$), *induced by radiolysis of water*

5.2 Materials and Methods

5.2.1 Preparation of Growth Solution for *In-Situ* Imaging

Growth solution, employed for *in-Situ* TEM experiments, was chosen regarding to our initial results obtained during batch synthesis of gold nanorods (*See Chapter IV*). Basically, a growth condition (Table V.1) known to produce nanorods only in presence of CTAB capped seeds has been analyzed in the liquid sample holder.

All chemicals are mixed prior to insertion within the microscope. Initial reduction to reduce Au(III) to Au(I) is achieved via L-ascorbic acid, whereas further reduction of Au(I) into Au(0) is performed in the liquid cell. In the first set of experiments no additional treatment is applied on growth solution prior to injection into the liquid cell. In the second set of experiments, similar growth conditions presented in Table V.1, is flushed with Nitrogen for 15 minutes before loading the solution into liquid cell. In all cases, the temperature of the solution before loading the liquid cell is maintained at 30°C to avoid crystallization of CTAB during the preparation of the cell.

Table V. 1 *Chemical Reagents used in the preparation of growth solution for In-Situ imaging*

REAGENTS	**Quantity (mL)**	**[C_{final}] (mM)**
0.05M $HAuCl_4 \bullet 3H_2O$	0.1	0.5
0.01 M CTAB (Cetyltrimethylammonium bromide)	10	10
0.01 M $AgNO_3$	0.045	0.045
0.1 M Ascorbic Acid	0.075	0.75

5.2.2 Loading Growth Solution into Liquid Cell

The liquid sample holder was developed by Protochips Inc. (Figure V.4a) [16]. 7 µL of prepared growth solution is enclosed between a stack of two consumable semiconductor devices called e-chips (Figure V.4b) The small e-chip has a 170 nm thick Si_3N_4 membrane with micro-fabricated 10µm by 10 µm micro-wells. Those 150 nm deep micro-wells are used as reservoirs of the growth solution. The large e-chip has a 30 nm thick Si_3N_4 membrane and used to seal the reservoirs. In situ STEM experiments are performed in this electron transparent static liquid cell (Figure V.4c). Before the deposition of growth solution into micro-wells, plasma cleaning of the e-chips was necessary to eliminate any organic residues on the surface and to create hydrophilic surface. Prior to insertion to microscope, sample holder is first loaded in a pressure control chamber to ensure no leaking of the assembled e-chips. Then, it is introduced into the JEOL ARM 200 F transmission electron microscope operating at 200 kV. This microscope installed at Paris Diderot University is equipped together with a CEOS image corrector and a cold field emission gun.

STEM-HAADF imaging was performed by using the smallest probe size and the condenser aperture to minimize the dose rate.

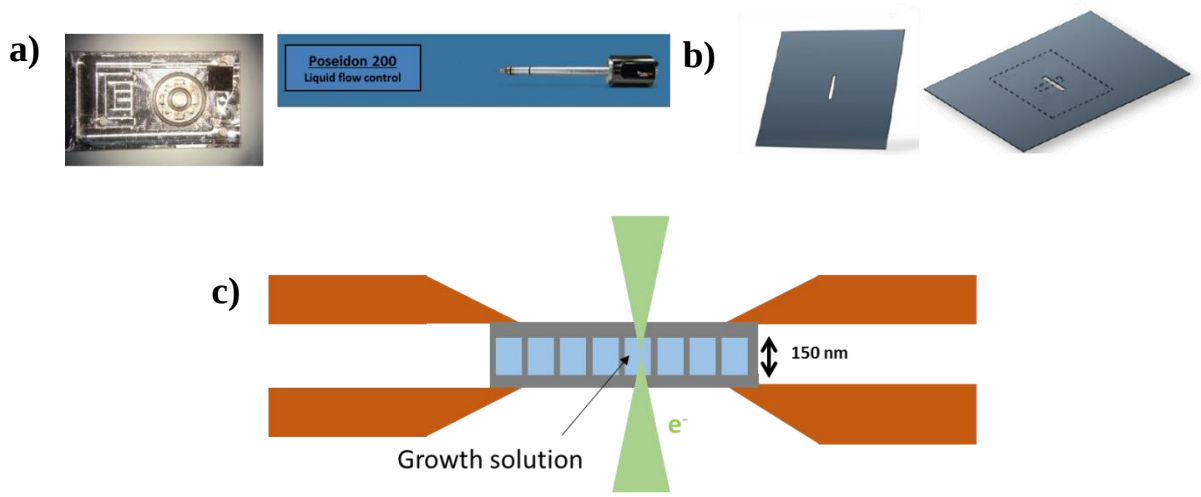

Figure V. 4 *a) Photopgraphs of liquid sample holder b) Schematic representation of e-chips c) Schematic representation of liquid STEM cell design featuring the micro-wells used to contain the growth solution*

5.2.3 Observation Conditions & Calculation of Dose rate

Continuous imaging of the nanoparticle growth were recorded in STEM mode at constant beam current (i_e = *20 pA)* with a *1024*1024* pixel resolution and a dwell-time per pixel of *2* μs. The equivalent dose rate for each set of experiments is calculated in $e^-/s\text{Å}^2$ (Eq. 5.2) and converted into Gy/s units. Results are given in column 3 and 4 in Table V.2 for varied magnifications.

Table V. 2 *Calculation of dose rates for different magnifications*

Magnification (*xk*)	**Area ($Å^2$)**	**Dose rate ($e^-/s/\text{Å}^2$)**	***Dose rate* (*Gy/s*)**
150	$2.47\ 10^8$	0.505	$2.26\ 10^6$
250	$8.90\ 10^7$	1.400	$6.29\ 10^6$
400	$3.48\ 10^7$	3.600	$1.61\ 10^7$
600	$1.54\ 10^7$	8.080	$3.62\ 10^8$

To construct the figures, snap shots of the movies were collected with the time interval of 30 seconds and the particles size analyses were performed by using *ImageJ* software. We systematically subtracted the first image from the following series and adjusted the threshold to remove the unwanted background leaving behind only the particles.

5.3 Results and Discussions

5.3.1 *In-situ* Growth of AuNPs Under e^--Beam

The synthesis of anisotropic gold nanoparticles requires a non-negligible concentration of surfactant. As described previously, nanorods or bipyramids are generally produced in a 0.1M CTAB concentration i.e. 200 times higher than the gold concentration (0.5 mM). High concentration of organic compounds can cause multiple problems for *in-situ* TEM/STEM experiments, including contamination during experimental observations. In Chapter IV, we have detailed the possibility to reduce the concentration of CTAB by a factor 10 and still

produce nanorods, even though obtained particles exhibit more polydisperse sizes with respect to high CTAB concentration. Thus, for liquid cell experiments, 10 mM CTAB concentration is employed to minimize any contamination due to high concentration of surfactant.

During microcopy observations, the nucleation and the growth of nanoparticles mainly occurred in the region stimulated by the initial electron beam (Figure V.5), even though due to diffusion of the radicals produced by radiolysis, formation of some particles has been observed in the surrounding of the irradiation area [7].

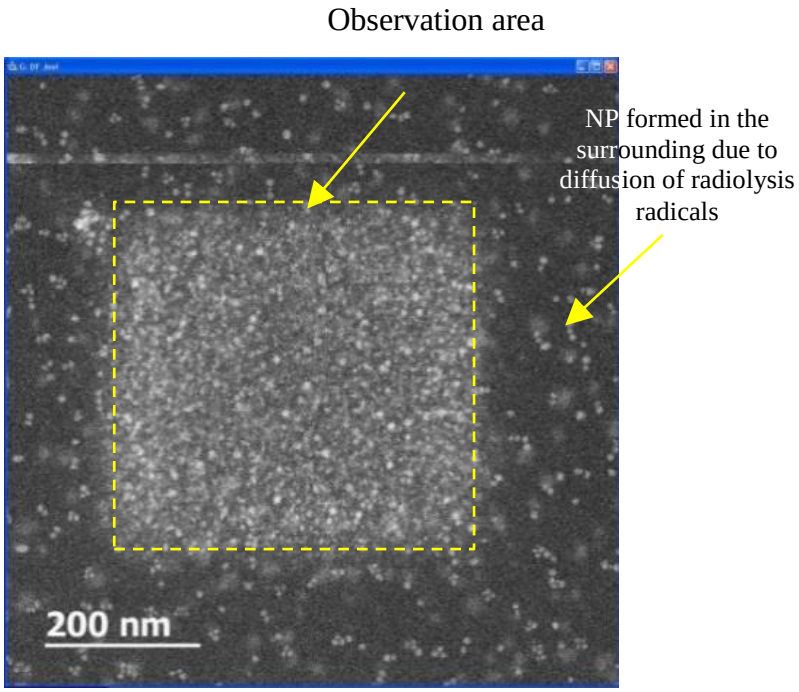

Figure V. 5 *Overview image showing the zone of irradiation*

As stated previously, we have used *in-situ* STEM to initiate and to observe the formation of gold nanoparticles from Au(I)-CTAB precursors in the presence of AA (*in stoichiometric ratio*). Two main studies have been performed with a previously given growth solution (Table V.1) with respect to the presence of O_2 in the reaction media. Mainly, aerated growth presents the solution saturated with oxygen, whereas deaerated experiments is recorded in the initially Nitrogen environment in the absence of O_2.

5.3.1.1 Aerated Growth

A typical time sequential image of growth of gold nanoparticles, initiated by e^- beam in an oxygen saturated environment, is given in Figure V.6. Observed particles are attached to the silicon nitride membrane. Given sequential images correspond to same area ($8.9\ 10^7 Å^2$) of irradiation at magnification of *250k* and a pixel dwell time of *2 µs*. Recording starts with the introduction of e^- beam into the zone of interest at t=2 s (*time for acquiring the first image*). The formation of the nanoparticles is followed during 420 seconds.

In given sequence, small nanoparticles starts to appear at *t*=2s. They continue to increase their dimensions and start to form some isotropic and anisotropic morphologies with continuous irradiation. A zoom in the last figure on the final image clearly shows the formation of both bipyramid and star shapes.

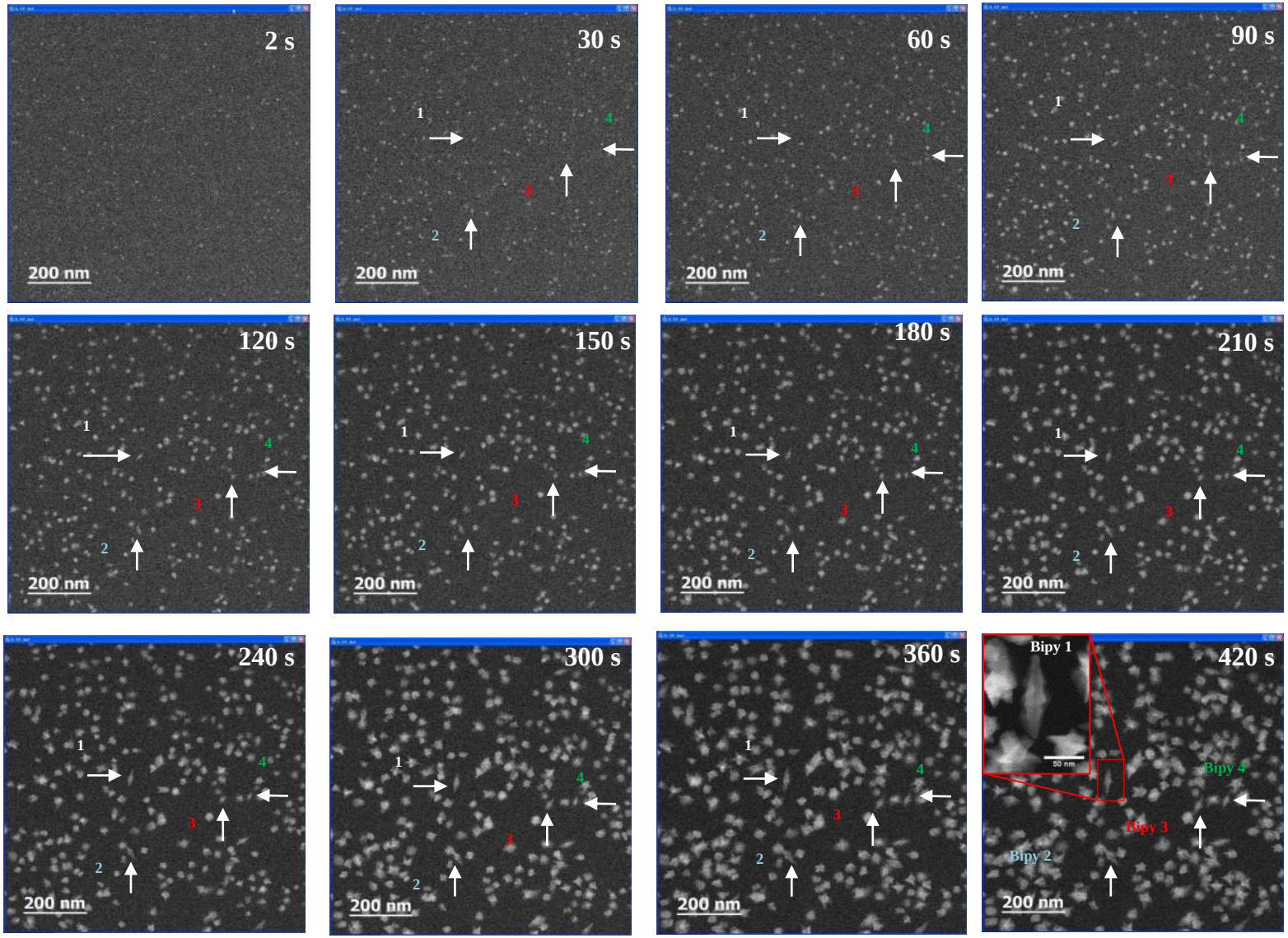

Figure V. 6 *Time resolved sequential images of Au NP growth at magnification 250k and pixel time 2 µS*

Although, it is difficult to have a precise view of the nucleation stage at this magnification, it is possible to detect the growth of nanoparticles with dimension above 7 nm. In particular, we have considered the growth of four bipyramids, marked by an arrow in the time-lapsed series (Figure V.7) and four nanostars (*chosen particles of interest is indicated in the same series in Appendix 4*), starting from 30th seconds of irradiation. Evolution of the average diameter of nanostars-NS, and both dimension of bipyramids-Bipy (*length & diameter*) with time for a given dose rate is shown in Figure V.7a-c. (*For branched and anisotropic structures the diameter is defined through the fit of a spherical circle sketched around the nanoparticle*).

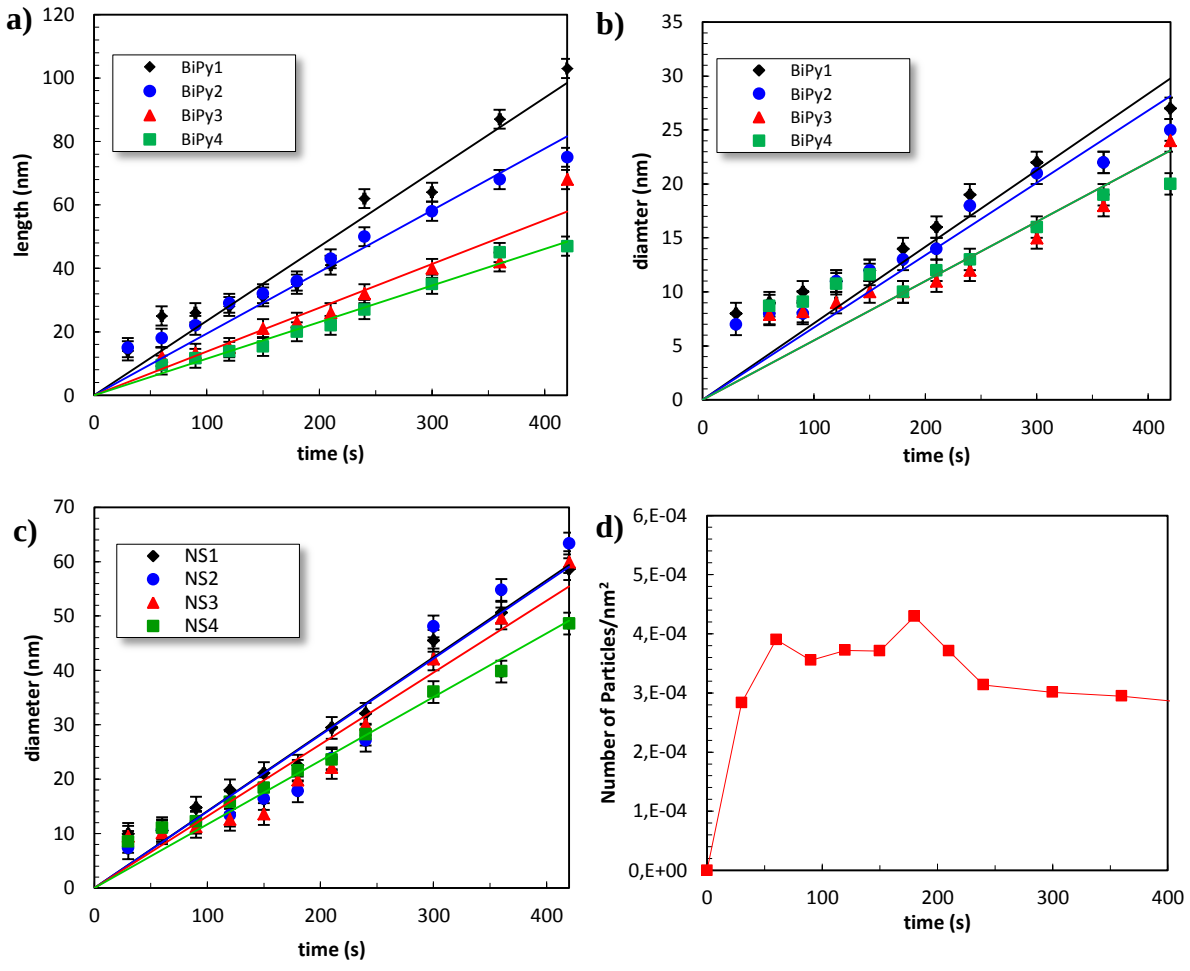

Figure V. 7 *Evolution of a) length b) diamater of four distiguished bipyramids c) diameter of four nanostars with time obtained at dose rate of 1.40 e^-/sÅ^2 d) Variation of the number of particles in unit area (nm^2) with time*

We can remark the linear increase of the length of the bipyramids (Figure V.7a) and the diameter of the nanostars (Figure V.7c). In the case of the bipyramid diameter, this linear increase is mostly is lost, at small sizes (<10 nm), in the beginning of the growth (Figure V.7b). To explain this deviation from continuous increase, the variation of the nanoparticle density (*number of particles per unit area (nm^2)*) in time is plotted and given Figure V.7c. It is probable that, since the initial particles are formed by burst of nucleation, the increase of the diameter at small sizes (<10 nm) is not linear. The growth does not reach to a plateau even after 420 s in particular for the diameter of both bipyramids and nanostars. Even at small sizes, bipyramids bear small elongations, as in the example of Bipy2 (l_{Bipy2}*=14 nm ± 3nm,* d_{Bipy2}*= 7 nm ±1 nm*). At the end of the irradiation, bipyramids are mainly polydisperse in size with aspect ratios found above 2.4 (*AR_{Bipy1}= 3.8, AR_{Bipy2}= 3.0, AR_{Bipy3}=2.8, AR_{Bipy4}=2.4*), meaning that particles exhibit high anisotropies.

Comparison of the structure of two bipyramids obtained through the growth of seeds generated through two different methods a) under electron beam and b) via chemical reduction (*See Chapter IV*) is compared in Figure V. 8. Although, both particles generate sharp tips and pitched external surfaces, bipyramid induced via electron beam exhibits highly tapered surface with multiple corrugations. Structure of larger size bipyramids (*~1µm*), bearing similar morphologies, was described previously by Boya et al. as a pentagonal bipyramid with surface corrugations assignable to high index planes [20].

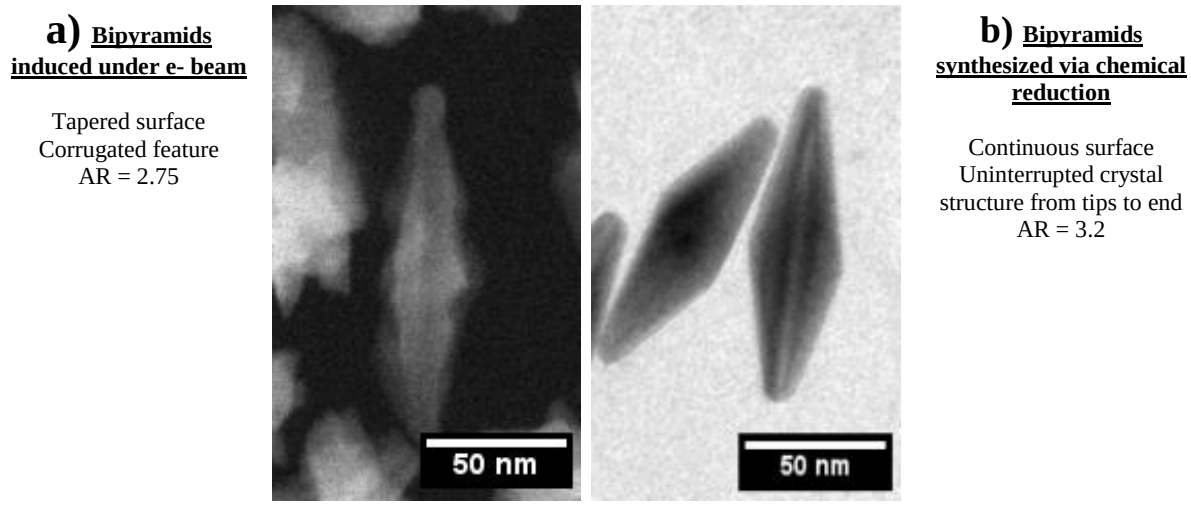

Figure V. 8 *Comparison of bipyramids induced via a) reduction under e^- beam b) chemical reduction*

To go deeper in the understanding of the mechanism, the magnification of the STEM observation used in previous section, were varied to modulate the total dose rate generated during the process. (*Similar chemical conditions were used, as previously given in Table V.1, during preparation of each sample*).

5.4.1.1.1 Effect of Dose Rate on Nucleation and Growth

- **Effect of Dose Rate on Nucleation**

In previous section, we have demonstrated the time sequential series of gold nanoparticle growth in a given magnification (*x250k*) and a dose rate (*1.40* e^-/sÅ^2*)*. We have followed the growth at varied magnifications to observe the direct effect of dose rate on the growth of nanoparticles with time. Basically, the magnification is varied between 150k to 600k at constant beam current (i*= 20 pA*) and pixel dwell time (*2* μs). This corresponds to respectively an increase of the dose rate from *0.505* e^-/sÅ^2 to *8.080* e^-/sÅ^2. Results are represented in Figure V.9 and higher scale figures are reproduced in Appendix 4.

When we look at the first column, which represents the nanoparticles at *t=2 s* at variable dose rates, we see that the particles gain high contrast and become visible mainly at high dose rates (*8.08* e^-/sÅ^2). In case of low dose rates, nearly no particles exist in similar time (*t=2 s*) since, the induction threshold dose for the nucleation is not reach yet. Indeed Woehl at al. [6] have demonstrated that the only criterion for nucleation is that a threshold number of electrons must hit the sample in a maximum amount of time, set by the nanocrystal growth threshold. Therefore if the cumulative electron dose received in 2 seconds is not enough, super saturation will not be achieved and nucleation will not start.

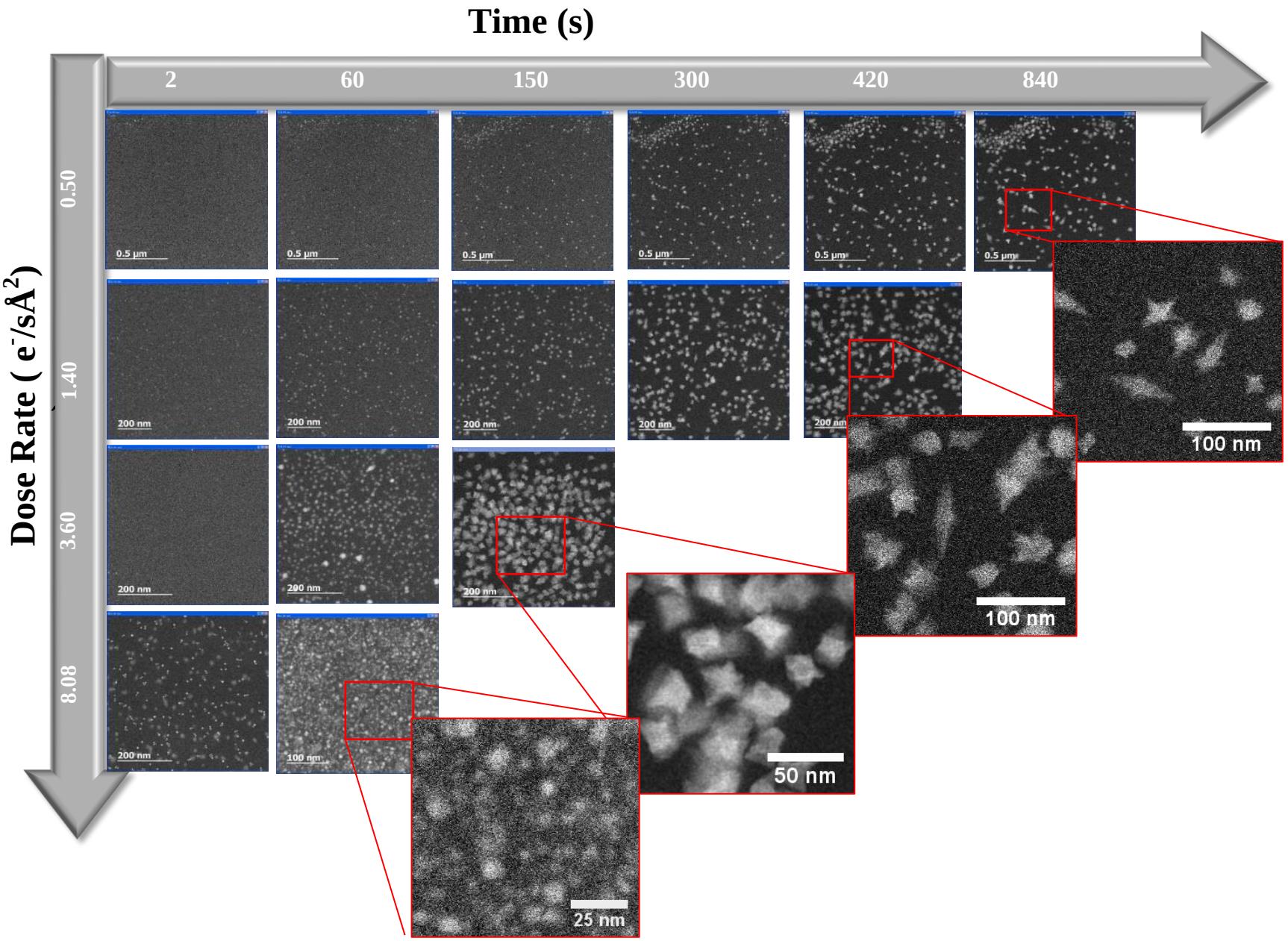

Figure V. 9 *Growth of gold nanoparticle as function of time for variable dose rates at 2 µs pixel dwell time*

Variation of nanoparticle density in time is given in Figure V.10 for varied dose rates. At *t=60 s* NP density reaches *1.29 10^{-5}* for dose rate of *0.50 $e^-/sÅ^2$*. Going to higher dose rates, at *t= 60 s*, result in an increase in NP density (*2.83 10^{-4} and 6.16 10^{-4} for 1.4 $e^-/sÅ^2$ and 3.6 $e^-/sÅ^2$ respectively*). And finally at *8.08 $e^-/sÅ^2$*, area of scanning is highly saturated with huge population of spherical particles (*Number density = 4.20 10^{-3}*). For this observation, record is stopped the since resolution of image is highly reduced due to contamination at this magnification caused by the surfactant. With these results, we can then conclude that higher dose rate is boosting the nucleation of particles resulting in higher density of nanoparticles.

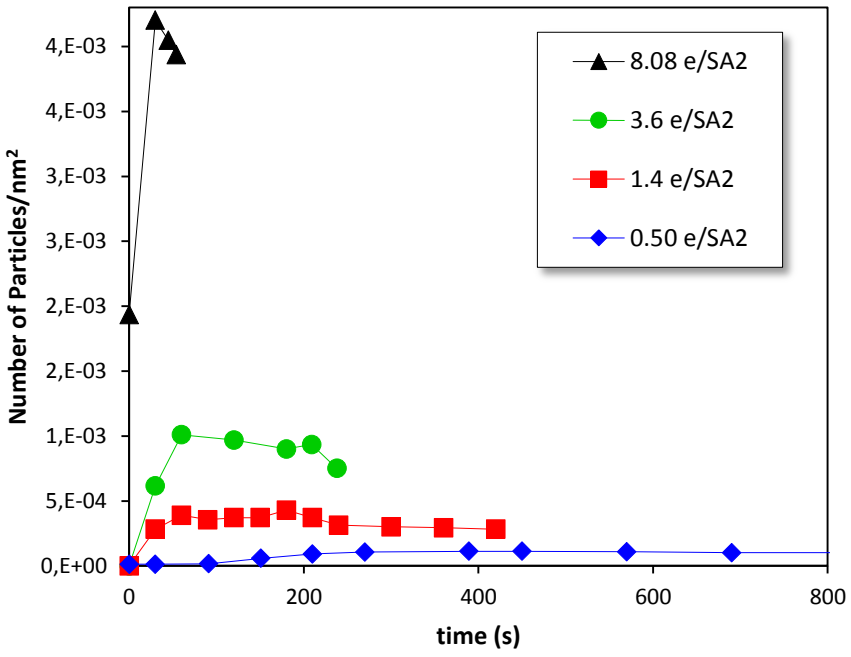

Figure V. 10 *Variation of the total number of particles with time for different dose rates*

- **Effect Dose Rate on Nanoparticle Growth**

In figure V.11, we have plotted the evolution of nanoparticle length with time, for nanoparticles obtained at variable dose rates. In case of *0.50* and *1.40 $e^-/sÅ^2$*, the dimension corresponds to length of the nanoparticle whereas for high dose rates diameter is accounted as the dimension. We can see that the size of nanoparticle varies almost linearly with time. However with increasing dose rate the slope of this linear dependency is also increasing.

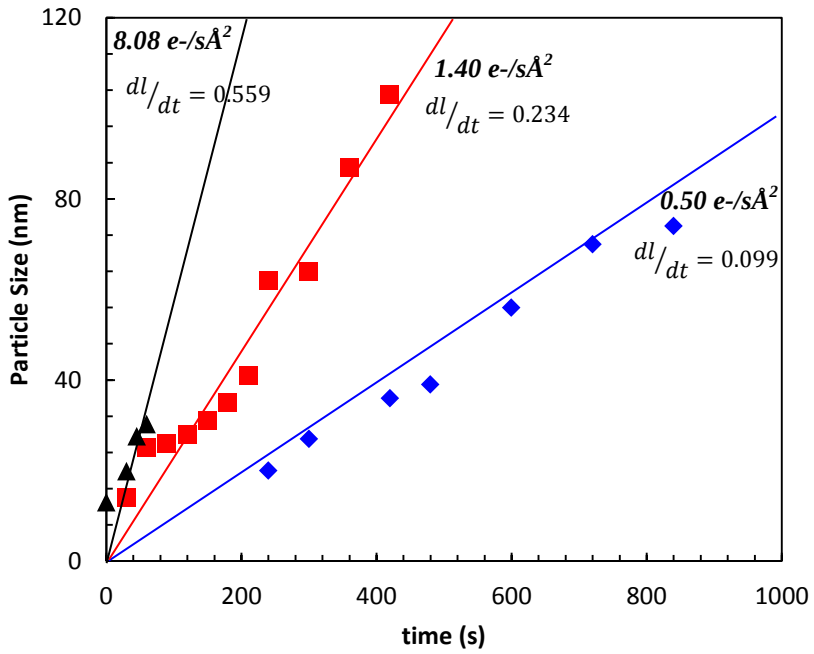

Figure V. 11 *Evolution of particle size in function of time for varied dose rates*

Growth kinetics (*nm/s*) for different dose rates has been determined by the slope of given curves for initial time of growth. Mainly, for high dose rates ($8.08\ e^{-}/s\text{Å}^2$) dimension of the particle increases much more rapidly (*0.559 nm/s*) than low dose rates (*0.099 nm/s for dose rate of 0.50* $e^{-}/s\text{Å}^2$). This faster growth kinetic (*nm/s*) at high dose rate is due to the higher concentration of beam-induced reducing agents (e_h^-, H•) and demonstrate the drastic effects of the optical parameters on the growth of inorganic nanomaterials.

Due to rapid growth kinetic at high dose rates, formed particles exhibit isotropic structures whereas for low dose rates ($\leq 3.60\ e^{-}/s\text{Å}^2$) formed particles exhibit multiple number of branches with sharper tips and few of them start to elongate to form anisotropic bipyramids. Growth of highly anisotropic bipyramid for dose rate of 0.50 $e^{-}/s\text{Å}^2$ is observed at 840 seconds of record *(l = 74 nm, d = 22 nm).* This effect of the dose rate on the shape of the nanoparticles indicates that the formation of anisotropic nanostructures is favored for slow growth kinetic (=*low dose rate*).

Summary of the experiments given in this section over the control of nanoparticle growth by altering dose rate is reported in Table V.4. Principally, at high dose rates many nuclei are generated and then they grow into isotropic nanoparticles due to the fast growth kinetics, whereas at smaller dose rates much less nuclei are generated and then they transform into branched nanoparticles and in some cases tapered bipyramids due to slow growth kinetics. It is remarkable that, those branched nanoparticles and tapered bipyramid shapes were never obtained during *ex-situ* synthesis of gold nanoparticles with chemical reducing agent for the growth conditions given in Table V.1 (*See Chapter IV*). The e_h^- and the other radicals produced by the water radiolysis have certainly a predominant effect during *in-situ* synthesis of gold nanoparticles, resulting in much faster growth kinetics.

Table V. 3 *Summer of obtained nanoparticle morphology and size for given magnification and dose rates*

Sample	***Magnification (xk)***	***d*** $(e^-/s/Å^2)$	***d (Gy/s)***	***Number of Particles/nm^2 (at t=60 s)***	***Growth kinetics-dl/dt (nm/s)***	***Final Morphology***
1	150	0.505	$7.21\ 10^{6}$	$1.5\ 10^{-5}$	$0.9\ 10^{-1}$	Nanostars/ Bipyramids
2	250	1.400	$2.00\ 10^{7}$	$3.9\ 10^{-4}$	$2.3\ 10^{-1}$	Nanostars/ Bipyramids
3	400	3.600	$5.13\ 10^{7}$	$1.0\ 10^{-3}$	$2.6\ 10^{-1}$	Nanostars
4	600	8.080	$1.15\ 10^{8}$	$3.9\ 10^{-3}$	$5.6\ 10^{-1}$	Nanostars

Better STEM images of the bipyramids, formed during the *in-situ* STEM experiments, were captured after the evaporation of the solvent and are given in Appendix 4.

5.3.1.2 Deaerated Growth

It is known that for low dose rates, the amount of oxygen in the initial solution can interplay with the electrons and change completely the reactions. We have studied this particular effect by reproducing the reaction with a fully deaerated solution (*i.e. in the absence of O_2 in the reaction environment*). The object of this study is to understand the effect of O_2 on the growth of nanoparticles.

Growth solution is flushed with Nitrogen, for *15* minutes, to make sure maximum amount of oxygen is removed. Given results are the representatives of preliminary experiments. In Figure V.12 evolution of the zone of irradiation with time at magnification of *x250k* and dwell time of *5 µs* is shown for a deaerated solution (*We have started the irradiation in this experiment in Zone 1. After the formation of initial NPs in this zone, the beam is shifted towards to Zone 2, to capture the nucleation of the freshly formed NPs. In this way both the generation of new particles and the growth of previously formed NPs was captured in the same screen).*

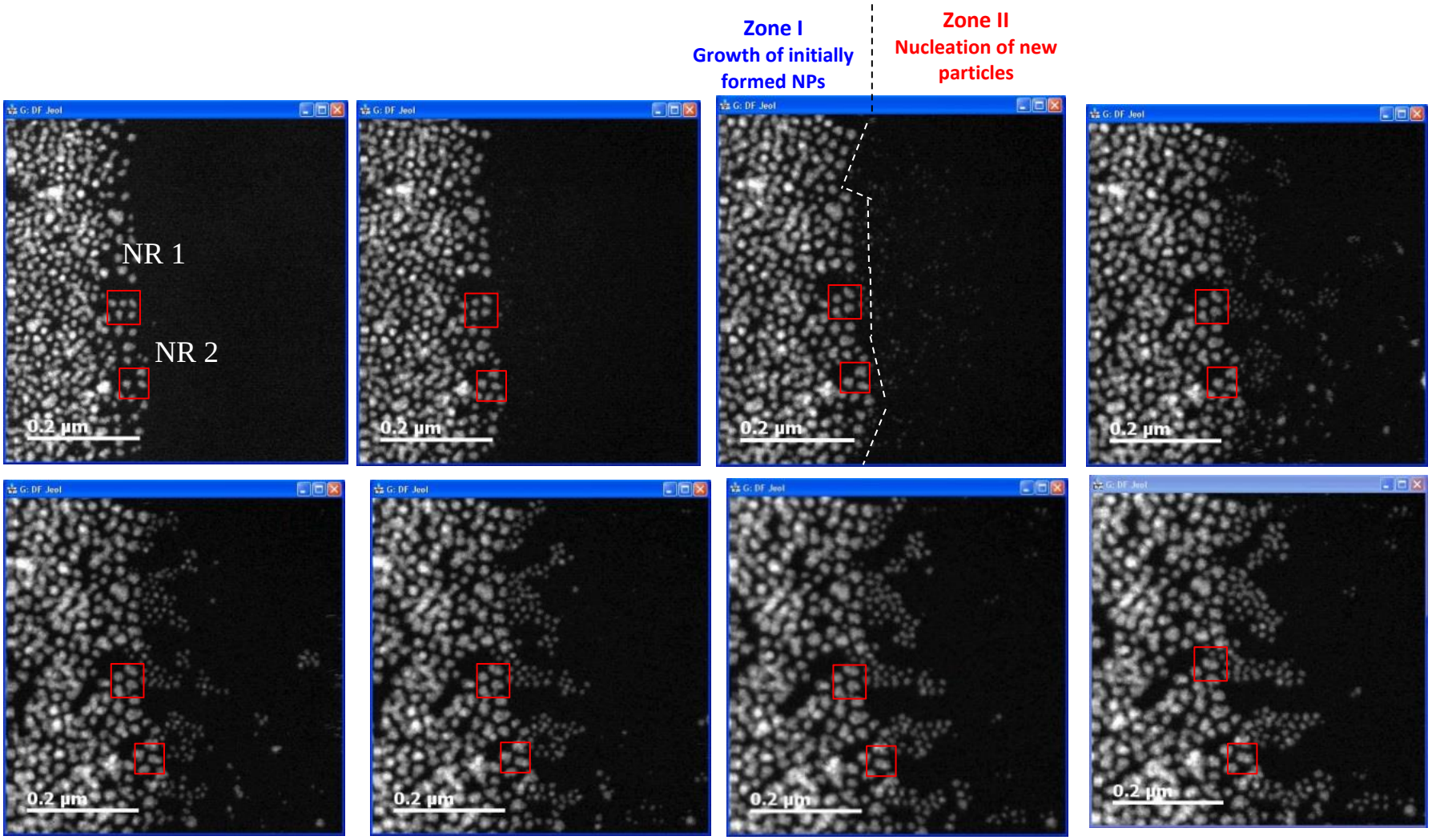

Figure V. 12 *Growth of initially formed particles with nucleation of newly created crystals at magnification of x250k and dwell time of 5µs (t_{elapse}= 30 seconds)*

Two types of events occur simultaneously in the scanning area. First in Zone 1, previously formed nanoparticles increase their sizes, under continuous irradiation, by monomer attachment. When the particles become too close to each other, they start to coalesce with neighboring NPs. Second, in Zone 2, the nucleation and the growth of freshly formed nucleus, by monomer attachment, can be seen.

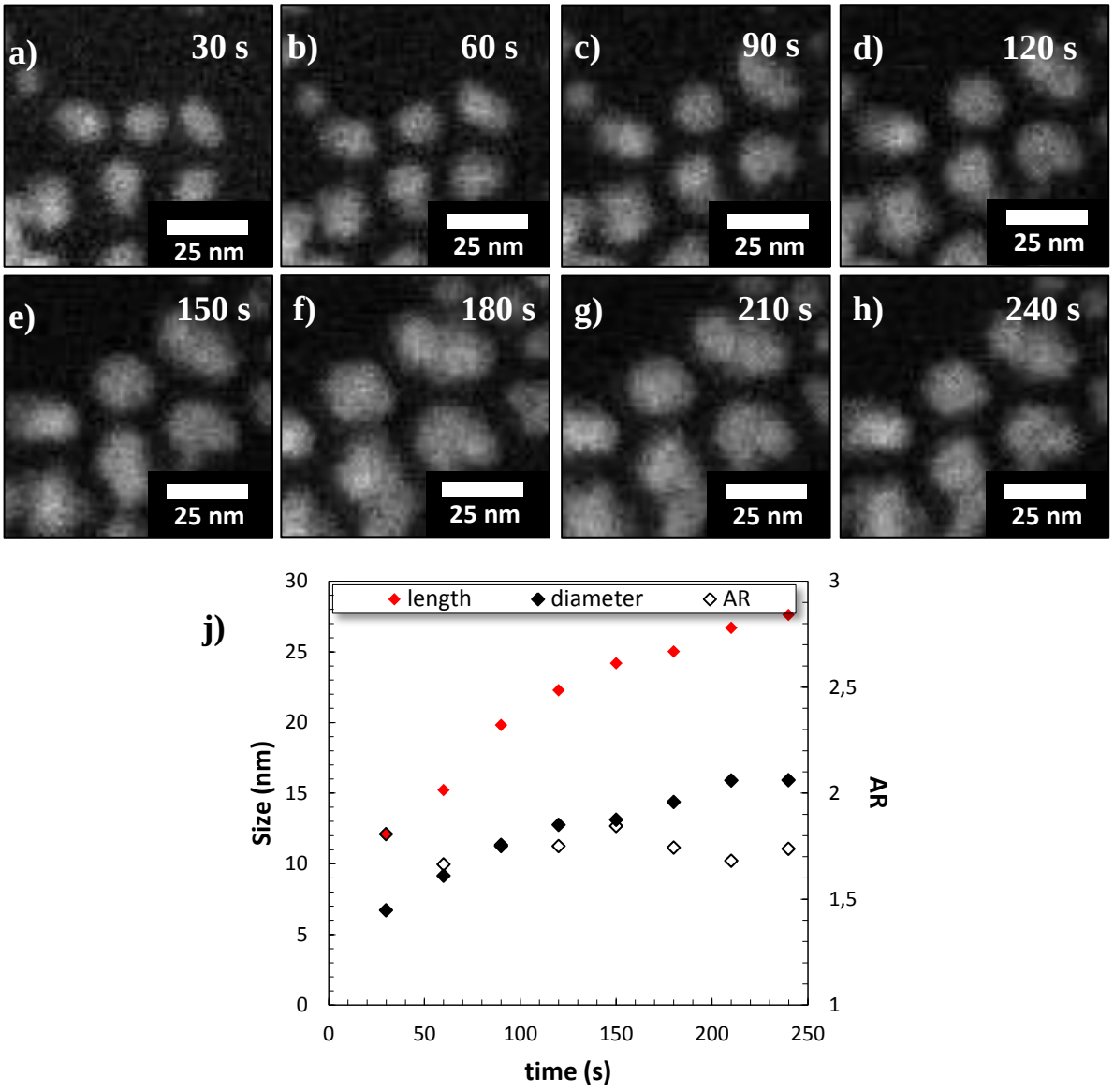

Figure V. 13 (a-h) *Formation of elongated NP under e beam;* ***(j)*** *Evolution of size and aspect ratio with time for given particle*

Growth of some elongated NPs found in Zone I is analyzed, with respect to the evolution of its length, diameter and aspect ratio in time and given in Figure V.13. Given nanoparticle at *t=2* already exhibits anisotropy with an AR of 1.8. For both dimension by the slopes of the given curves we have found that the length is increasing in higher speed (*with an order of 1.74*) than the diameter in the beginning stage of the reaction (until 90 s) and then the ratio remains constant. Controlled growth of the nanoparticle continuous until the environment is saturated and when the neighboring NPs become too close, particles start to agglomerate with surrounding NPs.

One remarkable feature occurring, for the samples without O_2, is that on e-ship many nanorods with well-defined structures are also observed, even though, their growth is not directly visualized (Figure V.14*a*). Two nanorods formed under e^- beam with an aspect ratio of 2.9 and 1.9 is given in the same figure with higher magnification showing that particles are single crystalline (Figure V.14*b-c*).

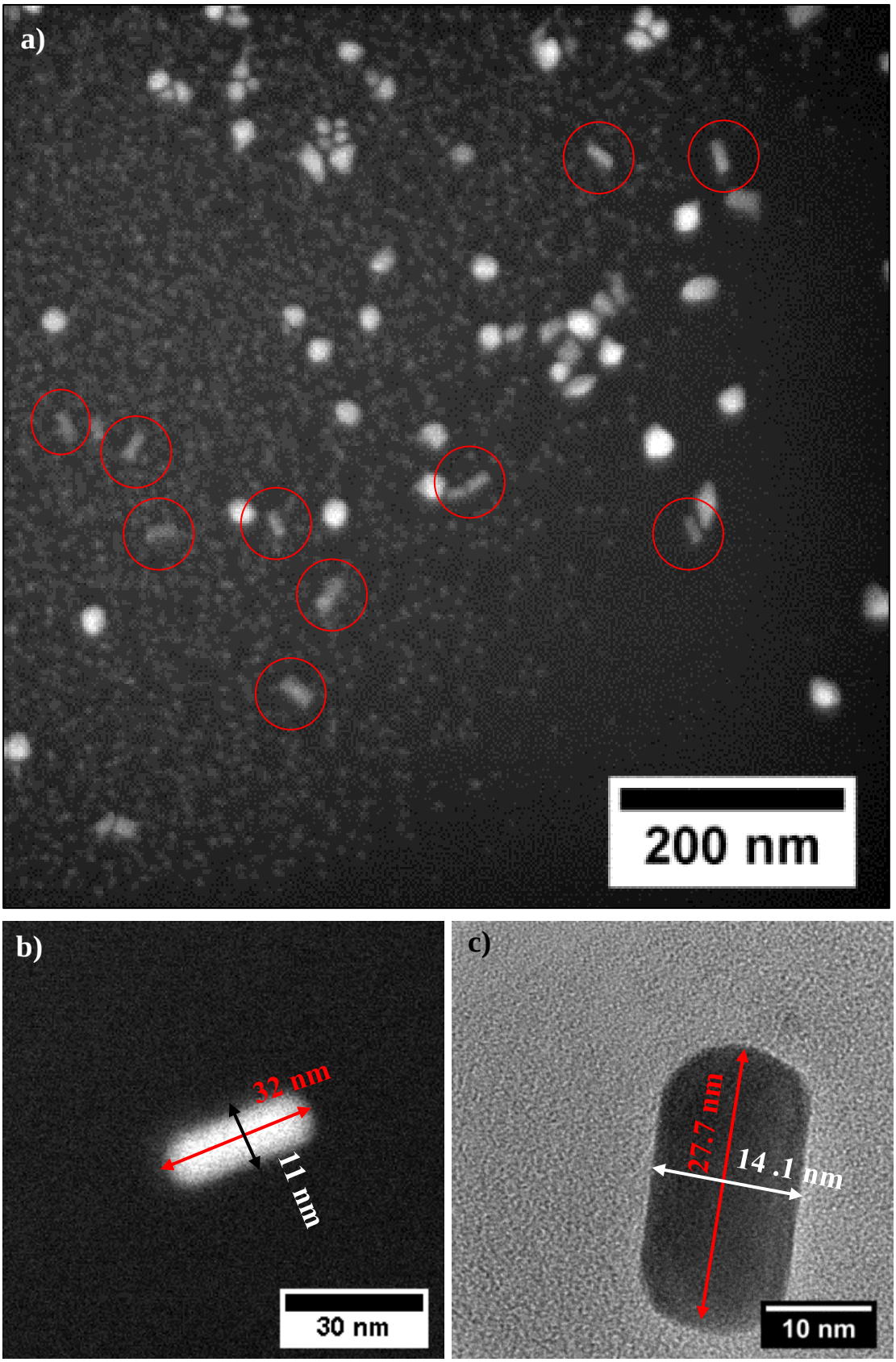

Figure V. 14 *Final nanorods found in the membrane showing single crystal structure*

To sum up, in case of deaerated experiments, the main observed difference is the final structure of the nanoparticles in comparison to the aerated case. In case of aerated experiments mainly branched structures are observed forming additionally some bipyramidal particles, whereas in deaerated experiments, particles are spherical with additional single crystalline nanorods. No branched nanoparticles are observed in this condition.

5.3.2 Synthesis of Gold Nanoparticles via Radiolysis

The formation of gold nanoparticles via radiolysis has been described in detail by various groups [17]. In this method, gold nanorods are obtained with the aspect ratio range of *1.7-5.2* and their formation is generally achieved by the complex growth solutions. Few examples, including only four component growth solution (*0.01 CTAB, 0.045 mM $AgNO_3$, 0.5 mM $HAuCl_4$ and 0.75 mM AA*) rather than complex systems can be found. Remita et al. [17] have produced gold nanorods, from a growth solution made of CTAB, TOAB, $HAuCl_4$, acetone, cyclohexane, $AgNO_3$, starting from Au(III) precursor after *14* hours of irradiation at *2.3 kGy/h*. Biswal et al. [21] have obtained slight number of nanorods, by adding as-synthesized seeds in a simpler compositional growth solution (*CTAB, $AgNO_3$, $HAuCl_4$, isopropanol*) under low dose rate irradiation (< *0.8 kGy/h*), without introducing further characterization of final nanorods. Finally, Hori et al. [22] have produced some nanorods from the irradiation of a growth solution containing *CTAB + $HAuCl_4$ + $AgNO_3$ +AA + H_2SO_4* under variable dose rates (*0.4-13.6 kGy/h*). They have concluded that higher anisotropy is attained at elevated dose rates, even though; final nanoparticles again, are not well characterized.

Additional to the e^--beam induced formation of gold nanoparticles by *in-situ* STEM, we have performed some classical radiolysis experiments to compare our initial results. Similar type of growth solution (*composition defined previously in Table V.1*), is irradiated for 13 minutes by using ^{60}Co panoramic Gamma irradiation source at dose rate of *8.6 10^1 Gy/s*. (*The growth solution is flushed by argon during 5 minutes prior to their irradiation and UV-Vis Spectra is taken 10 minutes after termination of irradiation).*

UV-Vis spectra of the final solution, shown in Figure V.15, exhibits two well separated distinct plasmon peaks, T-SPR (~ 520 nm) and L-SPR (745 nm) which is characteristics of

anisotropic shapes. Even though the intensity of T-SPR is higher than L-SPR, meaning that high yield of nanorods is not achieved shortly after irradiation (10 minutes), AR of nanorods can be deduced as 2.7 via simple relation between the absorption maximum of L-SPR (λ_{max}) and the aspect ratio (*See Chapter II*).

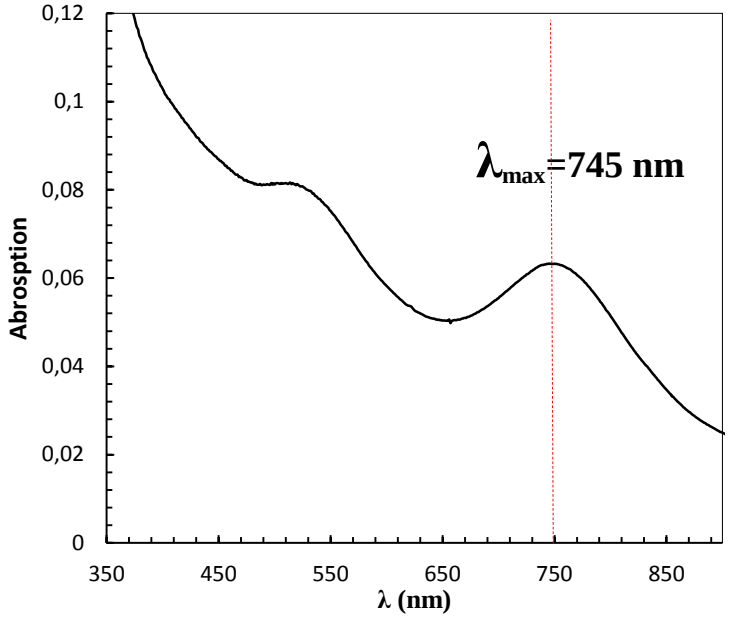

Figure V. 15 *UV-Vis Spectrum gold nanorods obtained directly after 13 minutes radiolysis*

The sample was purified 24 hours after the synthesis via one step centrifugation (8440 g, 20 min). TEM image of the same sample, after purification, is given in Figure V.16a. Microscopy results reveal that sample contains high yield of monodisperse nanorods (*with an average AR of 2.8)*, exhibiting well alignment on the carbon support. Even though the sample is largely purified from isotropic NPs, the final nanorods are still slightly polluted by isotropic NPs as it can be seen clearly in *L,D* plot given in Figure V.16c. The large difference between the UV spectrum (*showing strong T-SPR signal of isotropic shapes*) and TEM images (*exhibiting largely anisotropic nanorods*) can also be explained by the fact that growth of nanorods has not terminated shortly after the radiolysis experiments and nanorods continue to increase their yield after the irradiation, probably because of the AA present in the solution.

HRTEM image of a final nanorod, exhibiting single crystalline structure, is demonstrated in Figure V.16b.

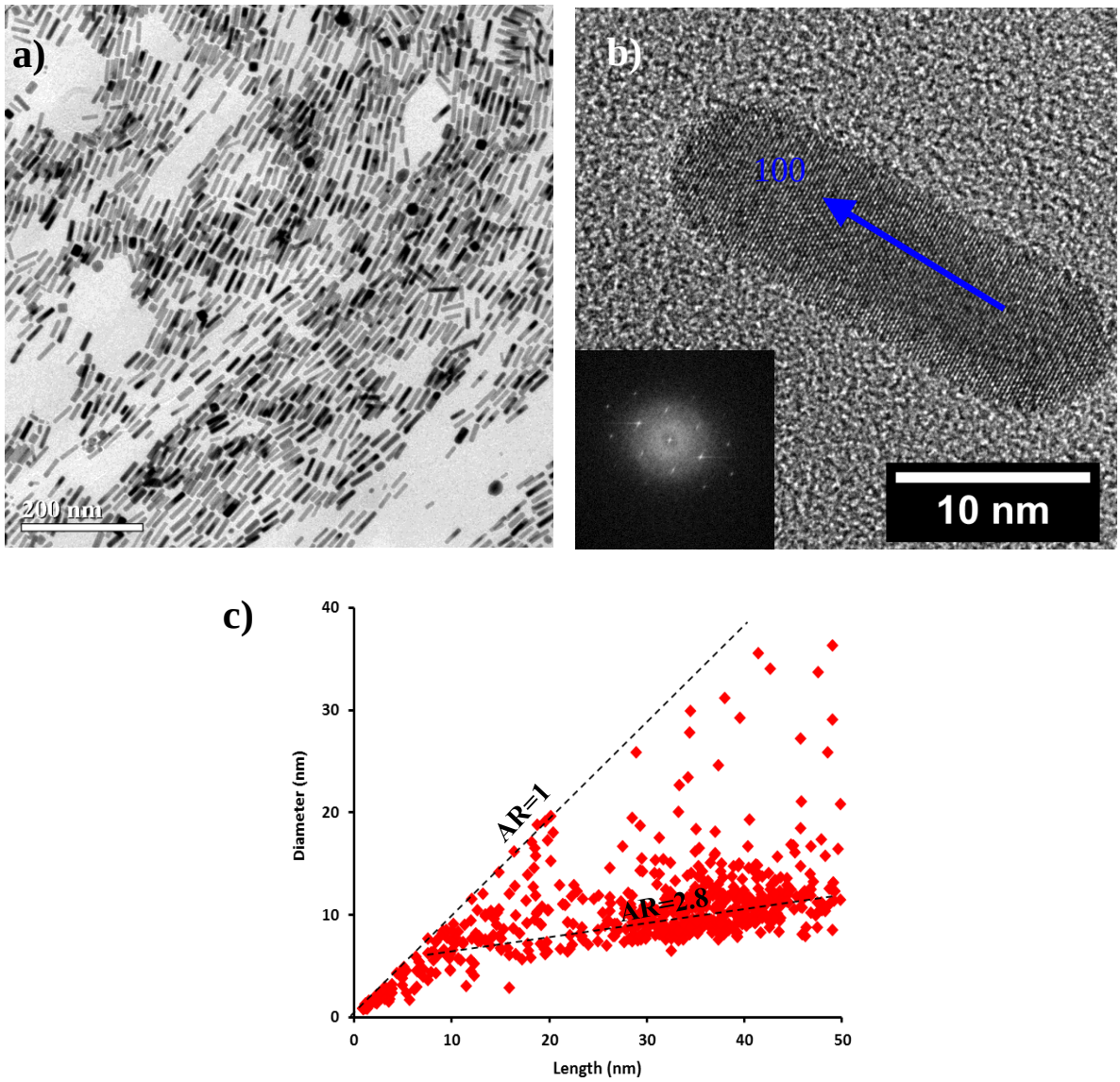

Figure V. 16 *a) TEM image of the gold nanorods obtained by radiolysis with exposure time of 13 minutes and the dose rate of 8.6 10^1 Gy/S b) HRTEM image of a single nanorod oriented in 100 direction, exhibiting single crystalline structure c) L,D plot of corresponding sample*

It is remarkable to attain such monodispersity with radiolysis *i*) in the absence of added seeds *ii*) for a growth solution with very simple chemical composition and *iii*) with small time of irradiation.

This is the first time that so well defined and monodisperse nanorods are produced under radiolysis conditions with simple chemical conditions. Synergism obtained from the combination of the chemical reducing agent (AA) and the radiolysis induced reducing agents is needed to synthesize large number of nanorods.

In radiolysis experiments, isopropanol or formate is added to scavenge oxidizing species and acetone is added to scavenge the electrons. In our growth experiments, the effect of acetone, on the final nanoparticles, has also been studied by adding 2 mL acetone in a similar growth solution given before (Table V.1). During formation of nanorods with radiolysis, in the presence of acetone, entirely different reactivity has been observed. Mainly, the reduction of Au(I) started immediately after the addition of acetone, probably because of the disparities of the CTAB micelles in the acetone/water media or the change in the formation of the CTA-gold or silver complexes. The redox potentials in this case, are modified and the chemical reactions are different.

If we compare, both radiolysis experiments and *in-situ* experiments performed in absence of initial O_2, we see that both methods produce gold nanorods even though the performance of production varies vastly due to large difference in dose rates (Table V.5). The dose rate associated to conditions used *in-situ* TEM experiments in previous section is 5 orders of magnitude greater than the dose rate generated by ^{60}Co radiation source.

Table V. 4 *Comparison of final nanoparticle morphology for in-Situ and Radiolysis Experiments*

	In-Situ* TEM** ***Dose rate (2.26 10^6-3.62 10^8 Gy/s)		**Radiolysis** *Dose Rate =8.6 10^1 Gy/s*
	With O_2	**Without O_2**	**Without O_2**
Final Morphology	Branched Nanoparticles / Bipyramids	Spherical Nanoparticles with minority of nanorods	Nanorods/Spherical and Cubic particles

5.4 Discussions

As stated previously, in *in-situ* TEM growth of gold nanoparticles, the incident electron beam is designed to achieve two tasks simultaneously; *i*) as radiation source responsible for reduction of gold precursor and *ii*) real time imaging of particles of interest in a thin layer of liquid. However, for previously described chemical system (Table V.1) the number of complex equilibrium reactions between the reduction and the oxidation of Au precursor should be taken into account for further interpretation.

- *Reduction Reactions*

Hydrated electrons (e_h^-) and the hydrogen radicals ($H^\bullet$), created by the radiolysis of water, play an important role during the formation of nanoparticles. Those reagents works synergistically as strong reducing agents to induce following chemical reactions:

$$Au^I + e_h^- \rightarrow Au^0$$

$$Au^I + H. \rightarrow Au^0$$

The produced Au(0) is the origin of the formation of the seeds in the growth solution. Following growth can be obtained later by both *i*) reduction by e_h^- and $H^\bullet$ and *ii*) reduction by mild reducing agent (*ascorbic acid*) which could only reduce CTA-Au^I into CTA-Au^0 in the presence of gold surface (*generated by previously described reactions via e_h^- and $H^\bullet$*).

- *Oxidation Reactions*

Between the radicals generated by the radiolysis of water (e_h^-, H_3O^+, $H^\bullet$, H_2, $OH^\bullet$, H_2O_2), $OH^\bullet$ is known to be a strong oxidizing agent especially when high concentration of Br^- is present in the solution (*CTAB*). These hydroxide radicals react with Br^- leading to the formation of Br_2^- and Br_3^-/Br_2. Those formed species are also oxidative and can cause a reverse oxidation of the gold low valence ions or atoms. At the end, Au^I can disproportionate into Au^0 and Au^I on the gold nanoparticle. Additionally, Au^{II} can also disproportionate into Au^{III} and Au^I. One of the strong advantages to work with a lower CTAB concentration (*0.01 M*) is the possibility to avoid these unfavorable reactions.

- *Growth Mechanism of Formed Nuclei into Final Nanoparticles with O_2*

For experiments including O_2 in the growth media, the phenomena behind the formation of anisotropic bipyramids and branched NPs (*for low dose rates*) can be explained by multiple mechanisms.

We can compare it with the growth mechanisms of the batch synthesis of gold nanoparticles via chemical reduction, in the presence of strong a reducing agent (i.e. $NaBH_4$) and excess AA. It is known that branched nanoparticles can easily be obtained with chemical reduction; by decreasing the initial Au^{1+} concentration and increasing the AA in a similar type of growth solution given in Table V.1 [23]. Mainly, at low dose rate, the situation would be comparable to the case where slight amount of strong reducing agent is added to the growth solution. In such a case, small amount of Au(I) is reduced into Au(0) which further aggregates to form stable nuclei. Only limited numbers of initial nuclei are formed due to deficiency of strong reducing agent. Then the remaining Au(I) is slowly reduced on the surface of these few nuclei by the ascorbic acid and by the radicals induced by radiolysis during *in-situ* STEM experiments. Slow growth kinetics caused by low dose rate, provokes the formation of branches on the surface of limited number of seeds and sometimes leads to elongated bipyramidal shapes (Figure V. 17*b*).

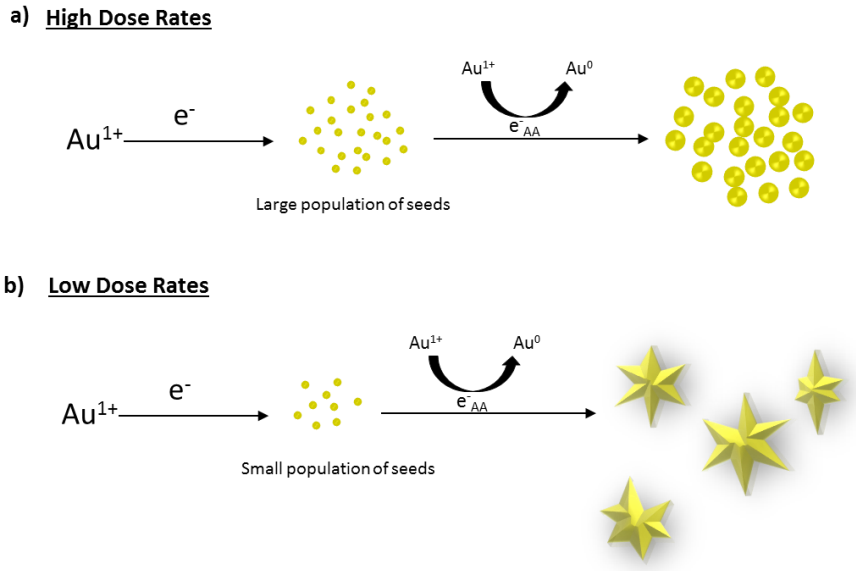

Figure V. 17 *Scheme illustrating the formation of NPs under e^- beam for different dose rates*

On the contrary, at high dose rates, the situation would be analog with the addition of a high concentration of strong reducing agent into the solution. A large number of Au(0) is formed due to burst of nucleation due to high amount of reducing agent in the reaction media (Figure V. 157*a*). In this case, the nucleation rate increases as the size of the first stable nuclei decreases. Growth of large number of nuclei will be rapid due to constant illumination at high dose rates, leading to the formation of isotropic shapes (in this case growth probably does not proceed through AA reduction).

Finally in the intermediate dose rates, modest numbers of nuclei are formed. Average growth rate of nucleus (*due to medium growth kinetics*) occurs by both process simultaneously; feeding of the particle by initially reduced Au(0) and by the surface catalyzed reduction of Au(I) into Au(0) on the growing nanoparticles. In this case less elongated branched nanoparticles are formed.

- *Growth Mechanism of Formed Nuclei into Final Nanoparticles Without O_2*

In case of deaerated experiments, radiolysis has crucial importance since, removal of molecular oxygen (O_2), known as a scavenger for hydrated electrons, results is drastic increase in the concentration of hydrated electrons [17,19,24]. To explain the growth in such complex condition, we should readdress to the graph given in Figure V.3 (*Figure V.2 is reproduced as Figure V.18*).

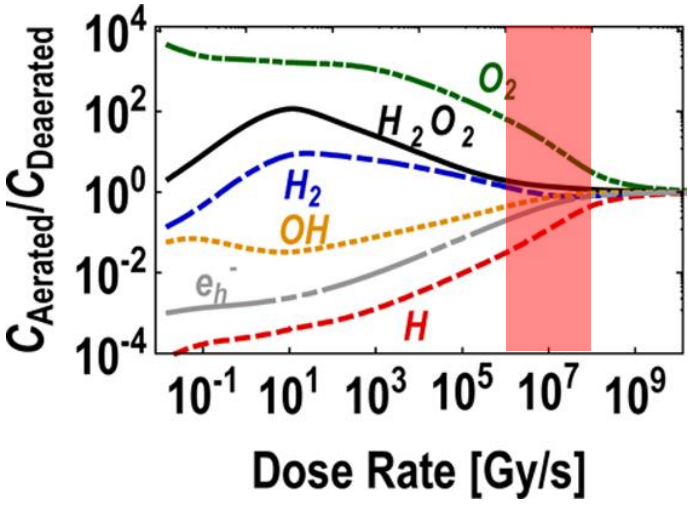

Figure V. 18 *Ratio of aerated to deaerated steady state concentrations of e_h^-, $H^\bullet$, H_2, H_2O_2, $OH^\bullet$ and O_2 (re-produced from [19]) presenting the range of dose rate used during our in-situ STEM experiments (10^6-10^8Gy/s)*

If we consider the dose rate of 6.3 10^6 *Gy/s*, for performed *in-situ* STEM experiments (*where the concentration of radiolysis species shows strong dependence to dose rate*), and the figure V.18, we see that the ratio between aerated and deaerated concentration of reducing radiolysis species is below one. Presence of high concentration of hydrated electrons (e_h^-), due to radiolysis without initial O_2, results with the formation of large number of seeds and lead to rapid growth into isotropic nanoparticles.

If we compare given experiment with the bulk radiolysis synthesis of nanoparticles, the only difference would be the dose rate. It is probable that in radiolysis, the limited numbers of hydrated electrons do not permit to obtain large number of seeds and their growth, into anisotropic shapes, continue by the autocatalytic AA reduction on the surface of the pre-formed seeds even after the irradiation is terminated. In *in-situ* STEM, the number of reducing species is higher so a few nanoparticles can develop anisotropic growth by the autocatalytic process.

Finally, different final states between the aerated and the deaerated experiments are probably due to different crystal structure of the initially formed seeds. Even though multi-twinned seeds would be expected for aerated experiments (*where major final shape being nanostars or bipyramids*) and the single crystalline seeds for deaerated case (*where mainly spherical nanoparticles and some nanorods are formed*), such point needs to be verified by further HRTEM analysis.

5.5 Conclusion

For the first time to our knowledge, gold nanoparticle growth was initiated and captured by e^--beam in relatively high surfactant concentration (0.01 M CTAB) by using *in-situ* STEM. Here, we have demonstrated a successful control over the growth of gold nanoparticles by varying only the electron beam parameter (*magnification*). *In-situ* formation and growth of seeds is realized by following complex chemical reactions generated in solution *i*) the reduction by hydrated electrons, continuously produced by radiolysis under e^--beam *ii*) the reduction by ascorbic acid catalyzed by the gold surface.

Regarding the difference in the shape of the nanoparticles in function of the magnification (*i.e. the dose rate*), we can propose that at low dose rate, few number of

produced seeds are able to grow into branched nanoparticles due to slow kinetics, caused simultaneously by slow ascorbic acid reduction at the surface of the nanoparticles and low number of radicals induced by electron beam, while at higher dose rate, the concentration of strong reducing agent is so high that the alimentation of the seeds will certainly proceed initially by fast feeding by pre-reduced Au(0) due to aqueous electrons and strong reducing agent and the slow feeding due to ascorbic acid reduction at the surface of the particles. This can explain why no pyramids are obtained with increasing the dose.

Note that the presence of O_2 in the reaction media plays an important role during the reduction of gold precursor. These chemical reagents act as scavengers for aqueous electrons, which directly alters the morphology of the final nanoparticles.

5.6 References

[1] C. Mueller, M. Harb, J.R. Dwyer, R.J.D. Miller, J. Phys. Chem. Lett. 4 (2013) 2339.

[2] Y. Liu, X.-M. Lin, Y. Sun, T. Rajh, J. Am. Chem. Soc. 135 (2013) 3764.

[3] T. Kraus, N. de Jonge, Langmuir 29 (2013) 8427.

[4] T.J. Woehl, C. Park, J.E. Evans, I. Arslan, W.D. Ristenpart, N.D. Browning, Nano Lett. 14 (2013) 373.

[5] A. De Clercq, W. Dachraoui, O. Margeat, K. Pelzer, C.R. Henry, S. Giorgio, J. Phys. Chem. Lett. 5 (2014) 2126.

[6] T.J. Woehl, J.E. Evans, I. Arslan, W.D. Ristenpart, N.D. Browning, ACS Nano 6 (2012) 8599.

[7] J.E. Evans, K.L. Jungjohann, N.D. Browning, I. Arslan, Nano Lett. 11 (2011) 2809.

[8] Y. Liu, K. Tai, S.J. Dillon, Chem. Mater. 25 (2013) 2927.

[9] N.T.K. Thanh, N. Maclean, S. Mahiddine, Chem. Rev. 114 (2014) 7610.

[10] H.-G. Liao, K. Niu, H. Zheng, Chem. Commun. 49 (2013) 11720.

[11] L. Marton, Phys Rev 46 (1934) 527.

[12] M.J. Williamson, R.M. Tromp, P.M. Vereecken, R. Hull, F.M. Ross, Nat Mater 2 (2003) 532.

[13] H. Zheng, R.K. Smith, Y. Jun, C. Kisielowski, U. Dahmen, A.P. Alivisatos, Science 324 (2009) 1309.

[14] H. Zheng, S.A. Claridge, A.M. Minor, A.P. Alivisatos, U. Dahmen, Nano Lett. 9 (2009) 2460.

[15] Hong-Gang Liao,, Likun Cui,, Stephen Whitelam,, and Haimei Zheng, Science 336 (2012) 1011.

[16] N. de Jonge, D.B. Peckys, G.J. Kremers, D.W. Piston, Proc. Natl. Acad. Sci. 106 (2009) 2159.

[17] W. Abidi, P.R. Selvakannan, Y. Guillet, I. Lampre, P. Beaunier, B. Pansu, B. Palpant, H. Remita, J. Phys. Chem. C 114 (2010) 14794.

[18] E. Gachard, H. Remita, J. Khatouri, B. Keita, L. Nadjo, and Jacqueline Belloni, New J Chem 22 (1998) 1257.

[19] N.M. Schneider, M.M. Norton, B.J. Mendel, J.M. Grogan, F.M. Ross, H.H. Bau, J. Phys. Chem. C 118 (2014) 22373.

[20] G. Mettela, R. Boya, D. Singh, G. V. P. Kumar and G. U. Kulkarni, (2013) 1793.

[21] J. Biswal, S.P. Ramnani, R. Tewari, G.K. Dey, S. Sabharwal, Radiat. Phys. Chem. 79 (2010) 441.

[22] T. Hori, K. Nagata, A. Iwase, F. Hori, Jpn. J. Appl. Phys. 53 (2014) 05FC05.

[23] R.G. Weiner, C.J. DeSantis, M.B.T. Cardoso, S.E. Skrabalak, ACS Nano 8 (2014) 8625.

[24] J.M. Joseph, B. Seon Choi, P. Yakabuskie, J. Clara Wren, Radiat. Phys. Chem. 77 (2008) 1009.

GENERAL CONCLUSIONS

Our main goal in this work was to reveal the reasons promoting anisotropy in size controlled synthesis of gold nanoparticles in aqueous phases. The classical way used to produce anisotropic gold nanoparticles is based on seeded growth method where pre-prepared seeds are added in a growth solution. Through a systematic study on the genesis of anisotropy with respect to "seed size" and "crystal morphology", we particularly focused on the complete structural characterization of initial and final objects. It is known form the literature that the formation of anisotropy results from an intricacy between the initial structure of seeds and the kinetic conditions controlled by the composition of the growth solution. While the majority of studies concentrate on the growth conditions, a few of them describe the key role of the seed structure. The main reason is the difficulty to attain the characterization of small size seeds. Today, thanks to the development in microscopic technics, characterization of small size particles becomes possible. Here, we take benefit of these progresses to investigate a quantitative study on the impact of seed internal structure on the development of anisotropy in gold nanoparticles known to be FCC in bulk structure. The thesis brings some answer to the two main questions used as a guideline of this thesis:

I. How to control the crystal structure and the size of seeds?
II. What are the influences of controlled seed size and structure on the kinetics of growth?

III. How to control the crystal structure and the size of seeds?

To be able to study the impact of seeds used in seeded growth method, the first objective was to synthesize seeds with different characteristics in size, shape and structure. Seeds with tunable sizes and crystal structures were obtained with respect to the surface ligand and the reducing agent employed during their synthesis. Small sized precursors (2.0 nm) without any crystal defects can be obtained easily via chemical reduction method with the use of cationic surfactant (CTAB) and strong reducing agent (i.e. $NaBH_4$). Change of the ligand to tri-sodium citrate lead to transformation of the crystal structure of the seed as well as their size. To be specific, nanoparticles are no longer single crystalline (*defects and twining's*

are introduced) and size of seed is increased (4.9 nm). Induced twinings tends to be well organized around a common 5-fold twining axis for a given size (4.9 nm). Size of these defected particles can be control additionally by changing the reducing conditions. Namely, employment of another type of reducing agent (*i.e. ascorbic acid*) will increase the seed size. In parallel, for similar ligand (citrate) but different chemical reducing conditions (*high temperature in reverse Turkevitch conditions*) bigger size (8.7 nm) and different structure is obtained. The originality of this first part was to give quantitative characterizations of four different seeds prior to their used in growth solutions. Their use in a chosen growth media lead to complete different final structures for each of them.

For the control of seeds, a change of the ligand and the reducing conditions is needed. The main point is certainly the difficulty to obtain single crystal seeds. Only one condition (with CTAB 0.1 M) permit to attain such structure and small size.

IV. What are the influences of controlling seed size and structure on the final nanoparticle?

- By using different seeds in a given growth solution, nanoparticles with different final structure can be obtained. Regardless of the size, change in the crystal structure of the nanoparticle is an inherited process, meaning that the particle will remember such transformation in the crystal structure at all times. When 2 nm CTAB single crystalline seeds are used as precursors in a growth solution with the following chemical composition, CTAB 0.1M, $HAuCl_4$ 0.5 mM, AA 0.75 mM, $AgNO_3$ 0.045 mM, high yield (> 95%) of single crystalline nanorods are obtained. The variation of the amount of added seeds only influences the final aspect ratio, but not the internal structure of the final nanorods. On the contrary, when sub-5 nm defected citrate capped seeds are used as precursors, in the same growth media, final nanoparticles exhibit small elongation (AR~1.7) with morphologies similar to bean shapes (*bearing penta-twinned structures*). These beans elongate into bipyramids (*having similarly penta twinned structure with sharper tips and high index surface steps {151}*) when the amount of added seeds is decreased or when the initial pH of the growth solution is decreased.

In contrary when the size of the defected seeds is increased over 5 nm (*seeds stabilized by ascorbate*), the anisotropy is lost vastly for given growth condition. In other words, for this

large size seeds, with penta-twinned structures, the performance of the seed to form anisotropy is decreased yielding only spherical nanoparticles. At the end, the large sized multi-twinned seeds (*obtained by reverse Turkevitch method*), possess in majority crystal structures much complex than penta-twinned and yield only spheroid particles after growth for the growth solution with similar chemical composition listed in previous part (CTAB 0.1M, $HAuCl_4$ 0.5 mM, AA 0.75 mM, $AgNO_3$ 0.045 mM).

This means that the growth of seeds, with inherited crystal structures, will cause final states exhibiting similar type of crystal structures; single crystalline seeds yielding single crystalline nanorods, defected seeds yielding defected nanoparticles.

- Through an original competitive growth between two families of seeds (*2 nm CTAB single crystal and sub-5nm citrate penta-twinned seeds*) in the same growth solution, we demonstrated the higher reactivity of multi-twinned seeds over single crystalline ones. Since surface of both seeds (*2 nm CTAB capped and sub-5 nm citrate capped*) are quite reactive for colloidal gold to promote desired shape (*one being nanorod and other nanobean*), their simultaneous growth in the same reaction container, will result in a competition for gold source between given precursors. At the end, both structure will be formed (*single crystalline and multi twinned*) but the higher surface reactivity of penta-twinned seeds will favor the formation of higher percentage of final multi-twinned nanoparticles. Single crystal seeds could not grow by depletion of reactant if only few amounts of multi-twinned seeds are initially present. The final yield of nanorods will decrease from 82% to 20% when the number percent of the penta-twinned seeds in the initial added seed is increased from 1.5% to 12%.

Both anisotropic final states (*nanorods and nanobeans*) can be related to the initial precursors by complex growth mechanism dictated by the chemical reagents in the growth solution. In other words, employed shape directing agent and surface ligand would control the formation of anisotropic shapes from given seed by preserving the inherited crystalline structure.

Such competitive approach between two other families of multi-twinned particles does not evidence higher reactivity for one of them even though it has been demonstrated that the crystal structure of both precursor differ from each other (*8.7 nm citrate capped seed bearing complex internal structures in majority, 5.6 nm ascorbate seeds bearing mainly penta-twinned structures*). In this case the final nanospheres obtained from the competitive growth

of both seeds will have an intermediate size (~ *25 nm*) between the final nanoparticles obtained from the single growth of each seed *(~35 nm for the spheroids obtained from large sized citrate capped seeds and ~17 nm for the spherical particles obtained from ascorbate seeds*).

- Using HRTEM and electron tomography, we definitely proved the penta-twinned structure of the nanobeans and bipyramids. This structure was determined for different size of nanoparticles (*representing the different steps of growth*). In the framework of an atomistic modelisation, it was also demonstrated that environment can control to the nature of the most stable shape in elongated penta-twinned structure to yield penta-twinned nanorods or penta-winned bipyramids. Such stabilization supports the experimental feature of the formation of:

  i. penta-twinned bipyramids from sub 5-nm penta-twinned citrate seeds in silver(I) assisted seed mediated growth
  ii. few penta-twinned nanorods from sub 5-nm penta-twinned citrate seeds without silver in similar seed mediated growth

Changing the ligands from CTAB to CTASB drastically changes the orientation of the final structure (*nanorods obtained rather than bipyramids*).

- Finally, to follow different steps during the development of anisotropy in gold nanoparticle formation, we went towards recent *in-situ* STEM experiments by using a liquid cell. The originality of the experiment was to follow the gold reduction directly in a CTAB media for the first time. Contrary to the batch reaction used in first three chapters, we take benefit of the reducing species (*aqueous electrons and radicals*), produced by the radiolysis of water under electron beam, to proceed to the total reaction: *in-situ* production of seeds and *in-situ* growth. The limitations for microscopy observations (*such as presence of surfactant*) have been overcome by the use of a surfactant concentration relatively lower than the classical growth conditions (*10 mM rather than 100 mM*). In these conditions the concentration of oxygen (O_2) in the media appears to be a key parameter. Under the electron beam,

- in aerated sample, seeds generated by *in-situ* STEM, tend to form branched structures with additional tapered bipyramids. Anisotropy of these branched nanoparticles, to yield bipyramids, can be controlled easily by optimization of the reduction conditions with respect

to dose rate (*in other words with modification of electron beam parameters*). Formation of such branched particles rather than well-defined shapes (*such as nanorods or solid bipyramids*) can be justified by the fact that, reduction achieved in high dose regime of microscopy is not directly comparable to the chemical reduction of gold precursor by mild reducing agent to form rigid shapes. For *in-situ* STEM the concentration of reducing species is larger than the traditional batch conditions (C_{eh}^{-}~3 mM $C_{Ascorbic\ Acid}$=0.75 mM). The first conclusion is clearly a strong dependence of the final structure on the injection rate of reducing species in the solution. While high dose rate lead to the loose of anisotropy, lower dose rate lead to bipyramids and stars shapes. In relation to the observation on the batch formation of nanoparticles, we expect multi-twinned structured seeds formed under electron beam to explain the formation of bypiramids.

- In the absence of O_2 in the growth solution, the results are completely different since this reagent is a scavenger for aqueous electrons. This induces different reduction kinetics (*rapid nucleation of large number of seeds due to presence of vast number of reducing agent, e^{-}_{aq}*) and favors the formation of more spherical shapes and additional single crystalline nanorods. This experiment was additionally compared to a traditional radiolysis experiment (*via γ irradiation source*), operated on similar chemical conditions, which mainly give single crystalline nanorods. In deaerated system even though the dose is largely different *(~ 10^1 Gy/s for γ irradiation source and ~10^7 Gy/s for in situ STEM*) few single crystalline nanorods are formed as in radiolysis studies. From this study, 1) we have obtained an original and simple way to produce single crystalline nanorods via radiolysis and 2) we have demonstrated the possibility to follow the kinetic by *in-situ* STEM. Yet, this last set of experiments represents initial results and asked for further investigations to conclude on the final mechanism.

To conclude, although these *in-situ* STEM experiments are preliminary experiments, they will open the way to new approaches to investigate mechanism working during the formation of anisotropic nanoparticles. The importance of radiolysis events under electron beam has to be considered for interpretation and appears as the key factor to control the formation of nanoparticles. It is interesting to retrieve the same tendencies of batch reaction, where higher reducing agent concentrations lead to a loose of anisotropy. The key role of oxygen was evidenced and analyzed by an original comparison with traditional γ irradiation process.

As a final conclusion, we have demonstrated the importance of the nature of seeds used in seeded growth method to produce anisotropy. The kinetic influences of the composition of the growth solution only modulate the ratio between the anisotropic and isotropic shapes but do not transform the initial crystal structure of the added seeds. Quantitative analysis of seeds with *in-situ* STEM experiment offers a complete study in the influence of the structure of seeds on final shape.

APPENDICES

Appendix 1

Characterization Techniques

1. Transmission Electron Microscopy (TEM)

Imaging, measuring, modeling and manipulating nano matters has been much easier since the development of TEM. Today, for nano materials, it is obvious that TEM is the central tool for the complete characterization of nanoscale materials and devices.

The smallest distance between two points that we can resolve with our eyes is around 0.1 – 0.2 mm assuming that our eyes are in perfect health and there is a sufficient illumination in the environment. To explain the resolution of the microscope in such a manner, we should introduce Rayleigh Criterion. According to Rayleigh criterion, the smallest distance that can be resolved, δ, is given by;

$$\delta = \frac{0.61\lambda}{\mu \sin \beta} \tag{1.1}$$

Here, λ refers to the wavelength of the radiation, μ to refractive index of the medium and β the semi angle of the collection of the magnifying lens [1]. So by using the equation in 1.1 we can approximate the average resolution in conventional TEM's as 0.2-0.5 nm [2] .

The column in TEM bears an electron gun source, electromagnetic lens system, sample holder and an imaging system (Figure 1). Electron source consists of a tungsten filament which emits electron when it is heated. Created beam of electrons is accelerated to energy in the range 20-1000 keV in the electron gun and then directly is focused on the specimen by using electromagnetic lenses. Electrons passed through the specimen are then reflected on a phosphorescent plate. The transmitted electron beam is highly dependent on the properties of the material (*density, composition, porosity, etc.*) that is under examination. In case of obtaining information at atomic sizes, mode of operation changes to High Resolution TEM, meaning that machines operates at higher magnifications to obtain details in real space as well as reciprocal space.

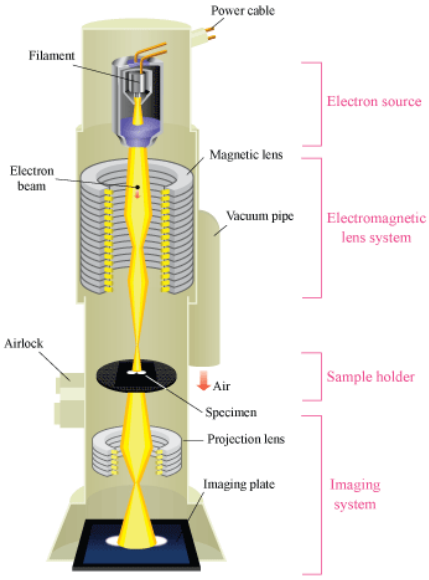

Figure 1 *Schematic Outline of a TEM [3]*

2. UV-Vis Spectroscopy (UV-Vis)

When sample molecules are exposed to light, having an energy that matches a possible electronic transition within the molecule, some of the light energy will be absorbed as the electron is promoted to a higher energy orbital. An optical spectrometer records the wavelengths at which absorption occurs, together with the degree of absorption at each wavelength. The resulting spectrum is presented as a graph of absorbance (A) versus wavelength as in the case of Figure 2 [4]. The Beer-Lambert law states that the absorbance of a solution is directly proportional to the concentration of the absorbing species in the solution and the path length. Thus, for a fixed path length, UV-Vis spectroscopy can be used to determine the concentration of the absorber in a solution. The change in intensity could be described by the Beer Lambert law as shown below in equation 1.2 [5].

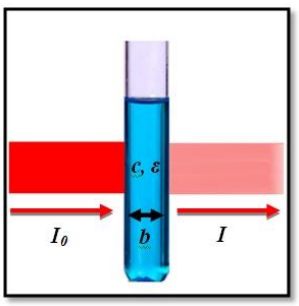

Figure 2 *Presentation of UV Spectroscopy*

$$A = -\log T = -\log(\frac{I}{I_0}) = \varepsilon bc \quad (1.2)$$

In Eq. 1.1 A is the measured absorbance, T is the transmittance, I_0 and I are the intensities of incoming and transmitted light, respectively, ε is the molar absorptivity (L mol^{-1} cm^{-1}), b is the path length of the cell (cm) and c is the concentration (mol/L).

Usually a deuterium discharge lamp is used as a light source for UV measurements and a tungsten-halogen lamp for visible and NIR measurements. The wavelengths of these continuous light sources are typically dispersed by a holographic grating in a single or double monochromator or spectrograph. The spectral band pass is then determined by the monochromator slit width or by the array-element width in array-detector spectrometers. Spectrometer designs and optical components are optimized to reject stray light, which is one of the limiting factors in quantitative absorbance measurements. The detector in single-detector instruments is a photodiode, phototube, or photomultiplier tube (PMT).

3. Small Angle X-Ray Scattering (SAXS)

Other than electrons, x-rays may also be used to investigate the structural properties of materials at different states up to 1-2 nm resolution. X-ray scattering techniques became one of the major tools to characterize broad range of materials, from small peptides to huge macromolecules by using brilliant synchrotron sources.

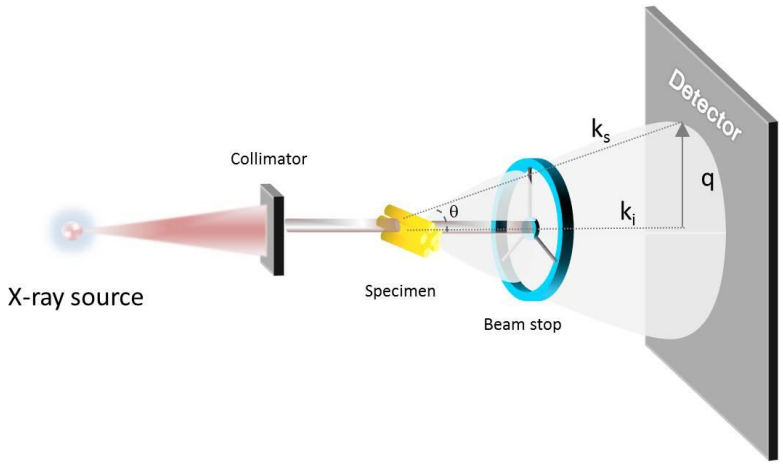

Figure 3 *Schematic representation of SAXS apparatus*

The main principle of SAXS was developed in late 1930s by A. Guinier. He used scattering, to analyze characteristics of metallic alloys such as size, shape and internal structure. Conceptually, typical SAXS experiment starts when the emitted x-ray beam reaches to the sample with incident wave vector of k_i. Density variations in the sample will scatter some of the x-rays away from the primary beam with an angle so called scattering angle, 2θ. The unscattered radiation is than stopped by the beam stop to prevent damage to the detector. After, scattered radiations interfere with one another, there will be constructive interference along certain angles, causing peaks to present themselves [6]. Recorded spectra contain information on scattered intensity as a function of scattering angle, 2θ. The interference pattern is characteristic to the internal structure of the material [7].

$$q = \frac{4\pi \sin(\theta)}{\lambda} \tag{1.3}$$

There are several reasons that SAXS is more advantageous than other comparable techniques. One of the biggest advantages is that solutions can be analyzed via SAXS and sample does not need to be crystallized. Those reasons allow analyzing large number of different sized particles than many other methods [6].

4. Dynamic Light Scattering (DLS)

Dynamic Light Scattering (DLS) is another powerful and well-established scattering technique to measure size and size distribution nanoparticles in suspension under submicron region. Basically, due to Brownian motion of particles or molecules in suspension, light is scattered at different intensities causing a fluctuation in intensity. Technique is based on analysis of those fluctuations to obtain the velocity of the Brownian motion thus, the particle size by using the Stokes-Einstein relationship [8].

The primary result from DLS is typically the mean value from the intensity distribution (*called the Z average*) and the polydispersity index (PDI) to describe the distribution width. It is possible to convert from the intensity to a volume or number distribution in order to compare to other techniques.

The systems having Pdl value less than 0.1, is generally defined as “monodisperse”. The formula of Pdl is;

$$Pdl = (\frac{\sigma}{d})^2$$

where σ is the standard deviation and d is the mean diameter.

Appendix 2

Further Analysis on Varied Type of Seeds

- ***Estimation of Size from microscopy observations for CTAB capped seeds (Type 1)***

To obtain more statistical data on the size and the crystal structure of CTAB capped seeds (*Type 1*), we have captured multiple HRTEM images of single nanoparticles (~10 images) at 80 kV. In the next figure, some of the observed nanoparticles are summarized. The average diameter of the seed is calculated as 2.1 nm. Most of the seeds bear single crystalline structure for given size average.

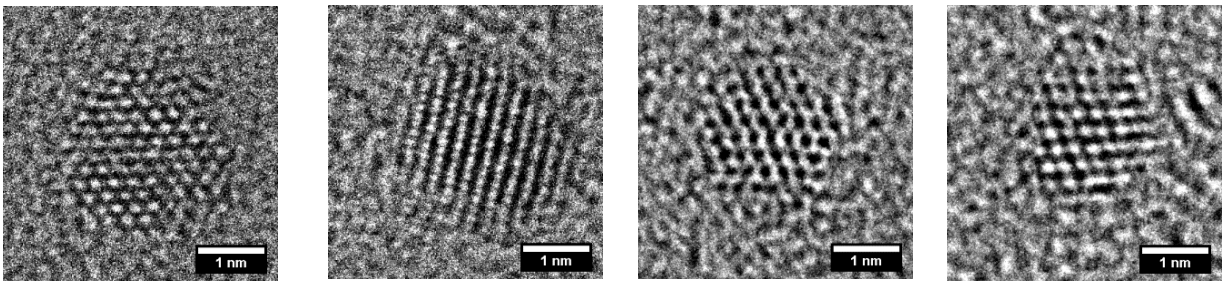

Figure 4 *HRTEM images of Type 1(CTAB capped) seeds*

- ***Further analysis on Citrate capped seeds (Type 2)***

The volume size distribution of Type 2 seeds (*obtained by DLS*), acquired on different dates, is summarized in Figure 5a. To be specific, given DLS spectrums correspond to the same chemical compositional seed (*same preparation method*) and the only variable is the time of preparation. The large variation in the particle diameter shows the low reproducibility of the nanoparticle size.

The TEM observations on freshly prepared Type 2 seeds reveal that the particles form large aggregates on the carbon support when solvent is evaporated (Figure 5b). Such reason prevents any attempts of high resolution imaging on Type 2 seeds, to reveal the real crystal structure of particle before aggregation (*TEM sample is prepared 5 minutes after the synthesis of seed*).

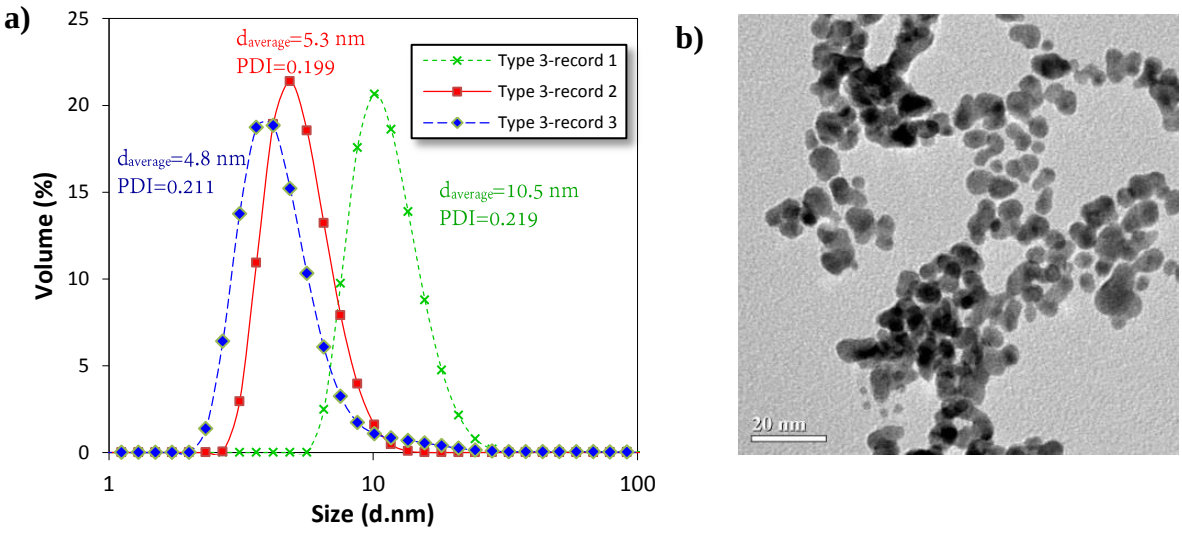

Figure 5 a) *Volume size distribution of various type 2 nanoparticles (prepared in presence of citrate when NaBH4 is used as reducing agent) acquired at different times* ***b)*** *TEM image of Seed 2 prepared 5 minutes after synthesis*

- ***HRTEM images of Type 3 Seeds***

As we explained previously, citrate capped seeds, prepared by Reverse Turkevich method, exhibit complex internal structures. Further images of same type of seeds are given in the following figure showing that particles bear multiple twinning faults. Even though some decahedral particles are observed, most of the particles have spherical profiles like the ones given in Figure 6 with unknown crystal structures (the *morphology resembles to icosahedron but additional characterization is needed to reveal complex internal structure of the particle*).

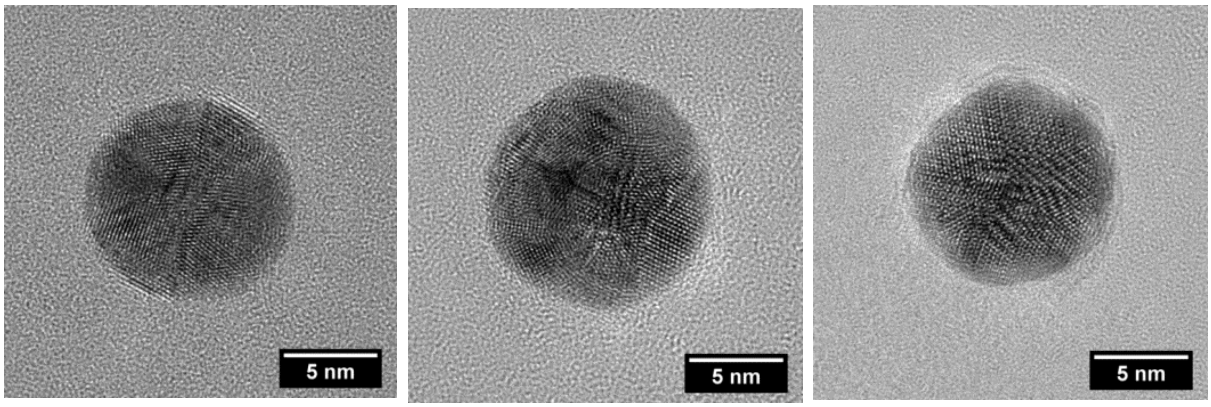

Figure 6 *HRTEM images of Type 3 seeds prepared by reversion the order of addition of reactants in classical Turkevich method*

- ***HRTEM images of Type 4 Seeds***

During microscopy observations on Type 4 seeds, prepared via milifluidic set-up, two different crystalline structures were revealed; large size penta-twinned particles (>5 nm) as given in Chapter II and small sized single crystalline particles (<5 nm) as given in Figure 7. Mainly, the crystalline structure is a mixture of both types.

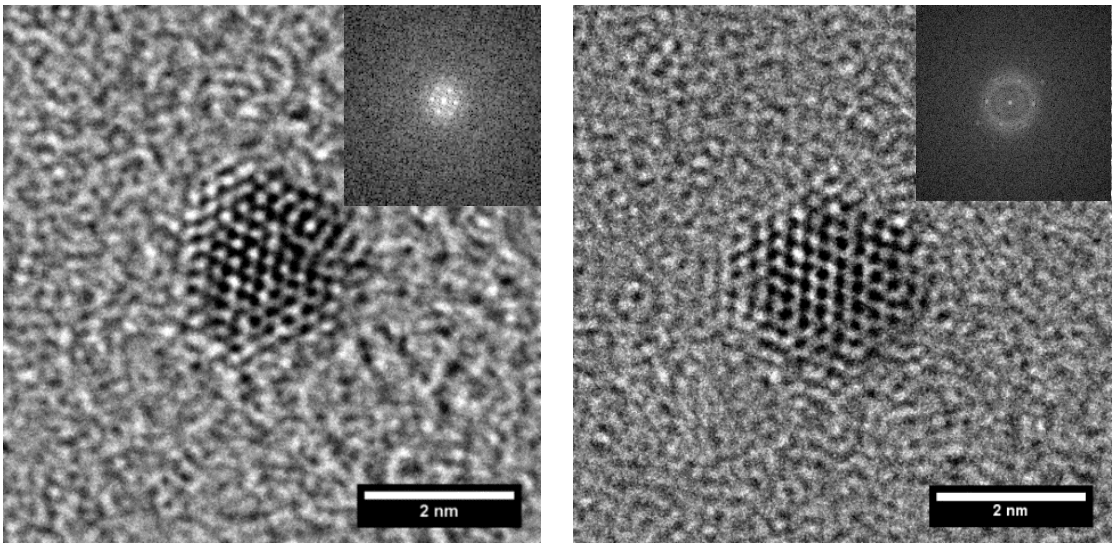

Figure 7 *HRTEM images of Type 4 seeds obtained by milifluidic set-up*

Appendix 3

Analysis of UV-Vis Spectrums of Final Nanoparticles

The UV-Vis spectra's of the gold nanorod samples, (*corresponding TEM images given in Chapter IV.A.4.3.1*), are shown in Figure 8 with detailed analysis of each spectrum summarized in Table 1.

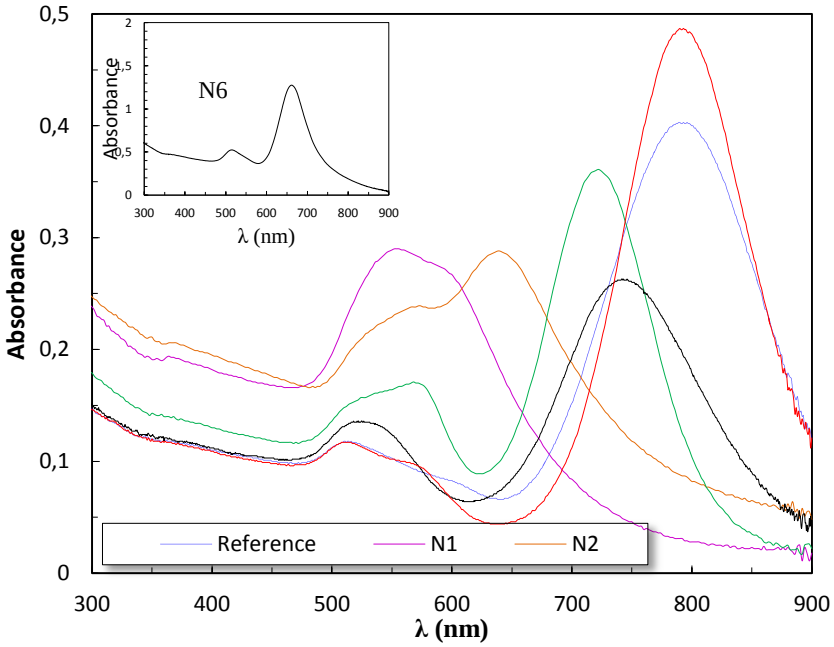

Figure 8 *UV-Vis Spectra's corresponding to nanorod solutions at different aspect ratios, given in Chapter IV (A.4.3.1)*

High yield and aspect ratio nanorods only obtained when the concentration of CTAB is over 100 mM (Ref, N5). For the other samples, mainly with decreasing CTAB, AR is decreased (the position of $\lambda_{l\text{-}SPR}$) is shifted to lower wavelengths than reference sample with decreasing absorbance value. Apart from N2, N3 and N4, other spectrums have similar absorbance value (0.11) at 400 nm, meaning that final Au(0) concentration integrated into NPs is quite similar (~0.44 mM). In case of N2, N3 and N4, presence of high concentration of NaBr prevents us to calculate the gold concentration, by the direct relation, given in Chapter 2 (Eq. 2.4), between the absorbance (400 nm) and the colloidal gold concentration, since the extinction coefficient varies for these samples. In the concentrated sample (N_6) 1.76 mM

Au(0) concentration means that only 70% of the initial Au(3+) is reduced ($[Au(3+)]_{initial}$=2.5 mM).

Table 1 *Analysis of UV-Vis Spectra's for corresponding nanorod solutions given in Chapter IV (part A)*

Sample	$\lambda_{l\text{-}SPR}$	$A_{l\text{-}SPR}$	$\lambda_{t\text{-}SPR}$	$A_{t\text{-}SPR}$	$A_{400\ nm}$	**[Au(0)]**	**AR (from UV)**	**AR (from TEM)**
Ref	790	0.403	510	0.117	0.108	0.432	3.2	2.70
N_1	590	0.274	550	0.290	0.182	0.728	1.2	1.50
N_2	645	0.286	570	0.238	0.194	0.776	1.7	1.55
N_3	725	0.360	530	0.157	0.130	0.520	2.6	2.10
N_4	740	0.265	525	0.136	0.108	0.432	2.6	2.30
N_5	790	0.487	510	0.117	0.108	0.432	3.3	2.75
N_6	655	1.250	512	0.520	0.440	1.760	1.90	2.10

The aspect ratios of final nanorods are both calculated from UV-Vis spectrums (Chapter II, Eq.2.3) and corresponding TEM images. The large variation between both values can be explained by the fact that, ARs obtained by UV corresponds to the samples right after the termination of growth and before applying any purification. Decrease of the ARs (obtained by TEM) of nanorods mean that particles reshape easily under rapid centrifugation and exhibit smaller sizes.

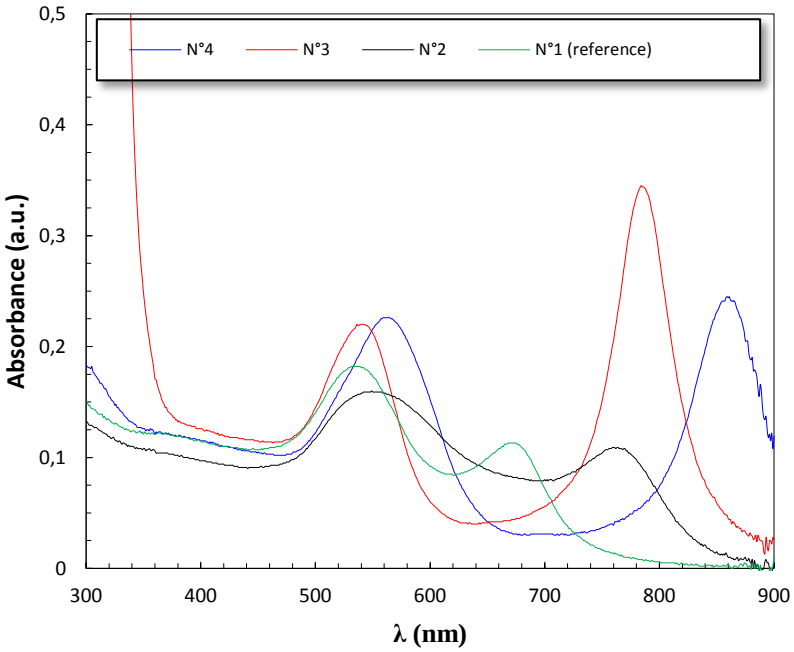

Figure 9 *Corresponding UV-Vis Spectrums of Bipyramids given in Chapter IV (B.4.3.1)*

The UV-Vis spectra's of bipyramids (*the chemical composition of the growth solutions are given in Chapter IV, Table IV.4*) characterized by TEM in previous chapters are given in Figure 9. Only the sample N3 and N4 bear sharp $\lambda_{l\text{-}SPR}$ peaks as we seen previously in Chapter II (Figure II.18), meaning that mostly these sample contain large amount of bipyramids with sharp tips. Additionally, positioning of $\lambda_{l\text{-}SPR}$ at higher wavelengths (~800 nm) for those samples, mean that bipyramids bear high aspect ratios than the other samples, where major of the structure is composed by nanobeans.

The colloidal gold concentration (*calculated by using Eq. 2.4 given in Chapter II*), deviates slightly from each other, but the most of the Au(III) is converted in final for all cases (yield of conversion for N°3> 78%*).

Table 2 *Analysis of the UV-Vis Spectra's for corresponding bipyramid solutions given in Chapter IV (part B)*

Sample	**$\lambda_{l\text{-}SPR}$ (nm)**	**$A_{l\text{-}SPR}$**	**$\lambda_{t\text{-}SPR}$ (nm)**	**$A_{t\text{-}SPR}$**	**$A_{400\ nm}$**	**[Au(0)] (mM)**
N°1(reference)	669	0.113	541	0.181	0.114	0.456
N°2	767	0.108	556	0.164	0.097	0.388*
N°3	783	0.343	539	0.220	0.125	0.500
N°4	858	0.244	559	0.226	0.114	0.456

HRTEM Study of Gold Bipyramids with different AR

In Figure 10 and 11, both bipyramids are analyzed with the same methodology described previously in Chapter II, Part B. These bipyramids correspond to the reference sample (N°1) reference composition, given in Table IV.4 and analysis of spectrum given in Figure 9).

In Figure 10, in this orientation, the crystals located on the sides of the bipyramid (a) have the same orientation: e.g. <112> zone axis (b). This result can be interpreted in agreement with a penta-twinned structure of the bipyramid (c).The corresponding SAED pattern may be analyzed as the superimposition of <211>, <112>, <001> zone axes diffraction patterns (d). The supplementary weak reflections observed in the SAED pattern are due to multiple scattering.

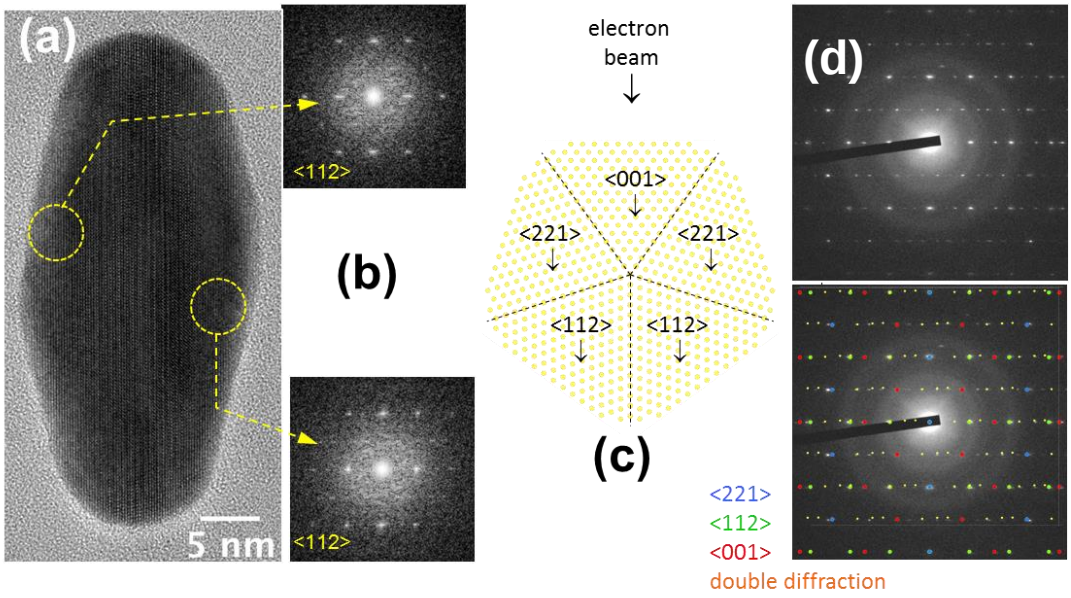

Figure 10 *Structure analysis of large sized bipyramids with the crystal on the sides located oriented along <112> zone axis's*

The bipyramid, given in Figure 11, is observed with the same direction as in the one observed in Chapter IV, Figure IV.15. In this orientation, crystals located on the sides of the bipyramid (a) have different orientations: <110> and <111> zone axis (b) respectively. This result supports the assumption of a penta-twinned structure of the bipyramid (c).

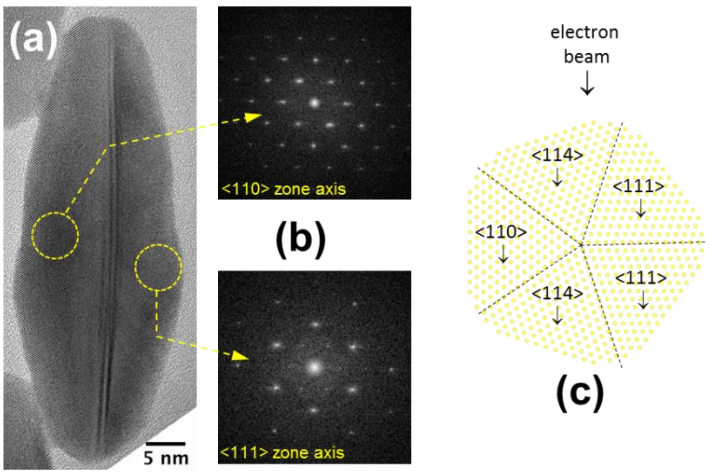

Figure 11 *Structure analysis of large sized bipyramids with crystals on the each sides oriented along <110> and <111> zone axis's*

Mathematical Model Developed for Elongated Bipyramids

The CrystalMaker software was used to reproduce the structure of a bipyramid observed along different zone axis's, to explain the variation of the thickness of the twinning plane for each different bipyramids.

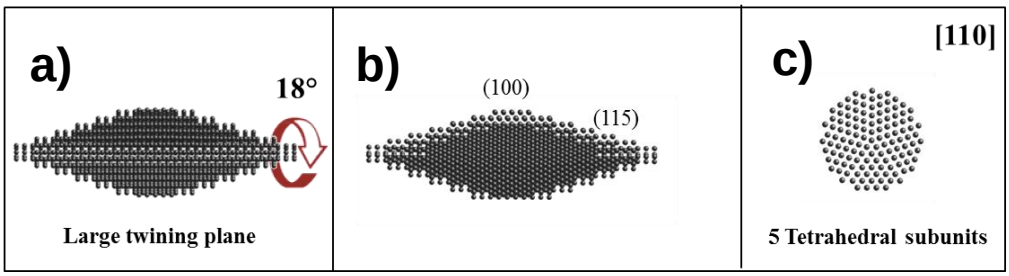

Figure 12 *Different orientation of 3D mathematical model developed for elongated bipyramids.*

Mainly, the thickness of the twinning plane varies depending on the orientation of the nanoparticle; *i.e.* when the particle is observed on [110] direction (*along the twinning axis*), decahedral cross section of the bipyramid seen clearly (Figure 12c), whereas the view, from perpendicular direction to the twinning axis, results with the visualization of entire bipyramid on TEM support with thick twining area (Figure 12a). By turning the model 18°, around the twining axis with respect to the initial orientation, we obtain the view in Figure 12b. In this orientation the observed twining plane is thinner than the previous case (Figure 12a). This model helped us to explain the large variation in the size of the twining planes of different bipyramids.

Appendix 4

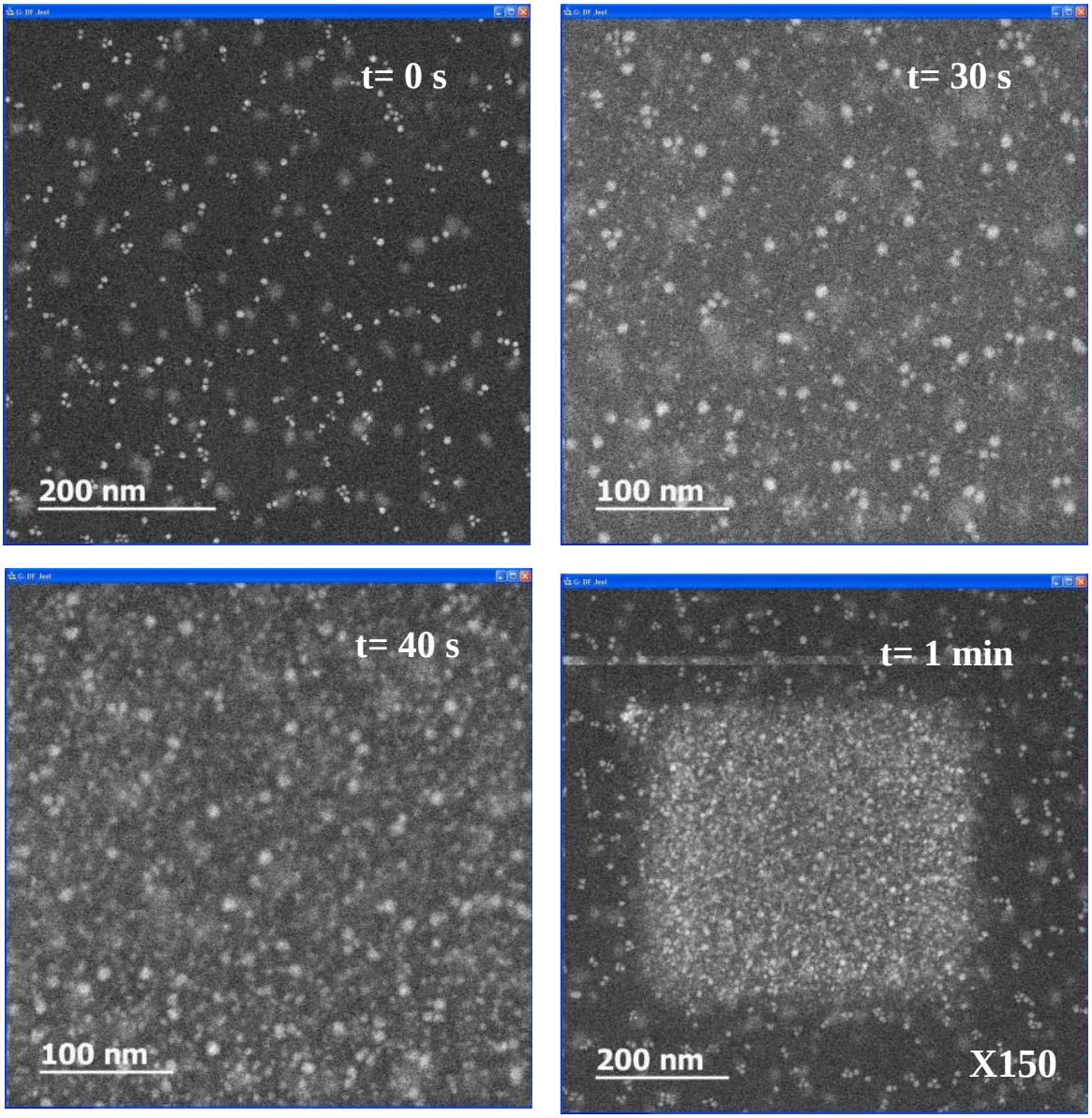

Record 1- *Magnification of x600k (dose rate of 8.08 $e^-/sÅ^2$) and Pixel Dwell Time of 2 µs (in the last image magnification is decreased to 150k)*

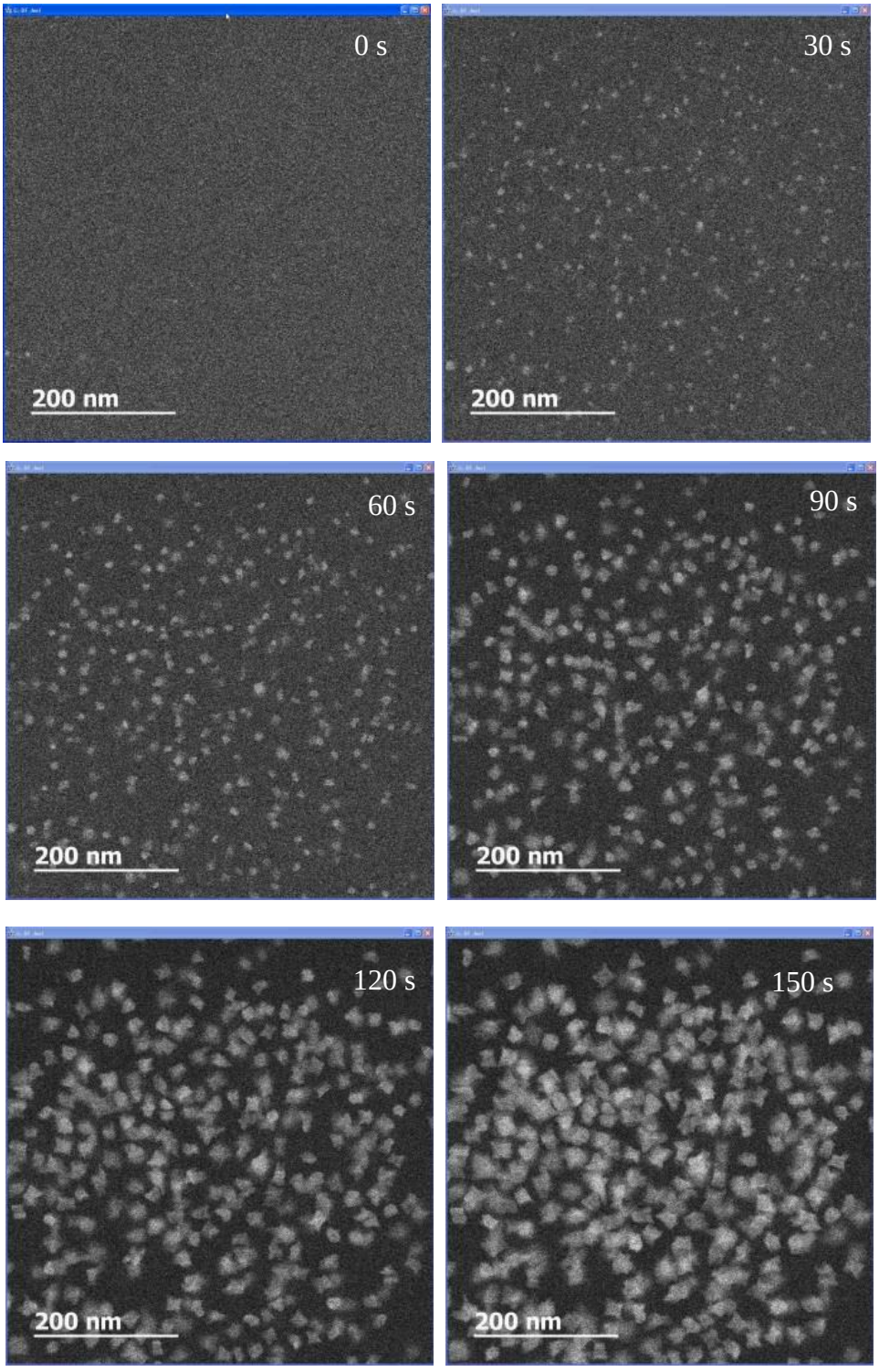

Record 2 *- Magnification of x400 (dose rate of 3.60* $e^{-}/s\text{Å}^{2}$ *) and Pixel Dwell Time of 2 µs*

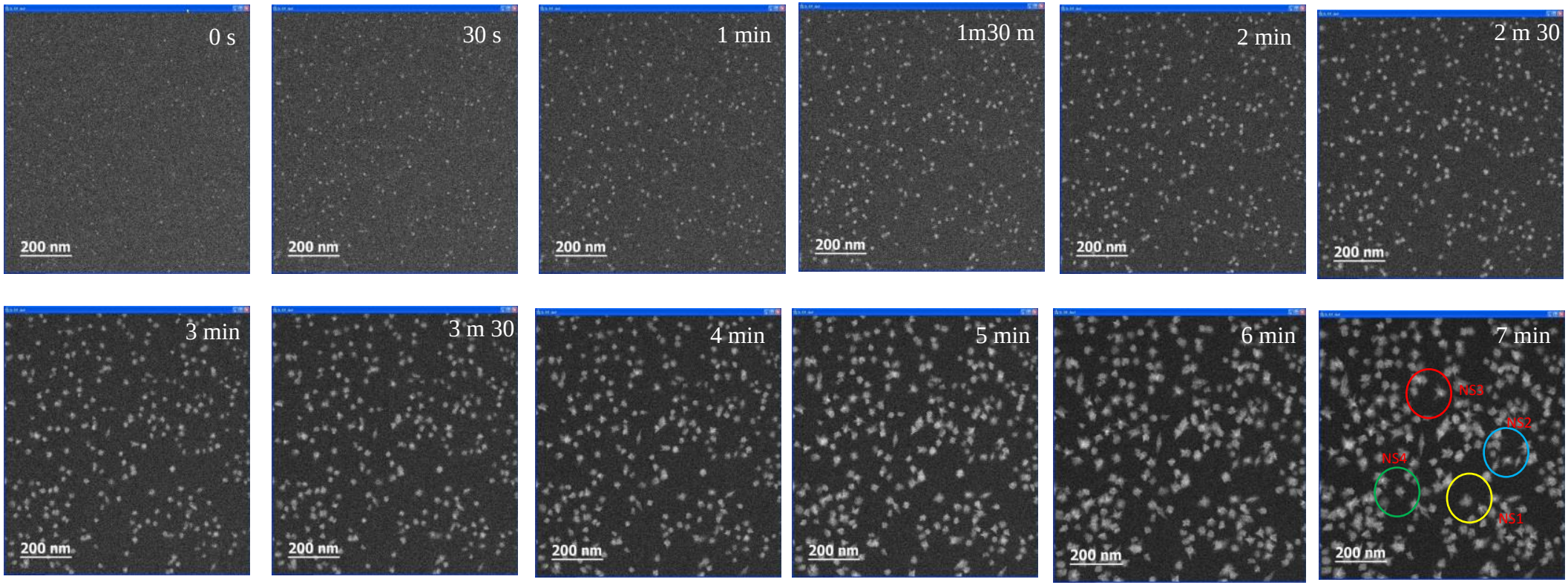

Record 3 *- Magnification of x250 (dose rate of 1.40 $e^{-}/sÅ^{2}$) and Pixel Dwell Time of 2 µs*

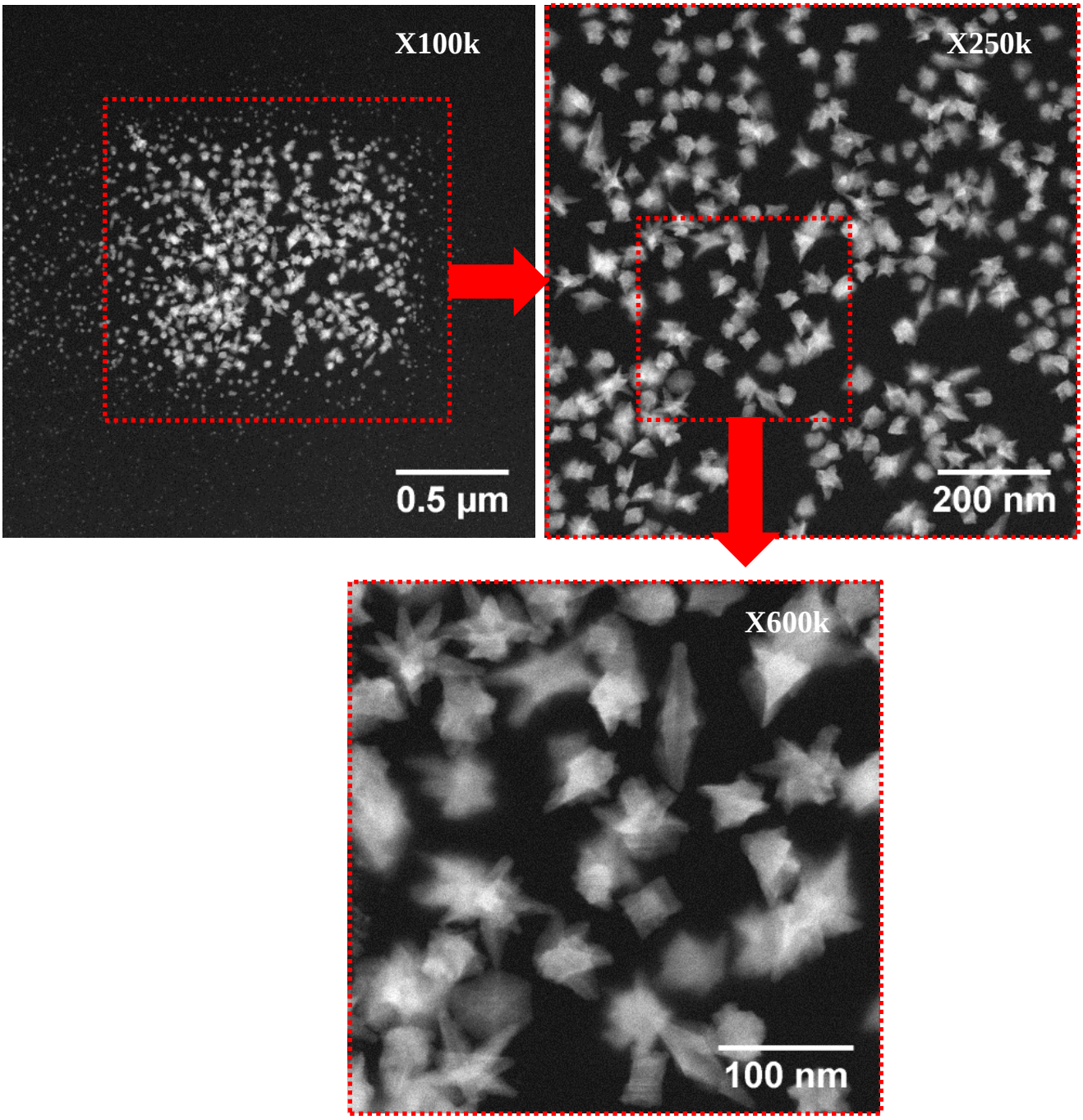

Record 3 *– High Magnification STEM images of the irradiation area after drying*

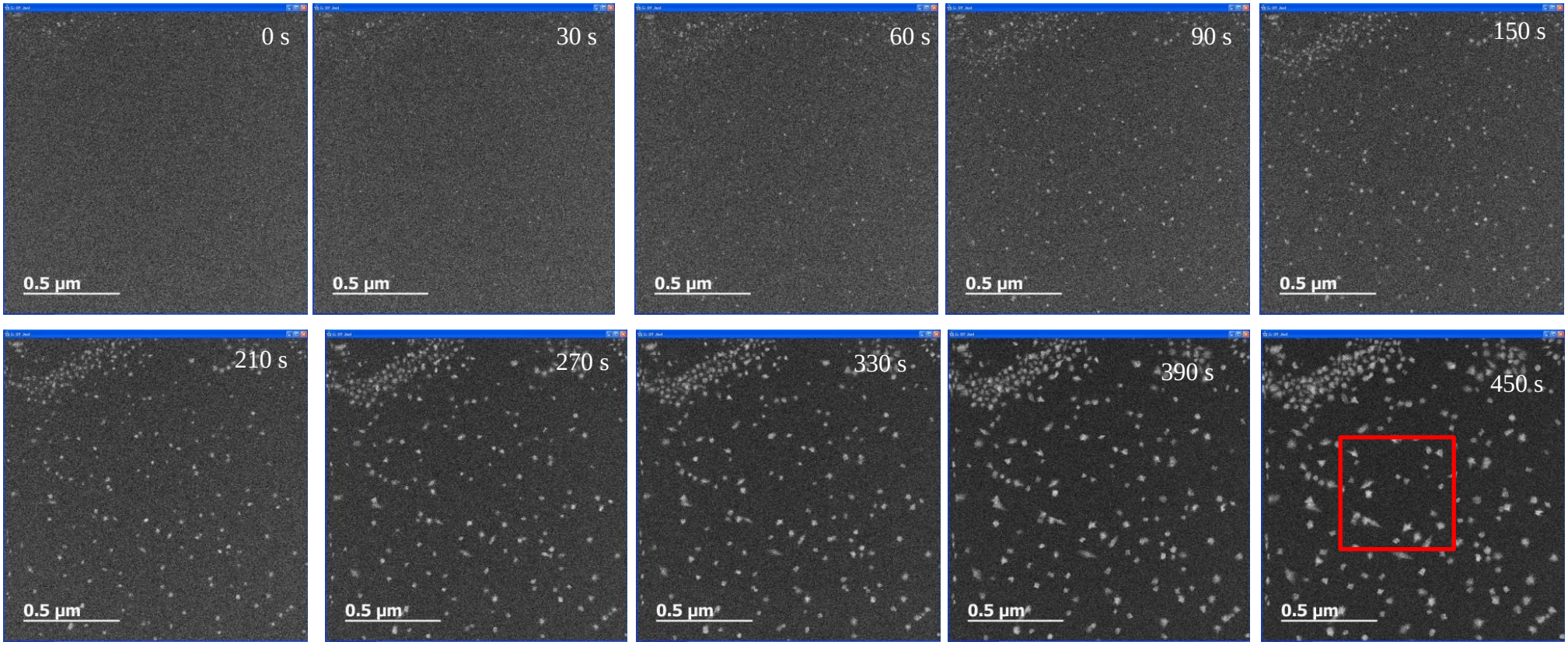

Record 4 *- Magnification of x150 (dose rate of 0.50* $e^{-}/sÅ^{2}$ *) and Pixel Dwell Time of 2 µs*

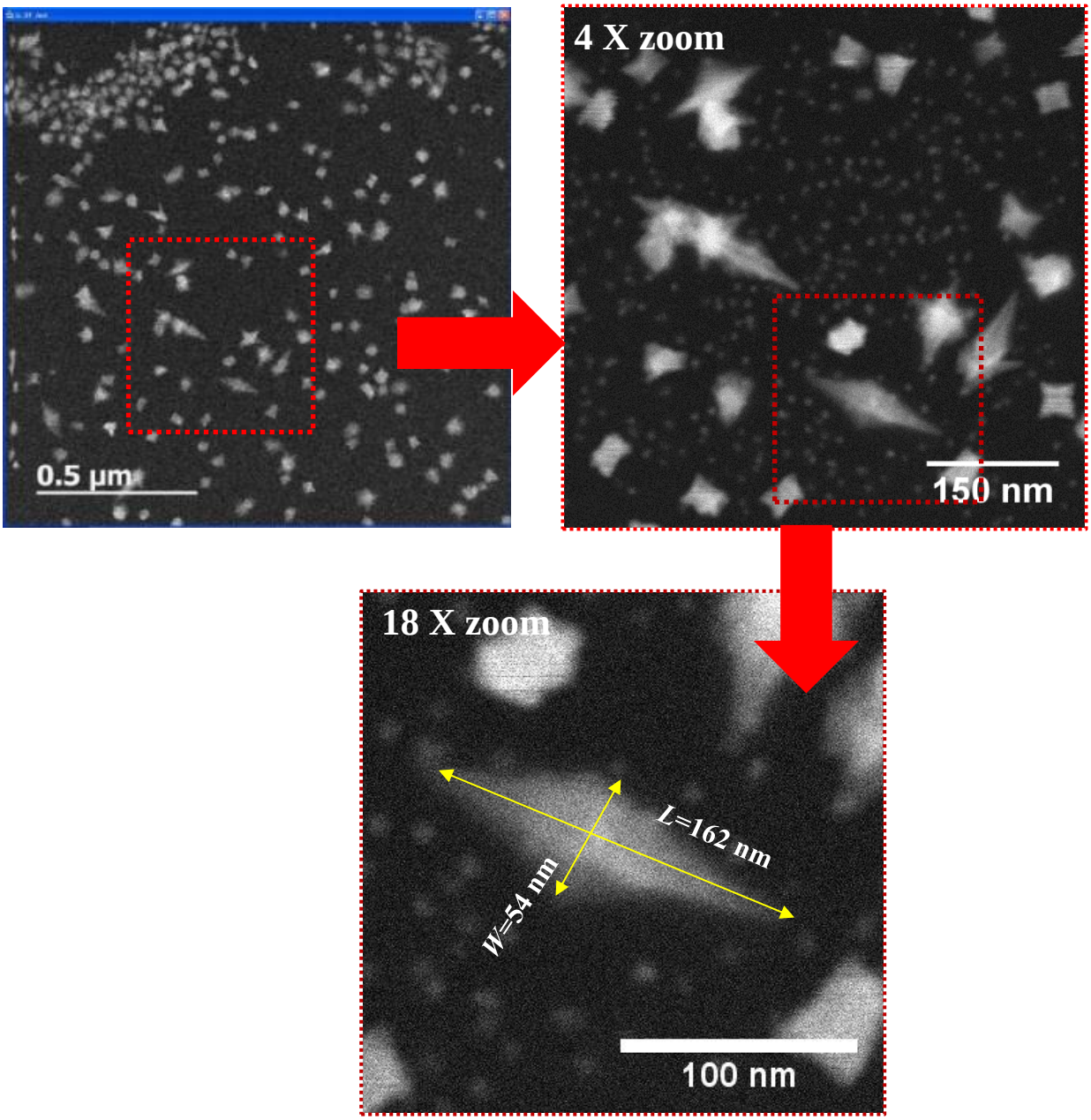

Record 4 *– High Magnification STEM images of the irradiation area, indicated in previous serie, after drying*

References

[1] D.B. Williams, C.B. Carter, Transmission Electron Micriscopy, 2nd ed., Springer, 2009.

[2] M. De Graef, Introduction to Conventional Transmission Electron Microscopy, Cambridge University Press, 2003.

[3] Basic Principles of Transmission Electron Microscope, n.d.

[4] W. Reusch, (2013).

[5] D.A. Skoog, S.R. Crouc, F.J. Holler, Principles of Instrumental Analysis, 6th ed., Belmont, CA : Thomson Brooks/Cole, 2007.

[6] C.E. Williams, R. P.May, A. Guinier, in:, X-Ray Charact. Mater., Wiley-VCH,, 1999.

[7] H. Schnablegger, Y. Singh, in:, SAXS Guide, 2nd ed., Anton Paar GmbH, Austria, 2011.

[8] Horiba Scientifique, (2014).

Direction de la Recherche des Etudes Doctorales et de la Volarisation

55 Avenue de Paris

78035 Versaille CEDEX

Tél. : 01 39 25 41 55 http://www.uvsq.f

Mot Clés : Anisotropie, Nanoparticule d'or, MET, Cristallographie, Control de la forme, In-situ MEBT

Key words : Ansiotropy, Gold Nanoparticles, TEM, crystallography, shape control, In-situ STEM